A Spectroscopic Investigation into the Photophysics of Donor-Acceptor Emitters Intended for Use in Thermally Activated Delayed Fluorescence Based Optoelectronic Systems: A Comparison of Excited State Dynamics in Solution and Solid-State

by

Lloyd Steven Fisher, Jr.

A dissertation submitted in partial fulfillment
of the requirements for the degree of
Doctor of Philosophy
(Chemistry)
in the University of Michigan
2023

Doctoral Committee:

Professor Theodor G. Goodson III, Chair
Professor Bart M. Bartlett
Professor Charles McCrory
Professor Pierre Ferdinand P. Poudeu

Lloyd S. Fisher, Jr.

lsfisher@umich.edu

ORCID ID: 0000-0002-6792-7199

© Lloyd S. Fisher, Jr. 2023

DEDICATION

This dissertation is dedicated to those that work towards their goals despite what obstacles may stand in their path. You're good enough to get here, you're good enough to finish it out!

ACKNOWLEDGEMENTS

Completing this dissertation has been a journey that would have been impossible for me to complete without the support I received. Thank you to each of my family members that nurtured my enthusiasm for learning and reading as a child. You all always believed in my abilities and that certainly influenced my decision to become a chemist.

To the different scholars that I have met along the way, thank you for the wonderful conversations. They've always provided new insights and different perspectives which were always welcoming. I have to give a particular thanks to the members of the Goodson Group, both past and present. You all helped me to navigate research and learn the different spectroscopic techniques in the lab. Special thanks to Dr. Ricardo Vázquez, Dr. Angelar Muthike, and Dr. Oleg Varnavski for introducing me to the field of TADF, always being there to help me troubleshoot issues with the nsTAS system, and answer any questions I had about research. And of course, thank you Prof. Theodore Goodson, III for giving me the opportunity to try new things and investigate new systems through the lens of laser spectroscopy. Your focus on the details has certainly helped me become the researcher I am.

To my dissertation committee: Dr. Bart Bartlett, Dr. Charles McCrory, and Dr. Pierre P. Poudeu, thank you for feedback throughout my time at UofM. Your advice and recommendations were immensely helpful in shaping the course of this dissertation.

To my friends, Kwasi, Reggie, and Elijah, thank you all for always being there to listen whenever things weren't going the way I hoped they would. It's also good to have someone there to tell you when you're overacting, so I greatly appreciate having you all in my corner.

To my undergraduate professors at Mercer University, thank you for teaching me the fundamentals of keeping a good lab notebook, conducting research in a safe manner, how to read a paper effectively and search through the literature for information. And thank you especially for helping me fine tune my writing and presentation style, both of which I've received recognition for. Without these skills my time as a PhD student would certainly have been more difficult.

To my mother, grandmother, and godmother, you all were there from the very beginning. To say that you all shaped me into the person I am today would be an understatement. You always uplifted me when I was down and talked me through the toughest of times. Mama, our talks helped me get through the roughest patch of my dissertation. Thank you.

To my wife, you've been my biggest supporter throughout this entire journey. You've sat through multiple versions of each of my presentations, watched me stress about the laser and research, and got me to and from lab. I'm so happy that I had you here with me, not just as my biggest supporter, but as my greatest and closest friend.

TABLE OF CONTENTS

DEDICATION ii

ACKNOWLEDGEMENTS iii

LIST OF FIGURES viii

LIST OF TABLES xiii

ABSTRACT xiv

CHAPTER

1. Background of Organic Emitters for Optoelectronic Applications 1
   1.1. A Brief Overview of Photoluminescence Pathways 1
   1.2. A Brief History of Organic Light Emitting Diodes (OLEDs) 4
      1.2.1 First Generation: Fluorescence-based OLEDs 6
      1.2.2 Second Generation: Phosphorescence-based OLEDs 9
      1.2.3 Third Generation: Thermally Activated Delayed Fluorescence-based OLEDs 11
   1.3. The rate of rISC (k_{rISC}) and TADF-activity 13
      1.3.1 Dependence On and Competition With Other Pathways 13
      1.3.2 Experimental Methods for Determining k_{rISC} 14
   1.4. Considerations for Achieving TADF 17
      1.4.1 Overlap of the Highest Occupied and Lowest Unoccupied Molecular Orbitals 17
      1.4.2 Locally Excited Triplet (LE^3) and Spin-Orbit Coupling (SOC) 18
      1.4.3 Predicting TADF Efficiency 21
      1.4.4 Typical Design Motifs of TADF Emitters 23
   1.5 Influence of Environment on TADF-activity 27
   1.6 Similar Emissive Mechanism to TADF 32
   1.7 Larger Picture and Dissertation Outline 36
2. Experimental Methods and Techniques 53
   2.1 Overview 53
   2.2 Stead-State Absorption and Emission Spectroscopy 53
   2.3 Two-Photon Absorption Spectroscopy 58
   2.4 Ultrafast Fluorescence Up-Conversion Spectroscopy 61
   2.5 Time-Correlated Single Photon Counting Spectroscopy 62
   2.6 Nanosecond Transient Absorption Spectroscopy 64
3. Investigation of Thermally Activated Delayed Fluorescence in Donor-Acceptor Organic Emitters with Time-Resolved Absorption Spectroscopy 72
   3.1 Original Publication Information and Author Contribution 72
   3.2 Abstract 72

3.3 Introduction 73
3.4 Experimental Methods....78
3.4.1 Synthesis and Characterization 78
3.4.2 Steady-State Absorption and Emission Measurements....79
3.4.3 Fluorescence Quantum Yield Calculation 79
3.4.4 Two-Photon Absorption....80
3.4.5 Time-Resolved Fluorescence Up-conversion 81
3.4.6 Time-Correlated Single Photon Counting (TCSPC)....81
3.4.7 Nanosecond Transient Absorption (nsTAS) 82
3.4.8 Reverse Intersystem-Crossing Rate Calculations 82
3.4.9 Quantum Chemical Calculations 83
3.5 Results 83
3.5.1 Stead-State Absorption Measurements 84
3.5.2 Fluorescence Measurements 85
3.5.3 Two-Photon Absorption....87
3.5.4 Time-Resolved Fluorescence Up-Conversion 89
3.5.5 TCSPC 91
3.5.6 nsTAS....94
3.5.7 Quantum Chemical Calculations 98
3.6 Discussion....102
3.7 Conclusion....110
3.8 Supporting Information 122
4. Investigating the Opto-Electronic Properties of Carbazole-Substituted Benzobisoxazoles for Organic Light-Emitting Diodes 133
4.1 Original Publication Information and Author Contribution....133
4.2 Abstract....133
4.3 Introduction 134
4.4 Experimental Methods....137
4.4.1 Computational Methodology 137
4.4.2 Materials and Characterization 137
4.4.3 Synthesis of Precursors 139
4.5 Results and Discussion....145
4.5.1 Computational Predictions....145
4.5.2 Synthesis and Characterization 148
4.5.3 Electronic Properties....150
4.5.4 Steady-State Optical Properties 151
4.5.5 nsTAS....155
4.5.6 Device Properties 159
4.6 Conclusion....162
4.7 Supporting Information 168
4.7.1 Materials and Measurements....170
5. A Spectroscopic Investigation to Better Understand the Changes in the Excited State Dynamics and Emissive Mechanism of BCC-TPTA from Solution to Solid-State 185
5.1 Overview 185
5.2 Abstract....185
5.3 Introduction 186

5.4 Experimental Methods....193
5.4.1 Aggregate Solution and Film Fabrication....193
5.4.2 Steady-State Absorption and Emission....194
5.4.3 Absolute Photoluminescence Quantum Yields....194
5.4.4 Time-Correlated Single Photon Counting....194
5.4.5 Time-Resolved Emission and Transient Absorption Spectra....195
5.4.6 Emission Intensity vs Laser Excitation Energy....195
5.5 Results....197
5.5.1 Steady-State Absorbance....197
5.5.2 Steady-State Fluorescence....198
5.5.3 Nanosecond Transient Absorption Spectra....201
5.5.4 Time-Resolved Emission Spectra....204
5.5.5 Time-Correlated Single-Photon Counting (TCSPC) Results....209
5.5.6 Emission Intensity vs Laser Energy....212
5.6 Discussion....214
5.7 Conclusions....218
5.8 Supporting Information....229
6. Dissertation Summary, Conclusions, and Future Outlook....237
6.1 Dissertation Summary....237
6.2 Conclusions....240
6.3 Future Outlook....241

LIST OF FIGURES

Figure 1.1.1 Jablonski diagram depicting the various excited state decay pathway.....2

Figure 1.1.2 Emissive pathway of a fluorescent chromophore 3

Figure 1.1.3 Emissive pathway of a phosphorescent chromophore.....3

Figure 1.1.4 Emissive pathway of thermally activated delayed fluorescence 4

Figure 1.2.1 Typical OLED device architecture.....5

Figure 1.2.1.1 Molecular structure of 8-hydroxyquinoline aluminum 6

Figure 1.2.1.2 Molecular structures of DCMI and DCM2 7

Figure 1.2.1.3 Molecular structure of FVIN.....8

Figure 1.2.1.4 Molecular structures of 2Pan and ^{t}Bu2NapAn.....9

Figure 1.2.2.1 Molecular structures of Ir(ppy)$_{t}$tmd, BPYThIr, and Ir-2.....10

Figure 1.2.3.1 Molecular structure of 2Cbz-PN 11

Figure 1.2.3.2 Molecular structures of DMAC-TRZ and spiroAC-Trz.....12

Figure 1.3.1.1 Typical rates of the common excites state decay pathways 13

Figure 1.3.2.1 Molecular structure, emissive lifetime, and nsTAS spectrum of BCC-TPTA.....16

Figure 1.4.2.1 Molecular structure of DPTZ-DBTO2.....19

Figure 1.4.2.2 Energy levels of the three types of TADF.....20

Figure 1.4.3.1 Genetic algorithm for purpose of predicting TADF emitter design.....21

Figure 1.4.4.1 Molecular structures of carbazole based TADF-emitters.....23

Figure 1.4.4.2 Molecular structures of 1,3-dicyanobenzene, 1,2-dicyanobenze, and 1,4-dicyanobenze.....24

Figure 1.4.4.3 Molecular structure of mono-core and dual-core emitters 25

Figure 1.4.4.4 Examples of multi-resonance thermally activated delayed fluorescent emitters ...26

Figure 1.5.1 Effect of solvent polarity on the energy gap between the excited states.....27

Figure 1.5.2 Photophysical properties of 4CzIPN in four solvent of varying polarities 28

Figure 1.5.3 Emissive lifetimes as concentration of camphoric anhydride is increased in solid-state mCP host material.....30

Figure 1.6.1 Energy diagram depicting the triplet-triplet annihilation mechanism 33

Figure 1.6.2 Energy diagram depicting the different triplet exciton transfer mechanisms based on confinement of the emitter's triplet excitons 35

Figure 2.2.1 Electromagnetics spectrum of radiation in nanometers (nm).....54

Figure 2.2.2 Schematic of the Agilent 8453 UV-Vis spectrophotometer.....56

Figure 2.2.3 Schematic of the Horiba Scientific Fluorimeter.....56

Figure 2.3.1 Process of two-photon absorption 58

Figure 2.3.2 Schematic of the two-photon absorption laser system 59

Figure 2.4.1 Schematic of the ultra-fast fluorescence up-conversion laser system.....61

Figure 2.5.1 Schematic of the time-correlated single photon counting laser system 63

Figure 2.6.1 Schematic of the Q-switch assembly utilized in the nanosecond transient absorption (nsTAS) system's laser head.....65

Figure 2.6.2 Schematic of the nanosecond transient absorption (nsTAS) laser system 66

Figure 2.6.3 Laser-induced emission sample chamber configuration 67

Figure 2.6.4 5wt% BCC-TPTA/DPEPO film before measurement and after measurement 70

Figure 3.3.1 Decay processes of excited states and associated rate constants.....74

Figure 3.3.2 Structures of investigated chromophores where the donor unit is blue and acceptor unit is red.....78

Figure 3.5.1.1 Absorbance spectra of Trz-acceptor and PN-acceptor compounds in toluene.....84

Figure 3.5.2.1 Fluorescence spectra of Trz-acceptor and PN-acceptor compounds in toluene.....86

Figure 3.5.3.1 Two-photon induced fluorescence scans of the Trz-acceptor and PN-acceptor compounds. Insets are logarithmic plots of two-photon absorption power dependence versus fluorescent intensities.....88

Figure 3.5.4.1 Time-resolved fluorescence up-conversion results of the Trz-acceptor compounds and PN-acceptor compounds in toluene 90

Figure 3.5.5.1 Time-correlated single photon counting measurements of BFCbz-Trz and BFCbz-PN in unpurged and purged toluene solutions. Inset is a zoom-in of the emission lifetime.....92

Figure 3.5.6.1 Nanosecond transient absorption spectra of BFCbz-Trz in purged toluene. The insert displays the SE peak at 80 ns.....95

Figure 3.5.6.2 Nanosecond transient absorption spectra of BFCbz-PN in purged toluene. The inset displays the SE peak at 80 ns.....96

Figure 3.5.6.3 Ground state bleach and excited state absorption decays of BFCbz-PN in unpurged and purged toluene solutions. The red lines represent the mono-exponential decay fittings 97

Figure 3.5.7.1 Optimized ground state (from ωB97X-D) dihedral angles of BFCbz-Trz and BFCbz-PN.....99

Figure 3.5.7.2 Natural transition orbitals (from ωB97X-D) for charge transfer states of BFCbz-Trz and BFCbz-PN.....100

Figure 3.8.1 Emissive lifetime results of investigated compounds in toluene.....123

Figure 3.8.2 Logarithmic plots of emissive lifetime results of investigated compounds in toluene. Inset is from 0 – 200 ns.....124

Figure 3.8.3 Nanosecond transient absorption spectra of Cbz-Trz and BTCbz-PN in purged toluene. The insets display the SE at 80 ns.....125

Figure 3.8.4 Nanosecond transient absorption spectra of 2Cbz-PN and BTCbz-PN in purged toluene. The insets display the SE at 80 ns.....126

Figure 3.8.5 Kinetic traces of Trz-acceptor compounds taken at the wavelengths thought to represent excited state absorption in purged toluene.....127

Figure 3.8.6 Ground state bleach and excited state absorption decays of 2CBz-PN in unpurged and purged toluene. The red line represent the mono-exponential decay fits.....128

Figure 3.8.7 Ground state bleach and excited state absorption decays of BTCbz-PN in unpurged and purged toluene. The red lines represent the mono-exponential decay fits.....129

Figure 4.3.1 General structure of the BBO core. Conjugation can take part at the 2 and 6 positions (axis) or the 4,8 axis.....136

Figure 4.5.1.1 FMOs and electronic energy levels of C1 through C6.....147

Figure4.5.2.1 Synthesis of precursor material 1-8.....149

Figure 4.5.2.2 Synthesis of final molecules C1 – C6.....150

Figure 4.5.4.1 Steady-state absorbance spectra of C1-C6 in chloroform at 0.01 gL^{-1} and photoluminescence spectra of C1-Ct thin film.....152

Figure 4.5.5.1 Nanosecond transient absorption spectra of the six BBOs.....157

Figure 4.5.6.1 Bond diagram of active layer materials using BBO-based dopants.....161

Figure 4.7.1 ^{1}H NMR of 1.....171

Figure 4.7.2 ^{1}H NMR of 2.....171

Figure 4.7.3 ^{1}H NMR of 3.....172

Figure 4.7.4 ^{1}H NMR of 4.....172

Figure 4.7.5 ^{1}H NMR of 5.....173

Figure 4.7.6 ^{1}H NMR of 6.....173

Figure 4.7.7 ^{1}H NMR of 7.....174

Figure 4.7.8 ^{1}H NMR of 8 174

Figure 4.7.9 ^{1}H NMR of C1.....175

Figure 4.7.10 ^{13}C NMR of C1.....175

Figure 4.7.11 ^{1}H NMR of C2.....176

Figure 4.7.12 ^{1}H NMR of C3.....176

Figure 4.7.13 ^{13}C NMR of C3.....177

Figure 4.7.14 ^{1}H NMR of C4.....177

Figure 4.7.15 ^{1}H NMR of C5.....178

Figure 4.7.16 ^{13}C NMR of C5.....178

Figure 4.7.17 ^{1}H NMR of C6.....179

Figure 4.7.18 UV-vis and photoluminescence spectra of the six BBOs as thin films.....179

Figure 4.7.19 Kinetics traces of the excited state absorbance and phosphorescent features. Excitation peak was taken from the maxima of each feature in the transient absorbance curves 181

Figure 4.7.20 AFM images of the active layer of each OLED device.....182

Figure 4.7.21 Current-voltage-luminance data of the six BBOs 183

Figure 5.3.1 Diagram displaying the thermally activated delayed fluorescence mechanism.....187

Figure 5.3.2 The emitters investigated in our most recent spectroscopic study of relating TADF-activity to emitter structure 198

Figure 5.3.3 Molecular structures of the BCC-TPTA emitter and host materials used in this study 193

Figure 5.5.1.1 Absorbance spectra of BCC-TPTA in THF/water solutions and solid-state host materials.....198

Figure 5.5.2.1 Normalized steady-state fluorescence spectra of BCC-TPTA in 0% and 80% H_2O fractions and host materials 199

Figure 5.5.2.2 The different THF/H_2O fractions, where 0% is pure THF solution, under UV excitation.....200

Figure 5.5.3.1 Transient absorption spectra of BCC-TPTA in 0% H_2O fraction and mCP host material 202

Figure 5.5.3.2 Kinetic lifetime traces of the BCC-TPTA excited states in different host materials 204

Figure 5.5.4.1 Time-resolved emission spectra of BCC-TPTA in 0% and 80% H_2O fractions..205

Figure 5.5.4.2 Time-resolved emission spectra of BCC-TPTA in solid-state hosts.....207

Figure 5.5.4.3 Emission lifetime traces of the emissive peaks observed in the time-resolve emission spectra of the 0% and 80% H_2O fractions and 5wt% films, zoomed in to display the second-emissive component. 209

Figure 5.5.5.1 Emission decay traces of the two emissive maxima seen in the time-resolved emission 211

Figure 5.5.6.1 New nsTAS laser setup used to obtain log/log plots of emission intensity vs laser energy 212

Figure 5.5.6.2 Log/log plots of integrated emission intensity vs laser energy of the 5wt% films 213

Figure 5.8.1 Normalized absorbance spectra of the 20% - 60% and 99% H_2O fractions 230

Figure 5.8.2 Emission intensities of the investigated THF/H_2O solutions and films 231

Figure 5.8.3 Transient absorption spectra of BCC-TPTA in 20% - 99% H_2O fractions 232

Figure 5.8.4 Transient absorption spectra of BCC-TPTA in DPEPO, PMMA, and PS films 233

Figure 5.8.5 Time-resolved emission spectra of the 20% - 60% and 99% H_2O fractions 234

Figure 5.8.6 Emission lifetime traces of the 0% - 40% H_2O fractions obtained using the TCSPC technique 235

Figure 5.8.7 Log-log plots of emission intensity vs excitation energy of the 0% and 80% H_2O fractions 235

Figure 6.3.1 Schematic of the conventional absorbance setup vs the scattering chamber setup 243

Figure 6.3.2 Total reflectance of PTFE sheet at 0.5 mm thickness (S4) and 2mm thickness (S10) 245

Figure 6.3.3 Signal obtained with no scattering chamber (left) and with the scattering chamber (right), each without a sample placed in the holder 246

Figure 6.3.4 Transient absorption spectra of dilute $[Ru(bpy)_3]^{2+}$ solution obtained without the scattering chamber (left) and with the scattering chamber (right) 247

LIST OF TABLES

Table 1.5.1 Photophysical properties of 4CzIPN in four solvents of varying polarities 28

Table 3.5.3.1 Photophysical properties of investigated chromophores in toluene 89

Table 3.5.4.1 Up-conversion emissive lifetime values of investigated compounds in unpurged toluene.....90

Table 3.5.5.1 Lifetimes of the components of fluorescence in toluene solutions.....94

Table 3.5.6.1 Decay lifetimes of the transient states of PN-acceptor compounds in unpurged and purged toluene. Also included are k_{risc} values using two different methods 97

Table 3.5.7.1 Quantum chemical results for investigated compounds, along with experimental and calculated k_{rISC} 102

Table 3.8.1 Ground and Excited Singlet and Triplet Geometries Dihedral Angles for PN's and Trz's 130

Table 4.5.3.1 Computed electronic and geometric properties of the six BBO materials 151

Table 4.5.4.1 Measured steady-state optical and electronic properties for BBOs C1-C6 154

Table 4.5.5.1 Transient properties and kinetics traces of the T group BBOs 158

Table 4.5.6.1 Device properties of the fabricated OLEDs.....162

Table 5.5.2.1 Photophysical properties of BCC-TPTA in different THF/water solutions and film 201

Table 5.5.3.1 Excited state lifetimes observed for the BCC-TPTA films 204

Table 5.5.4.1 Emissive peaks observed for the different samples in the time-resolved emission spectra 208

Table 5.5.4.2 Lifetimes of the second emissive components observed for the 80% H_2O fractions and solid-state films 209

Table 5.5.5.1 Emissive lifetimes of BCC-TPTA in the different H_2O fractions and host materials taken at the emissive maxima observed in the time-resolved emission spectra 210

Table 5.8.1 The lifetime values of the second emissive component for the peaks observed in the time-resolved emission spectra 235

ABSTRACT

Optoelectronic systems have become an integral part of day-to-day life for a significant portion of the world for use in information sharing, entertainment, and communications. The need for high quality displays became particularly apparent during the height of the Covid-19 pandemic where the majority of business and formal interactions had to take place virtually. While the past generations of organic light emitting diodes (OLEDs) have achieved success utilizing phosphorescent compounds, there is still significant room for improvement. Namely, the phosphorescent compounds that are used as emitters have heavy rare metals (such as iridium and platinum) incorporated into their molecular design. This limits the molecular structures available, makes them relatively expensive to produce, and causes competition with other fields that utilize the same metals such as catalysis. Beyond this, there are still OLED stability issues that plague these systems such as triplet-triplet annihilation. This is especially true for blue OLEDs, where the high energy need to excite the blue emitters causes device degradation faster than the red and green OLEDs.

Thus, there is a need for a cheaper and more stable alternative that can reach the same or better device efficiencies as the phosphorescent based OLEDs. One promising class of emitters that meet these qualifications is known as thermally activated delayed fluorescence (TADF). The TADF mechanism is the idea that non-emissive triplet excited states can be converted into emissive

singlet excited states via a reverse intersystem crossing process. This process is energized by the thermal energy of the surroundings and can occur at room temperature. Additionally, TADF emitters can be purely organic allowing a wider range of molecular designs and making them relatively cheaper than the previous generation of phosphorescent emitters.

However, it is still unclear what molecular design best lends itself to the TADF mechanism and how the emitter photophysics are influenced by guest-host interactions that occur in solid-state films. These factors are critical if the current OLED efficiencies are to be improved. Understanding these factors would also aid other areas of optoelectronics, particularly those that utilize solid-state host materials. As a result, the focus of this thesis is to utilize both time-resolved and nonlinear optical techniques to: 1) investigate and improve the understanding of the structure-function relationships that govern the TADF mechanism, and 2) determine what guest-host interactions result in changes in emitter photophysics.

Regarding the first point, it was found that emitters that incorporate linkers into their molecular design are not well suited for TADF-activity. This is due to the linker inhibiting sufficient HOMO/LUMO separation which results in large singlet-triplet energy gaps (ΔE_{ST}) and prevents spin-orbit coupling (SOC) between the singlet and triplet manifolds. However, emitters that have multiple identical donors directly attached to the acceptor unit were found to be better suited for TADF-activity. This is due to sufficient HOMO/LUMO separation being achieved with this molecular design, allowing for a significantly smaller ΔE_{ST}, greater SOC, and a sufficing rate of reverse intersystem crossing (k_{rISC}). Further investigation revealed that utilizing the linker and multiple identical donors does enhance SOC, but results in phosphorescence and not TADF.

Regarding the second goal, it was determined that guest-host interactions play a significant role in determining the emissive mechanism of the guest chromophore. Specifically, results indicate that hydrogen bonding interactions can induce TADF-activity for the BCC-TPTA emitter while non-bonding interactions between the aromatic moieties of the guest and host results in triplet-triplet annihilation up-conversion. Overall, this work utilized established spectroscopic techniques of the Goodson lab and required the development of a new addition to the nanosecond transient absorption system. Each of these techniques were utilized to elucidate which molecular structure is better suited for TADF-activity and the relevant guest-host interactions within solid-state films.

Chapter 1: Background of Organic Emitters for Optoelectronic Applications

1.1. A Brief Overview of Photoluminescence Pathways

Luminescence, from the Latin root word *lumen* (meaning of light), is the spontaneous emission of light from a compound in an electronic excited state.[1] There are different types of luminescence (bioluminescence, thermoluminescence, electroluminescence, etc.), each defined by the method of excitation. Photo- and electroluminescent emitters are utilized in various aspects of modern life: from computer and TV monitors, biological imaging, lasers, forensics, glow in the dark paints, street signs, lane markers, and numerous others. The efficiency of a display is closely related to the emissive mechanism it employs. There are three emissive mechanisms that this report will focus on: fluorescence, phosphorescence, and thermally activated delayed fluorescence.

A basic understanding of the underlying principles of excited states and the rules governing emission must be obtained before a description of the different emissive mechanisms can be appreciated. Specifically, one must have some understanding of the Boltzmann distribution of excited states and Kasha's rule.[2,3] Boltzmann's distribution is described by **Eqn. 1.1.1**

$$p_i \propto e^{-\epsilon_i/(kT)} \qquad \textbf{Equation 1.1.1}$$

Where p_i is the probability that a system is in state i, ε_i is the state's energy, k is Boltzmann's constant, and T is the temperature of the system. Through the lens of emissive processes, Boltzmann distribution dictates that the singlet excited states are more populated at higher temperatures while the triplet excited states is more populated at lower temperatures.[4–6]

Kasha's rule is plainly: "The emitting level of a given multiplicity is the lowest excited level of that multiplicity.[2,7] This due largely to internal conversion and intersystem crossing, displayed in **Fig. 1.1.1**.[8] Internal conversion (IC) is the radiationless transition between an excited state of a certain multiplicity and a lower energy state of the same multiplicity. Evidence of IC is shown when an emitter is excited with a photon of high energy and it emits a photon of significantly lower energy. This is because the excited state relaxed to the lowest energy excited state before emitting a photon. Intersystem crossing (ISC) is the radiationless transition from one excited state to another of a different multiplicity. The rate of ISC is determined by the strength of an emitter's spin-orbit coupling and will be discussed further in later sections.

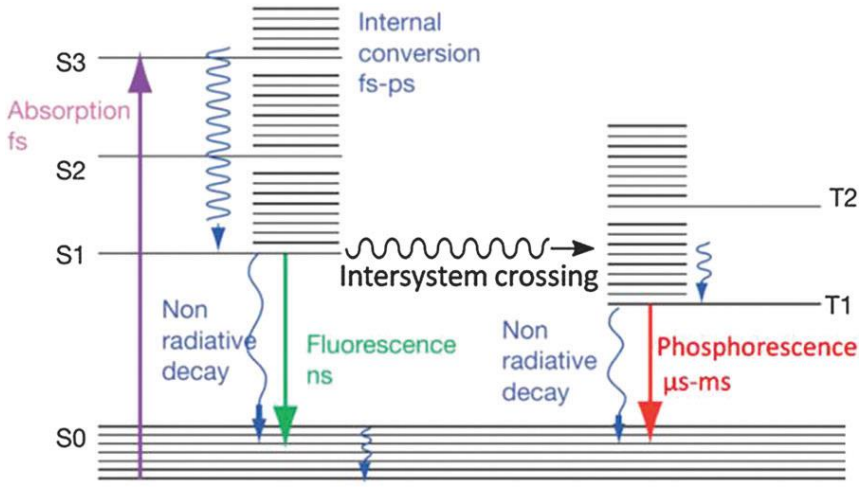


Figure 1.1.1. Jablonski diagram depicting the various excited state decay pathways.

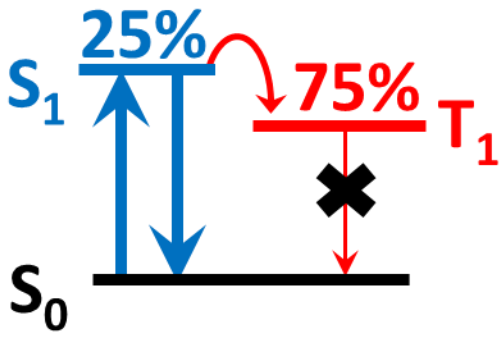


Figure 1.1.2. Emissive pathway of a fluorescent chromophore.

Upon excitation, an emitter in the electronic ground state (S_0) is promoted to one of two electronic excited states, the singlet excited state (S_1) or the triplet excited state (T_1). Whether the emitter is excited through the absorption of a photon of appropriate energy or electrical excitation, 25% of the generated excited states will be S_1 and the remaining 75% will be T_1. In the typical case of fluorescent emitters, the S_1 relaxes back to S_0 and releases a photon, as displayed in **Figure 1.1.2**. This spontaneous emission of a photon occurs from the lowest excited state according to Kasha's rule. However, the T_1 states relax to S_0 through non-radiative means.

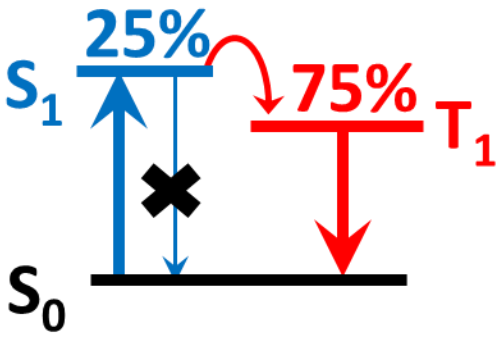


Figure 1.1.3. Emissive pathway of a phosphorescent chromophore.

Conversely, phosphorescent emitters utilize a different emissive pathway, displayed in **Figure 1.1.3**, that allows for utilization of the generated triplet states for emission. The triplet state is

populated via the singlets undergoing ISC to populate the triplet manifold. The newly populated triplet manifold then undergoes IC to the lowest energy triplet excited state (T_1). Once in the T_1, the electrons relax back to S_0 through both radiative and non-radiative means. Radiative relaxation to S_0 from T_1 requires a spin-flip and thus has a significantly longer lifetime than fluorescence.[1,9] This longer lifetime also opens up T_1 states to more non-radiative relaxation pathways, adding considerations when one plans to utilize this method for optoelectronic applications.

Finally, there is thermally activated delayed fluorescence (TADF), displayed in **Figure 1.1.4**, which is the idea that both S_1 and T_1 states can be utilized to generate light. The thermal energy of the surroundings is absorbed by the emitter and is then used to promote what would typically be non-emissive T_1 into emissive S_1. This is known as reverse intersystem crossing and is another

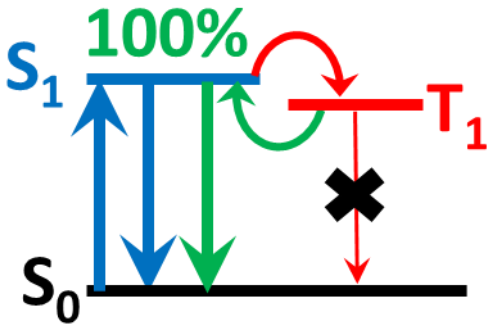


Figure 1.1.4. Emissive pathway of thermally activated delayed fluorescence.

spin-flip mechanism. Thus, similar to phosphorescence, it has a longer lifetime than typical fluorescence. TADF is a rare phenomenon. As such, an emitter that is TADF-active must possess particular properties which will be discussed at length further in this work.

1.2. A Brief History of Organic Light Emitting Diodes

Each of the above discussed emissive mechanisms have been investigated for use in organic light emitting diodes (OLEDs). OLEDs are, typically colored, light sources utilized in various display applications such as smartphones and TV screens. Displays that utilize OLED technology

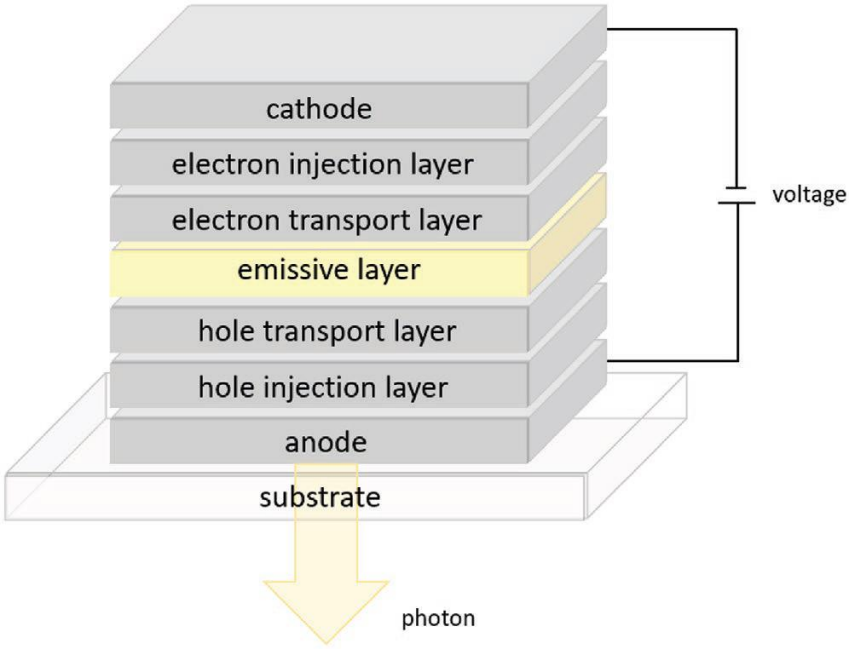


Figure 1.2.1. Typical OLED device architecture.

differ from liquid crystal displays in that they do not require a backlight, which makes them more energy efficient. OLED displays are also considerably thinner, allowing them to be applied to a wider range of applications.

The typical device architecture of current OLEDs, displayed in **Figure 1.2.1**, consists of a hole injection layer, hole transport layer, electron blocking layer, emissive layer, electron transport layer, hole blocking layer, and electron injection layer. Charge carriers, holes and electrons, are injected into the hole and electron injection layers, respectively. These charge carriers then migrate through their respective transport layers and recombine in the emissive layer. This recombination generates the excited states required for electroluminescence.

The OLED performance is typically determined by calculating its external quantum efficiency (EQE). EQE is a measure of the number of charge carriers that are collected against the number of incident photons. It can be calculated using **Equation 1.2.1**:

$$EQE = \gamma \times \eta_{S/T} \times \eta_{PL} \times \eta_{out} \qquad \textbf{Equation 1.2.1}$$

Where γ represents the electron-hole balance, $\eta_{S/T}$ the singlet-triplet factor, η_{PL} the photoluminescence quantum yield, and η_{out} the outcoupling efficiency.[10]

Which of the previously described emissive processes that the emissive layer utilizes plays a critical role in the efficiency of the OLED. As such, a large body of academic and industrial research is focused on this layer, with three "generations" of OLEDs being developed over the lifetime of the field. Much of this research focused on developing green, red, and blue OLEDs with narrow emission bands and high photoluminescent quantum yields as they are essential for creating quality images.

1.2.1. First Generation: Fluorescence-based OLEDs

Fluorescent based OLEDs are able to utilize the 25% singlet excited states for emission, while access to the 75% triplet excitons is spin-forbidden.[11] This limits the EQE of fluorescent based

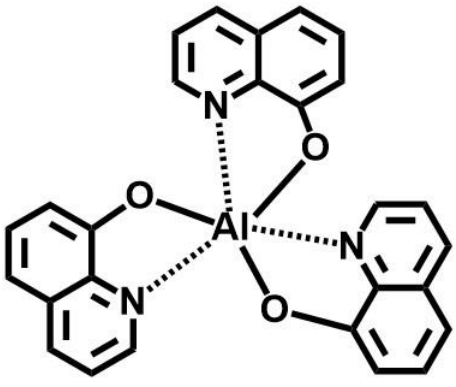


Figure 1.2.1.1. Molecular structure of 8-hydroxyquinoline aluminum.

OLEDs to ~5%.[12] However, fluorescent based emitters have the benefit of narrow emission bandwidths which is useful for generating clear images.

The first OLED device was reported by Tang and VanSlyke in 1987.[13] They developed a green OLED (emission localized at 550 nm) with an EQE of 1% based on the fluorescent emitter 8-hydroxyquinoline aluminum **(Figure 1.2.1.1)**. The device was able to operate at a driving voltage of less than 10 V and is what generated interest in the field of OLEDs.

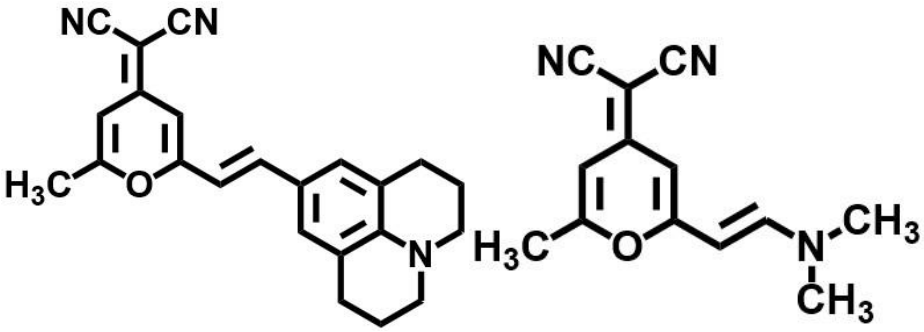


Figure 1.2.1.2. Molecular structures of DCM1 (left) and DCM2 (right).

The first red OLED utilized a dopant-based emissive layer that was developed by Chen et.[14] al.[15] They used 4-(dicayanomethylene)-2-methyl-6-[4(dimethylaminostyryl)-4H-pyran] (DCM) derivatives as the emitters DCM1 and DCM2, displayed in **Figure 1.2.1.2**. The emission of these OLEDs ranged from 570 – 620 and 610 - 650 nm, respectively, depending on the doping concentrations of the emitters, with device EQEs reported to be 2.3%.

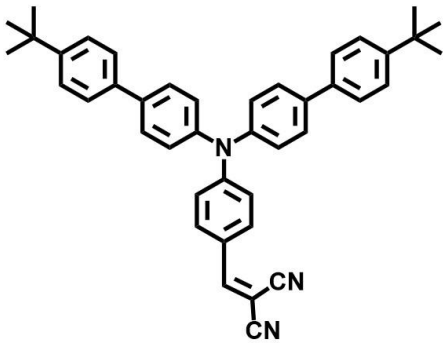


Figure 1.2.1.3. Molecular structure of FVIN.

The general molecular structure of the red OLED emitters limited them to being used in dopant-based systems. This is due to them largely having but π-conjugated structures, which lead themselves to π-stacking and aggregate formation, hindering device performance.[12] Thus, new emissive layer designs were developed to overcome these challenges. The red fluorescent emitter FVIN, displayed in **Figure 1.2.1.3**, was developed by Forget and coworkers with the intention of overcoming the aggregation effects that limit the device EQE.[15] They adjusted the doping rates of FVIN in an Alq_3 matrix from 5% - 40% and found that the EQE of 1.5% remained constant. However, the maximum EQE they achieved was at a doping rate of 2%. These results highlight the FVIN structure as an alternative to the traditional DCM emitters.

Blue fluorescent OLED emitters were largely based on anthracene derivatives.[16] Their wide bandgap, thermal stability, and ridged structure make them attractive as emitters, though their planar structures lead them to similar issues as the red OLEDs. This was made apparent when a blue OLED with an EQE of ~2.8% was reported to form aggregates in film.[17]

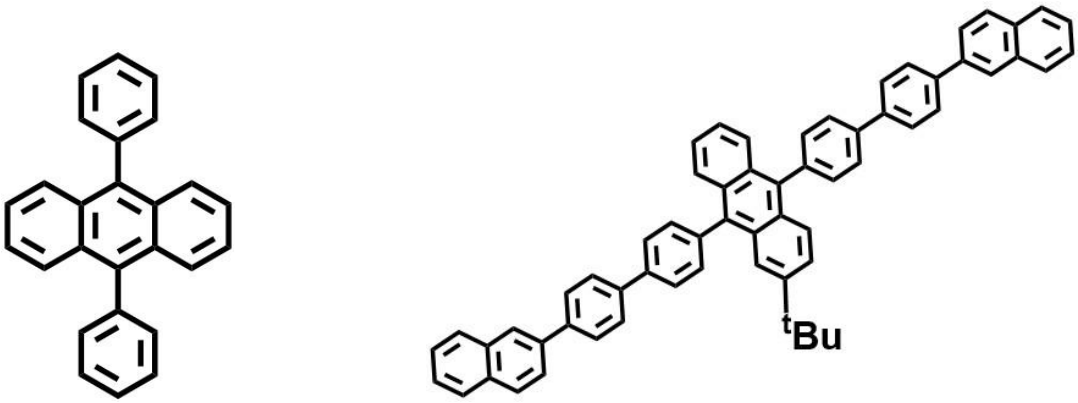


Figure 1.2.1.4. Molecular structures of 2Pan (left) and ^{t}Bu2NapAn (right).

This issue was overcome by incorporating different moieties into the molecular design of emitters that would suppress aggregation. An example of this is the emitter ^{t}Bu2NapAn (**Figure 1.2.1.4**) with an emission at 444 nm.[18] The tert-butyl group of this emitter aids in preventing aggregation, allowing for the EQE of the device to reach the upper limit of fluorescent-based OLEDs (EQE_{max} = ~5%).

1.2.2. Second Generation: Phosphorescence-based OLEDs

Phosphorescent-based OLEDs were developed with the intention of accessing and utilizing the 75% T_1 excited states. As stated previously, this requires a change in the multiplicity from T_1 to S_0, causing phosphorescence to have a significantly longer lifetime than fluorescence. This process also requires strong spin-orbit coupling interactions to make it spin-allowed.[19] As such, particular molecular design strategies have been adopted to enhance the spin-orbit coupling effect to increase phosphorescence efficiency.

Many phosphorescent emitters incorporate heavy metals, such as iridium and platinum, into their structure.[9,20,21] This is because such metals induce what is known as the *heavy ion effect*, which enhances spin-orbit coupling (SOC) and allows for ISC and phosphorescence to occur more efficiently.[19,22,23] Great success has been had with such emitters in the field of OLEDs, with many achieving appreciable external quantum efficiencies (EQE's).[12]

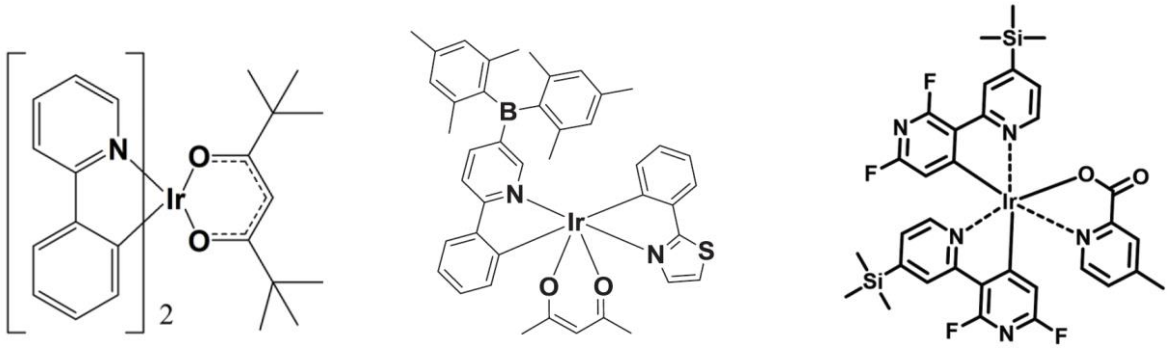


Figure 1.2.2.1. Molecular structures of $Ir(ppy)_2tmd$ (left), BPyThIr (center), and Ir-2 (right).

An OLED with and EQE of ~32% was developed by Kim and coworkers.[24] They utilized the iridium-based emitter $Ir(ppy)_2tmd$ (**Figure 1.2.2.1)**. This green OLED displays the high efficiencies possible through the use of heavy-metal phosphorescent emitters. A similarly high EQE of 28% was achieved by Wong and coworkers when they fabricated an red-OLED using PyThIr, another iridium-based emitter (**Figure 1.2.2.1**).[25] The researchers had incorporated a diarylboron group into the molecular design which increased the electron-transport ability of the emitter. And finally, there is the blue iridium-based emitter simply reported as Ir-2 (**Figure 1.2.2.1**).[26] This emitter has a narrow emission bandwith of 445-450 nm and a device EQE of 31.9% was achieved using it as the emitter.

The high EQE's of these devices is closely related to the emitters being able to harvest the T_1 for emission. However, there are sustainability concerns with this class of emitters. This is largely

because of their reliance on rare heavy metals that increase the synthesis costs considerably. Thankfully research is being conducted on purely organic emitters that can utilize the triplet state.

1.2.3. Third Generation: Thermally Activated Delayed Fluorescence-based OLEDs

The third generation of OLEDs are based on thermally activated delayed fluorescence (TADF) emitters. As stated previously, TADF emitters are able to harness both the singlet and triplet excited states while being purely organic compounds. This allows for a wide range of molecular designs and emissive colors. I highly encourage the interested reader to do further reading to appreciate the various TADF-emitter designs.[27–35]

While there was great success with second generation red and green phosphorescent OLEDs, the blue OLEDs still faced material degradation and high efficiency roll-off challenges related to the higher energy requirements necessary to generate blue light.[36–38] Thus, there was great interest in developing a TADF-emitter that would not have these same issues. The well-known sky-blue TADF-emitter 2Cbz-PN is one such emitter (**Figure 1.2.3.1)**.[39–45]

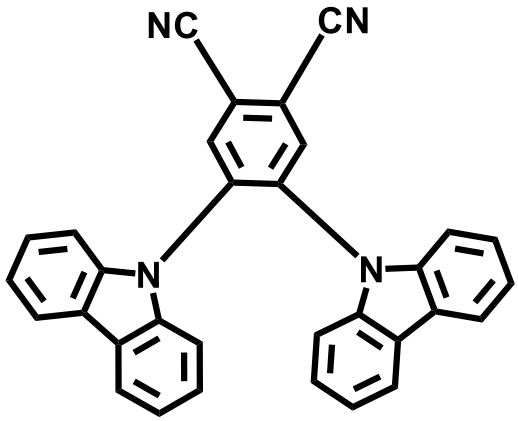


Figure 1.2.3.1. Molecular structure of 2Cbz-PN.

Adachi et al. fabricated an OLED using 2Cbz-PN as the emissive material. They achieved an EQE of 8%, higher than the maximum of fluorescent-based OLEDs.[46] Adachi's group also developed a blue emitter that would reduce the efficiency roll-off of the OLED at high luminance.[11] This was achieved by increasing the twist angle between the donor and acceptor units of the chromophore, which stabilizes the charge transfer states and increases the energy of the triplet local exciton state. They were able to design an emitter with a small energy gap between the singlet and triplet charge transfer states, while ensuring that the triplet local exciton state had greater energy than the triplet charge transfer state. The OLED fabricated with this emitter was able to achieve an EQE of 19.5%, comparable to the phosphorescent-based OLEDs at the time.

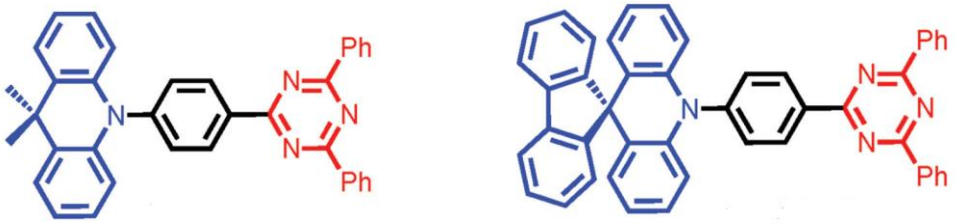


Figure 1.2.3.2. Molecular structures of DMAC-TRZ (left) and spiroAC-Trz (right).

An exceptionally high EQE was reported by Wu and coworkers in a OLED that utilized spiroAC-TRZ.[47] This emitter was derived from their previous emitter DMAC-TRZ (**Figure 1.2.3.2**), which achieved an EQE of 26.5% when placed in an OLED.[48] The spiroAC-TRZ emitter (**Figure 1.2.3.2**) had significantly greater photoluminescence quantum yield than DMAC-TRZ, being 100% and 90%, respectively. It also had a significantly higher ΔE_{ST} at 72 meV against DMAC-TRZ's at 62 meV. Despite this, the OLED that utilized spiroAC-TRZ was able to achieve an EQE of 36.7%. This result highlights not only the efficiencies that are possible with TADF-emitters, but also that more than ΔE_{ST} can influence EQE.

1.3. The Rate of rISC (k_{rISC})

1.3.1. Dependence on and Competition with Other Pathways

As described in previous sections, reverse intersystem crossing (rISC) is a non-emissive mechanism through which non-emissive low-energy triplet excited states (T_1) are converted into emissive low-energy singlet excited states (S_1).[37,49,50] In the case of TADF emitters, this mechanism is powered through the absorption of the ambient thermal energy. As such the energy gap between S_1 and T_1 should be close to that of room temperature (300 K = 0.0257 eV).[51] This mechanism is critical for achieving efficient TADF-activity, and thus it is important for one to have an understanding of the other processes that impact rISC (**Figure 1.3.1.1**).[52]

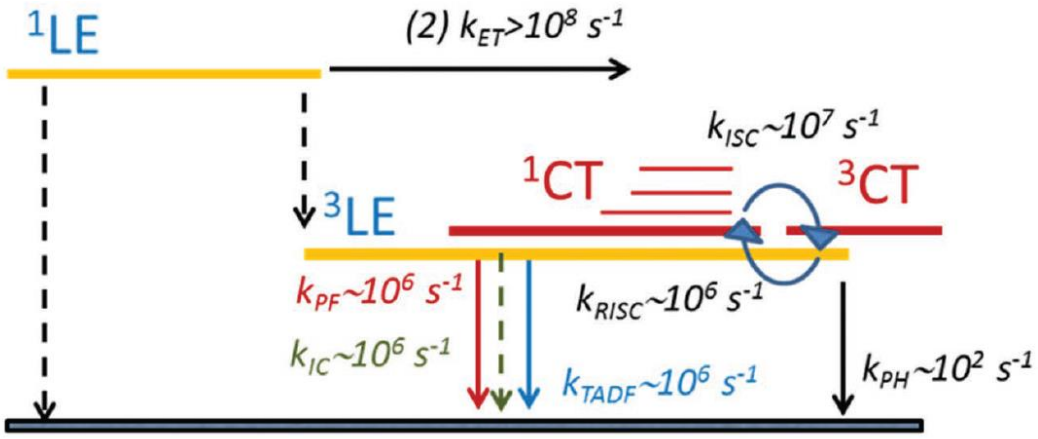


Figure 1.31.1. Typical rates of the common excited state decay pathways: PF = prompt fluorescence, IC = internal conversion, TADF = thermally activated delayed fluorescence, PH = phosphorescence, ISC = intersystem crossing, and rISC = reverse intersystem crossing.

The first class of processes that have significant impact of rISC are those that populate T_1, such as internal conversion. Internal conversion (IC) is a non-emissive process through which a higher energy state decays to a lower energy state of the same multiplicity. [53–55] As this process does not alter the spin of the excited state, it is a relatively fast mechanism with a rate (k_{IC}) of $10^{9\text{-}11}$.[56] In the case of populating T_1, a higher energy triplet state (T_n) will relax down to T_1.

Intersystem crossing is another method of populating T_1, however it has barriers that IC does not, due to it being a spin-forbidden process according to Fermi's golden rule.[57,58] Intersystem crossing (ISC) is a non-emissive process through which the spin-multiplicity of the emitter is changed from S_1 to T_1.[59–64] This requires a spin-flip, and thus occurs on longer timescales, having a typical rate (k_{ISC}) of 10^7 s^{-1} for fluorescent emitters.

The other class of processes that impact rISC are those that deplete the T_1 population. These include both phosphorescence and other, non-radiative, decay pathways. These pathways require a spin-flip, similar to ISC, and thus also have a long lifetime having typical rates (k_{phos} and k_{nr}) of $10^0 – 10^3$ s^{-1}. As rISC also depletes T_1, it must have a rate (k_{rISC}) greater than k_{phos} and k_{nr}. However, the value of k_{rISC} cannot exceed that of k_{ISC} or k_{IC}, as these mechanisms populate T_1. Thus, the most efficient TADF emitters will have a k_{rISC} within the range of $10^4 – 10^6$.[52]

1.3.2. Experimental Methods of Determining k_{rISC}

As k_{rISC} is of critical importance to the efficiency of TADF, considerable research has been conducted to experimentally determining its value for various emitters. The first experimental method of k_{rISC} determination depends on utilizing other experimental results and some key assumptions.[65] They approximated the value of k_{rISC} using the following equation:

$$k_{rISC} = \frac{k_{DF}\Phi_{rISC}}{1-\Phi_{ISC}\Phi_{rISC}} \qquad \textbf{Equation 1.3.2.1}$$

where k_p and k_d represent the prompt and delayed fluorescence rate constants, respectively, k_{ISC} is the ISC rate constant from S_1 to T_1, and Φ_P and Φ_D are the photoluminescence quantum yields of the prompt and delayed components, respectively. This equation is derived from the

following that relates the various rate constants that connect the prompt and delayed fluorescence components.

$$k_{PF}, k_{DF} = \frac{k^S{}_r + k^S{}_{nr} + k_{ISC} + k^T{}_{nr} + k_{rISC}}{2} \qquad \textbf{Equation 1.3.2.2}$$

Eqn 1.3.2.2 was then simplified to

$$k_{PF} = k^S{}_r + k^S{}_{nr} + k_{ISC} \qquad \textbf{Equation 1.3.2.3}$$

$$k_{DF} = k^T{}_{nr} + (1 - \frac{k_{ISC}}{k^S{}_r + k^S{}_{nr} + k_{ISC}}) k_{rISC} \qquad \textbf{Equation 1.3.2.4}$$

This simplification required the assumption that k_r^S, k_{nr}^S, and k_{ISC} are all significantly larger than both k_{nr}^T and k_{rISC}. This assumption is sound, as k_{nr}^T and k_{rISC} are both dependent on k_{ISC} which must compete with k_r^S and k_{nr}^S.

This **Eqn 1.3.2.1** has been used to determine k_{rISC} for a number of emitters designed for TADF-activity.[46,66] And while the assumptions made in developing **Eqn 1.3.2.1** are sound, there are many variables within the equation. Errors in assumptions or in acquiring the experimental data could compound into a larger error of the final k_{rISC} value. Such errors could lead to incorrect designations of emitters as being TADF-active, as is the case with BCC-TPTA.

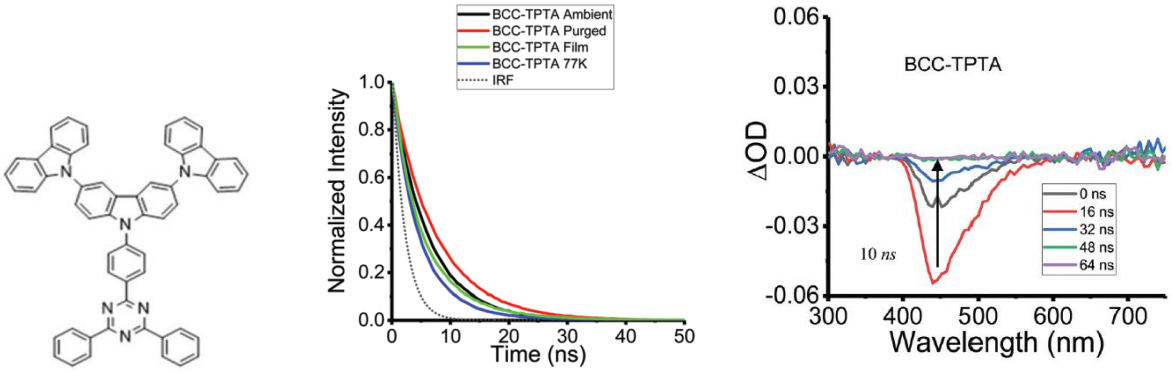


Figure 1.3.2.1. Molecular structure (left), emissive lifetime (center) and nsTAS spectrum (right) of BCC-TPTA.

BCC-TPTA is an emitter that was reported to be TADF-active, based on its long-lived emissive lifetime in solid-state, appreciable quantum yield, and ΔE_{ST}.[46] However, an investigation conducted by Vasquez and coworkers in solution revealed that the long-lived emission component is not observed for BCC-TPTA in solution.[67] They also reported a lack of triplet excited states in the nanosecond transient absorption (nsTAS) spectra, indicating that BCC-TPTA is not TADF-active (**Figure 1.3.2.1**). This led to the development of a new and direct method of determining k_{rISC}.

Vasquez and coworkers utilized the nsTAS system to directly observe the excited state dynamics of different emitters reported to be TADF-active.[68] They were particularly interested in observing excited states with triplet characteristics. By obtaining the lifetime of these states and the quantum yield enhancement after oxygen purging, the following equation was produced:

$$k_{rISC} = k_{Triplet} * \Phi_{TADF} \qquad \textbf{Equation1.3.2.5}$$

Where $k_{Triplet}$ is the rate of triplet excited state decay and Φ_{TADF} is the quantum yield enhancement as a result of TADF. Tne benefit of the above equation is that it has far fewer variables and assumptions than **Eqn. 1.3.2.1**, which should lead to a lower potential for error in the final k_{rISC} value. In addition to this, it also requires that one observes the triplet state in the nsTAS spectrum of the emitter. If no triplet states are observed, then the emitter is not designated as being TADF-active. This requires that the measurement be conducted in solution, so as to prevent guest-host interactions that could lead to false positives, as was the case for BCC-TPTA. However, it is important that the proper solvent is chosen as solvents also affect emitter photophysics and subsequent TADF-activity.

1.4. Considerations for Achieving TADF

1.4.1. Overlap of the Highest Occupied and Lowest Unoccupied Molecular Orbitals

The overlap of the highest occupied molecular orbital (HOMO) and lowest unoccupied molecular orbital (LUMO) is of great importance to TADF efficiency, as ΔE_{ST} can be described through the degree of HOMO/LUMO overlap.[51] Increased spatial separation of the HOMO and LUMO leads to decreased ΔE_{ST}, critical for high k_{rISC} and strong spin-orbit coupling (SOC).[32] This is typically achieved through localizing the HOMO on the donor subunit and the LUMO on the acceptor subunit.[32,69] However, achieving a small ΔE_{ST} through spatial separation of the HOMO and LUMO alone is not sufficient for TADF-activity.[70] This is because large separation of the HOMO and LUMO results in large degrees of CT character and low radiative rates. It is also necessary for the T_1 manifold to also have some degree of LE character. The importance of this is discussed further in the next section.

The energy gaps between the excited states have a direct impact on k_{rISC}, significant research has been conducted on how to tune this through the lens of altering the HOMO/LUMO overlap.

As LE excited states are more resistant to having their energies altered than those with CT character, it is recommended to focus on altering the CT states. One popular method of doing this is by reducing the energy gap between the HOMO and LUMO (ΔE_{H-L}) of the donor or acceptor subunits to subsequently reduce ΔE_{ST} of the overall emitter.[34,70] This alters the singlet CT (CT^1) state's energy to be within the ΔE_{ST} range necessary for TADF.

Another recommended method is to increase the number of donor units. The donor units must be of the same species, such as carbazole donors. Not only does this reduce ΔE_{ST}, it also adds CT character to the typically LE triplet manifold. Efficient rISC would not be allowed if the triplet manifold did not have some degree of CT character.[71] The following section goes into more detail regarding the interaction between these three states.

1.4.2. Locally Excited Triplet (LE^3) and Spin-Orbit Coupling (SOC)

Spin-orbit coupling (SOC) is a relativistic interaction between a particle's spin and momentum within a potential.[62] This interaction allows for spin-forbidden processes such as intersystem crossing to occur. The SOC strength for a typical 2p element ranges from a few tenths of a milli eV while it is several eV for 6p elements.[72] Thus heavy metal elements, such as iridium and platinum, are often included in the molecular design of emitters to achieve strong SOC.[20,23,26] However, a small coupling matrix can induce ISC if the electronic states of different multiplicity (e.g. S_1 and T_1 manifolds) are close in energy.[72] The relative energies of the singlet charge-transfer (CT^1), triplet charge-transfer (CT^3), and triplet local exciton (LE^3) states need to be considered in the case of TADF emitters. As such considerable research has been conducted to better understand the interactions between these states and how they can be tuned.

In an investigation on the TADF-emitter DPTZ-DBTO2 (**Figure 1.4.2.1**), Dias and coworkers found that a small singlet-triplet energy gap (ΔE_{ST} = 0.01 eV) can be achieved through a near-orthogonal donor-acceptor-donor (D-A-D) molecular geometry.[52] Unfortunately , rigidly

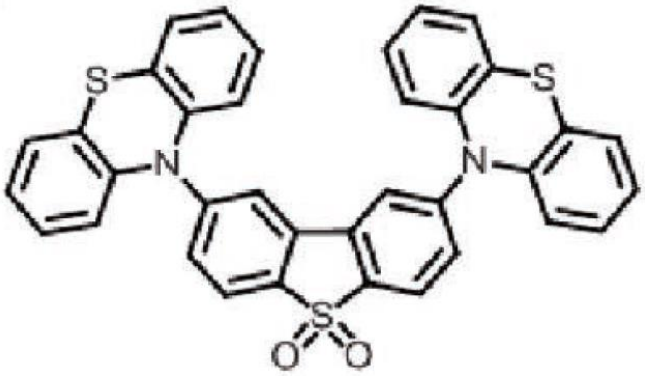


Figure 1.4.2.1. Molecular structure of DPTZ-DBTO2.

constraining the emitter in this geometry restricts electronic coupling between the LE^3 and CT^1, subsequently quenching TADF emission. One may suspect then that the answer lies in allowing a more planar geometry. However, ΔE_{ST} increases substantially (ΔE_{ST} = 0.8 eV) in a planar geometry which prevents rISC from occurring. The answer then, is to allow for the emitter to remain in a nearly-orthogonal geometry so that the interaction between CT^1 and LE^3 can occur.

However, an orthogonal geometry would make TADF-activity very difficult for many emitters.[73] There is additional evidence that a second-order spin-vibronic coupling mechanism is also at play, involving the CT^3 state.[52,74] Such second-order coupling is required as SOC between CT^1 and CT^3, states commonly produced as a result of the D-A-D molecular structure, is forbidden.[75] Although hyperfine coupling between CT^1 and CT^3 is possible, the energy gap required for this phenomenon is extremely small (<<1 meV) and any resulting rISC has a rate much too small to outcompete phosphorescence and other triplet decay pathways.[52,73,76]

$$k_{rISC} = \frac{2\pi}{h}\left|\langle \Psi_{^3CT}|\hat{H}_{vib}|\Psi_{^3LE}\rangle\right|^2 \delta(E_{^3CT} - E_{^3LE}) \qquad \textbf{Equation 1.4.2.1}$$

$$k_{rISC} = \frac{2\pi}{h}\left|\frac{\langle \Psi_{^1CT}|\hat{H}_{SOC}|\Psi_{^3LE}\rangle\langle \Psi_{^3LE}|\hat{H}_{vib}|\Psi_{^3CT}\rangle}{E_{^3CT} - E_{^3LE}}\right|^2 \delta(E_{^1CT} - E_{^3LE}) \quad \textbf{Equation 1.4.2.2}$$

The above equations describe a two-step mechanism, where the first step involves the vibronic coupling between the ^{3}LE and ^{3}CT causes an equilibrium between the two states (**Eqn. 1.4.2.1**). The position of the equilibrium depends on the strength of the vibronic coupling and the energy gap between these states. The second step couples the ^{1}CT and ^{3}CT by using ^{3}LE as an intermediate (**Eqn. 1.4.2.2**). This requires vibrational overlap between the two CT states.[73,74] These equations indicate that TADF is dominated by the $CT^1 - CT^3$ energy gap rather than the $CT^1 - LE^3$ energy gap.[77]

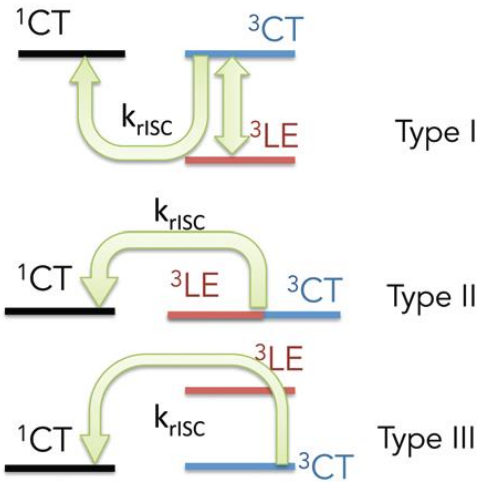


Figure 1.4.2.2. Energy levels of the three types of TADF.

Of course, the strength of the SOC and second-order interactions are closely tied to the relative energies of the excited states, and thus play a crucial role in determining the efficiency of TADF and k_{rISC}. Various studies have been conducted with the goal of elucidating which orientation of

the excited states (CT^1, CT^3, and LE^3) leads to the greatest TADF-activity (**Figure 1.4.2.2**).[77] They report that the ideal TADF-emitter should be designed so that the CT^1 is degenerate with LE^3, which allows for a large radiative rate and efficient TADF.[70,73] Such a strategy has the added advantage of somewhat relaxing the small HOMO/LUMO overlap design principle which, if separated to too large a degree, will lower the radiative rate by introducing to great a CT character to the excited states.

1.4.3. Predicting TADF Efficiency

Accurate predictions of what molecules would be best suited for TADF emission would be of great benefit with regards to generating emitters with high k_{rISC}.[69] Thus, there have been various computational studies conducted with the goal of determining which structures achieve the best HOMO/LUMO separation, smallest ΔE_{ST}, and greatest k_{rISC}.[43,51,64,78,79] Shu et al. conducted a study utilizing a genetic algorithm (**Figure 1.4.3.1**) in a chemical space of 10^6 molecules.[80]

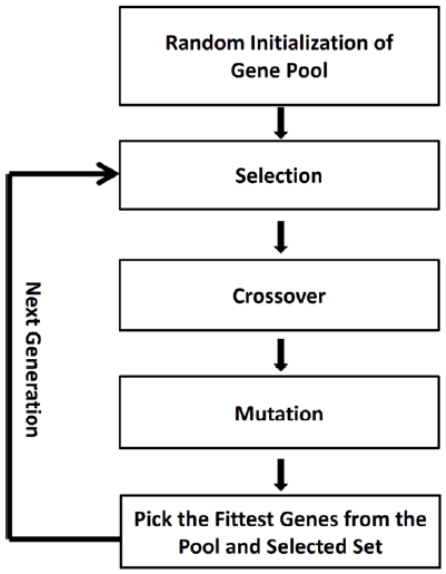


Figure 1.4.3.1. Genetic algorithm for purpose of predicting TADF emitter design.

First a pool of molecules is generated, creating the *first generation*. A molecule is selected at random from a vast collection of molecules and its *fitness* as a TADF emitter is calculated. This continues until enough molecules of sufficient fitness are selected to create the first generation. Then the molecules are paired together and randomly exchange molecular fragments with the hope of enhancing their fitness. These are comparable to the *second generation* of mating animals. Finally, random fragments of these second-generation molecules are *mutated* by exchanging them with random fragments. The fittest of this generation are then used to repeat the process.

To demonstrate the merit of this approach, the researchers computed the efficiency of the known TADF emitter 4CzIPN.[66,81] Their HOMO/LUMO calculations for 4CzIPN show that the HOMO is localized on the Cbz donor subunits and the LUMO is localized on the dicyanobenzene acceptor, consistent with what's required for TADF-activity. Unfortunately, the ΔE_{ST} was calculated to be 0.41 eV. This is significantly greater than the experimental results (ΔE_{ST} = 0.083 eV). This is significant, as k_{rISC} efficiency is reliant on small ΔE_{ST}. Thus, more accurate predictive methods would be ideal.

The approach by computational approach by Penfold builds off of the genetic algorithm approach previously described.[51] In this new approach Penfold focuses on the exchange interactions between the S_1 and T_1 states. This is due to this interaction increasing S_1 energy while lowering T_1 energy, its relationship to HOMO/LUMO overlap, and being computationally inexpensive to determine. This approach shows good correlation between the computed HOMO/LUMO overlap and experimental ΔE_{ST}. However, these calculations are meant as a guide, and are not 100% accurate at predicting how an emitter will behave in different environments. Therefore, experimental investigations are needed to determine which design principles are truly better suited for OLED applications and will better inform the predictive methods.

1.4.4. Design Motifs of TADF Emitters

One design concern for TADF emitters is the relationship between efficient radiative decay and ΔE_{ST}. A small ΔE_{ST} is critical to achieve a k_{rISC} that can outcompete other T_1 decay pathways. It is also important that the radiative rate (k_r) of S_1 excitons be large obtain a high fluorescence quantum yield (Φ_F). This unfortunately requires a rather large S_1 energy which conflicts with the small ΔE_{ST} requirement. Thus, it is important that design strategies of TADF emitters achieve a moderate k_r and a small ΔE_{ST}. This is commonly achieved by pairing one or more strong electron-

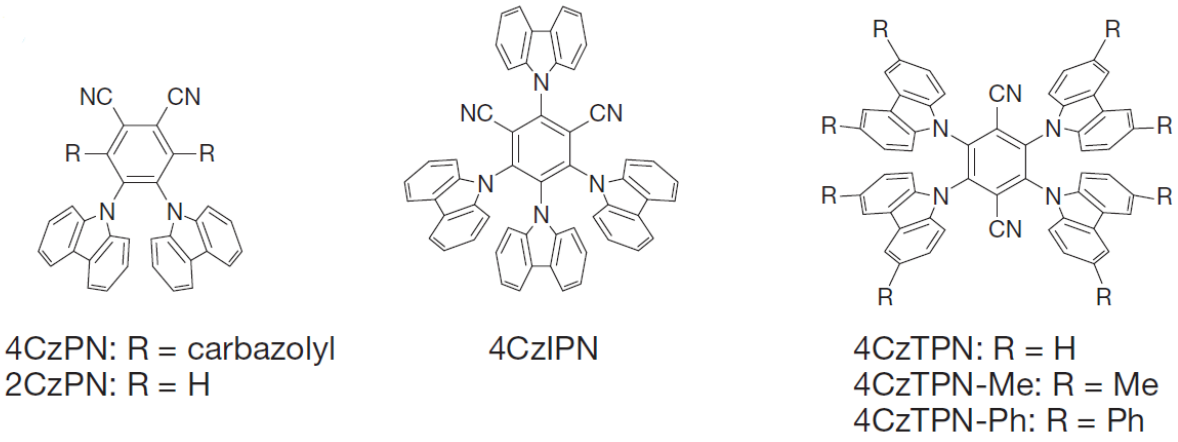


Figure 1.4.4.1. Molecular structures of carbazole based TADF-emitters.

donor(s) with one or more strong electron-acceptor(s) in a purely organic donor-acceptor (D-A) or donor-acceptor-donor (D-A-D) molecular design that promotes the formation of charge-transfer (CT) excited states.

A common design motif is to couple multiple donor units to one or more acceptor units (**Figure 1.4.4.1**). A very popular choice for a donor is carbazole and its derivatives. Carbazole's (Cbz) high energy and stable triplet states, bulk, ease of tunability, and relatively low cost make it a particularly attractive donor unit for TADF emitter structures.[32,69,82] Numerous high-performing

emitters have paired Cbz with different acceptor units such as phthalonitrile, triazine, pyridines, benzophenones, and thioxanthones to name but a few. In a study conducted by Adachi et al., Cbz and Cbz-derivatives were used to synthesize multiple TADF emitters.[66] By changing the number of donors and their location, the researchers were able to achieve a wide range of emissive colors. The 2Cz-PN, 4CzIPN, and 4CzTPH-PH emitters are particularly noteworthy due to their sky blue, green, and orange emissive colors, respectively. The researchers fabricated OLEDs using these emitters and achieved external quantum efficiencies (EQEs) of 8.0%, 11.2%, and 19.3%, respectively, breaking the theoretical max EQE of fluorescent-based OLEDs.

Another design strategy is to utilize stronger Cbz derivatives instead of adding more Cbz units to the acceptor. The carbazole derivates BFCbz and BTCbz were utilized as donors and paired with a phthalonitrile acceptor as a means to investigate whether this would result in a better performing OLED. The resulting BFCbz-PN and BTCbz-PN were compared to the 2CzPN emitter from the previously discussed study. Lee and coworkers found that both BFCbz-PN and BTCbz-PN have greater Φ_F than 2CzPN in an mCP doped film, indicating greater TADF activity. The researchers then fabricated OLEDs using BFCbz-PN and BTCbz-PN as the emitters and achieved EQEs of 12.1% and 11.8%, respectively.[83] This is appreciably better than the 2CzPN OLED, indicating that the use of stronger donors is a viable option to enhance TADF-activity.

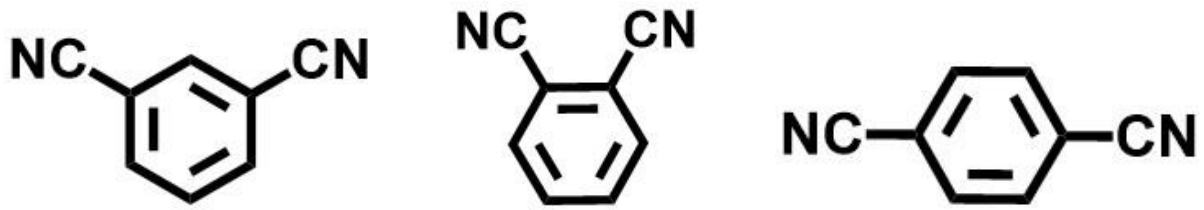


Figure 1.4.4.2. Molecular structures of 1,3-dicyanobenzene (left), 1,2-dicyanobenze (center), and 1,4-dicyanobenzene (right).

One of the more popular acceptors paired with Cbz and Cbz derivatives are those classified as dicyanobenzes (**Figure 1.4.4.2**). They are attractive as acceptors due to the cyano groups having strong electron-withdrawing capabilities and the benzene ring having multiple attachment sites

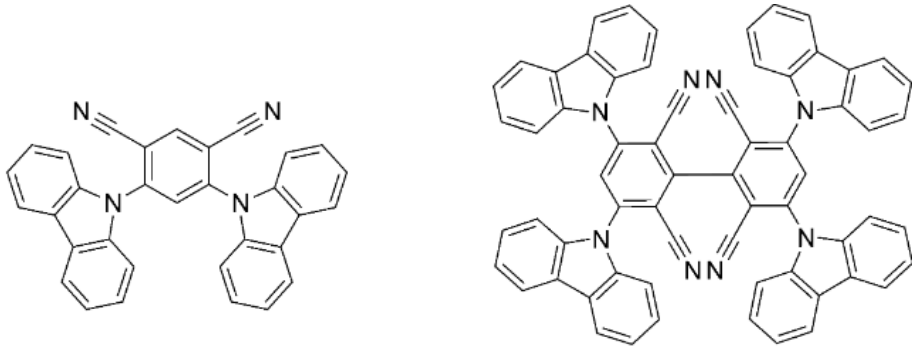


Figure 1.4.4.3. Molecular structure of mono-core (left) and dual-core (right) emitters.

allowing for a wide range of molecular design strategies. Lee et al. successfully synthesized an emitter with two acceptors as the core by linking two emitters through their dicyanobenzene acceptors.[84] The authors first synthesized mono-core emitter DCzIPN and then conducted a hydroquinone-mediated coupling of two DCzIPN emitters to obtain the dual-core emitter DDCzIPN (**Figure 1.4.4.3**).

They found that DDCzIPN had a significantly higher Φ_F than its mono core counterpart, having a Φ_F of 91% vs 67%. The highest occupied molecular orbital (HOMO) and lowest unoccupied molecular orbital (LUMO) were sufficiently separated, with the HOMO being localized on the Cbz donors and the LUMO being largely localized on the dual-acceptor core. This separation allowed for a small ΔE_{ST} of 0.13 eV, allowing for DDCzIPN to have greater TADF-activity than DCzIPN.

The other common design motif for TADF-emitters is to utilize a linker to couple the donor and the acceptor in a donor-linker-acceptor structure. However, there are some concerns with using this design approach. The disagreement between the report of BCC-TPTA being a TADF-emitter but not displaying TADF-activity in solution has been described in an earlier section.[46,67] A theoretical paper by Gao and workers explores the influence of small changes to the emitter structure and the resulting TADF-activity.[85] They found that a significant portion of HOMO/LUMO overlap occurs on the linker between the donor and acceptor subunits. This prevents the separation required for SOC and subsequent rISC. However, greater separation is observed when a sufficiently strong donor is used. This theoretical work is supported by the work done on BCC-TPTA, and thus calls into question the efficiency of this particular design motif for achieving TADF.

Color purity is also important for commercial application of TADF-based OLEDs. A relatively new design for TADF emitters focuses on addressing this issue and is known as magnetic resonance TADF (MR-TADF).[86–92] MR-TADF emitters utilize the resonance effects of electron-deficient and electron-rich elements to separate the HOMO and LUMO to achieve a small ΔE_{ST}. Examples of MR-TADF emitters are provided in **Figure 1.4.4.4**. These molecular structures are typically more rigid than their D-A counterparts, which lends itself to high photoluminescence quantum yields and narrowband emission. One of the earliest MR-TADF emitters was developed

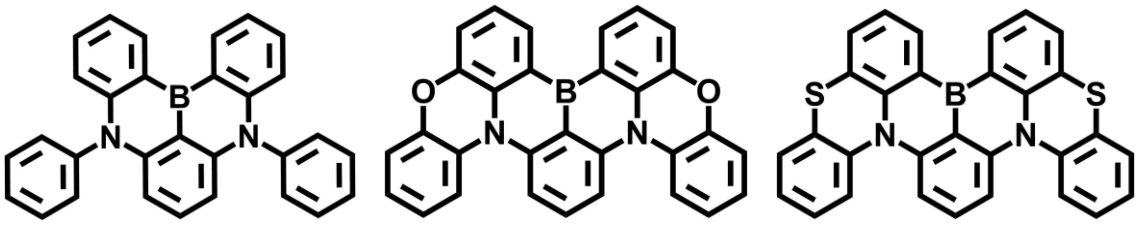


Figure 1.4.4.4. Examples of multi-resonance thermally activated delayed fluorescent emitters.

by Hirai and coworkers, where boron and oxygen were incorporated into the molecular design to localize the HOMO and LUMO of the emitter.[93]

Other atoms can be incorporated into MR-TADF emitter designs, namely nitrogen and sulfur.[94,95] Hua and coworkers were able to fabricate an OLEDs with appreciable EQEs of 19.9 – 34.8%. The emission maximum was able to be tuned from 490 nm to 468 nm through the incorporation of diphenylamine and sulfone units to the boron/nitrogen core of the emitter. These works serve to highlight the vast amount of synthesis and molecular design strategies conducted to make use of the TADF mechanism.

1.5. Influence of Environment on TADF-activity

The environment of a TADF emitter has significant impact on its efficiency. Polarity of the environment, whether it be solution or solid-state material, is of particular importance as it affects

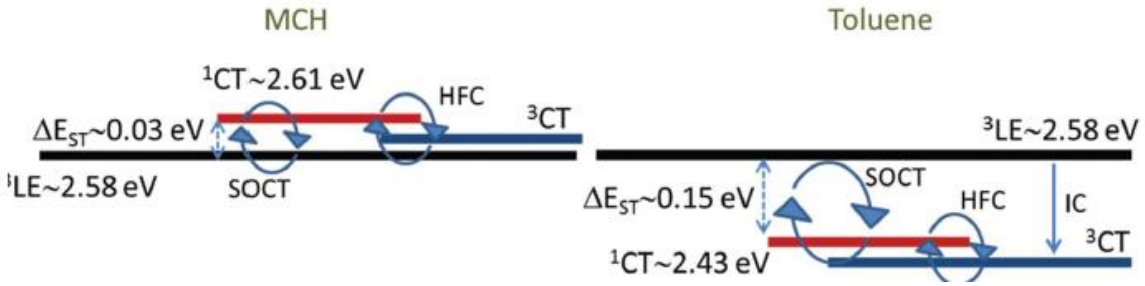


Figure 1.5.1. Effect of solvent polarity on the energy gap between the excited states.

ΔE_{ST} and subsequently k_{rISC}.[96–102] The degree of influence an environment has on the energies of the excited states largely depends on the character of the excited states. For example, the S_1 typically has a large degree of charger transfer character and can be designated as CT^1. The T_1 state typically has a mix of charger transfer and local exciton characters, being designated as CT^3 and LE^3, respectively.

Charge transfer states, such as the CT^1 and CT^3 states, are polar and are more stabilized by polar environments, such as ethanol.[103,104] Conversely, they are less stabilized in non-polar environments, such as toluene. The LE^3 is largely unaffected by environmental polarity.[102,105] As the energy of these states are altered, the efficiency of rISC and SOC are also affected (**Figure 1.5.1**).[52] What follows is a brief description of the influence of the environment, both solution and solid-state, on the relative energies of these states and the resulting TADF-activity.

Solvent	Emission Max (nm)	Quantum Yield
Acetonitrile	551	0.18
Ethanol	549	0.14
Dichloromethane	536	0.54
Toluene	507	0.94

Table 1.5.1. Photophysical properties of 4CzIPN in four solvents of varying polarities.

The effects of solvent polarity on TADF-activity were investigated by Ishimatsu and coworkers in their study on 4CzIPN.[106] They observed the emissive dynamics of 4CzIPN in

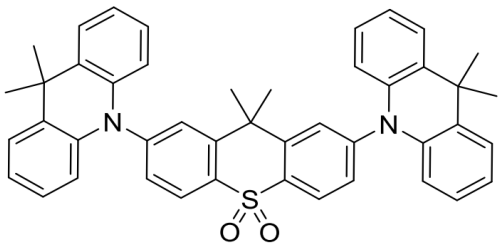


Figure 1.5.2. Molecular structure of DDMA-TXO2.

acetonitrile, ethanol, dichloromethane, and toluene. As show in **Table 1.5.1**, they found that the quntum yield of the emitter is significantly greater in nonpolar toluene (0.94) than it is in the polar acetonitrile (0.18). These results highlight the importance of carefully considering which solvent to use when designing experiments that explore and emitter's TADF-activity.

Solid-state host materials can induce a similar affect via solid-state solvation interactions. A study conducted by los Santos and coworkers investigated the proper host material to reduce the rISC barrier of the TADF emitter DDMA-TXO2 **Figure 1.5.2**.[105] The researchers observed that the emission intensity increased by a factor of 3.70 when a toluene solution of DDMA-TXO2 was purged of oxygen. This indicated a rISC mechanism and TADF-activity. When placed within a zeonex solid-state host, DDMA-TXO2 is reported to have a Φ_F of ~18% under ambient conditions and ~30% in a nitrogen atmosphere. The enhancement from ambient to nitrogen conditions is indicative of a TADF mechanism. It was also determined that the ΔE_{ST} of DDMA-TXO2 when embedded into zeonex material is ~0.15 eV. When placed in the more polar DPEPO solid-state host material, the ΔE_{ST} of DDMA-TXO2 is significantly reduced to ~0.01 eV. A significant enhancement to Φ_F was also observed, with it being ~92% in ambient conditions and ~95% under nitrogen atmosphere. This enhancement is attributed to the higher polarity of DPEPO causing the CT states to be energetically closer to LE^3. This work highlights that an emitter's innate TADF capabilities can be dramatically enhanced when paired with the proper host material.

Other investigations have shown that the polarity of the host material be altered through the addition of optically-inert components, to better fine-tune the TADF-activity of an emitter. One such study conducted by Haseyama and coworkers added varying concentrations of camphoric anhydride (CA) to a mCP host material to alter the emissive lifetime dynamics of the TADF emitter 2Cbz-PN.[107] They observed that the emissive lifetime was significantly shorter at higher CA

concentrations, indicating that TADF-activity is suppressed in too polar an environment (**Figure 1.5.3**).

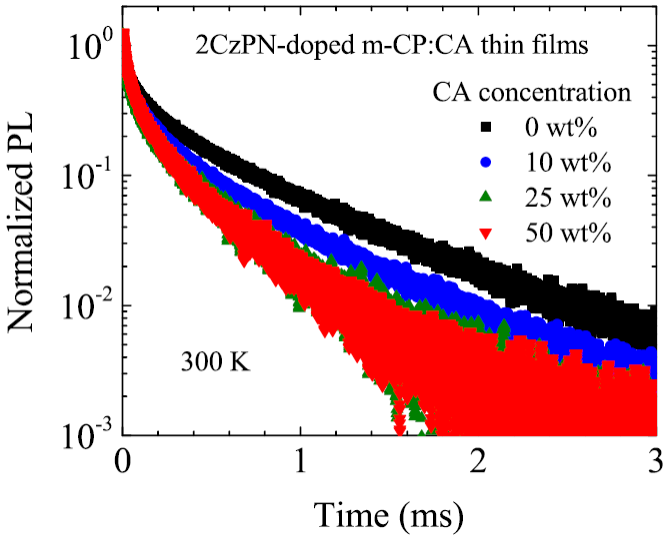


Figure 1.5.3. Emissive lifetimes as concentration of camphoric anhydride is increased in solid-state mCP host material.

Another study involving CA was conducted by Cotts et al, where CA was added to a non-polar polystyrene host material in increasing concentrations. They observed a red-shift in the emission of their chosen emitter, 2PXZ-OXD, as they increased the concentration of CA in the film. This indicates successful stabilization of the CT^1 state by increasing the polarity of the host matrix.[97,101] In addition to this, they also observe that the quantum yield increases over the CA concentration range of 2.5 – 10%. However, the quantum yield begins to decrease at CA concentrations greater than 10%. This result suggests that while CT^1 and CT^3 can be stabilized by increasing the polarity of the host matrix, and thus enhancing TADF-activity, too much stabilization will inhibit TADF-activity. This is likely due to the CT^1 and CT^3 no longer interact with the local excited triplet (LE^3) required for rISC to occur.[74] The interactions between these three states is expanded upon in later in this work.

Another property of the host material that is worthy of consideration is its rigidity in the solid-state. There are studies that indicate that rigidity may play a more impactful role in the observed emissive dynamics than the host polarity. Servicius and coworkers conducted a study that served to elucidate the which host material property is responsible for the shift in emission maximum that was observed in the time-resolved emission spectrum of a TADF emitter.[108] The researchers utilized the nonpolar polymethylmethacrylate (PMMA) and polystyrene (PS) as host materials, with PS being the more rigid of the two. They found that the PS film had a smaller degree of emission maximum shifting than the PMMA film. The researchers then tuned the polarity of these hosts by altering the doping concentration of CA. They observed an increase in the dielectric constants of both hosts as they increased the wt% of CA to 20% with the TADF emitter set to 1 wt%. They found that the degree of spectral shift did not follow a solvation model, but instead followed a conformational disorder model. This report suggest that host rigidity may play a more significant role in the temporal shifts in emission than host polarity.

This determination is supported by a study conducted by Penfold et al., where they utilized bis(2-diphenylphosphino)phenyl ether oxide (DPEPO), 4,4-N,N-dicarabazole-biphenyl (CBP), and 2,6-dicarbazolo-1,5-pyridine (PYD2) as host materials.[102] The researchers found that the emitter did not display a large shift from the absorbance to emission energy when placed in the more rigid PYD2 host. This was ascribed to rigidity of PYD2 restricting the host from reorienting after guest excitation. However, a more significant shift was observed for the DPEPO and CBP hosts which more closely resemble traditional solvation.

The host material also determines the orientation and degree of aggregation of the emitter. Noriega and coworkers utilized PMMA and PS as hosts to determine the influence of host material properties on the heterogeneity of single molecule and small aggregate emission.[109] They found

that the PMMA film had a greater degree of single emitters and the PS film has a greater degree of small aggregates. A decrease in the heterogeneity of the emission spectrum was observed with increased aggregation. The emitter also adopts a more twisted conformation in PS, which is beneficial for TADF, and a more planar conformation in PMMA. This is attributed to stronger π–π interactions between the side chains of PS and the emitter. However, these interactions also lead to a greater rate of non-radiative decay resulting in lower photoluminescence quantum yield.

Guest-host interactions could also aid in achieving TADF-activity. Many MR-TADF emitters only display TADF-activity in certain solid-state host materials. This suggests a particular interaction that is specific to that emitter-host pairing. Wu and coworkers report that this interaction is exciplex formation between the guest emitter and host material.[110] They report that exciplex formation depends on alignment of the orbital energy of the guest and host. They also report that such exciplex formation is available to emitters with thermally accessible ΔE_{ST}, such as BCC-TPTA. Each of these studies highlight the importance of selecting the proper host material to enhance TADF activity and the subsequent EQE of the OLED.

1.6. Similar Emissive Mechanism to TADF

Another emissive mechanism that has garnered interest as a method of converting non-emissive triplets into emissive singlets is triplet-triplet annihilation (TTA-UC). Unlike TADF, which is a process that takes place within one molecule, TTA-UC requires multiple molecules. **Figure 1.6.1** displays the non-emissive and emissive steps required to achieve TTA-UC mechanism.[111] Two species, known as the *sensitizer* (or *donor*) and *emitter* (or *acceptor*) are required for TTA-UC. First, the sensitizer absorbs the incident photon and then populates the triplet state. This requires the sensitizer to have a high intersystem crossing rate. Next, the triplet energy of the sensitizer is transferred to the triplet manifold of the emitter through a process known

as triplet-triplet energy transfer (TTET). The final step occurs when two emitters with populated triplet states interact, where one is promoted to the singlet excited state and the other is relaxed back to the ground state. The emitter that is now in the singlet excited state finally emits a photon through via fluorescence.[111–114] An Anti-Stokes shift is often a key indicator of TTA-UC, due to the emitter's singlet excited state being of a higher energy than the incident photon.[115–117]

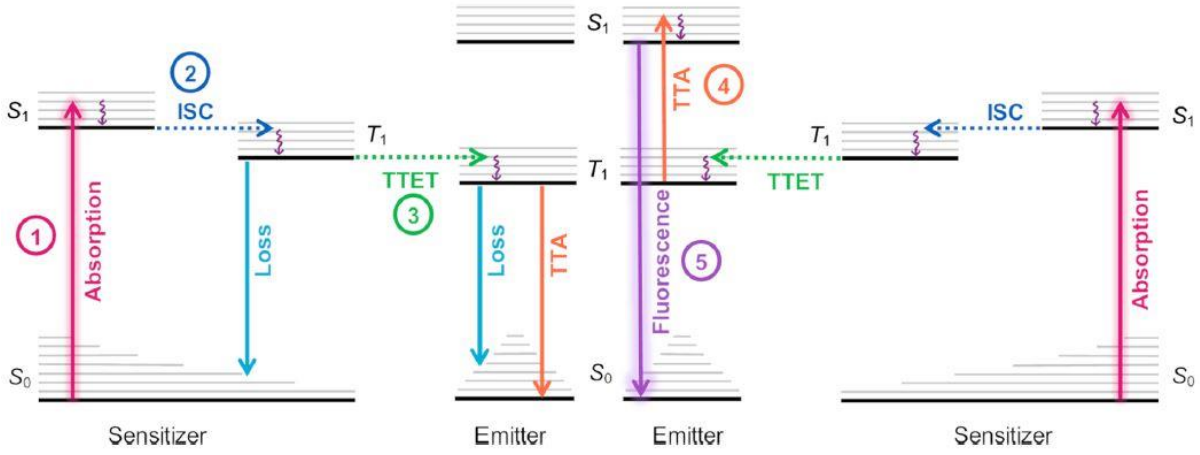


Figure 1.6.1. Energy diagram depicting the triplet-triplet annihilation mechanism.

It is worth noting that there is another nonlinear process that can result in an Anti-Stokes shift known as two-photon absorption upconversion (TPA-UC).[114] There are key differences between the mechanisms of TPA-UC and TTA-UC that aid in determining which process is occurring in a system. TPA-UC is the absorption of two photons of lower energy that promote an electron to a higher energy state. This requires high excitation intensity as this process requires both photons to be simultaneously absorbed. Thus, this process often involves the use of short pulse lasers with high peak intensities. A laser setup that utilizes two-photon absorption is described in more detail in Chapter 2. Alternatively, TTA-UC occurs when two neighboring emitters that have been promoted to the excited triplet state interact. This means that simultaneous absorption of multiple photons is not necessary. TTA-UC just requires that the interaction between the two excited

emitters takes place within the lifetime of their triplet states. Thus, TTA-UC can be achieved with a high intensity continuous wave laser or an incoherent lamp. Therefore, if an Anti-Stokes shift in emission is observed without the use of a high intensity laser then it is likely due to TTA-UC and not TPA-UC.

As stated previously, TTA-UC requires sensitizers and emitters to interact. Thus, TTA-UC efficiency is determined by the rate that the excited molecular species can interact with each other, often times in solution environment.[118] It is common for metals to be used in the molecular design of the sensitizer, due to sufficient SOC being required for efficient ISC to populate the triplet manifold.[111,112,114,119] Though in some cases the sensitizer can fully organic or be the same molecule as the emitter, so long as sufficient SOC is achieved.[120,121] Typically, a high concentration of emitter and sensitizers are used as this mechanism requires interaction between multiple species in the triplet excited state. The more of these species that are present, the more efficient the TTA-UC mechanism. However, high concentration of molecular species can also lead to aggregation which can lead to decay pathways that lower TTA-UC efficiency.[113] However, not all aggregation is detrimental to TTA-UC. In some cases aggregation can lead to more efficient transfer of triplet energy.[122,123]

TTA-UC can also occur in the solid-state, despite being a diffusion-controlled process in solution. This requires careful consideration of the host material as the host will need to enable efficient triplet energy transfer between neighboring emitters. This leads to different types of TTA-UC which are dependent on the triplet confinement abilities of the host (**Figure 1.6.2**).[124]

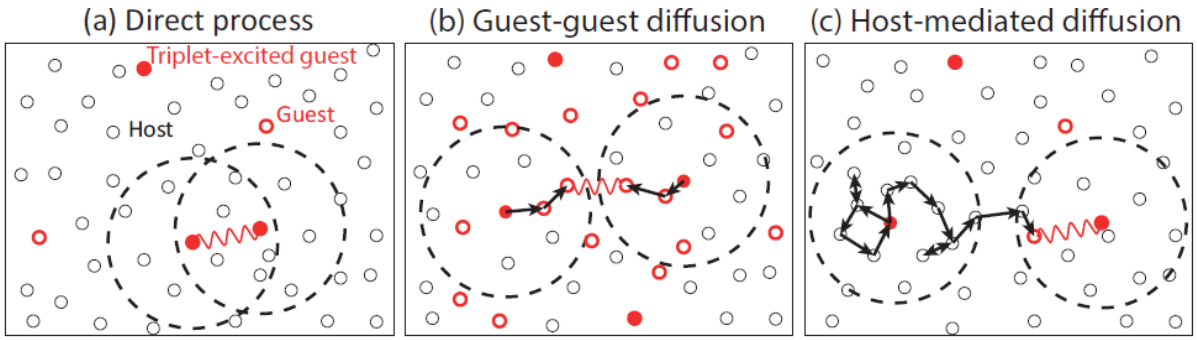


Figure 1.6.2. Energy diagram depicting the different triplet exciton transfer mechanisms based on confinement of the emitter's triplet excitons.

Ligthart and coworkers determined that when there is a large difference between the emitter and host triplet energies (large confinement) and a small emitter concentration then TTA is controlled by a single-step mechanism (**Figure 1.6.2a**). When the emitter concentration is increased (**Figure 1.6.2b**) then TTA is a multi-step process. And when there is a small difference in emitter and host triplet energies (weak confinement) then TTA is controlled by host-mediated diffusion, where the triplet exciton can travel over the host molecules until it reaches two emitters within close proximity to each other (**Figure 1.6.2c**). The host material must also be able to protect the excited states of both the sensitizer and emitter from oxygen, which is known to quench the triplet state.[111,114,125] The host material can also substantially enhance the triplet lifetime due to the molecular species being in a rigid environment.[126] However, a more flexible host would allow for better triplet exciton diffusion, albeit at the drawback of allowing for more oxygen quenching.[111,127]

Both TTA-UC and TADF share many similarities and requirements to be efficient emissive decay pathways. They each require protection from oxygen quenching, the host material affects their rate limiting steps (k_{rISC} and the triplet exciton diffusion rate), and each have appreciable emissive lifetimes with a second emissive component.[90,118,120,123,126,128] Because of these

parameters it would be easy to mistake one for the other. However, it is important to be able to distinguish between these emissive mechanisms as this will inform what methods should be taken to improve OLED efficiency. For example, while each mechanism requires a host that will protect it from oxygen quenching TTA-UC requires a host that will allow for efficient triplet exciton migration. TADF does not have this consideration, as triplet exciton migration would suppress TADF activity. Conversely a host that does not allow for triplet exciton migration would suppress TTA-UC activity.

1.7. Larger Picture and Dissertation Outline

The Covid-19 pandemic highlighted the importance of high-efficiency and high-quality displays for entertainment and communication. There has been significant industrial investment and academic research conducted on materials to achieve higher levels of color purity, high brightness, and device stability. However, more research is needed to determine the best emitters for this purpose. Therefore, this thesis focuses on using nonlinear optical and time-resolved spectroscopic techniques to better understand the excited state dynamics critical to the thermally activated delayed fluorescence mechanism for organic optoelectronic systems.

In chapter one, a brief history of OLEDs and their emitters is provided where the advantages and disadvantages of the different generations of OLEDs are highlighted and compared to their counterparts. The emitter structure of TADF-emitters in particular have been discussed, along with the conditions required to achieve TADF-activity and what external forces can alter TADF efficiency.

In chapter two, the experimental methods and techniques that were used in these investigations are discussed. With the most common design of TADF-emitters utilizing donor and acceptor units, significant research has been conducted to determine the best combination of donors and acceptors

with the aim of achieving TADF-emitters with the greatest k_{rISC}. Much of this research utilizes computationally predictions with the experimental studies being conducted in solid-state materials which can alter the emitter photophysics. Thus, various time-resolved and nonlinear optical spectroscopic techniques are utilized, for solution and film samples, to better understand the excited state dynamics of these emitters, with particular attention on the triplet excited state and emissive dynamics.

In chapter three, the first spectroscopic study that seeks to relate the emitter molecular design to TADF-activity is discussed. Specifically, the k_{rISC} of emitters that either have multiple donors directly attached to the acceptor or a donor connected to the acceptor via a linker are experimentally determined and compared. While various studies have reported on these and other emitters of similar structure, which design motif better lends itself to TADF-activity is still unclear. It was found that utilizing a linker to attach a single donor to the acceptor unit impedes sufficient HOMO/LUMO separation that's required for a small ΔE_{ST}. This in turn leads to a small k_{rISC} and no TADF-activity in solution. In contrast to this, emitters utilizing multiple donors directly linked to the acceptor unit displayed sufficient HOMO/LUMO separation, a smaller ΔE_{ST}, and $k_{rISC} \geq 10^3$. These results indicate that, while it may be possible for TADF-activity to be achieved with the donor-linker-acceptor design, future TADF-emitter designs should focus on connecting multiple donors attached to the acceptor. This work was accepted and published by *Chemistry of Materials*.

In chapter four, a second study that seeks to determine the feasibility of a benzo[1,2-d:4,5-d']bisoaxazole (BBO) ring system as a acceptor core for TADF emitters. Multiple carbazole donors were attached to the BBO core via phenylene linkers, similar to the emitters discussed in chapter three. It was found that the emitters that utilized one carbazole donor per linker were fluorescent emitters with no triplet states being observed in their transient absorption spectra. It

was thus determined that these emitters were not TADF-active and are instead fluorescent emitters. Those emitters that utilized two carbazole donors per linker displayed more interesting dynamics. While triplet states were observed in their transient absorption spectra, it was determined that these are not efficient TADF emitters. This is due to phosphorescence being observed in their transient absorption spectra with a phosphorescence rate of 10^5. Thus, these emitters were determined to be more efficient phosphorescent emitters and not TADF-active. Computational results revealed that the linker inhibited sufficient HOMO/LUMO separation which resulted in the lack of TADF characteristics. This work has been, at the time of writing, submitted for review and eventual publication to the *Journal of Materials Chemistry C*.

In chapter five, the changes of emitter photophysics as it is taken from a solution environment and placed in a solid-state environment is investigated. Specifically, the emitter BCC-TPTA, which has been observed to display TADF characteristics in solid-state but not solution, is placed in different THF/H_2O fractions aggregation and host materials with different properties (DPEPO, mCP, PMMA, and polystyrene). The different THF/H_2O fractions induced aggregation of the emitter which surprisingly induced a blue-shift of emission. These aggregates also displayed a second emissive component similar to what's observed for emissive processes that utilize triplet excited states. However, the lifetime of this second component is relatively short compared to what's typically observed with TADF emitters. This second component is observed in each of the solid-state hosts, with some having a significantly longer lifetime than others indicating that the host plays in important role in the emissive dynamics. However, the emissive mechanism was still not clear using the established spectroscopic measurements in the Goodson lab. Therefore a new experimental setup was made utilizing the emission detection capabilities of the nsTAS system. This new setup allowed for log/log plots of emission intensity vs laser excitation energy to be

obtained, revealing the emissive mechanisms of the films. The plot obtained for the DPEPO film has a slope of 1, indicating a monomolecular emissive process. This, in conjunction with the other data, indicates a TADF mechanism. However, the 99% H_2O fraction gave a slope of 0.36. This result shows a need for refinement of this technique and that further work is required.

In chapter six, a brief description of attempts to enhance ESA signal utilizing a novel scattering chamber is provided. The principle behind this scattering chamber is that the pathlength component of optical absorption signal could be artificially enhanced by increasing the number of times that the probe light interacts with the sample. This would be done by inducing scattering of the probe light within a chamber that housed the sample, and only allowing light that interacted with the sample multiple times to escape the chamber and reach the detector. While this first iteration of the chamber did not work as intended, it does provide a basis for future iterations.

In chapter seven, a summary of the work described in this dissertation is given as well as proposals for future direction. This work would further elucidate the interactions that cause the stark change in emissive dynamics that are observed for emitters that are taken from a solution environment and placed in a solid-state environment.

References:

(1) Valeur, B.; Berberan-santos, M. N. A Brief History of Fluorescence and Phosphorescence before the Emergence of Quantum Theory. *J. Chem. Educ.* **2011**, No. 88, 731–738.

(2) Kasha Michael. Characterization of Electronic Transitions in Complex Molecules. *Discuss. Faraday Soc.* **1950**, *9* (c), 14–19.

(3) Sharp, K.; Matschinsky, F. Translation of Ludwig Boltzmann's Paper "on the Relationship between the Second Fundamental Theorem of the Mechanical Theory of Heat and Probability Calculations Regarding the Conditions for Thermal Equilibrium" Sitzungberichte Der Kaiserlichen Akademie D. *Entropy* **2015**, *17* (4), 1971–2009. https://doi.org/10.3390/e17041971.

(4) Asano, M.; Kaizu, Y.; Kobayashi, H. The Lowest Excited States of Copper Porphyrins. *J. Chem. Phys.* **1988**, *89* (11), 6567–6587. https://doi.org/10.1063/1.455379.

(5) Knowles, K. E.; Nelson, H. D.; Kilburn, T. B.; Gamelin, D. R. Singlet-Triplet Splittings in the Luminescent Excited States of Colloidal Cu+:CdSe, Cu+:InP, and CuInS2 Nanocrystals: Charge-Transfer Configurations and Self-Trapped Excitons. *J. Am. Chem. Soc.* **2015**, *137* (40), 13138–13147. https://doi.org/10.1021/jacs.5b08547.

(6) McDowell, S. A. C. A Simple Derivation of the Boltzmann Distribution. *J. Chem. Educ.* **1999**, *76* (10), 1393–1394. https://doi.org/10.1021/ed076p1393.

(7) Del Valle, J. C.; Catalán, J. Kasha's Rule: A Reappraisal. *Phys. Chem. Chem. Phys.* **2019**, *21* (19), 10061–10069. https://doi.org/10.1039/c9cp00739c.

(8) Chen, Y.; Bai, Y.; Han, Z.; He, W.; Guo, Z. Photoluminescence Imaging of Zn2+ in Living Systems. *Chem. Soc. Rev.* **2015**, *44* (14), 4517–4546. https://doi.org/10.1039/c5cs00005j.

(9) Volz, D.; Wallesch, M.; Fléchon, C.; Danz, M.; Verma, A.; Navarro, J. M.; Zink, D. M.; Bräse, S.; Baumann, T. From Iridium and Platinum to Copper and Carbon: New Avenues for More Sustainability in Organic Light-Emitting Diodes. *Green Chem.* **2015**, *17* (4), 1988–2011. https://doi.org/10.1039/c4gc02195a.

(10) Qin, Z.; Gao, H.; Dong, H.; Hu, W. Organic Light-Emitting Transistors Entering a New Development Stage. *Adv. Mater.* **2021**, *33*, 1–17. https://doi.org/10.1002/adma.202007149.

(11) Zhang, Q.; Li, B.; Huang, S.; Nomura, H.; Tanaka, H.; Adachi, C. Efficient Blue Organic Light-Emitting Diodes Employing Thermally Activated Delayed Fluorescence. *Nat. Photonics* **2014**, *8* (4), 326–332. https://doi.org/10.1038/nphoton.2014.12.

(12) Hong, G.; Gan, X.; Leonhardt, C.; Zhang, Z.; Seibert, J.; Busch, J. M.; Bräse, S. A Brief History of OLEDs—Emitter Development and Industry Milestones. *Adv. Mater.* **2021**, *33* (9). https://doi.org/10.1002/adma.202005630.

(13) Tang, C. W.; Vanslyke, S. A. Organic Electroluminescent Diodes. *Appl. Phys. Lett.* **1987**, *51* (12), 913–915. https://doi.org/10.1063/1.98799.

(14) Tang, C. W.; Vanslyke, S. A.; Chen, C. H. Electroluminescence of Doped Organic Thin Films. *J. Appl. Phys.* **1989**, *65* (9), 3610–3616. https://doi.org/10.1063/1.343409.

(15) Forget, S.; Chenais, S.; Tondelier, D.; Geffroy, B.; Gozhyk, I.; Lebental, M.; Ishow, E. Red-Emitting Fluorescent Organic Light Emitting Diodes with Low Sensitivity to Self-Quenching. *J. Appl. Phys.* **2010**, *108* (6). https://doi.org/10.1063/1.3481460.

(16) Huang, J.; Su, J. H.; Tian, H. The Development of Anthracene Derivatives for Organic Light-Emitting Diodes. *J. Mater. Chem.* **2012**, *22* (22), 10977–10989. https://doi.org/10.1039/c2jm16855c.

(17) Adachi, C.; Tsutsui, T.; Saito, S. Blue Light-Emitting Organic Electroluminescent Devices. *Appl. Phys. Lett.* **1990**, *56* (9), 799–801.

(18) Zheng, C. J.; Zhao, W. M.; Wang, Z. Q.; Huang, D.; Ye, J.; Ou, X. M.; Zhang, X. H.; Lee, C. S.; Lee, S. T. Highly Efficient Non-Doped Deep-Blue Organic Light-Emitting Diodes Based on Anthracene Derivatives. *J. Mater. Chem.* **2010**, *20* (8), 1560–1566. https://doi.org/10.1039/b918739a.

(19) Yersin, H.; Rausch, A. F.; Czerwieniec, R.; Hofbeck, T.; Fischer, T. The Triplet State of Organo-Transition Metal Compounds. Triplet Harvesting and Singlet Harvesting for Efficient OLEDs. *Coord. Chem. Rev.* **2011**, *255* (21–22), 2622–2652. https://doi.org/10.1016/j.ccr.2011.01.042.

(20) Gildea, L. F.; Williams, J. A. G. *Iridium and Platinum Complexes for OLEDs*; Woodhead Publishing Limited, 2013. https://doi.org/10.1533/9780857098948.1.77.

(21) Baldo, M. A.; an dY. You, D. F. O.; Shoustikov, A.; Sibley, S.; Thompson, M. E.; Forrest, S. R. Highly Efficient Phosphorescent Emission from Organic Electroluminescent Devices. *Nature* **1998**, *395* (September), 151.

(22) Rortais, F.; Lee, S.; Ohshima, R.; Dushenko, S.; Ando, Y.; Shiraishi, M. Spin-Orbit Coupling Induced by Bismuth Doping in Silicon Thin Films. *Appl. Phys. Lett.* **2018**, *113* (12). https://doi.org/10.1063/1.5046781.

(23) Cariati, E.; Forni, A.; Lucenti, E.; Marinotto, D.; Previtali, A.; Righetto, S.; Botta, C.; Bold, V.; Kravtsov, V.; Fonari, M. S. Extrinsic Heavy Metal Atom Effect on the Solid-State Room Temperature Phosphorescence of Cyclic Triimidazole. *Chem. Asian J.* 2019, pp 853–858.

(24) Kim, K. H.; Moon, C. K.; Lee, J. H.; Kim, S. Y.; Kim, J. J. Highly Efficient Organic Light-Emitting Diodes with Phosphorescent Emitters Having High Quantum Yield and Horizontal Orientation of Transition Dipole Moments. *Adv. Mater.* **2014**, *26* (23), 3844–3847. https://doi.org/10.1002/adma.201305733.

(25) Yang, X.; Guo, H.; Liu, B.; Zhao, J.; Zhou, G.; Wu, Z.; Wong, W. Y. Diarylboron-Based Asymmetric Red-Emitting Ir(III) Complex for Solution-Processed Phosphorescent Organic Light-Emitting Diode with External Quantum Efficiency above 28%. *Adv. Sci.* **2018**, *5* (5), 1–7. https://doi.org/10.1002/advs.201701067.

(26) Shin, H.; Ha, Y. H.; Kim, H. G.; Kim, R.; Kwon, S. K.; Kim, Y. H.; Kim, J. J. Controlling

Horizontal Dipole Orientation and Emission Spectrum of Ir Complexes by Chemical Design of Ancillary Ligands for Efficient Deep-Blue Organic Light-Emitting Diodes. *Adv. Mater.* **2019**, *31* (21), 1–6. https://doi.org/10.1002/adma.201808102.

(27) Goushi, K.; Yoshida, K.; Sato, K.; Adachi, C. Organic Light-Emitting Diodes Employing Efficient Reverse Intersystem Crossing for Triplet-to-Singlet State Conversion. *Nat. Photonics* **2012**, *6* (4), 253–258. https://doi.org/10.1038/nphoton.2012.31.

(28) Zhang, Y. L.; Ran, Q.; Wang, Q.; Liu, Y.; Hänisch, C.; Reineke, S.; Fan, J.; Liao, L. S. High-Efficiency Red Organic Light-Emitting Diodes with External Quantum Efficiency Close to 30% Based on a Novel Thermally Activated Delayed Fluorescence Emitter. *Adv. Mater.* **2019**, *31* (42), 1–7. https://doi.org/10.1002/adma.201902368.

(29) Li, M.; Liu, Y.; Duan, R.; Wei, X.; Yi, Y.; Wang, Y.; Chen, C. F. Aromatic-Imide-Based Thermally Activated Delayed Fluorescence Materials for Highly Efficient Organic Light-Emitting Diodes. *Angew. Chemie - Int. Ed.* **2017**, *56* (30), 8818–8822. https://doi.org/10.1002/anie.201704435.

(30) Endo, A.; Sato, K.; Yoshimura, K.; Kai, T.; Kawada, A.; Miyazaki, H.; Adachi, C. Efficient Up-Conversion of Triplet Excitons into a Singlet State and Its Application for Organic Light Emitting Diodes. *Appl. Phys. Lett.* **2011**, *98* (8), 10–13. https://doi.org/10.1063/1.3558906.

(31) Ha, J. M.; Hur, S. H.; Pathak, A.; Jeong, J. E.; Woo, H. Y. Recent Advances in Organic Luminescent Materials with Narrowband Emission. *NPG Asia Mater.* **2021**, *13* (1). https://doi.org/10.1038/s41427-021-00318-8.

(32) Ledwon, P. Recent Advances of Donor-Acceptor Type Carbazole-Based Molecules for Light Emitting Applications. *Org. Electron.* **2019**, *75* (August 2019), 105422. https://doi.org/10.1016/j.orgel.2019.105422.

(33) Volz, D. Review of Organic Light-Emitting Diodes with Thermally Activated Delayed Fluorescence Emitters for Energy-Efficient Sustainable Light Sources and Displays. *J. Photonics Energy* **2016**, *6* (2), 020901. https://doi.org/10.1117/1.jpe.6.020901.

(34) Lee, D. R.; Choi, J. M.; Lee, C. W.; Lee, J. Y. Ideal Molecular Design of Blue Thermally Activated Delayed Fluorescent Emitter for High Efficiency, Small Singlet-Triplet Energy Splitting, Low Efficiency Roll-off, and Long Lifetime. *ACS Appl. Mater. Interfaces* **2016**, *8* (35), 23190–23196. https://doi.org/10.1021/acsami.6b05877.

(35) Li, J.; Zhao, F.; Chen, Y.; Zhang, M.; Li, T.; Zhang, H. Color Tuning of Di-Boron Derived TADF Emitters: Molecular Design and Property Prediction. *Journal of Materials Chemistry C*. 2021, pp 15309–15320.

(36) Lee, J. H.; Chen, C. H.; Lee, P. H.; Lin, H. Y.; Leung, M. K.; Chiu, T. L.; Lin, C. F. Blue Organic Light-Emitting Diodes: Current Status, Challenges, and Future Outlook. *J. Mater. Chem. C* **2019**, *7* (20), 5874–5888. https://doi.org/10.1039/c9tc00204a.

(37) Murawski, C.; Leo, K.; Gather, M. C. Efficiency Roll-off in Organic Light-Emitting Diodes. *Adv. Mater.* **2013**, *25* (47), 6801–6827. https://doi.org/10.1002/adma.201301603.

(38) Wu, Z. G.; Zheng, Y. X.; Zhou, L.; Wang, Y.; Pan, Y. Suppression of Efficiency Roll-off in Highly Efficient Blue Phosphorescent Organic Light-Emitting Devices Using Novel Iridium Phosphors with Good Electron Mobility. *Org. Electron.* **2017**, *42*, 141–145. https://doi.org/10.1016/j.orgel.2016.12.032.

(39) Hosokai, T.; Matsuzaki, H.; Nakanotani, H.; Tokumaru, K.; Tsutsui, T.; Furube, A.; Nasu, K.; Nomura, H.; Yahiro, M.; Adachi, C. Evidence and Mechanism of Efficient Thermally Activated Delayed Fluorescence Promoted by Delocalized Excited States. *Sci. Adv.* **2017**, *3* (May), 1–10. https://doi.org/10.1126/sciadv.1603282.

(40) Samanta, P. K.; Kim, D.; Coropceanu, V.; Brédas, J. L. Up-Conversion Intersystem Crossing Rates in Organic Emitters for Thermally Activated Delayed Fluorescence: Impact of the Nature of Singlet vs Triplet Excited States. *J. Am. Chem. Soc.* **2017**, *139* (11), 4042–4051. https://doi.org/10.1021/jacs.6b12124.

(41) Sun, J. W.; Kim, K. H.; Moon, C. K.; Lee, J. H.; Kim, J. J. Highly Efficient Sky-Blue Fluorescent Organic Light Emitting Diode Based on Mixed Cohost System for Thermally Activated Delayed Fluorescence Emitter (2CzPN). *ACS Appl. Mater. Interfaces* **2016**, *8* (15), 9806–9810. https://doi.org/10.1021/acsami.6b00286.

(42) Masui, K.; Nakanotani, H.; Adachi, C. Analysis of Exciton Annihilation in High-Efficiency Sky-Blue Organic Light-Emitting Diodes with Thermally Activated Delayed Fluorescence. *Org. Electron.* **2013**, *14* (11), 2721–2726. https://doi.org/10.1016/j.orgel.2013.07.010.

(43) Olivier, Y.; Sancho-Garcia, J. C.; Muccioli, L.; D'Avino, G.; Beljonne, D. Computational Design of Thermally Activated Delayed Fluorescence Materials: The Challenges Ahead. *J. Phys. Chem. Lett.* **2018**, *9* (20), 6149–6163. https://doi.org/10.1021/acs.jpclett.8b02327.

(44) Rodriguez-Serrano, A.; Dinkelbach, F.; Marian, C. M. Intersystem Crossing Processes in The2CzPNemitter: A DFT/MRCI Study Including Vibrational Spin-Orbit Interactions. *Phys. Chem. Chem. Phys.* **2021**, *23* (5), 3668–3678. https://doi.org/10.1039/d0cp06011a.

(45) Masui, K.; Nakanotani, H.; Adachi, C. Analysis of Exciton Annihilation in High-Efficiency Sky-Blue Organic Light-Emitting Diodes with Thermally Activated Delayed Fluorescence. *Org. Electron.* **2013**, *14* (11), 2721–2726. https://doi.org/10.1016/j.orgel.2013.07.010.

(46) Hirata, S.; Sakai, Y.; Masui, K.; Tanaka, H.; Lee, S. Y.; Nomura, H.; Nakamura, N.; Yasumatsu, M.; Nakanotani, H.; Zhang, Q.; Shizu, K.; Miyazaki, H.; Adachi, C. Highly Efficient Blue Electroluminescence Based on Thermally Activated Delayed Fluorescence. *Nat. Mater.* **2015**, *14* (3), 330–336. https://doi.org/10.1038/nmat4154.

(47) Lin, T. A.; Chatterjee, T.; Tsai, W. L.; Lee, W. K.; Wu, M. J.; Jiao, M.; Pan, K. C.; Yi, C. L.; Chung, C. L.; Wong, K. T.; Wu, C. C. Sky-Blue Organic Light Emitting Diode with 37% External Quantum Efficiency Using Thermally Activated Delayed Fluorescence from Spiroacridine-Triazine Hybrid. *Adv. Mater.* **2016**, *28* (32), 6976–6983. https://doi.org/10.1002/adma.201601675.

(48) Niu, R.; Li, J.; Liu, D.; Dong, R.; Wei, W.; Tian, H.; Shi, C. A Versatile Carbazole Donor Design Strategy for Blue Emission Switching from Normal Fluorescence to Thermally Activated Delayed Fluorescence. *Dye. Pigment.* **2021**, *194* (June). https://doi.org/10.1016/j.dyepig.2021.109581.

(49) Chen, X. K.; Bakr, B. W.; Auffray, M.; Tsuchiya, Y.; Sherrill, C. D.; Adachi, C.; Bredas, J. L. Intramolecular Noncovalent Interactions Facilitate Thermally Activated Delayed Fluorescence (TADF). *J. Phys. Chem. Lett.* **2019**, *10* (12), 3260–3268. https://doi.org/10.1021/acs.jpclett.9b01220.

(50) Franco, O.; Jakoby, M.; Schneider, R. V.; Hundemer, F.; Hahn, D.; Richards, B. S.; Bräse, S.; Meier, M. A. R.; Lemmer, U.; Howard, I. A. Sensitizing TADF Absorption Using Variable Length Oligo(Phenylene Ethynylene) Antennae. *Frontiers in Chemistry*. 2020. https://doi.org/10.3389/fchem.2020.00126.

(51) Penfold, T. J. On Predicting the Excited-State Properties of Thermally Activated Delayed Fluorescence Emitters. *J. Phys. Chem. C* **2015**, *119* (24), 13535–13544. https://doi.org/10.1021/acs.jpcc.5b03530.

(52) Dias, F. B.; Santos, J.; Graves, D. R.; Data, P.; Nobuyasu, R. S.; Fox, M. A.; Batsanov, A. S.; Palmeira, T.; Berberan-Santos, M. N.; Bryce, M. R.; Monkman, A. P. The Role of Local Triplet Excited States and D-A Relative Orientation in Thermally Activated Delayed Fluorescence: Photophysics and Devices. *Adv. Sci.* **2016**, *3* (12), 1–10. https://doi.org/10.1002/advs.201600080.

(53) Kang, H.; Jung, B.; Kim, S. K. Mechanism for Ultrafast Internal Conversion of Adenine. *Journal of Chemical Physics*. 2003, pp 6717–6719. https://doi.org/10.1063/1.1566438.

(54) Teller, E. Internal Conversion In Polyatomic Molecules. *Isr. J. Chem.* **1969**, *7*, 227–235.

(55) Yoshihara Toshitada; Shimada Hirofumi; Shizuka Haruo; Tobita Seiji. Internal Conversion of O-Aminoacetophenone in Solution.Pdf. *Phys. Chem. Chem. Phys.* 2001, pp 4972–4978.

(56) Valiev, R. R.; Nasibullin, R. T.; Cherepanov, V. N.; Kurtsevich, A.; Sundholm, D.; Kurtén, T. Fast Estimation of the Internal Conversion Rate Constant in Photophysical Applications. *Phys. Chem. Chem. Phys.* **2021**, *23* (11), 6344–6348. https://doi.org/10.1039/d1cp00257k.

(57) Zhang, J. M.; Liu, Y. Fermi's Golden Rule: Its Derivation and Breakdown by an Ideal Model. *Eur. J. Phys.* **2016**, *37* (6). https://doi.org/10.1088/0143-0807/37/6/065406.

(58) Dirac, P. A. M. The Quantum Theory of Emission and Absorption of Radiation. *Sci. Glob. Secur.* **1990**, *1* (3–4), 265–285. https://doi.org/10.1080/08929889008426335.

(59) Hauser, A.; Vef, A.; Adler, P. Intersystem Crossing Dynamics in Fe(II) Coordination Compounds. *J. Chem. Phys.* **1991**, *95* (12), 8710–8717. https://doi.org/10.1063/1.461255.

(60) Lawetz, V.; Orlandi, G.; Siebrand, W. Theory of Intersystem Crossing in Aromatic Hydrocarbons. *J. Chem. Phys.* **1972**, *56* (8), 4058–4072. https://doi.org/10.1063/1.1677816.

(61) Valentine, A. J. S.; Li, X. Toward the Evaluation of Intersystem Crossing Rates with Variational Relativistic Methods Toward the Evaluation of Intersystem Crossing Rates with Variational Relativistic Methods. *J. Chem. Phys.* **2019**, *151* (August). https://doi.org/10.1063/1.5113815.

(62) Marian, C. M. Understanding and Controlling Intersystem Crossing in Molecules. *Annu. Rev. Phys. Chem.* **2021**, *72*, 617–640.

(63) Marian, C. M. Spin-Orbit Coupling and Intersystem Crossing in Molecules. *Wiley Interdiscip. Rev. Comput. Mol. Sci.* **2012**, *2* (2), 187–203. https://doi.org/10.1002/wcms.83.

(64) Xu, S.; Yang, Q.; Wan, Y.; Chen, R.; Wang, S.; Si, Y.; Yang, B.; Liu, D.; Zheng, C.; Huang, W. Predicting Intersystem Crossing Efficiencies of Organic Molecules for Efficient Thermally Activated Delayed Fluorescence. *J. Mater. Chem. C* **2019**, *7* (31), 9523–9530. https://doi.org/10.1039/c9tc03152a.

(65) Tao, Y.; Yuan, K.; Chen, T.; Xu, P.; Li, H.; Chen, R.; Zheng, C.; Zhang, L.; Huang, W. Thermally Activated Delayed Fluorescence Materials towards the Breakthrough of Organoelectronics. *Adv. Mater.* **2014**, *26* (47), 7931–7958. https://doi.org/10.1002/adma.201402532.

(66) Uoyama, H.; Goushi, K.; Shizu, K.; Nomura, H.; Adachi, C. Highly Efficient Organic Light-Emitting Diodes from Delayed Fluorescence. *Nature* **2012**, *492* (7428), 234–238. https://doi.org/10.1038/nature11687.

(67) Vázquez, R. J.; Kim, H.; Zimmerman, P. M.; Goodson, T. Using Ultra-Fast Spectroscopy

to Probe the Excited State Dynamics of a Reported Highly Efficient Thermally Activated Delayed Fluorescence Chromophore. *J. Mater. Chem. C* **2019**, *7* (14), 4210–4221. https://doi.org/10.1039/c8tc05957h.

(68) Vázquez, R. J.; Yun, J. H.; Muthike, A. K.; Howell, M.; Kim, H.; Madu, I. K.; Kim, T.; Zimmerman, P.; Lee, J. Y.; Iii, T. G. New Direct Approach for Determining the Reverse Intersystem Crossing Rate in Organic Thermally Activated Delayed Fluorescent (TADF) Emitters. *J. Am. Chem. Soc.* **2020**, *142* (18), 8074–8079. https://doi.org/10.1021/jacs.0c01225.

(69) Wex, B.; Kaafarani, B. R. Perspective on Carbazole-Based Organic Compounds as Emitters and Hosts in TADF Applications. *J. Mater. Chem. C* **2017**, *5* (34), 8622–8653. https://doi.org/10.1039/c7tc02156a.

(70) Samanta, P. K.; Kim, D.; Coropceanu, V.; Brédas, J. L. Up-Conversion Intersystem Crossing Rates in Organic Emitters for Thermally Activated Delayed Fluorescence: Impact of the Nature of Singlet vs Triplet Excited States. *J. Am. Chem. Soc.* **2017**, *139* (11), 4042–4051. https://doi.org/10.1021/jacs.6b12124.

(71) Penfold, T. J.; Gindensperger, E.; Daniel, C.; Marian, C. M. Spin-Vibronic Mechanism for Intersystem Crossing. *Chemical Reviews*. 2018, pp 6975–7025.

(72) Marian, C. M. Spin–Orbit Coupling and Intersystem Crossing in Molecules. *Advanced Review*. 2011, pp 187–203.

(73) Etherington, M. K.; Gibson, J.; Higginbotham, H. F.; Penfold, T. J.; Monkman, A. P. Revealing the Spin-Vibronic Coupling Mechanism of Thermally Activated Delayed Fluorescence. *Nat. Commun.* **2016**, *7*, 1–7. https://doi.org/10.1038/ncomms13680.

(74) Gibson, J.; Monkman, A. P.; Penfold, T. J. The Importance of Vibronic Coupling for Efficient Reverse Intersystem Crossing in Thermally Activated Delayed Fluorescence Molecules. *ChemPhysChem*. 2016, pp 2956–2961.

(75) Lim, B. T.; Okajima, S.; Chandra, A. K.; Lim, E. C. Radiationless Transitions in Electron Donor-Acceptor Complexes: Selection Rules for S1 → T Intersystem Crossing and Efficiency of S1 → S0 Internal Conversion. *Chem. Phys. Lett.* **1981**, *79* (1), 22–27. https://doi.org/10.1016/0009-2614(81)85280-3.

(76) Ogiwara, T.; Wakikawa, Y.; Ikoma, T. Mechanism of Intersystem Crossing of Thermally Activated Delayed Fluorescence Molecules. *J. Phys. Chem. A* **2015**, *119* (14), 3415–3418. https://doi.org/10.1021/acs.jpca.5b02253.

(77) Gibson, J.; Penfold, J. Nonadiabatic Coupling Reduces the Activation Energy in TADF.

Phys. Chem. Chem. Phys. 2017, pp 8428–8434.

(78) Liu, X.; Chen, Z.; Zheng, C.; Liu, C.; Lee, C.; Li, F. Prediction and Design of Effi Cient Exciplex Emitters for High-Effi Ciency , Thermally Activated Delayed-Fluorescence Organic Light-Emitting Diodes. *Adv. Mater.* **2015**, *27*, 2378–2383. https://doi.org/10.1002/adma.201405062.

(79) Aizawa, N.; Harabuchi, Y.; Maeda, S.; Pu, Y. J. Kinetic Prediction of Reverse Intersystem Crossing in Organic Donor–Acceptor Molecules. *Nat. Commun.* **2020**, *11* (1), 1–6. https://doi.org/10.1038/s41467-020-17777-2.

(80) Phys, J. C.; Levine, B. G. Simulated Evolution of Fluorophores for Light Emitting Diodes. *J. Chem. Phys.* **2015**, *142* (March). https://doi.org/10.1063/1.4914294.

(81) Kobayashi, T.; Niwa, A.; Takaki, K.; Haseyama, S.; Nagase, T.; Goushi, K.; Adachi, C.; Naito, H. Contributions of a Higher Triplet Excited State to the Emission Properties of a Thermally Activated Delayed-Fluorescence Emitter. *Phys. Rev. Appl.* **2017**, *7* (3), 1–10. https://doi.org/10.1103/PhysRevApplied.7.034002.

(82) Wang, K.; Liu, W.; Zheng, C. J.; Shi, Y. Z.; Liang, K.; Zhang, M.; Ou, X. M.; Zhang, X. H. A Comparative Study of Carbazole-Based Thermally Activated Delayed Fluorescence Emitters with Different Steric Hindrance. *J. Mater. Chem. C* **2017**, *5* (19), 4797–4803. https://doi.org/10.1039/c7tc00681k.

(83) Lee, D. R.; Hwang, S.; Jeon, S. K.; Lee, C. W.; Lee, J. Y. Benzofurocarbazole and Benzothienocarbazole as Donors for Improved Quantum Efficiency in Blue Thermally Activated Delayed Fluorescent Devices. *Chem. Commun.* **2015**, No. 440, 8105–8107. https://doi.org/10.1039/c5cc01940k.

(84) Cho, Y. J.; Jeon, S. K.; Chin, B. D.; Yu, E.; Lee, J. Y. The Design of Dual Emitting Cores for Green Thermally Activated Delayed Fluorescent Materials. *Angew. Chemie - Int. Ed.* **2015**, *54* (17), 5201–5204. https://doi.org/10.1002/anie.201412107.

(85) Gao, Y.; Su, T.; Zhao, L.; Geng, Y.; Wu, Y.; Zhang, M. How Does A Little Difference in Structure Determine Whether Molecules Have Thermally Activated Delayed Fluorescence Characteristic or Not ? **2017**, 1–22.

(86) Meng, G.; Liu, L.; He, Z.; Hall, D.; Wang, X.; Peng, T.; Yin, X.; Chen, P.; Beljonne, D.; Olivier, Y.; Zysman-Colman, E.; Wang, N.; Wang, S. Multi-Resonant Thermally Activated Delayed Fluorescence Emitters Based on Tetracoordinate Boron-Containing PAHs: Colour Tuning Based on the Nature of Chelates. *Chem. Sci.* **2022**, No. 6, 1665–1674. https://doi.org/10.1039/d1sc05692a.

(87) Wu, Y.; Zhu, Y.; Zhang, Z.; Zhao, C.; He, J.; Yan, C.; Meng, H. Narrowband Deep-Blue Multi-Resonance Induced Thermally. *Molecules* **2022**, No. 27, 1–11.

(88) Hua, T.; Miao, J.; Xia, H.; Huang, Z.; Cao, X.; Li, N.; Yang, C. Sulfone-Incorporated Multi-Resonance TADF Emitter for High-Performance Narrowband Blue OLEDs with EQE of 32%. *Adv. Funct. Mater.* **2022**, No. 32, 1–9. https://doi.org/10.1002/adfm.202201032.

(89) Yang, Y.; Li, N.; Miao, J.; Cao, X.; Ying, A.; Pan, K.; Lv, X.; Ni, F.; Huang, Z.; Gong, S.; Yang, C. Chiral Multi-Resonance TADF Emitters Exhibiting Narrowband Circularly Polarized Electroluminescence with an EQE of 37.2 %. *Angew. Chemie - Int. Ed.* **2022**, *61*, 1–7. https://doi.org/10.1002/anie.202202227.

(90) Gao, Y.; Wang, Y.; Guo, Z.; Wan, Y.; Li, C.; Yang, B.; Yang, W.; Ma, X. Ultrafast Photophysics of Multiple-Resonance Ultrapure Blue Emitters. *J. Phys. Chem. B* **2022**, No. 14, 2729–2739. https://doi.org/10.1021/acs.jpcb.2c00144.

(91) Shizu, K.; Kaji, H. Comprehensive Understanding of Multiple Resonance Thermally Activated Delayed Fluorescence through Quantum Chemistry Calculations. *Commun. Chem.* **2022**, *5*, 2–7. https://doi.org/10.1038/s42004-022-00668-6.

(92) Sun, D.; Suresh, S. M.; Hall, D.; Zhang, M.; Si, C.; Cordes, D. B.; Slawin, A. M. Z.; Olivier, Y.; Zhang, X.; Zysman-Colman, E. The Design of an Extended Multiple Resonance TADF Emitter Based on a Polycyclic Amine/Carbonyl System. *Mater. Chem. Front.* **2020**, No. 7, 2018–2022. https://doi.org/10.1039/d0qm00190b.

(93) Hirai, H.; Nakajima, K.; Nakatsuka, S.; Shiren, K.; Ni, J.; Nomura, S.; Ikuta, T.; Hatakeyama, T. One-Step Borylation of 1,3-Diaryloxybenzenes Towards Efficient Materials for Organic Light-Emitting Diodes. *Angew. Chemie - Int. Ed.* **2015**, No. 46, 13581–13585. https://doi.org/10.1002/anie.201506335.

(94) Hua, T.; Zhan, L.; Li, N.; Huang, Z.; Cao, X.; Xiao, Z.; Gong, S.; Zhou, C.; Zhong, C.; Yang, C. Heavy-Atom Effect Promotes Multi-Resonance Thermally Activated Delayed Fluorescence. *Chem. Eng. J.* **2021**, *426*, 1–8. https://doi.org/10.1016/j.cej.2021.131169.

(95) Zou, S. N.; Peng, C. C.; Yang, S. Y.; Qu, Y. K.; Yu, Y. J.; Chen, X.; Jiang, Z. Q.; Liao, L. S. Fully Bridged Triphenylamine Derivatives as Color-Tunable Thermally Activated Delayed Fluorescence Emitters. *Org. Lett.* **2021**, *23*, 958–962. https://doi.org/10.1021/acs.orglett.0c04159.

(96) Haseyama, S.; Niwa, A.; Kobayashi, T.; Nagase, T.; Goushi, K.; Adachi, C.; Naito, H. Control of the Singlet–Triplet Energy Gap in a Thermally Activated Delayed Fluorescence Emitter by Using a Polar Host Matrix. *Nanoscale Res. Lett.* **2017**, *12* (1), 1–5. https://doi.org/10.1186/s11671-017-2012-1.

(97) Cotts, B. L.; Mccarthy, D. G.; Noriega, R.; Penwell, S. B.; Delor, M.; Devore, D. D.; Mukhopadhyay, S.; Vries, T. S. De; Ginsberg, N. S. Tuning Thermally Activated Delayed Fluorescence Emitter Photophysics through Solvation in the Solid State. *ACS Energy Lett.* **2017**, *2*, 1526–1533. https://doi.org/10.1021/acsenergylett.7b00268.

(98) Zhang, W.; Kong, J.; Hu, D.; Tao, M.; Niu, X.; Vdović, S.; Aumiler, D.; Ma, Y.; Xia, A. Solvation-Dependent Excited-State Dynamics of Donor-Acceptor Molecules with Hybridized Local and Charge Transfer Character. *J. Phys. Chem. C* **2020**, *124* (10), 5574–5582. https://doi.org/10.1021/acs.jpcc.0c00003.

(99) Zhang, J.; Ding, D.; Wei, Y.; Xu, H. Extremely Condensing Triplet States of DPEPO-Type Hosts through Constitutional Isomerization for High-Efficiency Deep-Blue Thermally Activated Delayed Fluorescence Diodes. *Chem. Sci.* **2016**, *7* (4), 2870–2882. https://doi.org/10.1039/c5sc04848f.

(100) Xiao, Y.-F.; Chen, J.-X.; Li, S.; Tao, W.-W.; Tian, S.; Wang, K.; Cui, X.; Huang, Z.; Zhang, X.-H.; Lee, C.-S. Manipulating Exciton Dynamics of Thermally Activated Delayed Fluorescence Materials for Tuning Two-Photon Nanotheranostics. *Chem. Sci.* **2020**, *11* (D), 888–895. https://doi.org/10.1039/C9SC05817F.

(101) Delor, M.; McCarthy, D. G.; Cotts, B. L.; Roberts, T. D.; Noriega, R.; Devore, D. D.; Mukhopadhyay, S.; De Vries, T. S.; Ginsberg, N. S. Resolving and Controlling Photoinduced Ultrafast Solvation in the Solid State. *J. Phys. Chem. Lett.* **2017**, *8* (17), 4183–4190. https://doi.org/10.1021/acs.jpclett.7b01689.

(102) Northey, T.; Stacey, J.; Penfold, T. J. The Role of Solid State Solvation on the Charge Transfer State of a Thermally Activated Delayed Fluorescence Emitter. *J. Mater. Chem. C* **2017**, *5* (42), 11001–11009. https://doi.org/10.1039/c7tc04099g.

(103) Davis, K. M. C. Solvent Effects on Charge-Transfer Fluorescence Bands. *Nature* **1969**, *223* (5207), 728. https://doi.org/10.1038/223728a0.

(104) Wan, J.; Ferreira, A.; Xia, W.; Chow, C. H.; Takechi, K.; Kamat, P. V.; Jones, G.; Vullev, V. I. Solvent Dependence of the Charge-Transfer Properties of a Quaterthiophene-Anthraquinone Dyad. *J. Photochem. Photobiol. A Chem.* **2008**, *197*, 364–374. https://doi.org/10.1016/j.jphotochem.2008.01.016.

(105) Santos, P. L.; Ward, J. S.; Bryce, R.; Monkman, A. P. Using Guest Host Interactions to Optimise the Efficiency of TADF-OLEDs. *J. Phys. Chem. Lett.* **2016**, *7* (17), 3341–3346.

(106) Ishmatsu, R.; Matsunami, S.; Shizu, K.; Adachi, C.; Nakano, K.; Imato, T. Solvent Eff Ect on Thermally Activated Delayed Fluorescence by 1,2,3,5-Tetrakis(Carbzol-9-Yl)-4,6-Dicyanobenzene. *J. Phys. Chem. A* **2013**, *117*, 5607–5612.

(107) Haseyama, S.; Niwa, A.; Kobayashi, T.; Nagase, T.; Goushi, K.; Adachi, C. Control of the Singlet – Triplet Energy Gap in a Thermally Activated Delayed Fluorescence Emitter by Using a Polar Host Matrix. **2017**, 1–5. https://doi.org/10.1186/s11671-017-2012-1.

(108) Serevičius, T.; Skaisgiris, R.; Dodonova, J.; Fiodorova, I.; Genevičius, K.; Tumkevičius, S.; Kazlauskas, K.; Juršėnas, S. Temporal Dynamics of Solid-State Thermally Activated Delayed Fluorescence: Disorder or Ultraslow Solvation? *J. Phys. Chem. Lett.* **2022**, *13* (7), 1839–1844. https://doi.org/10.1021/acs.jpclett.1c03810.

(109) Noriega, R.; Barnard, E. S.; Ursprung, B.; Cotts, B. L.; Penwell, S. B.; Schuck, P. J.; Ginsberg, N. S. Uncovering Single-Molecule Photophysical Heterogeneity of Bright, Thermally Activated Delayed Fluorescence Emitters Dispersed in Glassy Hosts. *J. Am. Chem. Soc.* **2016**, *138*, 13551–13560. https://doi.org/10.1021/jacs.6b05488.

(110) Wu, X.; Su, B. K.; Chen, D. G.; Liu, D.; Wu, C. C.; Huang, Z. X.; Lin, T. C.; Wu, C. H.; Zhu, M.; Li, E. Y.; Hung, W. Y.; Zhu, W.; Chou, P. T. The Role of Host–Guest Interactions in Organic Emitters Employing MR-TADF. *Nat. Photonics* **2021**, *15* (10), 780–786. https://doi.org/10.1038/s41566-021-00870-3.

(111) Bennison, M. J.; Collins, A. R.; Zhang, B.; Evans, R. C. Organic Polymer Hosts for Triplet-Triplet Annihilation Upconversion Systems. *Macromolecules* **2021**, No. 12, 5287–5303. https://doi.org/10.1021/acs.macromol.1c00133.

(112) Healy, C.; Hermanspahn, L.; Kruger, P. E. Photon Upconversion in Self-Assembled Materials. *Coord. Chem. Rev.* **2021**, 213756. https://doi.org/10.1016/j.ccr.2020.213756.

(113) Goudarzi, H.; Keivanidis, P. E. All-Solution-Based Aggregation Control in Solid-State Photon Upconverting Organic Model Composites. *ACS Appl. Mater. Interfaces* **2017**, No. 1, 845–857. https://doi.org/10.1021/acsami.6b12704.

(114) Ye, C.; Zhou, L.; Wang, X.; Liang, Z. Photon Upconversion: From Two-Photon Absorption (TPA) to Triplet-Triplet Annihilation (TTA). *Phys. Chem. Chem. Phys.* **2016**, No. 16, 10818–10835. https://doi.org/10.1039/c5cp07296d.

(115) Huang, L.; Zhao, Y.; Zhang, H.; Huang, K.; Yang, J.; Han, G. Expanding Anti-Stokes Shifting in Triplet–Triplet Annihilation Upconversion for In Vivo Anticancer Prodrug Activation. *Angew. Chemie - Int. Ed.* **2017**, No. 46, 14400–14404. https://doi.org/10.1002/anie.201704430.

(116) Wang, Z.; Zhao, J.; Di Donato, M.; Mazzone, G. Increasing the Anti-Stokes Shift in TTA Upconversion with Photosensitizers Showing Red-Shifted Spin-Allowed Charge Transfer Absorption but a Non-Compromised Triplet State Energy Level. *Chem. Commun.* **2019**, No. 10, 1510–1513. https://doi.org/10.1039/c8cc08159j.

(117) Fan, C.; Wei, L.; Niu, T.; Rao, M.; Cheng, G.; Chruma, J. J.; Wu, W.; Yang, C. Efficient Triplet-Triplet Annihilation Upconversion with an Anti-Stokes Shift of 1.08 EV Achieved by Chemically Tuning Sensitizers. *J. Am. Chem. Soc.* **2019**, No. 38, 15070–15077. https://doi.org/10.1021/jacs.9b05824.

(118) Wei, Y.; Li, Y.; Li, Z.; Xu, X.; Cao, X.; Zhou, X.; Yang, C. Efficient Triplet–Triplet Annihilation Upconversion in Solution and Hydrogel Enabled by an S-T Absorption Os(II) Complex Dyad with an Elongated Triplet Lifetime. *Inorg. Chem.* **2021**, No. 24, 19001–19008. https://doi.org/10.1021/acs.inorgchem.1c02846.

(119) Gray, V.; Moth-Poulsen, K.; Albinsson, B.; Abrahamsson, M. Towards Efficient Solid-State Triplet–Triplet Annihilation Based Photon Upconversion: Supramolecular, Macromolecular and Self-Assembled Systems. *Coord. Chem. Rev.* **2018**, No. 362, 54–71. https://doi.org/10.1016/j.ccr.2018.02.011.

(120) Manna, M. K.; Shokri, S.; Wiederrecht, G. P.; Gosztola, D. J.; Ayitou, A. J. L. New Perspectives for Triplet-Triplet Annihilation Based Photon Upconversion Using All-Organic Energy Donor & Acceptor Chromophores. *Chem. Commun.* **2018**, No. 46, 5809–5818. https://doi.org/10.1039/c8cc01553h.

(121) Ieuji, R.; Goushi, K.; Adachi, C. Triplet–Triplet Upconversion Enhanced by Spin–Orbit Coupling in Organic Light-Emitting Diodes. *Nat. Commun.* **2019**, No. 1, 1–10. https://doi.org/10.1038/s41467-019-13044-1.

(122) You, A.; Be, M. A. Y.; In, I. Triplet — Triplet Annihilation and Delayed Fluorescence in Molecular Aggregates. **2011**, No. 38, 1326–1335.

(123) Lai, H.; Zhao, T.; Deng, Y.; Fan, C.; Wu, W.; Yang, C. Assembly-Enhanced Triplet-Triplet Annihilation Upconversion in the Aggregation Formed by Schiff-Base Pt(II) Complex Grafting-Permethyl-β-CD and 9, 10-Diphenylanthracence Dimer. *Chinese Chem. Lett.* **2019**, *30* (11), 1979–1983. https://doi.org/10.1016/j.cclet.2019.09.009.

(124) Ligthart, A.; de Vries, X.; Zhang, L.; Pols, M. C. W. M.; Bobbert, P. A.; van Eersel, H.; Coehoorn, R. Effect of Triplet Confinement on Triplet–Triplet Annihilation in Organic Phosphorescent Host–Guest Systems. *Adv. Funct. Mater.* **2018**, No. 52, 1–10. https://doi.org/10.1002/adfm.201804618.

(125) Zeng, L.; Huang, L.; Han, J.; Han, G. Enhancing Triplet-Triplet Annihilation Upconversion: From Molecular Design to Present Applications. *Acc. Chem. Res.* **2022**, No. 18, 2604–2615. https://doi.org/10.1021/acs.accounts.2c00307.

(126) Kashino, T.; Hosoyamada, M.; Haruki, R.; Harada, N.; Yanai, N.; Kimizuka, N. Bulk Transparent Photon Upconverting Films by Dispersing High-Concentration Ionic Emitters

in Epoxy Resins. *ACS Appl. Mater. Interfaces* **2021**, No. 11, 13676–13683. https://doi.org/10.1021/acsami.0c23121.

(127) Zimmermann, J.; Mulet, R.; Scholes, G. D.; Wellens, T.; Buchleitner, A. Improving Triplet-Triplet-Annihilation Based Upconversion Systems by Tuning Their Topological Structure. *J. Chem. Phys.* **2014**, No. 141. https://doi.org/10.1063/1.4901336.

(128) Chen, W.; Song, F. Thermally Activated Delayed Fluorescence Molecules and Their New Applications aside from OLEDs. *Chinese Chem. Lett.* **2019**, No. 10, 1717–1730. https://doi.org/10.1016/j.cclet.2019.08.032.

(129) Durandin, N. A.; Isokuortti, J.; Efimov, A.; Vuorimaa-Laukkanen, E.; Tkachenko, N. V.; Laaksonen, T. Critical Sensitizer Quality Attributes for Efficient Triplet-Triplet Annihilation Upconversion with Low Power Density Thresholds. *J. Phys. Chem. C* **2019**, No. 37, 22865–22872. https://doi.org/10.1021/acs.jpcc.9b08026.

Chapter 2: Experimental Methods and Techniques

2.1 Overview

An in-depth investigation of an emitter's excited state dynamics requires the use of the proper nonlinear optical and time-resolved spectroscopic techniques. The techniques described here are used to probe the excited state and emission dynamics of compounds designed to the thermally activated delayed fluorescence (TADF)-active when they are dissolved in solution or embedded in a solid-state host. Thus, an understanding of the techniques and methods used will aid in the appreciation of the observed photophysical characteristics of the investigated systems.

2.2 Stead-State Absorption and Emission Spectroscopy

The two steady-state spectroscopic techniques are critical to investigate the basic interactions between light and matter. The electromagnetic spectrum is made up of different distinct energy bands, as displayed in **Figure 2.2.1**.[1] The bands of interest for this investigations described in this work are the ultraviolet and visible regions. What occurs in a material depends on the energy, or wavelength, of the photon that interacts with said material.

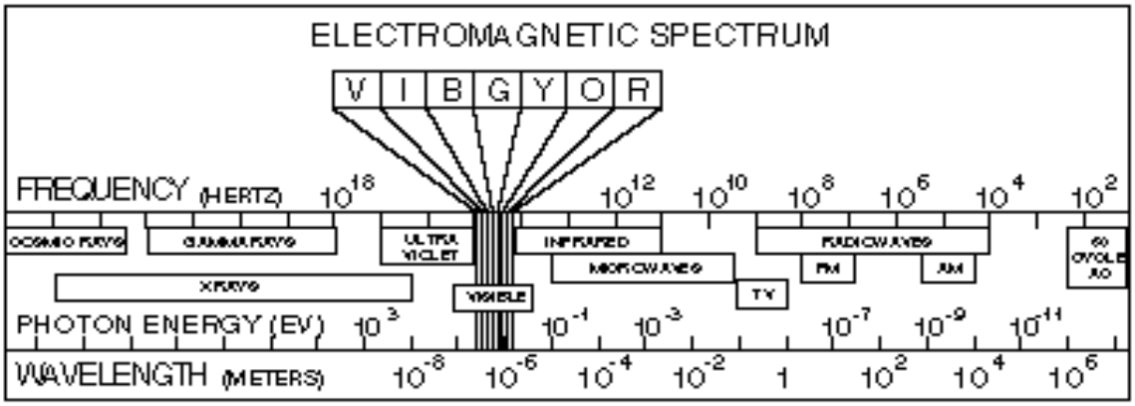


Figure 2.2.1. Electromagnetic spectrum of radiation in nanometers (nm).

It's desirable for the chromophore to be promoted from the ground state to the excited state for the purposes of TADF. For this to occur, the incident photon must be greater than or equal to the energy difference between the chromophore's electronic ground state and electronic excited state. Once a photon of sufficient energy interacts with the chromophore, an electron is promoted from the ground state to the excited state. This leaves behind a positively charged hole. The negatively charged electron is bound to the positively charged hole due to Coulombic forces and is known as an electron-hole pair or an exciton. The excited electron is located in the lowest unoccupied molecular orbital (LUMO) while the hole is located in the highest occupied molecular orbital (HOMO). The process of the chromophore absorbing light is known as absorption. The excited electron can then either decay to the ground state through fluorescence, phosphorescence, or non-radiative decay. Both fluorescence and phosphorescence are emissive decay processes, meaning they are decay pathways that cause a photon to be produced. In the vast majority of cases, the emitted photon is of a lower energy than the absorbed photon. The process of the chromophore relaxing back to the ground state with the release of a photon is known as emission. A more in-depth description of the different decay pathways is provided in **Section 1.**1 of the introduction.

Most chromophores intended for use in organic light emitting diodes (OLEDs) absorb photons within the UV and visible range of the electromagnetic spectrum. The UV-visible spectrometer is an instrument that allows one to determine which photons a material can absorb within the range of 190 nm – 1100 nm. The strength of a material's absorption is best described by the Beer-Lambert Law. A compound's absorbance is related to its transmission, concentration, and pathlength. These values are then used to determine the molar extinction coefficient for the compound at a particular wavelength (**Equation 2.2.1**).

$$A = -logT = log\frac{I_0}{I} = \varepsilon * c * l \qquad \textbf{Equation 2.2.1}$$

Where A is the absorbance intensity in *arbitrary units*, T is the transmittance, I_0 is the intensity of the incident beam, I is the intensity of the beam after it transmits through the sample, ε is the molar extinction coefficient in units of $mol^{-1}*cm^{-1}$, c is the concentration given in units of *mol*, and l is the pathlength of the sample that the beam passes through in units *cm*. The molar extinction coefficient is of particular importance, as it indicates a compounds ability to absorb photons at a particular wavelength. **Equation 2.2.1** can also be used to determine the concentration of an unknown sample. In this work, the absorbance spectra are presented as absorbance intensity vs wavelength. The Agilent 8453 UV-Vis absorption spectrometer was used to obtain the absorbance spectra presented in this work. A schematic of this instrument is provided in **Figure 2.2.2** below.[2]

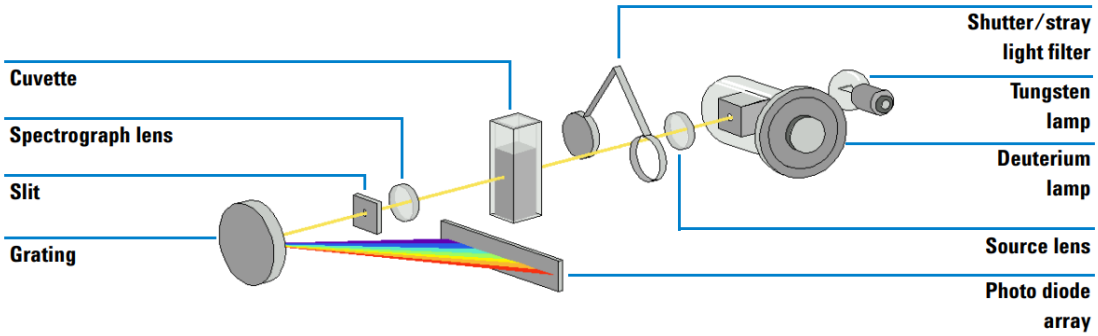


Figure 2.2.2. Schematic of the Agilent 8453 UV-Vis spectrophotometer.

The emission spectra of the investigated materials were obtained using a Horiba Scientific Fluorimeter, displayed in **Figure 2.2.3**.[3] In this instrument, the compound is excited using a xenon arc lamp capable of producing light from 190 nm to 2000 nm as the excitation source. The particular wavelength used to excite the sample is the maximum absorbance wavelength. The detector is a photomultiplier tube that is capable of detecting wavelengths within the range of 190 nm – 900 nm.

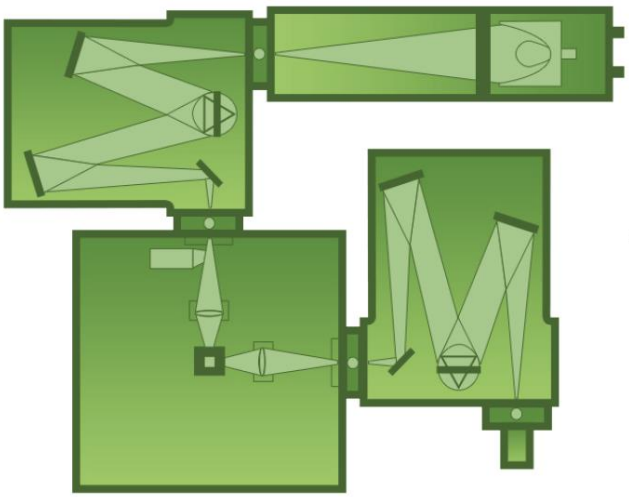


Figure 2.2.3. Schematic of the Horiba Scientific Fluorimeter.

Similar to absorbance, the emission intensity is directly proportional to the emitter's concentration as shown by **Equation 2.2.2**.[4]

$$I_F(C, \lambda_{em}, \lambda_{em}) = KCd\Phi(\lambda_{ex})\varepsilon(\lambda_{ex})I_{ex}(\lambda_{ex})E_M(\lambda_{ex}) \qquad \textbf{Equation 2.2.2}$$

Where I_F is the fluorescence intensity, C is the sample concentration, λ_{ex} is the excitation wavelength, λ_{em} is the emission wavelength, Φ is the quantum yield, ε is again the molar extinction coefficient, I_{ex} is the intensity of the excitation light, E_M is the characteristic emission profile of the emitter.

The emissive quantum yield, Φ, is a critical parameter to determine the emissive efficiency of a chromophore. It describes the ratio of the number of photons that are absorbed by the chromophore to the number of photons that are emitted by the chromophore at a particular wavelength. Each of the radiative and non-radiative pathways contribute to the overall quantum yield, as shown by **Equation 2.2.3**.[5]

$$\Phi = \frac{K_R}{K_R + \sum K_{NR}} \qquad \textbf{Equation 2.2.3}$$

Where K_R is the rate of the radiative decay pathways and K_{NR} is the rate of the non-radiative decay pathways.

The comparative solution method is a common method of calculating the fluorescence quantum yields of emitters, through the use of **Equation 2.2.4**.[5]

$$\Phi_U = \Phi_K \left(\frac{A_K}{A_U}\right)\left(\frac{E_U}{E_K}\right)\left(\frac{I_K}{I_U}\right)\left(\frac{\eta_U}{\eta_K}\right)^2 \qquad \textbf{Equation 2.2.4}$$

Where A is the absorption, E is the integrated fluorescence intensity, I is the excitation light intensity, and η is the refractive index of the solvent of the solution. The subscripts U and K

indicate where the value is for the sample or the known standard, respectively. **Equation 2.2.4** can be simplified to **Equation 2.2.5**.[5]

$$\Phi_U = \Phi_K \left(\frac{m_U}{m_k}\right)\left(\frac{\eta_U}{\eta_K}\right)^2 \qquad \textbf{Equation 2.2.5}$$

Where m_U and m_K are the slopes obtained by plotting the integrated fluorescence intensity vs absorbance intensity at the excitation wavelength. When using the comparative method, the acquisition settings are also of particular importance for this instrument, as they directly impact the observed emission intensity. Changing these parameters would then alter the resulting quantum yields for the sample. Thus, the acquisition settings are consistent for both the fluorescence standard and sample during each quantum yield calculation.

2.3 Two-Photon Absorption Spectroscopy

Two-photon absorption (TPA) spectroscopy is a nonlinear absorption process where two photons of the same or different energies excite a compound from the ground state to an electronic excited state as depicted in **Figure 2.3.1**.

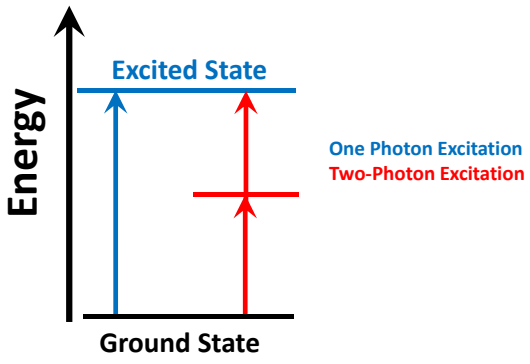


Figure 2.3.1. Process of two-photon absorption.

Nonlinear two-photon processes, such as two-photon emission (TPE) and two-photon absorption (TPA), were theorized in 1930 by Maria Goeppert-Mayer and experimentally observed around thirty years later.[6] A material's ability to undergo TPA is determined by its two-photon absorption cross-section (σ). A common method of determining σ is to obtain the two-photon excited fluorescence (TPEF), named such due to the two-photons inducing an electric field that has a nonlinear response to the polarization density of the absorbent compound. A schematic of the TPA laser setup utilized for the investigations in this work is displayed in **Figure 2.3.2**.

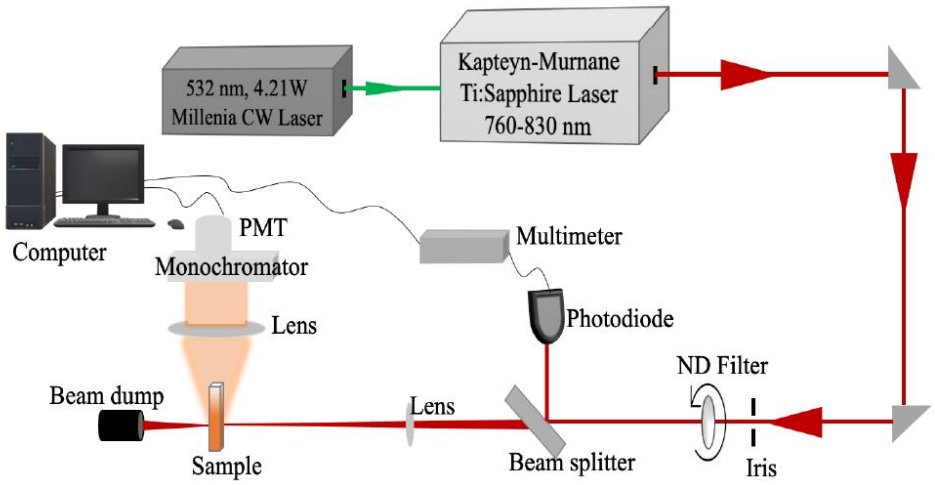


Figure 2.3.2. Schematic of the two-photon absorption laser system.

This setup utilizes a mode-locked Ti:Sapphire laser with a tunable wavelength in the range of 700 nm – 900 nm. The laser beam has a pulse of 110 fs and a repetition rate of 80 MHz. This beam is used to pump the OPAL optical parametric oscillator (OPO) lithium borate crystal. The interaction between the fundamental beam and lithium borate crystal generates a beam between 1.3 μm and 1.5 μm with an output power of ~200 mW. The beam is propagated through a series of mirrors to a neutral density filter that can be rotated to tune the power of the excitation beam. Before the beam can interact with the sample, an optical glass is used to send a small portion of

the excitation beam to a high-speed silicon photodiode. The photodiode is connected to a multimeter and is used to monitor the excitation beam power. The TPEF of the sample is collected at a right angle of the excitation beam, to avoid signal from the excitation beam, and detected by a photomultiplier tube.

The TPEF photons, F(t), is given by **Equation 2.3.1**

$$F(t) = \frac{1}{2}\Phi\sigma[c]\eta\frac{g_p}{\pi\upsilon\lambda\tau}f\langle P(t)\rangle^2 \qquad \textbf{Equation 2.3.1}$$

Where Φ is the fluorescence quantum yield of the sample, σ is the TPA cross-section of the sample, [c] is the sample concentration, η is the refractive index of the solvent, g_p is the shape factor of the excitation beam (0.66 for a Gaussian shape), ν is the frequency of the excitation beam, λ is the excitation wavelength, τ is the pulse duration, f is the collection efficiency, and P(t) is the input power intensity.

It's possible to express **Equation 2.3.1** in a linear regression form (y = mx + b) by converting it to a logarithmic form, displayed in **Equation 2.3.2**. The laser parameters can then be simplified into a constant, b. Thus, the quadratic response with a slope of two can be expected when a graph of fluorescence intensity as a function of the excitation beam's power is created for both the sample and the standard. When the logarithm of both the sample's and standard's input power is assumed to be zero, the equation can be simplified (**Equation 2.3.2 – Equation 2.3.5**) to give the TPA cross-section (σ).

$$Log\big(F(t)\big) = 2\log\langle P(t)\rangle + \log\left(\frac{1}{2}\Phi\sigma[c]\eta\frac{g_p}{\pi\upsilon\lambda\tau}f\right) \qquad \textbf{Equation 2.3.2}$$

$$Log\big(F(t)_{sample}\big) - b_{sample} = Log(F(t)_{standard}) - b_{standard} \qquad \textbf{Equation 2.3.3}$$

$$Log\left(F(t)_{sample}\right) - Log(F(t)_{standard}) = b_{sample} - b_{standard} \qquad \textbf{Equation 2.3.4}$$

$$\sigma = \frac{10^{(b_{sample} - b_{standard})} * \sigma_{standard} \Phi_{standard} [c]_{standard} \eta_{standard}}{\Phi_{sample} [c]_{sample} \eta_{sample}} \qquad \textbf{Equation 2.3.5}$$

2.4 Ultrafast Fluorescence Up-Conversion Spectroscopy

Ultrafast-fluorescence up-conversion (UFUC) is a spectroscopic technique that allows for the investigation of radiative processes within the timescale of hundreds of femtoseconds to hundreds of picoseconds. A schematic of the UFUC setup utilized for the investigations described in this work is displayed in **Figure 2.4.1**.

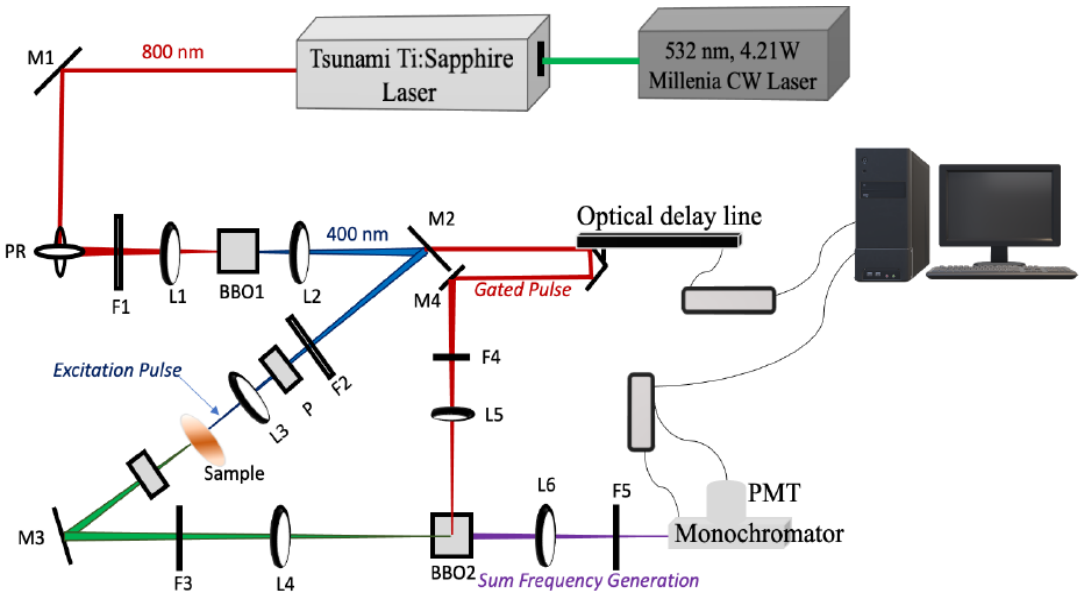


Figure 2.4.1. Schematic of the ultra-fast fluorescence up-conversion laser system.

The UFUC setup utilizes a Sectra-Physics Millenia laser with a neodymium-dope yttrium vanadate (Nd:YVO4) nonlinear crystal that produces a 4.21 W CW beam at a 532 nm wavelength once it's frequency doubled. The 532 nm beam, powered via a continuous laser diode, is the input for the Spectra-Physics Tsunami mode-locked laser which uses a Ti:Sapphire crystal to generate a

80 fs pulsed laser with a wavelength range of 780 – 820 nm, a pulse rate of 82 MHz, and a power between 680 – 720 mW. For the works included in this dissertation, the wavelength was set to 800 nm.

The 800 nm fundamental beam is propagated through an array of optics and focused on a β-barium borate (BBO) crystal to generate the second-harmonic of 400 nm. A dichroic mirror is then used to separate the generated 400 nm beam from residual 800 nm fundamental. This residual 800 nm fundamental is then sent to an optical delay line with a step size of 6.25 fs. The 400 nm beam is reflected to a circular cuvette with a pathlength of 1 mm. The cuvette sample holder rotates the sample to minimize the chance of photodegradation of the sample. The polarization of the beam is made to be parallel, the same plane as the sample, using a Berek compensator. The sample fluorescence is then collected using an achromat. The fluorescence is then directed to another BBO crystal to induce sum-frequency generation (SFG) between the fluorescence and fundamental to generate a wavelength range between 300 – 400 nm. The gate pulse of the fundamental has a step size of 6.25 fs to produce maximum fluorescence up-conversion.[7] This SFG beam is then focused onto a monochromator which is set to the desired wavelength of interest from the up-converted beam. A photomultiplier tube (Hamamatsu R152P) is used as the detector.

2.5 Time-Correlated Single Photon Counting Spectroscopy

Time-Correlated Single Photon Counting (TCSPC) is a spectroscopic technique utilized to characterize the emissive lifetime of compounds whose emission decay is longer than the range of the UFUC system described in section **2.4** above. The decay times able to be detected by the TCSPC system is within tens of nanoseconds to 2.5 microseconds. A schematic of the TCSPC setup used for the studies described in this dissertation is provided in **Figure 2.5.1**.

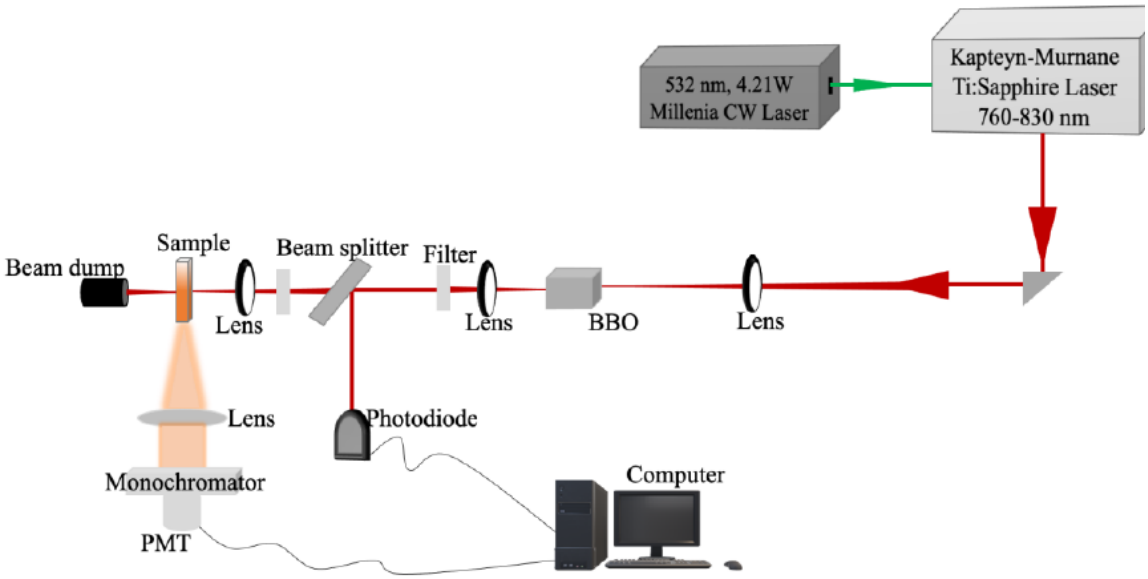


Figure 2.5.1. Schematic of the time-correlated single photon counting laser system.

The TCSPC system utilizes a 4W Spectra Physics Millenia CW Nd:YVO4 laser that generates a 532 nm fundamental beam that pumps a Kapteyn Murnane (KM) Laboratories Ti:Sapphire femtosecond laser. The KM laser has a tunable output range of 780 – 830 nm. For the works described in this dissertation, the KM output is set to 800 nm with a pulse duration of 30 fs and a repetition rate of 90 MHz. The 800 nm fundamental is frequency doubled through interaction with a β-barium borate (BBO) nonlinear crystal to a 400 nm pulsed beam. The residual 800 nm beam is not used in this setup, unlike the UFUC system. The 400 nm beam is then focused on the sample, either solid-state or solution, using a lens with a focal length of 11.5 cm. A quartz cuvette with a 1.0 cm pathlength is used for all solution measurements.

The sample emission is collected perpendicular to the excitation source to avoid electrical interference.[8] A monochromator is placed in front of the photomultiplier tube (PMT) to remove any external photons that could be converted into a signal. The PMT converts the emission signal into voltage and sends it to the computer through a TimeHarp 200 interface card.[9] The signal is

displayed as a histogram using the PicoQuant software. The histograms are created by detecting and resolving the arrival time of individual photons with respect to a the excitation source which acts as the triggering signal. The instrument response function is obtained through Rayleigh Scattering of a LUDOX solution to ensure that the histograms are the result of legitimate signal. The decay lifetimes are then determined by fitting log plots of the obtained spectra using a linear fit.

2.6 Nanosecond Transient Absorption Spectroscopy

Nanosecond transient absorption spectroscopy (nsTAS) is a pump-probe spectroscopic technique that is used to observe a system's emissive and non-emissive transient states to determine the excited state dynamics. A description of the method of operation is provided here, but the reader is encouraged to explore the details within the different manuals to gain a true appreciation of the numerous components of the nsTAS system.[10–13]

The nsTAS system's laser head consists of a Nd:YAG pump chamber assembly with two xenon flash lamps that excite Nd:YAG rods to produce a 1064 nm fundamental beam. A Q-switch comprised of a polarizer, quarter-wave plate, Pockels Cell, and high-reflector is used to obtain short pulses (10 ns) of high power (850 mJ) of the 1064 nm beam. A scheme depicting the orientation of these components is provided in **Figure 2.6.1**. The Q-switch delay circuit fires at a fixed delay which triggers the Marx bank, a circuit that produces high-voltage DC pulses. The high-voltage pulse is what triggers the Pockels Cell, an electro-optical crystal that alters the polarization of the 1064 nm fundamental. When there is no voltage applied to the Pockels Cell, the 1064 nm beam that enters the Q-switch cavity is horizontally polarized by the polarizer. The quarter-wave plate then converts it to a circular polarization. The circularly polarized light reflects off of the high-reflector and back towards the quarter-wave plate which converts the polarization

of the 1064 nm beam from circular to vertical. The polarizer only allows for the transmittance of horizontally polarized light, thus the vertically polarized 1064 nm beam is reflected out of the resonator. This is known as high cavity loss. When high voltage is applied to the Pockels cell, the effects of the quarter-wave plate are cancelled. This allows for horizontally polarized light to exit the Q-switch in short, high-power pulses.

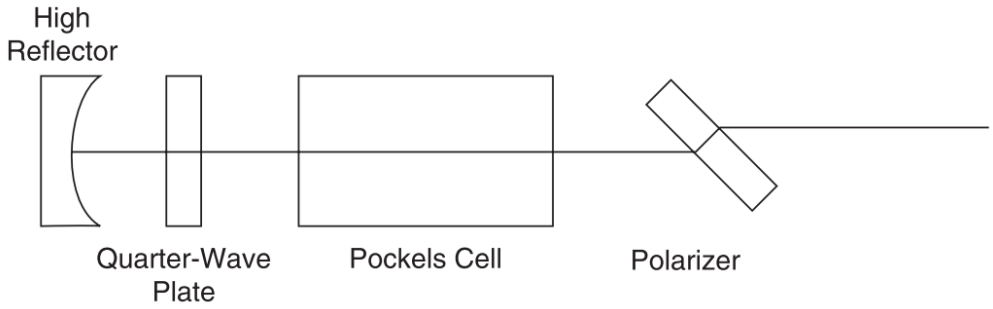


Figure 2.6.1. Schematic of the Q-switch assembly utilized in the nanosecond transient absorption (nsTAS) system's laser head.

The high-power 1064 nm pulses are used to pump the harmonic generator that houses potassium dideuterium phosphate (KD*P) crystals. Second harmonic generation (SHG) of the 1064 nm fundamental produces a 532 nm beam with an energy of 450 mJ. Sum-frequency mixing of the 532 nm and 1064 nm fundamental produces a 355 nm beam with an energy of 240 mJ. This 355 nm beam is utilized to pump the optical parametric oscillator (OPO) to produce the wavelength that best excite the sample. A schematic of the laser head and OPO are provided in **Figure 2.6.2**.

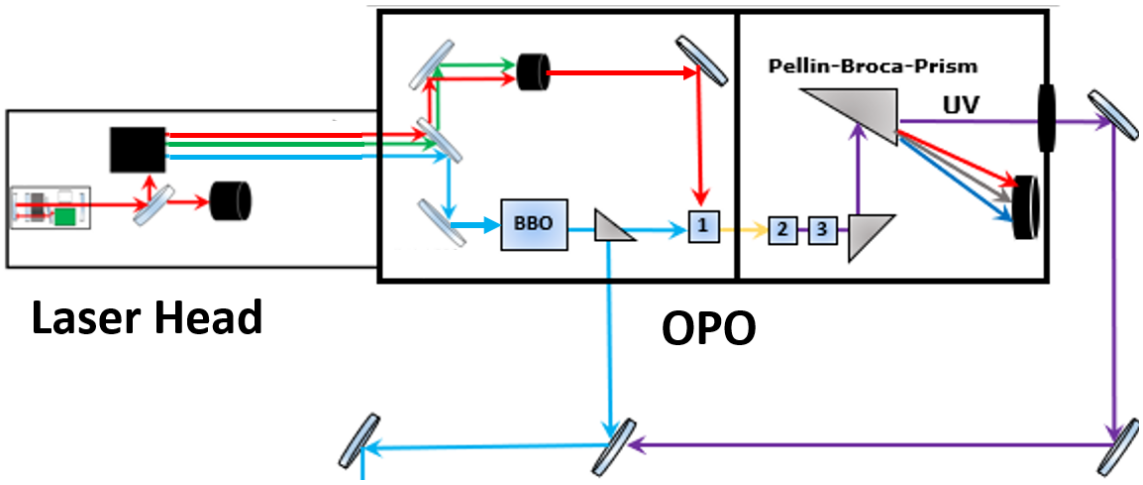


Figure 2.6.2. Schematic of the nanosecond transient absorption (nsTAS) laser system.

The OPO is comprised of a VersaScan and UVScan optical path. The VersaScan pathway allows for the generation of light within the visible range of the electromagnetic spectrum.[11] To produce visible light, the 1064 nm, 532 nm, and 355 nm beams are separated using dichroic mirrors. The 1064 nm and 532 nm beams are sent to a beam dump. The 355 nm beam is propagated through a nonlinear BBO crystal, generating two photons whose total energy equals that of the initial 355 nm beam. These two lower-energy photons are known as the signal and idler, where the signal is within the visible range (410 – 709 nm) and the idler the near-IR range (709 – 2630 nm). The angle at which the 355 nm beam interacts with the BBO crystal will determine the exact wavelengths of the resulting signal and idler. This light is then sent outside of the OPO using the OPO direct-out crystal, where it is then sent to the L980 Spectrometer. The UVScan pathway allows for the generation of light within the UV range of the electromagnetic spectrum (257 – 409 nm).[10] This is accomplished through sum-frequency mixing of the signal and residual 1064 nm fundamental beams, requiring that the OPO direct-out crystal be removed. Both modes of the OPO

are required for this process and must be calibrated. The calibration procedure for both the VersaScan and UVScan have been previously described.[14]

The nsTAS system has been utilized in previous studies to observe the properties of long-lived transient species. In this work, the potential of the nsTAS system is highlighted through the first-time use of the laser-induced emission sample chamber configuration (**Figure 2.6.3**).[15] Unlike the transient absorption measurement the probe beam shutter is permanently closed during the laser-induced emission experiment and only the laser pump beam is utilized to excite the sample. The sample emission is then focused onto the detector and collected with a fixed gain and gate width but with increasingly delayed gate opening. This never-before used configuration of the nsTAS system was utilized to inform the influence of the host material on emitter photophysics through the collection of time-resolved emission spectra and emissive lifetime characterization.

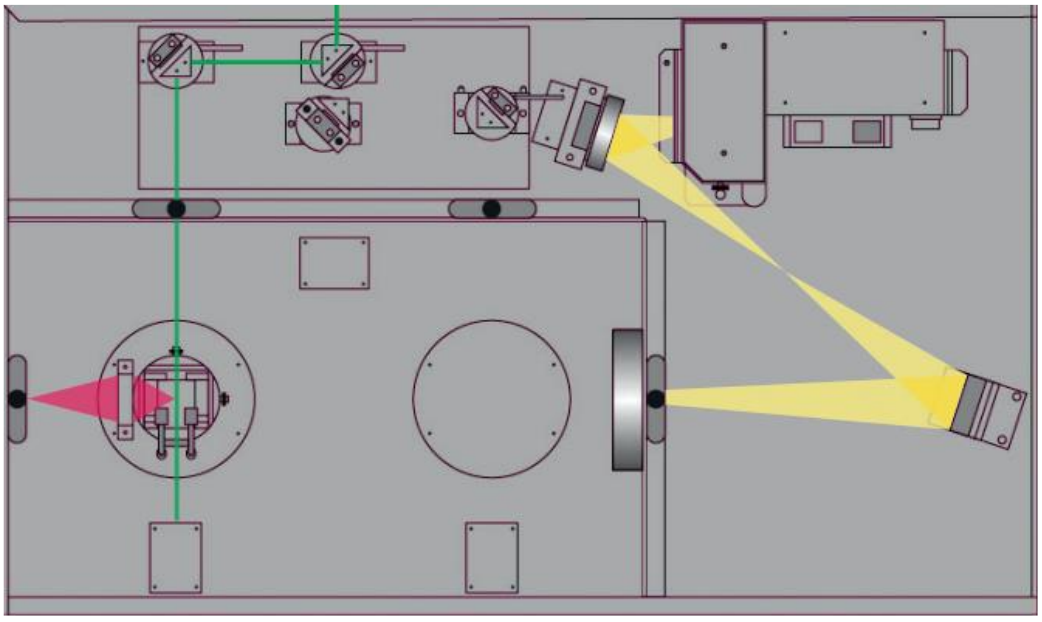


Figure 2.6.3. Laser-induced emission sample chamber configuration.

It is important that the emission intensity does not exceed 0.6 Volts during the measurement. To ensure this, it is advised that the user adjust the bandwidth and oscilloscope voltage to the appropriate sizes. A procedure of how to properly set these parameters is provided below.

1. Be sure that the pump laser controller is set to External/External and OSC is set to 9.

2. Launch the L900 software on the desktop computer. Select “Kinetic Emission” in the upper lefthand corner of the screen and select “Setup” from the drop-down menu.

3. Enter the emission maximum of the sample into the wavelength box underneath “Detector Monochromator” in the Controller tab. Set the bandwidth to 0.8 nm.

4. Click on the Oscilloscope tab and set the PMT channel to 1600 mV.

5. Once this is done, click “Apply” and then “Start”.

6. A trace should appear on the lefthand side of the screen at the selected wavelength. Press “Stop” to stop the measurement. Adjust the bandwidth as necessary to get the intensity at the emission maximum as close to 0.6 Volts as possible. Adjust the PMT channel to zoom in as much as possible on the trace.

7. Once the bandwidth and oscilloscope voltage of the emission maximum is properly set, enter the starting wavelength of the time-resolved emission spectrum measurement into the wavelength box. Do not change the bandwidth or the oscilloscope voltage. Click “Apply” and then “Start”. Allow the system to obtain one or more setup trace(s) at this wavelength. Click “Stop”, “Apply”, and then “Close”. This will ensure that the following time-resolved emission spectrum measurement properly begins at this wavelength.

The quality of the obtained time-resolved emission spectrum is heavily dependent on the selected step size and number of averages taken at each step. A procedure describing how to set these parameters is provided, along with examples of appropriate and poor parameters. Also provided is a brief analysis of the example time-resolved emission spectra and how they relate to the emissive process used by the sample. The following procedure assumes that the user has

already properly set the bandwidth so that the emission intensity does not exceed 0.6 Volts during the measurement.

1. Select “Kinetic Emission” in the upper lefthand corner of the screen and select “Emission Time Map” from the drop-down menu.

2. Click on the Measurement tab and click “Set wavelength ranges”. Set the desired wavelength range of the measurement along with the step size of the measurement in the pop-up box that appears. The recommended range is the excitation wavelength + 10 nm (example: if the excitation wavelength is 343 nm then the measurement should begin at 353 nm) to the end wavelength observed in the steady-state emission spectrum. Click “apply” and then “ok”.

3. Set the number of averages that should be taken at each wavelength in the “Shots” box. Click on the “Controller” tab and ensure that the wavelength in the detector monochromator box is the desired starting wavelength. Click “Apply” and then “Start”.

It is important to note that the signal-to-noise ratio improves with the number of averages taken. The amount of information that can be gleaned from the obtained spectrum also improves with smaller step sizes. However, a high number of averages in conjunction with a small step size will result in a particularly long measurement (2+ hours for one measurement). Conversely, a small number of averages with a large step size will result in a relatively fast measurement (20 minutes) but will also result in a poor-quality spectrum. It is up to the user to determine which combination of settings is appropriate for their measurement. However, the recommended settings for a sample where no previous measurements have been conducted is a step size of 13 nm and 8 averages per step. This typically results in a spectrum of respectable quality and the user can determine is a higher quality spectrum is necessary.

Additional considerations must be taken into account when conducting transient absorption measurements on solid-state film samples. Sample degradation of the solid-state film easily occurs due to the high power of the excitation beam (**Figure 2.6.4**). Thus, it is recommended that the user place an aperture in the excitation beam path within the sample chamber to appropriately adjust the beam intensity for longer measurements. This will aid in reducing the rate of sample degradation. It is also recommended that the film sample be placed at a 45° angle with respect to the excitation beam for best results.

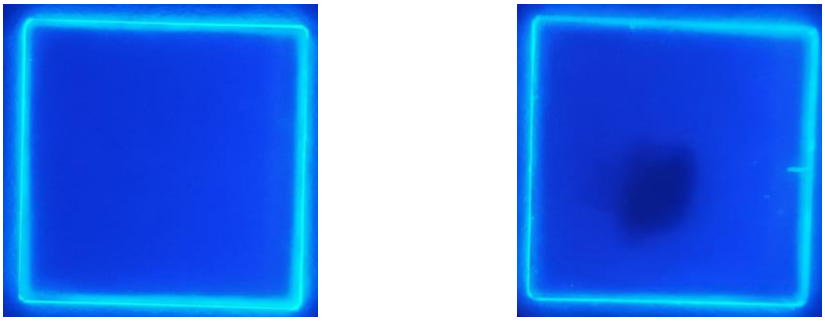


Figure 2.6.4. 5wt% BCC-TPTA/DPEPO film before measurement (left) and after measurement (right).

References

(1) Sankaran, S.; Ehsani, R. Introduction to the Electromagnetic Spectrum. *Imaging with Electromagn. Spectr. Appl. Food Agric.* **2014**, 17. https://doi.org/10.1007/978-3-642-54888-8_1.

(2) Agilent Technologies. *Agil. 8453 UV-Visible Spectrosc. Syst. Oper. Man.*

(3) Horiba Scientific Unique PTI QuantaMaster ™ Benefits Modular Research Fluorometers for Lifetime and Steady State Measurements. *Modul. Res. Fluorometers Lifetime Steady State Meas.*

(4) Kumar, K.; Tarai, M.; Mishra, A. K. Unconventional Steady-State Fluorescence Spectroscopy as an Analytical Technique for Analyses of Complex-Multifluorophoric Mixtures. *TrAC - Trends Anal. Chem.* **2017**, *97*, 216–243. https://doi.org/10.1016/j.trac.2017.09.004.

(5) Brandner, B. Implementation of a Comparative Method for Measuring Photoluminescence Quantum Yield of Novel Compounds in Solution. *Implement. a Comp. method Meas. photoluminescence quantum yield Nov. Compd. Solut. Oregon State Univ.* **2016**.

(6) Guarin, C. A.; Mendoza-Luna, L. G.; Haro-Poniatowski, E.; Hernández-Pozos, J. L. Two-

Photon Absorption Spectrum and Characterization of the Upper Electronic States of the Dye IR780. *Spectrochim. Acta - Part A Mol. Biomol. Spectrosc.* **2021**, *249*, 1–9. https://doi.org/10.1016/j.saa.2020.119291.

(7) Zhao, L.; Perez, J. L.; Farztdinov, V.; Ernsting, N. P. Femtosecond Fluorescence Spectroscopy by Upconversion with Tilted Gate Pulses. *Phys. Chem. Chem. Phys.* **2005**, *7*, 1716–1725.

(8) Wahl, M. Time-Correlated Single-Photon Counting Picoquant Technical Note. **2007**, 1–14.

(9) Timeharp 200 User Manual.

(10) GWU-Lasertechnik. *GWU uvScan User Man.* **2013**.

(11) GWU-Lasertechnik. *Borate, GWU VersaScan Beta-Barium Opt. Parametr. Oscil.* **2012**.

(12) Edinburg Instruments Ltd. *Nsta-Lp980-User-Manual* **2016**.

(13) Spectra Physics. *Quanta-Ray Lab-Series Pulsed NdYAG Lasers User Man.* **2003**, *Mountain V*.

(14) Muthike, A. *Investigating the Time-Resolved Spectroscopy of Singlet and Triplet Dynamics in Conjugated Rylene and Quinoline Derivatives for Efficient Optoelctronic Systems*; 2022; Vol. 33.

(15) LP980 Sample Holders LP980 Sample Holders L-F02 Diffuse Reflectance Option.

Chapter 3: Investigation of Thermally Activated Delayed Fluorescence in Donor-Acceptor Organic Emitters with Time-Resolved Absorption Spectroscopy

3.1 Original Publication Information and Author Contribution

The work presented in this chapter was accepted in *Chemistry of Materials* under the title:

"Investigation of Thermally Activated Delayed Fluorescence in Donor-Acceptor Organic Emitters with Time-Resolved Absorption Spectroscopy" Lloyd Fisher, Jr., Ricardo Javier Vazquez, Madeline Howell, Angelar K. Muthike, Meghan E. Orr, Hanjie, Jiang, Betsy Dodgen, Dong Ryun Lee, Jun Yeob Lee, Paul Zimmerman, and Theodore Goodson, III Chem. Mater., 2022, 34, 2161 – 2175.

As first author I worked as the lead investigator, conducted most of the measurements myself, interpreted the data, and wrote and edited the manuscript for publication. The manuscript was modified to fit the format of this dissertation. The references and supporting information accepted with the manuscript are also included in this chapter.

3.2 Abstract

In this contribution we utilize multiple time-resolved and nonlinear optical measurements, and quantum chemical simulations to investigate the excited state dynamics of organic chromophores with thermally activated delayed fluorescent (TADF) characteristics. We are most interested in probing the influence of a phenylene linker on the photophysical properties of emitters composed of carbazole based donors linked to either a phthalonitrile (PN) or diphenyltriazine (Trz) acceptor. The PN-acceptor compounds display a near double fluorescence quantum yield (Φ_F) enhancement

in oxygen free conditions. The fluorescent lifetime measurements indicate that the PN-acceptor compounds are the more efficient charge-transfer emitters and quickly go from a delocalized to a localized state. They also reveal that only the PN-acceptor compounds display a long-lived emissive lifetime component associated with TADF activity. Analysis of the nanosecond transient absorption (nsTAS) spectra and kinetics reveal long-lived excited state absorption (ESA) bands associated to triplet states for the PN-acceptor compounds. No ESA bands were observed for the Trz-acceptor compounds, despite observing a quantum yield enhancement for the Trz-acceptor compounds after oxygen purging. From the transient absorption measurements, it was determined that the PN-acceptor compounds have reverse intersystem crossing rates (k_{rISC}) that are able to compete with other triplet decay pathways. From quantum chemical calculations, it is proposed that inclusion of the phenylene linker prevents sufficient HOMO/LUMO separation and suppresses TADF activity and that directly linking multiple donors to the acceptor will activate TADF activity.

3.3 Introduction

Thermally activated delayed fluorescence (TADF) is an emissive mechanism proposed for use in organic light-emitting diodes to achieve internal quantum efficiencies (η_{IQE}) of ~ 100 %.[1–3] The high η_{IQE} is ascribed to the use of all charge carriers, through the conversion of non-emissive triplets into emissive singlets via a thermally-assisted reverse intersystem crossing (rISC) mechanism.[1,4,5] This mechanism is reportedly made possible by a small energy gap (< 0.1 eV) and sufficient spin-orbit coupling between the singlet–triplet manifolds.[2,6–8] As a result, purely organic TADF materials have attracted immense attention as potential replacements for rare metal-containing phosphorescent emitters in blue light-emitting diodes due to their advantageous properties such as: optical tuning via synthesis, device flexibility, and relatively lower costs.[3,9,10]

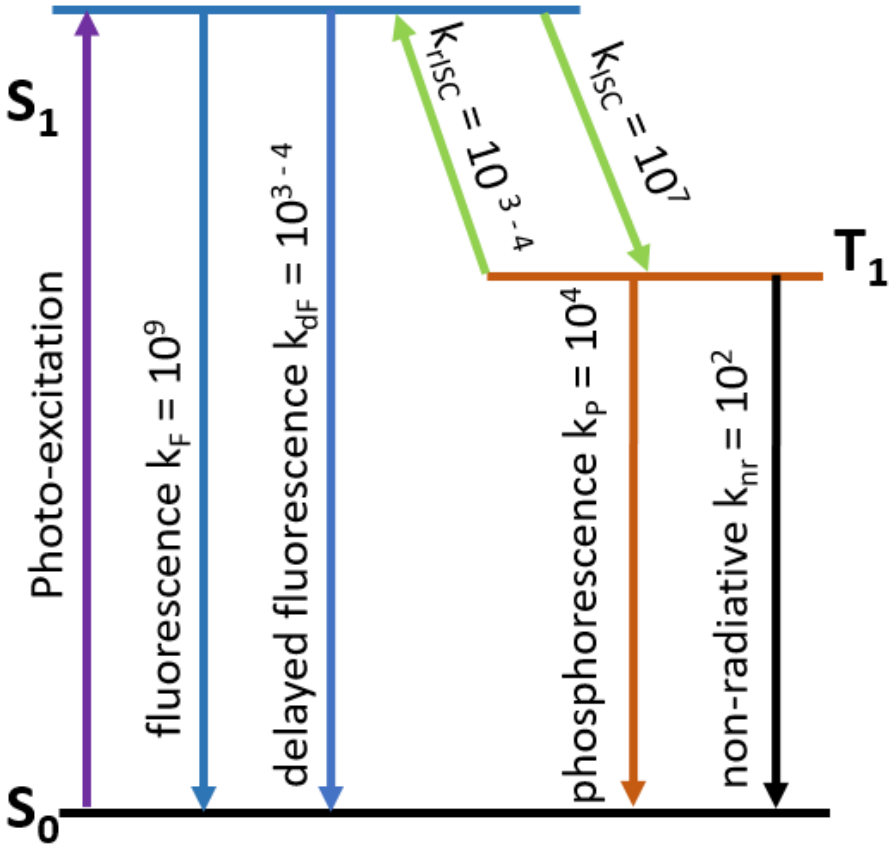


Figure 3.3.1. Decay processes of excited states and associated rate constants.

The different decay pathways of excited states, including the TADF process, are displayed in **Figure 3.3.1** along with their relative rates.[11–13] Upon photo-excitation, the singlet excited state (S_1) is populated. This state can undergo fluorescence, which will return it to the ground state (S_0), or undergo intersystem crossing (ISC), which will populate the triplet excited state (T_1). For T_1 to be populated, the rate of intersystem crossing (k_{ISC}) must be able to compete with the rate of fluorescence (k_F). Once populated, the T_1 state can undergo phosphorescence, non-radiative decay, or reverse intersystem crossing. The TADF mechanism depends on the rate of reverse intersystem crossing (k_{rISC}) out-competing the rates of phosphorescence (k_P) and non-radiative decay of T_1 (k_{nr}). Previous investigations into k_{rISC} have determined that efficient TADF depends on k_{rISC} >

10^3.[1,11,14] It is apparent that TADF is an unusual process that requires contributions from many different components, including a small singlet-triplet energy gap (ΔE_{ST}) and strong spin-orbit coupling (SOC).[7,11]

The design principle of achieving a small singlet-triplet energy gap (ΔE_{ST}) in fully organic chromophores consists of synthesizing a donor-acceptor complex with a partial break in the conjugation between the donor-acceptor junction.[1,7,15–18] This partial break allows for minimal overlap between the highest occupied molecular orbital (HOMO) and the lowest unoccupied molecular orbital (LUMO). By maximizing the dihedral angle of the junction, one can minimize ΔE_{ST} and enhance k_{rISC}.[18] Recent publications indicate that parameters other than HOMO/LUMO separation play an important role in the TADF process.[1,3,14] One such report highlights that maximizing spatial separation between the HOMO and LUMO does not necessarily result in effective energy transfer between the singlet and triplet manifolds. Instead, it suggests that enhancing the charge transfer character of the triplet state and increasing SOC between S_1 and T_1 may be a more effective route to enhancing k_{rISC}.[1,17] Yet another report suggests an alternative method of achieving TADF, by utilizing multiple resonance states instead of the traditional donor-acceptor design.[19] Unfortunately, the critical spectroscopic measurements to be conducted to fully comprehend the reverse intersystem crossing mechanism are not conducted on newly synthesized materials designed for TADF applications. The field has traditionally relied on steady-state and time-resolved microsecond measurements to determine TADF activity. However, some investigations have been conducted utilizing time-resolved spectroscopic techniques.

Choi et al[20] reported on the impact of solvent polarity and local environment on the excited state dynamics of a TADF emitter via femtosecond transient measurements. They observed that the excited state dynamics of DPA-AQ-DPA were completed within tens of picoseconds in polar

solvent, indicating that ISC did not occur. However, in a nonpolar solvent, the excited state dynamics continue past 3 ns, indicating that a triplet excited state had formed. As ISC to the triplet state is an important step for the TADF process, it was determined that for this compound the TADF mechanism does not occur in high polarity solvents. This is due to the interactions between the intramolecular charge transfer state (ICT) and polar solvents causing stabilization of this state. If the energy of the ICT state is made to be less than that of the $^3\pi\pi^*$, due to the interactions of ICT and polar solvent, then ISC from the singlet to triplet manifolds, and subsequently TADF, is inhibited. They found that in low polarity solvent, the ICT state is at a higher energy than the $^3\pi\pi^*$, allowing for ISC to the triplet state to occur. This finding shows the importance of considering which solvent is used for spectroscopic measurements in determining TADF activity.

He et al[21] performed nanosecond transient absorption spectroscopy (nsTAS) measurements on donor-acceptor complexes. While the compounds in their report were not determined to be TADF active, their findings provide a good demonstration of the merits of this spectroscopic technique for determining a compound's excited state dynamics. They found broad excited state absorption bands that were in the same region as the fluorescence emission. However, due to the long-time delay of the measurement, the fluorescence signal had little contribution to the transient spectra. The excited states observed via nsTAS displayed long lifetimes which were enhanced in purged solutions, indicating that the excited states are triplets. They found that the ICT state is stabilized in polar solvents while the triplet state is largely unaffected. Their results also support that compounds with a significant degree of charge-transfer character display smaller quantum yields in polar solvents due to strong interactions between the large dipole moments of the ICT state and the solvent.

Franca et al[22] utilized nsTAS, in combination with other techniques, to reveal the importance of the triplet local exciton ($^3LE_{A\ n\pi^*}$) state in TADF. Through the transient absorption measurements, they observed the population of the $^3LE_{\pi\pi^*}$ from the ^1LE_A. They report a TADF pathway for ACRSA, where the $^3LE_{A\ n\pi^*}$ state couples to the triplet charge-transfer (^3CT) and singlet charge-transfer (^1CT) states, allowing for rISC. The energy of the $^3LE_{A\ n\pi^*}$ state is increased with increasing solvent polarity, while the energy of the ^3CT and ^1CT are decreased. This increases the energy gap between these states and impedes the rISC mechanism. Also utilizing nsTAS, Vázquez et al determined that the emitter BCC-TPTA lacked a long-lived emissive component and excited state absorption bands characteristic of triplet states.[3] Conducted in solution, the nsTAS measurements revealed that BCC-TPTA has similar excited state dynamics as a fluorescent compound with minimal long-lived triplet excited states. This was despite BCC-TPTA displaying a quantum yield enhancement after purging oxygen from solution. A method for approximating k_{rISC} was also developed using the nsTAS technique to directly observe triplet state dynamics free of guest-host interactions. These reports demonstrate the capabilities of the nsTAS technique for probing the photophysics of various compounds and determining their emissive mechanism.

In this contribution, we utilize multiple steady-state and time-resolved spectroscopic techniques, with an emphasis on nanosecond transient absorption spectroscopy, to investigate the TADF activity of emitters with carbazole and carbazole-derivatives as donors and phthalonitrile (PN) or triazine (Trz) as acceptors (**Figure 3.3.2**). We focus on determining the influence of molecular structure, specifically the influence of a linker between donor and acceptor, on TADF activity. Our results reveal a relationship between differences in donor strength and the rate of reverse intersystem crossing (k_{rISC}). It is widely accepted that enhancement of the fluorescence

quantum yield is evidence that the excited state decay dynamics of an emitter are governed by a delayed fluorescence mechanism. However, our measurements reveal that this Φ_F enhancement is not the only metric of importance. The nsTAS technique reveals a connection between observable triplet transient states and the rISC mechanism, and allows us to determine a relationship between donor strength and k_{rISC} intensity. We also propose a connection between k_{rISC} and the external quantum efficiency of OLEDs fabricated with these emitters.

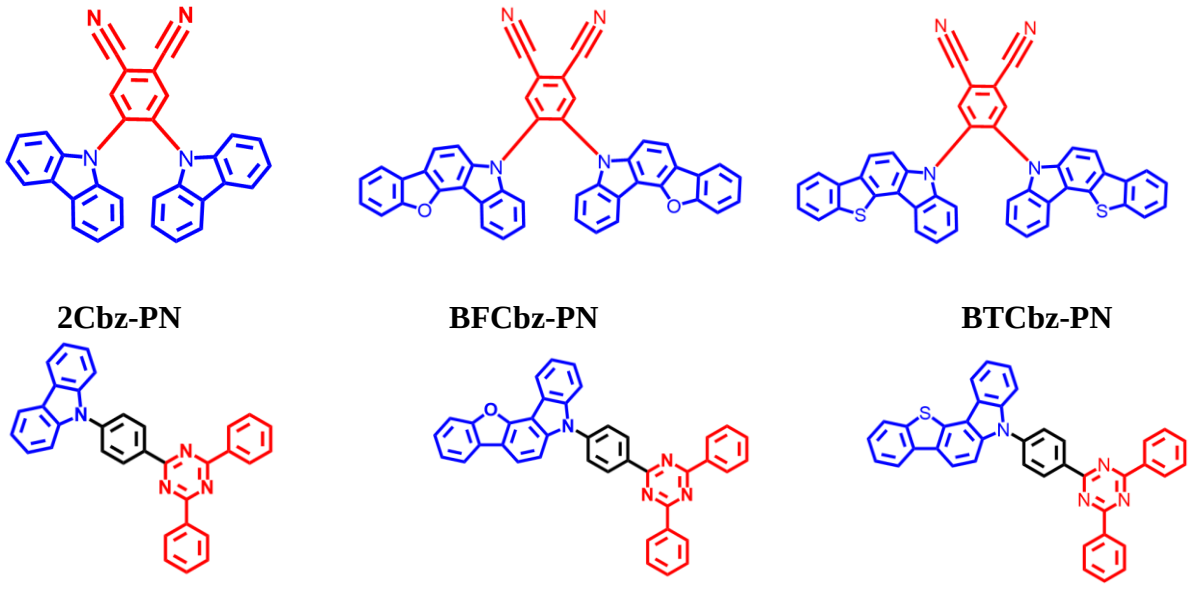


Figure 3.3.2. Structures of investigated chromophores (PN series above and Trz series below), where the donor unit is blue and acceptor unit is red.

3.4 Experimental Methods

3.4.1 Synthesis and Characterization

The reaction procedures of 5-(4-(4,6-diphenyl-1,3,5-triazin-2-yl)phenyl-5H-benzofuro[3,2-c]carbazole (BFCbz-Trz), 4,5-bis(benzofuro[3,2-c]carbazol-5-yl)phthalonitrile (BFCbz-PN), and 4,5-bis(benzo[4,5]thieno[3,2-c]carbazol-5-yl)phthalonitrile (BTCbz-PN) were previously

described.[23,24] What follows is the reaction procedure for 5-(4-(4,6-Diphenyl-1,3,5-triazin-2-yl)phenyl)-5H-benzo[4,5]thieno[3,2-c]carbazole (BTCbz-Trz). Sodium hydride, 2-chloro-4,6-diphenyl-1,3,5-triazine and (4-fluorophenyl)boronic acid (TCI Chem. Co.) were used without further purification. Tetrahydrofuran (THF) was distilled over sodium and calcium hydride.

Here, sodium hydride (0.07 g, 3.06 mmol) was then washed with hexane three times and dried under vacuum. 5H-benzo[4,5]thieno[3,2-c]carbazole (0.46 g, 1.68 mmol) was dissolved in THF (50 ml) and added to the flask. The reaction mixture was stirred for 30 min at room temperature under inert N_2 atmosphere and then 2-(4-fluorophenyl)-4,6-diphenyl-1,3,5-triazine (0.50 g, 1.53 mmol) was added. The reaction was quenched with distilled water (10 ml) at the 12-hour mark. The reaction mixture was extracted with MC and distilled water 3 times. The organic layer was dried over $MgSO_4$ and purified by column chromatography on silica gel using hexane:dichloromethane (1:2) as eluent. The product was purified by thermal gradient sublimation and pure BTCbz-Trz was obtained as a pale-yellow powder.

3.4.2 Steady-State Absorption and Emission Measurements

The absorption and emission measurements were carried out in dilute toluene solutions. The absorption spectra were collected via an Agilent 8341 spectrophotometer. The emission spectra were collected using a Fluoromax-4 fluorimeter, with entrance and exit slits set to 1.0 nm and an integration time of 1.0 s. Quartz cuvettes with 1.0 cm path lengths were used for all steady-state measurements.

3.4.3 Fluorescence Quantum Yield Calculation

The fluorescence quantum yields (Φ_F) were calculated utilizing the Williams comparative method.[25,26] A series of solutions of decreasing concentration were utilized for the calculations.

The optical densities of the solutions used for these measurements started at 0.10 and were systematically halved. The quantum yields were calculated using **Eqn. 3.4.3.1**:

$$\Phi_F = \Phi_{STD} \frac{Grad_x \eta_x^2}{Grad_{STD}\, \eta_{STD}^2} \qquad \textbf{Eqn. 3.4.3.1}$$

Where Φ_F is the calculated quantum yield, η is the refractive index of the solvent, and $Grad$ is the slope obtained from plotting the fluorescence area vs the optical density. The subscripts *STD* and *x* refer to the standard and investigated compound, respectively. The quantum yields for the investigated chromophores were calculated using Coumarin 6 in ethanol and Cascade Blue in water as standards.[27,28] Oxygen-free Φ_F were obtained by purging the solutions via nitrogen bubbling for ten minutes. The emission spectra were collected on a Cary Eclipse Fluorescence Spectrometer with slits set at 1.5 nm. Quartz cuvettes with 1.0 cm path lengths were used for all measurements.

3.4.4 Two-Photon Absorption

The two-photon absorption (TPA) spectroscopy technique, which has been previously described, was used to investigate the charge-transfer properties of the investigated chromophores in solution.[25,29–34] The optical densities of the solutions were kept to 0.10. TPA was conducted utilizing a mode-locked Ti:Sapphire laser tunable from 700 to 900 nm, delivering 110 fs output pulses at a repetition rate of 80 MHz. Emission scans were conducted at 800 nm excitation while scanning 400 – 700 nm emission. The emission detection wavelength for the power dependence scan was determined by the emission wavelength that produced the highest number of counts at 400 nm excitation (by simultaneously absorbing two 800 nm photons). Rhodamine B was used as the standard. Input power from the laser was adjusted via a variable neutral density filter. Two-

photon power-dependent fluorescence intensity was utilized to determine the TPA cross-section using the two-photon emission fluorescence method, in which a log-log plot of counts per second of two-photon induced emission versus beam power (mW) was constructed for each sample.

3.4.5 Time-Resolved Fluorescence Up-Conversion

Time resolved fluorescence decay measurements of the chromophores were detected at an up-converted wavelength of 287 nm using a FOG-100 (CDP Instruments, Inc.) system, a technique described previously.[35–38] A mode-locked Ti:Sapphire (Tsunami, Spectra Physics) laser source of 790 nm was used. The source beam underwent frequency doubling by passing through a β-barium borate (BBO) nonlinear crystal. By second harmonic generation (SHG), 395 nm light was produced which acted as the excitation source for the sample in solution phase (1 mm thick rotating sample cell). The remaining 790 nm light (the gate) passed through an optical delay line, which induced a delay in time by adjusting the path length of the gate beam. Both the gate and the sample fluorescence passed through a BBO crystal. Sum frequency generation (SFG) occurred when the gate pulse entered the BBO crystal at the same time as the sample fluorescence. As delay is introduced to the gate beam, fluorescence decay can be detected. The detected (up-converted) light is collected by a monochromator and photomultiplier tube (R1527P, Hamamatsu).

3.4.6 Time-Correlated Single Photon Counting (TCSPC)

The time-correlated single photon counting (TCSPC) technique, which has been previously described, was used to investigate the components of fluorescence and the fluorescence decay lifetime of the investigated chromophores.[3,14,25,32,33] The decay lifetimes were determined by fitting log plots of the obtained spectra to a linear fit. The measurements were conducted in dilute solutions in oxygen rich (unpurged/air) and oxygen-free (purged) environments. The solutions were purged by bubbling nitrogen for ten minutes. The laser used for the TCSPC measurements

was a Kapteyn Murnane (KM) mode-locked Ti-sapphire laser. The output beam of the KM laser was at a wavelength of 800 nm and a pulse duration of ~30 fs. The output beam was frequency-doubled using a nonlinear β-barium borate crystal to obtain a 400 nm beam. The beam was focused on the sample cuvette (1.0 cm path length) using a lens with a focal length of 11.5 cm. The emission collection was done perpendicular to the incident beam with the help of a monochromator, while the output of the monochromator was coupled to a photomultiplier tube. The monochromator was set to detect each samples' respective fluorescence maximum.

3.4.7 Nanosecond Transient Absorption (nsTAS)

The absorption and decay lifetime of emissive and non-emissive transient states were investigated using nanosecond transient absorption spectroscopy (nsTAS), which has been previously described.[3,14,32] A LP980 (Edinburgh) transient system, that contains a photomultiplier tube, was coupled with a Spectra-Physics QuantaRay Nd:YAG nanosecond pulsed laser and a GWU Optical Parametric Oscillator (OPO) tunable from 206 nm to 2600 nm for the pump beam. For this report, the pump beam was set to each sample's respective absorbance maximum. A pulsed broadband xenon lamp beam was used to probe the excited states. These measurements were conducted in both oxygen rich and oxygen free solutions.

3.4.8 Reverse Intersystem-Crossing Rate Calculations

The purged excited state absorption lifetimes, obtained from nsTAS, were used to calculate the reverse intersystem crossing rate (k_{rISC}) using **Eqn. 3.4.8.1**:[14]

$$k_{rISC} = k_{triplet} * \Phi_{TADF} \qquad \textbf{Eqn. 3.4.8.1}$$

Where $k_{triplet}$ is the rate of triplet state decay, and Φ_{TADF} is the direct difference between the purged and unpurged Φ_F. This method allows for the determination of k_{rISC} free of guest-host interactions and by directly observing triplet state decay.

3.4.9 Quantum Chemical Calculations

Quantum chemical simulations were performed on all Trz- and PN-acceptor chromophores to gain insight on how molecular structure affects the excited state dynamics and TADF activity. Atomistic models of the Trz- and PN-acceptor chromophores were constructed, with no truncation of the chromophore structure. Ground state (S_0) geometry optimizations were performed using density functional theory (DFT), and excited singlet (S_1) and triplet (T_1) state geometries were optimized using time-dependent DFT (TD-DFT). Optimizations were performed with B3LYP (hybrid) and ωB97X-D (range-separated hybrid [39,40]) with 6-31G* as the basis set. Single-point energies were performed to determine energies of excited singlet and triplet states for all optimized geometries using TD-DFT with functionals B3LYP and ωB97X-D and basis set 6-31G* in the gas phase. These computations provided the singlet-triplet energy gaps (ΔE_{ST}). Spin-orbit coupling constants (V_{SOC}) were calculated to determine the coupling between the S_1 and T_1 from the optimized excited triplet state geometries using TD-DFT with functionals B3LYP and ωB97X-D and basis set 6-31G* in the gas phase. Using ΔE_{ST}, V_{SOC}, and single point computations the reverse intersystem crossing rates for all Trz- and PN-acceptor chromophores were calculated. The formulas used for reverse intersystem crossing rate calculations, which have been previously described, are provided in the Supporting Information.[1,41,42] Natural transition orbitals (NTOs) from TD-DFT were visualized using IQMOL with isovalue of 0.07 $Å^{-3}$. All quantum chemical computations were performed using Q-Chem 5.2 software package.[43]

3.5 Results

3.5.1 Steady-State Absorption Measurements

The absorbance spectra of the investigated chromophores are displayed in **Figure 3.5.1.1**. Cbz-Trz has a broad absorbance band with a maximum absorbance at 360 nm, which can be attributed to intramolecular charge transfer (ICT) between the carbazole donor and triazine acceptor.[44,45] Various shoulders can also be observed in the absorbance spectrum which are assumed to be the result of intramolecular π–π* transitions. Interestingly, the peak and shoulders are redshifted when either benzofurocarbazole (BF) or benzothienocarbazole (BT) are used as the donor units. This shift indicates that these transitions are stabilized due to both BF and BT being stronger donors than carbazole.[21] Slight broadening in the absorbance range is also observed with the replacement of carbazole with BF or BT. This broadening has been attributed to increased donor contribution, oscillator strength, and steric hindrance in previous studies on carbazole derivatives.[44–47]

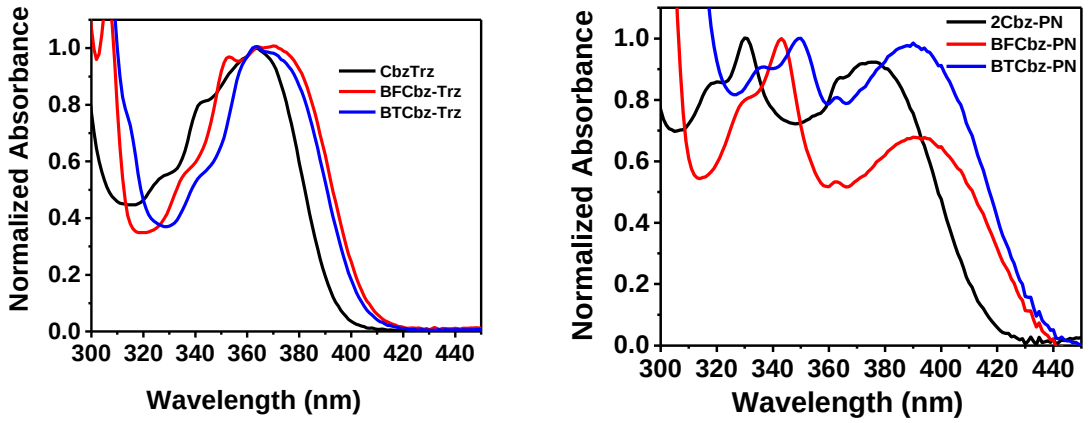


Figure 3.5.1.1. Absorbance spectra of Trz-acceptor (left) and PN-acceptor compounds (right) in toluene.

The steady-state absorbance spectrum of 2Cbz-PN displays two prominent absorption peaks at 330 nm and 370 nm for the first and second peak, respectively. These dual-bands are characteristic of donor-acceptor compounds with charge transfer (CT) character.[46,48,49] Various shoulders are also observed, assumed to be the result of different transitions. The high energy band

has been attributed to the π–π^* transition, while the second lower energy band has been attributed to the n-π* transition.[20,24] Similar to the Trz-acceptor compounds, a redshift is observed when the carbazole unit is replaced with BF or BT. Such shifts in absorbance bands have been observed for similar carbazole derivatives.[2,49] The redshift is attributed to the BF and BT substituents providing greater donor contribution and increasing π-conjugation. Comparison between the absorption spectra of the two series reveal that the PN-acceptor compounds have a slightly broader absorption spectrum than the Trz-acceptor compounds. The extinction coefficients provide some information on the photo-absorption capabilities of the compounds (**Table 3.5.3.1**). It is clear from the calculations that almost each PN-acceptor compound is more efficient at absorbing light than their Trz-counterpart by nearly an order of magnitude or greater. BFCbz-Trz is the exception to this, as it has an extinction coefficient of 1.16×10^5 only slightly less than BFCbz-PN.

3.5.2 Fluorescence Measurements

The fluorescence emission spectra of all compounds are displayed in **Figure 3.5.2.1**. Cbz-Trz displays a broad emission with a maximum at 420 nm. A slight redshift in emission maximum is observable when the carbazole donor is replaced with BF or BT along with a slight broadening of the emission range. These emissions have been attributed to relaxation of the intramolecular charge transfer (ICT) state.[44,45,47] The redshift is likely due to the stronger donors stabilizing the ICT state and increasing the dihedral angle between the donor and phenylene linker.[44]

2Cbz-PN also displays a broad emission with a single peak at 473 nm, suggesting emission from a singlet excited state. A slight redshift in the emission spectra is observed when BF or BT are the donor groups. This redshift is likely the result of the ICT state being stabilized by the

stronger donor groups.[2,10,44,47] The redshift could also be influenced by the electron-donating ability of BF or BT. As 2Cbz-PN has the weaker donor unit, its emission is at a shorter wavelength.[2] It is interesting that the degree of redshift is greater for the PN-acceptor compounds than the Trz-acceptor compounds, being ~27 nm and ~12 nm, respectively. This difference is likely due to there being two donor groups for the PN-acceptor compounds, causing greater distortion between the donors. It is also possible that having two donor groups increases π-conjugation, which has been observed to tune the emission wavelength.[47,48]

The fluorescence quantum yield (Φ_F) values, which were calculated before and after the oxygen purging process, are displayed in **Table 3.5.3.1.** Cbz-Trz has an unpurged Φ_F of 97%, indicating that it has a great deal of π-conjugation and charge-transfer character.[50,51] The Φ_F of BFCbz-Trz and BTCbz-Trz were equally impressive at 91% and 98%, respectively. Each compound displayed a Φ_F enhancement to 100% with oxygen purging. Such a large Φ_F suggests that these compounds are highly efficient fluorescent compounds. Thus the observed enhancement could be the result of oxygen no longer quenching singlet states.[52]

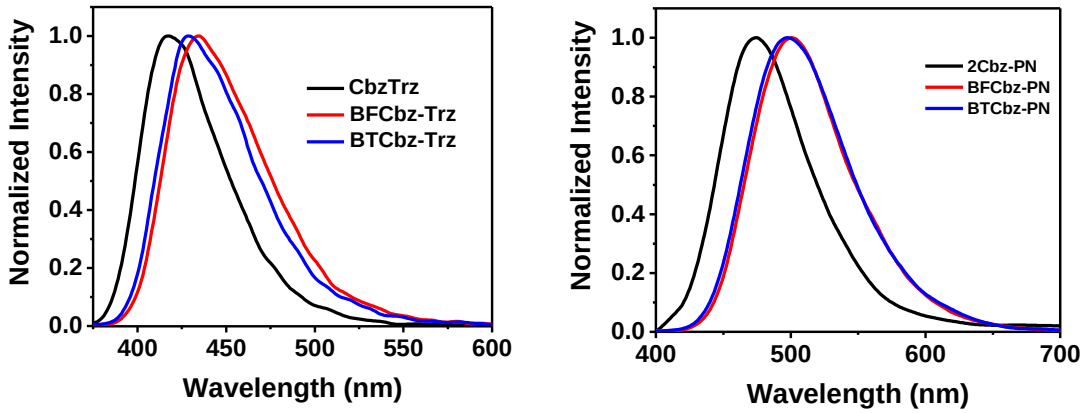


Figure 3.5.2.1. Fluorescence spectra of Trz-acceptor (left) and PN-acceptor compounds (right) chromophores in toluene.

The PN-acceptor compounds display much smaller Φ_F values. Unpurged Φ_F of 2Cbz-PN was calculated to be 17%, with the values for BFCbz-PN and BTCbz-PN being similar at 15% and 12%, respectively. These results indicate that these compounds are not efficient fluorophores. With oxygen purging, 2Cbz-PN displays a slight enhancement in Φ_F, increasing to 21%. However, the Φ_F of both BFCbz-PN and BTCbz-PN nearly double after oxygen purging, to 28% and 24%, respectively. Such enhancements have traditionally been attributed to the TADF mechanism, the reasoning being that the enhancement is due to the newly unquenched triplet states undergoing rISC. However, it is worth noting that the phosphorescence spectra of the investigated compounds display a large degree of overlap with the fluorescence spectra.[23,24] Thus it is possible that the observed Φ_F enhancements of the PN-acceptor compounds could be due to enhanced rare room-temperature phosphorescence. As such, Φ_F enhancement is a good indicator that the triplet state is utilized in the emissive mechanism but should not be used as the sole metric to indicate TADF activity for these compounds.

3.5.3 Two-Photon Absorption

The two-photon induced emission and two-photon absorption cross-sections were obtained to gain insight into the CT character of these emitters. This is because the TPA transition probability increases with increasing ICT character.[53–56] The two-photon induced emission of the investigated chromophores are displayed in **Figure 3.5.3.1**, and are in good agreement with the steady-state fluorescence spectra. A red-shift in the two-photon emission spectra is observed for BFCbz-Trz and BTCbz-Trz relative to that of Cbz-Trz. A similar trend is observed for the PN-acceptor compounds, with BFCbz-PN and BTCbz-PN emissions being redshifted from that of 2Cbz-PN.

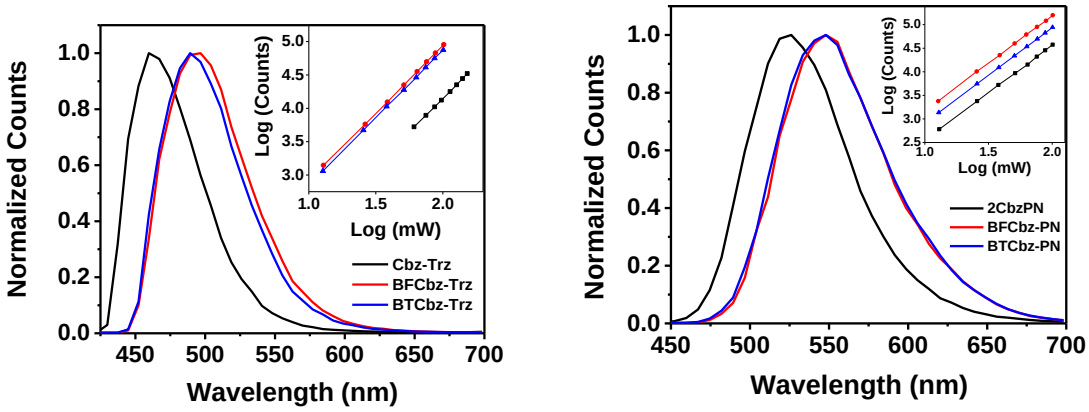


Figure 3.5.3.1. Two-photon induced fluorescence scans of the Trz-acceptor (left) and PN-acceptor (right) compounds. Insets are logarithmic plots of two-photon absorption power dependence versus fluorescent intensities.

Logarithmic plots of counts per second of two-photon induced emission versus beam power (mW) were constructed for each sample and are displayed as insets in **Figure 3.5.3.1**. These plots gave a linear fit with a positive slope of approximately two for all samples, confirming the TPA process. The TPA cross-section values are displayed in **Table 3.5.3.1**. Cbz-Trz has a relatively low cross-section value of 1.01 GM. This value was greatly enhanced when BF or BT are the donor moieties, to 14.9 and 8.8 GM, respectively. This finding confirms that BF and BT provide greater donor contribution than the carbazole unit, which is in agreement with previous studies that relate donor-acceptor strength to CT character.[21,57]

2Cbz-PN has a TPA cross-section of 15.9 GM, much higher than Cbz-Trz. This indicates that the combination of phthalonitrile acceptor and carbazole donor leads to greater ICT character. BTCbz-PN has a TPA cross-section of 21.8 GM, indicating that increasing the donor strength of the compound does increase its ICT character. This is in good agreement with the steady-state measurements. The TPA cross-section is enhanced to 44.4 GM with the BF donor. This is likely

because of the oxygen in the molecular structure being a better electron withdrawing group, increasing the ICT character even further. The order of increasing ICT character is consistent between both the Trz- and PN-acceptor compounds, where the compound with the BF donor displays the greatest ICT characteristics.

Compound	Abs max (nm)	Extinction Coefficient (M^{-1} cm^{-1})	Emission max (nm)	$\Phi_{Unpurged}/\Phi_{Purged}$ (%)	TPA Cross-Section (GM)
Cbz-Trz	363	2.37×10^4	420	97/100	1.01
BFCbz-Trz	370	1.16×10^5	432	91/100	14.9
BTCbz-Trz	370	9.97×10^3	432	98/100	8.8
2Cbz-PN	380	1.36×10^5	473	17/21	15.9
BFCbz-PN	395	2.34×10^5	500	15/28	44.4
BTCbz-PN	395	1.79×10^5	500	12/24	21.8

Table 3.5.3.1. Photophysical properties of investigated chromophores in toluene.

3.5.4 Time-Resolved Fluorescence Up-Conversion

Fluorescence decay measurements were conducted on all compounds in unpurged toluene. Purged solutions were not able to be tested due to limitations of the fluorescence up-conversion sample holder. Two decay components are observed for the Trz-acceptor compounds, with each component displaying different lifetimes (**Table 3.5.4.1**). These decay traces (**Figure 3.5.4.1)** were each fitted to a double exponential decay function, yielding an initial decay for the first component of 114 - 160 ps and a longer decay that exceeded 2 ns for the second component.

The decay profiles of the PN-acceptor compounds display different dynamics from those of the Trz-acceptor compounds. Here, we observe three decay components, each with a different lifetime. The decay trace was fitted using to a three exponential decay function, yielding a very fast initial decay (< 7 ps), fast second decay (30 - 60 ps), and a relatively long-lived final decay (> 2 ns). The first component is of particular interest, as it is consistent across all PN-acceptor

compound and is absent for the Trz-acceptor compounds. Thus, this component is likely tied to the molecular structure of the PN-acceptor compounds.

One possible explanation is that the PN-acceptor compounds have faster and more efficient charge transfer, going from a delocalized state to a localized state, due to their donor units being directly linked to the acceptor.[25] The differences between the emissive dynamics of the Trz- and PN-acceptors could also be due to how the two classes of compounds interact with the solvent toluene.[58] This would indicate that the charge-transfer characteristics of the two classes are significantly different, as solvent polarity is known to alter emissive properties.[57–62] As the decay of the longest component continues past the limit of detection for this system, the time-correlated single photon counting technique is utilized to further investigate the emissive dynamics of these compounds.

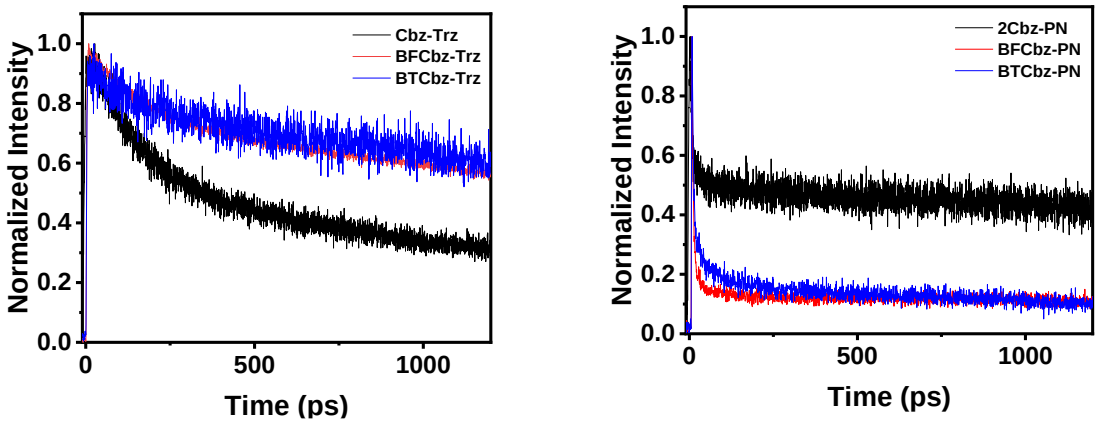


Figure 3.5.4.1. Time-resolved fluorescence up-conversion results of the Trz-acceptor compounds (left) and the PN-acceptor compounds (right) in toluene.

Compound	τ_1 (ps)	τ_2 (ps)	τ_3 (ps)
Cbz-Trz	149	>2,200	0
BFCbz-Trz	162	>2,200	0

BTCbz-Trz	114	>2,200	0
2Cbz-PN	4	31	>2,200
BFCbz-PN	5	40	>2,200
BTCbz-PN	4	64	>2,200

Table 3.5.4.1. Up-conversion emissive lifetime values of investigated compounds in unpurged toluene.

3.5.5 TCSPC

To better understand the emissive dynamics of the investigated compounds, the emissive lifetimes were obtained using the time-correlated single photon counting technique (TCSPC). As all the Trz-acceptor compounds display similar emissive dynamics, only the results for BFCbz-Trz are shown here. For similar reasons, only the results of BFCbz-PN are displayed here. The emission traces of BFCbz-Trz and BFCbz-PN are displayed in **Figure 3.5.5.1**, while the results for all other investigated compounds are provided in the supporting information (**Figure 3.5.5.1**). The emissive lifetimes of all investigated compounds are displayed in **Table 3.5.5.1**. The purged measurements were conducted to determine to what extent the triplet state is involved in the emissive mechanism. The understanding being that if the triplet state plays a role in emission, a long-lived emissive component should be observed. As oxygen is known to quench triplet states, an increase in the lifetime of the aforementioned long-lived component should be observed with oxygen purging.[3,52,63,64]

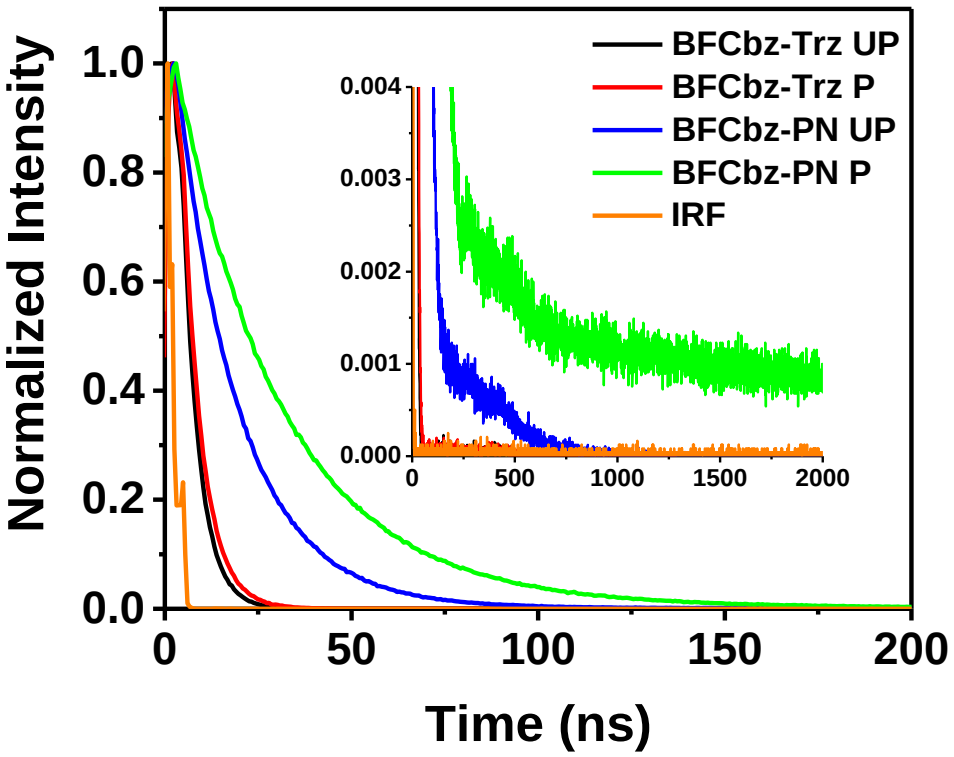


Figure 3.5.5.1. Time-correlated single photon counting measurements of BFCbz-Trz and BFCbz-PN in unpurged and purged toluene solutions. Inset is a zoom-in of the emission lifetime.

We immediately observe that the traces for BFCbz-Trz and BFCbz-PN are substantially different, an observation that is consistent with the other PN-acceptor compounds and their Trz-acceptor counterparts (**Figure 3.8.1)**. Cbz-Trz has an emissive lifetime of 4.6 ns that is only slightly enhanced with purging to 5.3 ns. There is little change in the emissive lifetime when BF or BT are used as the donor. BFCbz-Trz and BTCbz-Trz have emissive lifetimes of 4.8 and 4.2 ns that are only slightly enhanced with purging to 5.6 and 4.9 ns, respectively. These findings reveal that the Trz-acceptor compounds all have emissive lifetimes typical of fluorescent emitters.[3] The inset of **Figure 3.5.5.1** reveals that BFCbz-Trz lacks a long-lived emissive component that would indicate triplet states play a role in the emissive mechanism. Cbz-Trz and BTCbz-Trz also lack this component (**Figure 3.8.1**). This observation indicates that triplet states do not play a

substantial role in the emissive process. However, the results suggest that triplet states play an emissive role for the PN-acceptor compounds.

The inset of **Figure 3.5.5.1** reveals that BFCbz-PN has two fluorescent components. These two components were also observed for 2Cbz-PN and BTCbz-PN (**Figure 3.8.1**). The first component of 2Cbz-PN is rather short-lived compared to the second component, having a lifetime of 19 ns, which is enhanced to 30 ns with oxygen purging. The replacement of the carbazole donor with BF or BT only slightly enhances the first component lifetime, to 24 and 23 ns for BFCbz-PN and BTCbz-PN in unpurged toluene, respectively. These short-lived components are enhanced with oxygen purging, increasing to lifetimes of 39 for BFCbz-PN and 38 ns for BTCbz-PN. These lifetimes are significantly greater than those of the Trz-acceptor compounds, indicating that they are comparatively less efficient fluorophores.

The second emissive component displays a much more pronounced enhancement with the removal of oxygen (**Figure 3.8.2**). This is clearly observed for 2Cbz-PN, where the second component lifetime increases from 223 to 1,247 ns with oxygen purging. The enhancement observed for BFCbz-PN and BTCbz-PN was even more drastic, increasing from 196 to 2,090 ns and 201 to 1,980 ns, respectively. The presence of a long-lived emissive component that is altered by the presence of oxygen indicates that there is some emissive mechanism that utilized triplet states in the same wavelength region as singlet emission. The prompt component decay has been attributed to a decay process that primarily utilizes the singlet excited state, due to its lifetime being only slightly altered by oxygen purging. The long-lived component has been attributed to a decay process that primarily relies on the triplet excited state.

Compound	τ_{Short} Unpurged/Purged (ns)	τ_{Long} Unpurged/Purged (ns)
Cbz-Trz	4.6/5.3	0/0
BFCbz-Trz	4.8/5.6	0/0
BTCbz-Trz	4.2/4.9	0/0
2Cbz-PN	19/30	223/1247
BFCbz-PN	24/39	196/2090
BTCbz-PN	23/38	201/1980

Table 3.5.5.1. Lifetimes of the components of fluorescence in toluene solutions.

3.5.6 nsTAS

The nanosecond transient absorption spectroscopy (nsTAS) technique was utilized to investigate the decay lifetimes of both the emissive and non-emissive transient species of the chromophores. These species are observed as either a negative or positive change in optical absorption (ΔOD) and are the result of ground state bleach (GSB), spontaneous emission (SE), or excited state absorption (ESA), respectively. The lifetimes of these peaks provide information for determining the character of the transient species and the emissive mechanism. The transient absorption spectra for each of the Trz-acceptor and PN-acceptor compounds display similar dynamics to BFCbz-Trz and BFCbz-PN, respectively. As such, only BFCbz-Trz and BFCbz-PN are discussed here. Their transient absorption spectra are displayed in **Figure 3.5.6.1** and **Figure 3.5.6.2,** respectively, while the transient absorption spectra of the other compounds are provided in the supporting information (**Figure 3.8.3 and Figure 3.8.4**).

The nsTAS mapping of BFCbz-Trz reveals a large SE peak that has a maximum at the same wavelength as the steady-state fluorescence. There is also a short-lived GSB within the same region as the steady-state absorption. There appears to be ESA peaks at 350 and 650 nm. However, the kinetic traces taken at these wavelengths (**Figure 3.8.5**) reveal that these peaks are only noise.

The kinetic traces of the other Trz-acceptor compounds yielded similar results. Thus, it is determined that no long-lived ESAs are observed for any of the other Trz-acceptor compounds. This result further supports that these emitters utilize fluorescence and do not utilize the triplet state for emission.

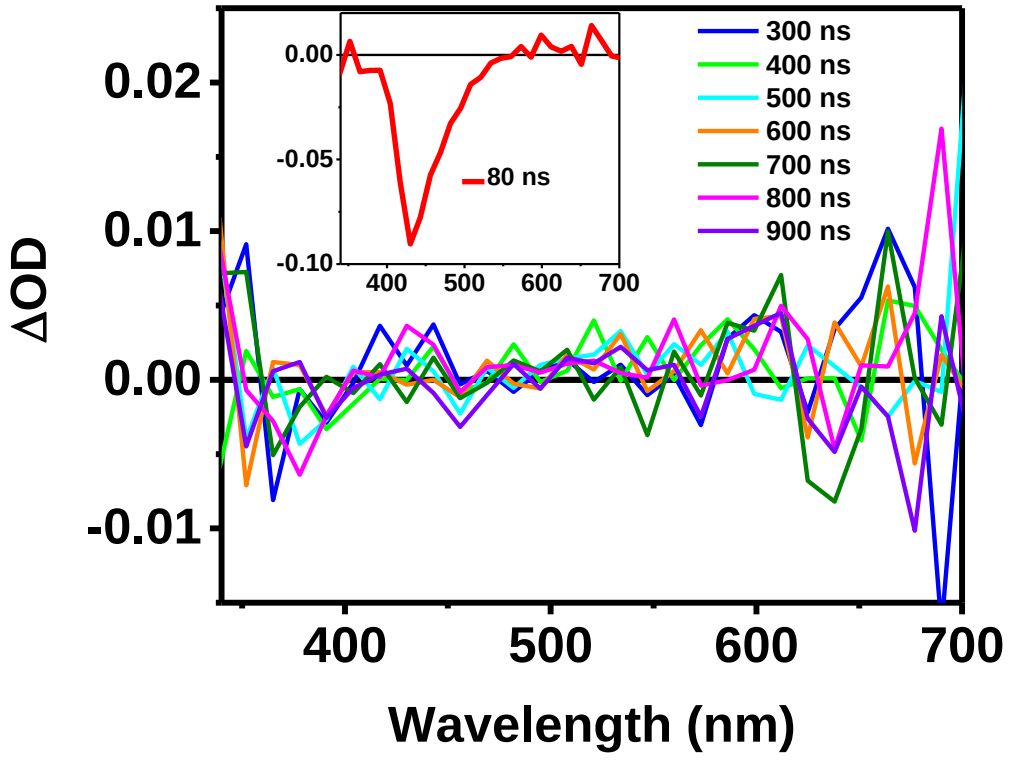


Figure 3.5.6.1. Nanosecond transient absorption spectra of BFCbz-Trz in purged toluene. The insert displays the SE peak at 80 ns.

The transient absorption spectrum for BFCbz-PN reveals excited state dynamics that are quite different from BFCbz-Trz. First, a GSB is observed at 400 nm and is attributed to depletion of the ground state and overlaps with the ICT transition observed in the steady-state absorbance spectrum. This is followed by a large SE peak, attributed to fluorescence. Unlike BFCbz-Trz, there is an ESA that is within the same region as the emission and is able to be resolved due to the time delay of the nsTAS technique.[21] This ESA is a long-lived state that that displays sensitivity to

oxygen in solution and is present in the transient absorption spectra of each of the PN-acceptor compounds. The ESA and GSB kinetic traces for BFCbz-PN are displayed in **Figure 3.5.6.3**, with the kinetic traces of the other PN-acceptor compounds available in the supporting information (**Figure 3.8.6 and Figure 3.8.7**). Decay lifetimes of these states in unpurged and purged solution are displayed in **Table 3.5.6.1**. The decay dynamics of each PN-acceptor compound is similar so only the dynamics BFCbz-PN will be described here. The GSB displays a lifetime of 230 ns that is enhanced to 652 ns with oxygen purging. This is expected, as the various triplet ESAs provide significant contribution to the GSB lifetime. The ESA lifetime is 488 ns in unpurged solution and is enhanced to 929 ns with oxygen purging. This supports the characterization of the ESA as a triplet state.

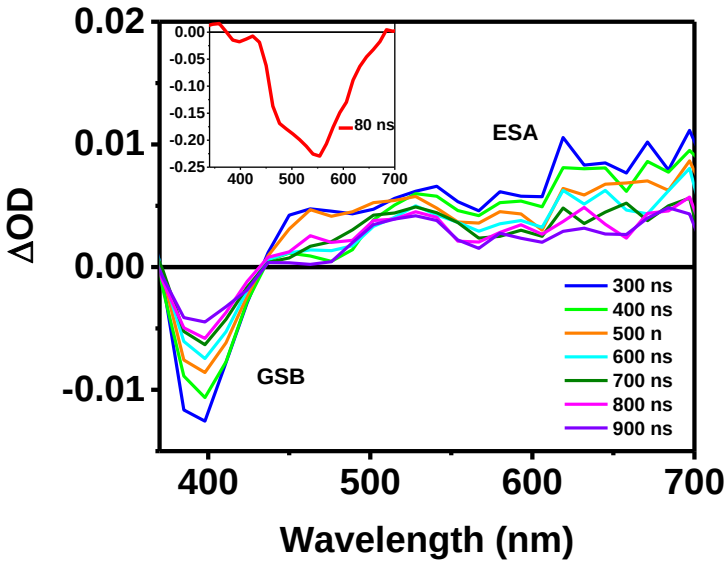


Figure 3.5.6.2. Nanosecond transient absorption spectra of BFCbz-PN in purged toluene. The inset displays the SE peak at 80 ns.

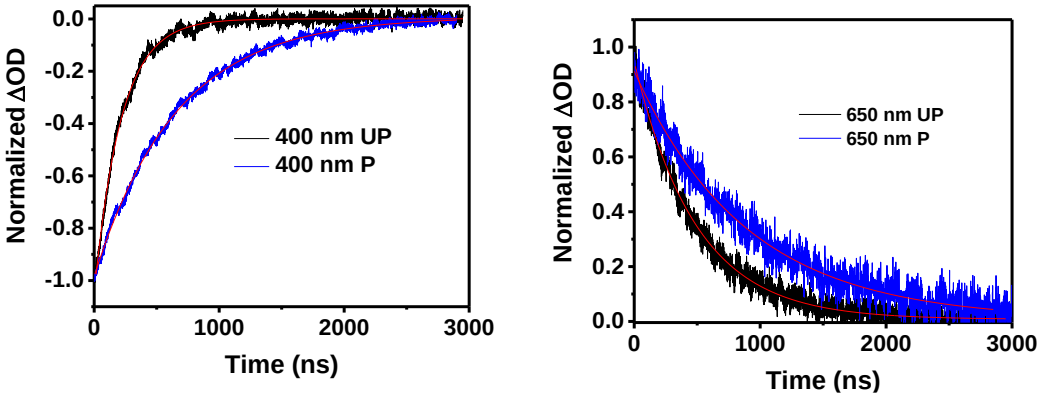


Figure 3.5.6.3. Ground state bleach (left) and excited state absorption (right) decays of BFCbz-PN in unpurged and purged toluene solutions. The red lines represent the mono-exponential decay fittings.

The ESA decay values obtained from nsTAS were utilized to calculate k_{rISC}. The k_{rISC} values, displayed in **Table 3.5.6.1**, for each PN-acceptor compound were approximated utilizing the previously described Vázquez and Masui methods.[11,14] While there is disagreement between the obtained values, the trend within the values is consistent. 2Cbz-PN has the lowest k_{rISC}, indicating that it is the least efficient TADF emitter amongst the PN-acceptor compounds. BFCbz-PN and BTCbz-PN have similar efficiencies to each other, regardless of which calculation method is used. It is worth noting that the method developed by Vázquez et al displays the same trend in efficiencies that was observed in previous studies.[24] We'd like to reiterate that no ESAs were observed for the Trz-acceptor compounds. As such, no ESA decay kinetics nor subsequent k_{rISC} values were obtained for the Trz-acceptor compounds.

Compound	τ_{GSB} UP(ns)	τ_{GSB} P(ns)	τ_{ESA} UP(ns)	τ_{ESA} P(ns)	k_{ESA} (s^{-1})	k_{rISC} (s^{-1}) Vázquez[16]	k_{rISC} (s^{-1}) Masui[11,14]
2Cbz-PN	307	695	325	775	1.29×10^6	5.16×10^4	8.51×10^3
BFCbz-PN	221	655	488	871	1.15×10^6	1.49×10^5	1.40×10^4
BTCbz-PN	217	585	208	856	1.17×10^6	1.40×10^5	1.54×10^4

Table 3.5.6.1. Decay lifetimes of the transient states of PN-acceptor compounds in unpurged and purged toluene. Also included are k_{rISC} values using two different methods

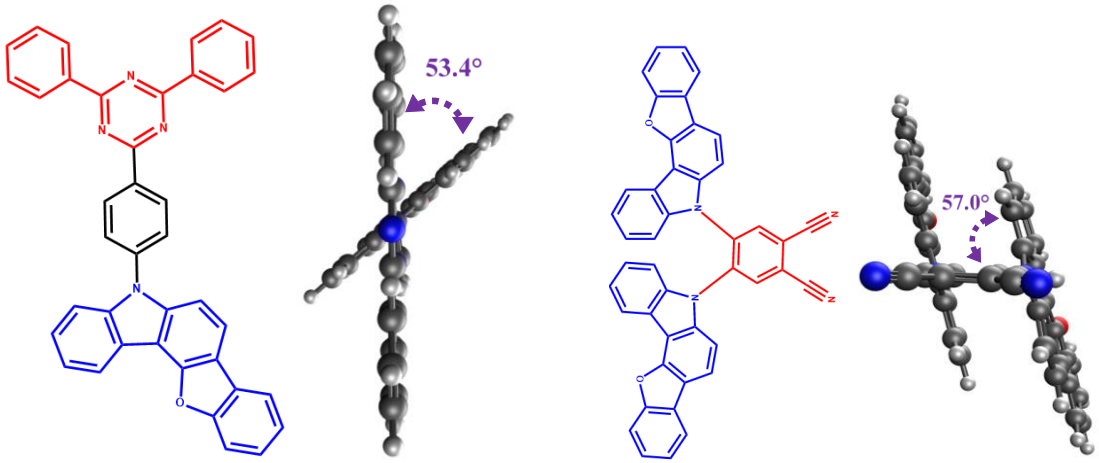
3.5.7 Quantum Chemical Calculations

In order to establish a connection between molecular structure and the observed photophysical properties, with a focus on the influence of the phenylene linker, quantum chemical calculations were conducted on all Trz- and PN-acceptor compounds based on the structures displayed in **Figure 3.3.2**. As the computational results for each of the Trz- and PN-acceptor compounds are similar to BFCbz-Trz and BFCbz-PN, respectively, only BFCbz-Trz and BFCbz-PN are discussed here. The computational results for all other compounds are displayed in the supporting information.

Optimized ground state geometries were obtained for each compound to investigate the influence of the phenylene bridge on the dihedral angle (**Figure 3.5.7.1 and Figure 3.8.8**). Our results show that the inclusion of the linker causes the dihedral angle to remain relatively the same, regardless of which donor unit is used. The Trz-acceptor compounds have strikingly similar dihedral angles, where the ground state dihedral angles of Cbz-Trz, BFCbz-Trz, and BTCbz-Trz are 54.3^{o}, 53.4^{o}, and 54.5^{o}, respectively. These results are interesting, as it was expected that the bulkier BF and BT donor units would cause an appreciable increase in dihedral angle. A likely reason for each Trz-acceptor compound having similar ground state dihedral angles is that there is little steric hindrance due to the linear structure of the Trz-acceptor compounds. Thus, the dihedral angle of the Trz-acceptor compounds does not change much, even with the use of BF or BT as donors (**Table 3.5.7.1**).

As the molecular structure of PN-acceptor compounds does not include a linker, the use of BF or BT as donor units has a greater influence on their dihedral angles. We observe this as 2Cbz-PN has a ground state dihedral angle of 49.5^{o}, which is increased to 57.0^{o} and 57.2^{o} for BFCbz-PN and BTCbz-PN, respectively. This increase is attributed to the branched molecular structure of the

PN-acceptor compounds, which induces steric hindrance between the two donor groups. Because BF and BT are bulkier than carbazole, steric hindrance between the two donors is increased leading



BFCbz-Trz **BFCbz-PN**

Figure 3.5.7.1: Optimized ground state (from ωB97X-D) dihedral angles of BFCbz-Trz and BFCbz-PN.

to larger dihedral angles. It is interesting that there is little difference between dihedral angles of the BF or BT derivatives. This slight difference suggests that the heteroatom plays only a small role in the ground state dihedral angles, with molecular structure and size of the donor group having the most significant contribution. When comparing the optimized ground state to the optimized excited singlet and triplet geometries of the Trz- and PN-acceptor chromophores, there are differences in dihedral angles due to the chromophores being in the relaxed versus excited state. However, the trends observed for the ground state geometries are also seen in the excited state geometries (**Table 3.8.1**).

The natural transition orbitals (NTOs) of the Trz- and PN-acceptor chromophores were obtained to further elucidate the influence of molecular structure on charge-transfer (CT) character and HOMO/LUMO separation (**Figure 3.5.7.2 and Figure 3.8.9**). Each compound has some

degree of CT character, and it can be seen in the transition from ground state to excited singlet state ($S_0 \rightarrow S_1$). The Trz-acceptor compounds have limited separation of the exciton NTO (HOMO) and hole NTO (LUMO). The HOMO is largely localized on the donor unit and phenylene bridge connecting the donor and diphenyltriazine acceptor. The LUMO is localized on the phenylene bridge and the triazine ring of the acceptor unit. Some electron density of the LUMO remains on the donor unit, with none present on the phenyl rings of the Trz acceptor. Such a large degree of HOMO/LUMO overlap suggests that the phenylene bridge inhibits HOMO/LUMO separation when only one donor unit is used.

Due to their donor and acceptor units being directly linked, most of the PN-acceptor compounds display substantial HOMO/LUMO separation. For 2Cbz-PN, the HOMO is localized on the two carbazole donors and the ring of the phthalonitrile acceptor. The LUMO has significant overlap with the HOMO, being localized almost entirely on the acceptor, with some electron density on the two donors (**Figure 3.8.9**). HOMO/LUMO separation is increased with the use of BF as the donor group, where the HOMO is mostly localized on the two donors while the

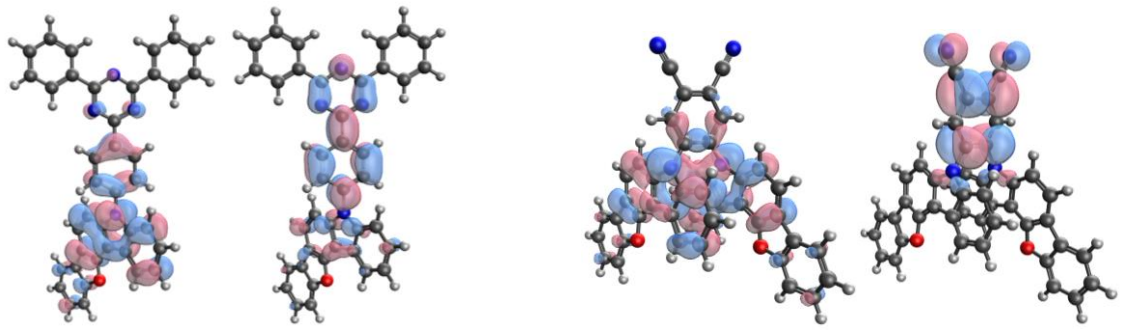


Figure 3.5.7.2. Natural transition orbitals (from ωB97X-D) for charge transfer states of BFCbz-Trz and BFCbz-PN.

localization of the LUMO is largely unaffected (**Figure 3.5.7.2**). For both the Trz- and PN-acceptor compounds, no significant differences in HOMO/LUMO separation are observed between using BF or BT as the donor unit. These results indicate that increasing donor strength increases HOMO/LUMO separation, provided that the donor and acceptor are directly linked without the use of a bridge.

The adiabatic energy gaps between the excited singlet and excited triplet states (ΔE_{ST}) and spin-orbit coupling constants (V_{SOC}) were calculated to determine k_{rISC} for the investigated compounds (**Table 3.5.7.1**). The trends and differences observed for dihedral angles and HOMO/LUMO separation are also observed for (ΔE_{ST}) and k_{rISC}. We observe that ΔE_{ST} for BFCbz-Trz (0.93 eV) is significantly larger (~3x) than that of BFCbz-PN (0.37 eV) (**Figure 3.8.10**). Similar results were obtained for the remaining Trz- and PN-acceptor compounds. The calculated k_{rISC} of BFCbz-Trz and BFCbz-PN, 1.1×10^{-7} and 9.3×10^{1}, respectively, suggests that only the PN-acceptor compounds are capable of undergoing rISC. This result suggests a correlation between ΔE_{ST} and k_{rISC}, where k_{rISC} decreases as ΔE_{ST} increases. This finding is in agreement with the current understanding of the TADF mechanism.[13] Based on these results, the PN-acceptor compounds have a significantly greater chance of undergoing rISC and achieving TADF than their Trz-acceptor counterparts. These results also indicate that both BFCbz-PN and BTCbz-PN are more efficient TADF emitters than 2Cbz-PN, consistent with previous reports.[24] This is associated to their smaller ΔE_{ST} and higher degree of HOMO/LUMO separation. This is also reflected in the results of the previously discussed optical measurements. Of the PN-acceptor compounds, BFCbz-PN has a slightly more efficient TADF mechanism due to its smaller ΔE_{ST} and higher electronegative heteroatom. This result is again consistent with previous reports.[24]

Compound	ΔE_{ST} (eV)	V_{SOC} (eV)	k_{rISC} P (s^{-1}) Vázquez[16]	TD-DFT k_{rISC} (s^{-1})
Cbz-Trz	1.00	$1.3x10^{-3}$	0/0	5.5×10^{-10}
BFCbz-Trz	0.93	$1.3x10^{-3}$	0/0	1.1×10^{-7}
BTCbz-Trz	0.95	$1.3x10^{-3}$	0/0	2.1×10^{-8}
2Cbz-PN	0.53	$1.5x10^{-4}$	5.16×10^{4}	1.1×10^{-1}
BFCbz-PN	0.37	$1.3x10^{-4}$	1.49×10^{5}	9.3×10^{1}
BTCbz-PN	0.38	$1.3x10^{-4}$	1.40×10^{5}	3.8×10^{1}

Table 3.5.7.1. Quantum chemical results for investigated compounds, along with experimental and calculated k_{rISC}.

3.6 Discussion

In this report, we utilize high-resolution steady-state, time-resolved, and nonlinear optical spectroscopic techniques, as well as quantum chemical calculations to investigate the photophysical properties of carbazole based emitters. Our measurements reveal stark differences in the emissive mechanism between the Trz- and PN-acceptor compounds. These differences are based on the molecular structure, namely the presence or absence of the phenylene linker. To aid in the clarity of this section, the Trz-acceptor compounds are discussed first followed by the PN-acceptor compounds.

The steady-state measurements reveal that the Trz-acceptor compounds have an extremely high Φ_F (>90%) that displays a slight enhancement when oxygen is purged from solution. This enhancement could indicate that triplet states play a role in their emissive mechanism. However, such high Φ_F in unpurged solution indicates that k_F is so efficient that it heavily outcompetes the rates of other singlet decay pathways including k_{nr} and k_{ISC}. In addition to this, oxygen has also

been observed to quench singlet states.[52] Thus, emissive lifetime measurement were conducted to aid in determining the role of excited triplets in the emissive mechanism. These measurements reveal that Trz-acceptor compounds have emissive lifetimes of ~5 ns which is largely unaffected by oxygen purging. Long-lived emissive components, which would indicate emission that relies on excited triplets, were not observed for any of the Trz-acceptor compounds.[3] This matches expectations, as it would be unusual to observe a long-lived emissive component for compounds with such high Φ_F. This expectation arises from the understanding that the longer the lifetime of the excited states, the greater the chance that they will be quenched by a non-radiative process. The nsTAS results support this, as no triplet states are observed in the transient absorption spectra for these compounds. This is significant, as some triplet states should be observed if k_{ISC} was able to compete with k_F. A likely cause for low k_{ISC} is the relatively high singlet-triplet energy gap for these compounds (0.93 – 1.0 eV). Such a large gap impedes spin-orbit coupling which is required for ISC. Due to these factors, k_F is able to substantially outcompete k_{ISC} and the observed Φ_F enhancement is determined to be the result of newly unquenched singlet states.

The substantial Φ_F of the Trz-acceptor compounds is also the result of the phenylene linker. It was expected that a significant amount energy would be dissipated via molecular motion, thus impacting Φ_F. However, the quantum chemical calculations reveal that this is not the case. The dihedral angles between the donor and phenylene linker (**Table 3.8.1**), show there is little difference between the ground and excited state dihedral angles (~2^o). These results indicate that only a small portion of energy is lost to molecular motion. The likely cause for such a small change in dihedral angle is that by physically separating the donor and acceptor units, such as via a phenylene linker, electron repulsion is reduced thus diminishing the dihedral angle.

The phenylene linker also affects the HOMO/LUMO separation, as shown by the NTO results. For each Trz-acceptor compound, the HOMO is localized on the donor and phenylene linker while the LUMO is mostly centered on the phenylene linker and the central ring of the triazine acceptor. It appears that the dual phenyl rings of the acceptor unit do not provide significant contribution as electron withdrawers. A particularly interesting observation is that the stronger BF and BT donors reduce HOMO/LUMO separation, causing some of the LUMO to be on the donor unit. As significant separation is considered to be a requirement for TADF activity, it is little wonder that these compounds do not display any of the characteristics commonly associated with the TADF process.[1,2,11,22] The ΔE_{ST} of these compounds are also relatively large, being significantly greater than the reported energy required for rISC to take place (**Table 3.5.7.1**).[4,17] It appears that having the donor and acceptor connected via a bridge does not aid in HOMO/LUMO separation, as both HOMO and LUMO density of these compounds are localized on the phenylene linker.

The steady-state measurements show that the PN-acceptor compounds have significantly lower Φ_F than the Trz-acceptor compounds. Such Φ_F indicate that other processes that deplete the singlet excited state, such as k_{ISC}, take place for these compounds. These compounds also display significantly larger enhancements when oxygen is purged from the solution than the Trz-acceptor compounds. As stated previously, this could indicate that these compounds utilize the triplet state for emission. The up-conversion results reveal that 2Cbz-PN has a more complex emissive decay process than Cbz-Trz. We observe three components with the third and last component having an extremely long lifetime. The third component has the greatest contribution to the emission. However, similar to Cbz-Trz, the total lifetime was not able to be resolved by the time-resolved fluorescence up-conversion technique. Thus, the TCSPC technique was again used to fully resolve the emissive lifetime. The TCSPC technique was also used to further determine to what degree the

triplet state plays a role in emission. It is apparent that the PN-acceptor compounds have two emissive components on the ns timescale. However, the second emissive component could be the result of phosphorescence that overlaps with the fluorescence spectrum. This could be the reason for it having such low intensity when compared to the first component, as room temperature phosphorescence is not expected to be very intense. Instead, our focus is on the first emissive component, as it displays some interesting dynamics.

The lifetime of the first emissive component is nearly 6 – 7 times longer than those of the Trz-acceptor compounds. This supports the determination that k_F is not as efficient for the PN-acceptor compounds, as this longer lifetime indicates a diminished k_F, consistent with Φ_F results. Also consistent with Φ_F results, the first component lifetime is significantly enhanced with oxygen purging. This was unexpected, as the emissive trace for the Trz-acceptor compounds, which is also determined to be from fluorescence, shows little enhancement with oxygen purging. The observation of two emissive components, with the second component being long-lived, is often associated with the TADF process.[23,65] However, it was expected that emission from TADF emitters would have a similar lifetime as emission from fluorescent compounds. This expectation arises from the understanding that rISC results in emission from the singlet state. Such an emission should display similar dynamics as typical fluorescence. Here it is important to note that the phosphorescence spectra of each of the PN-acceptor compounds has a high degree of overlap with the fluorescence spectra.[11,24] The overlap is such that the fluorescence peak, which the TCSPC detector is set to, there is possibly some phosphorescence activity. If emission from both singlet and triplet states occur at the same wavelength, as is the case with these compounds, the TCSPC technique cannot distinguish between the two. This means that the observed long-lived emissive component could be the result of phosphorescence. However, room temperature phosphorescence

is expected to be an inefficient process for organic compounds. This could explain why the long-lived emissive component has such low signal when compared to the short-lived first component. Thus, TCSPC is not used to definitively determine TADF activity and more thorough investigation utilizing nsTAS is conducted.

Similar to the report by He et al.[21], a large SE peak was observed in the same region as the ESA peaks. These peaks were able to be resolved due to the time-delay of the nsTAS technique. It was confirmed that these peaks were above the noise level and are triplet excited states for the PN-acceptor compounds. The broadness of the ESA peaks indicate that the PN-acceptor compounds are able to populate triplet states of various energies.[13] As expected, the lifetime of the triplet state is enhanced with oxygen purging. Analysis of τ_{ESA}, k_{ESA}, and k_{rISC} reveals a connection between the triplet state and the Φ_F and emissive lifetimes. 2Cbz-PN has the longest ESA lifetime, lowest k_{ESA}, and lowest k_{rISC}. These characteristics indicate that processes that deplete the triplet state, including k_{rISC}, are inefficient for this compound. This is one cause for 2Cbz-PN displaying a smaller Φ_F enhancement when compared to BFCbz-PN and BTCbz-PN. However, BFCbz-PN and BTCbz-PN have shorter ESA lifetimes, and more efficient k_{ESA} and k_{rISC}. This result follows the same trend as their greater Φ_F enhancement and longer emissive component lifetimes. It is thus determined that the PN-acceptor compounds utilize the triplet states in a rISC process. The TPA and quantum chemical calculations aid in understanding the structure-function relationship for the observed excited state and emissive dynamics.

The lack of a phenylene linker in the PN-acceptor molecular design results in very different characteristics than what was observed for the Trz-acceptor compounds. Firstly, the larger TPA cross-section of the PN-acceptor compounds indicate that they have greater charge-transfer

character than the Trz-acceptor compounds. This comes from the understanding that stronger donors increase the charge transfer character thus enhancing the transition moment of two-photon absorption.[53,54,56]

This interpretation of the TPA cross-section results are supported by the quantum chemical calculations, which reveal that the PN-acceptor compounds also have a greater degree of HOMO/LUMO separation than the Trz-acceptor compounds. 2Cbz-PN has its HOMO localized on the two carbazole donors and the ring of the phthalonitrile acceptor with the LUMO being localized almost completely on the entire acceptor unit. This localization indicates that the phthalonitrile acceptor acts as an efficient electron withdrawing group, aiding in HOMO/LUMO separation. This separation is enhanced with the use of BF or BT as donor groups, where the HOMOs of BFCbz-PN and BTCbz-PN are completely localized on the donor units. The LUMO is largely unaffected, still being somewhat present on the donor units, which maintains the partial overlap required for TADF. Interestingly, there is little difference in HOMO/LUMO separation between BFCbz-PN and BTCbz-PN, indicating that different heteroatoms play only a small role in this. The ΔE_{ST} of these compounds is also significantly smaller than their Trz-counterparts. This small ΔE_{ST} allows for greater spin-orbit coupling between the singlet and triplet manifolds and an enhanced k_{rISC}.[1] ΔE_{ST} of the BF and BT derivatives are smaller than that of 2Cbz-PN (**Table 3.5.7.1**). This is likely due to the HOMO/LUMO energy gap of the BF and BT donor units being smaller than that of carabzole.[1,66,67] The greater HOMO/LUMO separation observed for the PN-acceptor compounds has been attributed to two factors: 1) the donors are directly linked to the acceptor unit, and 2) there are two donor units that further contribute to the overall donor strength. All of these factors contribute to the PN-acceptor compounds demonstrating TADF properties.

Two experimental methods and quantum chemical calculations were utilized to approximate k_{rISC} for all investigated compounds. No k_{rISC} values for the Trz-acceptor compounds could be determined using either experimental method due to no long-lived emissive component or triplet states being observed. However, using quantum chemical calculations k_{rISC} values on the order of 10^{-7} – 10^{-10} were obtained for the Trz-acceptor compounds. These values indicate that the rISC process is unlikely to occur in these compounds, which is consistent with all experimental results. All methods of calculation indicate that the rISC process is accessible to the PN-acceptor compounds. While there is disagreement in the actual values, as is to be expected, the trend is clear. Both BFCbz-PN and BTCbz-PN display greater k_{rISC} than 2Cbz-PN, indicating that increasing donor-contribution enhances TADF activity. Our results display a clear correlation between molecular design and TADF activity, where the PN-acceptor compounds are TADF active while the Trz-acceptor compounds are not. This is reflected in the external quantum efficiencies (EQE) of OLEDs fabricated with these compounds as emitters.

Devices that utilize the PN-acceptor compounds as emitters generally have better performance than those that utilize Trz-acceptor compounds.[24,68] At 10 wt% and DPEPO as the host, an OLED using Cbz-Trz as the emitter achieved an EQE of 4.2%.[68] However, using mCP as the host and only 1 wt% 2Cbz-PN, a device was fabricated that had an EQE of 7%.[24] Under identical device parameters and using BFCbz-PN or BTCbz-PN as the emitter, the EQE is almost doubled to ~12%.[24] Based on our time-resolved, steady state, and quantum chemical simulations, we assert that the PN-acceptor compounds are TADF active emitters while the Trz-acceptor compounds are not. However, our results do not fully agree with the reported device properties of BFCbz-Trz, where at 10 wt% in DPEPO many of the characteristics associated with TADF were observed.[23]

This raises two questions: 1) why is the TADF affect observed for BFCbz-Trz and not Cbz-Trz, and 2) why are TADF characteristics observed for BFCbz-Trz in solid-state but not in solution.

Regarding the first question, it is important to note that all device parameters of the Cbz-Trz and BFCbz-Trz OLEDs are identical, save the emissive layer.[23,68] This indicates that the differences in device properties are related to this layer. Thus any differences between the two OLEDs can be attributed to the different donor unit of the emitter, either carbazole or BF. It is likely that BFCbz-Trz has guest-host interactions that induce the TADF characteristics due to its donor unit. More in-depth studies are needed to determine what these interactions are and how they can be utilized to improve device EQE.

Regarding the second question, the interactions between guest and host materials are still not well understood. However, it is well established that the device properties can be dramatically altered depending on the wt% of emitter used and choice of host material.[11,23,24,69,70] One proposed explanation for guest-host interactions has been described as solid-state solvation, where the properties of the host matrix, such as polarity, can alter the emissive properties of the embedded chromophore.[61,62] From the TPA results, we determined that BFCbz-Trz has the greatest CT character of the Trz-acceptor compounds. This indicates that it would be the most affected by host polarity, and thus the energy levels of its singlet and triplet excited states being greatly diminished in polar hosts such as DPEPO. If this is the case, then it is perhaps possible to induce the TADF mechanism by utilizing the correct guest-host blend. This assertion is supported by the different device properties obtained for Cbz-Trz and BFCbz-Trz, where the only difference in the emissive layer was the emitter itself. Determining the exact parameters that would match a host and emitter to induce the TADF mechanism would require its own in-depth investigation and would likely be

time-consuming. Thus, it is more favorable to begin TADF-based OLED design and fabrication with an emitter that displays TADF characteristics in solution and free of guest-host interactions.

3.7 Conclusion

Our study has revealed that despite both classes of compounds being designed to be TADF active compounds, the Trz- and PN-acceptor compounds display very different excited state dynamics in solution. The Trz-acceptor compounds display only one of the characteristics expected of a TADF emitter, that being Φ_F enhancement with oxygen purging. However, they have short emissive lifetimes and lack an ESA which could be associated to triplet states. Due to the lack of these components, no k_{rISC} values could be determined for these compounds with our experimental methods. Thus, the Trz-acceptor compounds are determined to be TADF-inactive materials.

Unlike their Trz-counterparts, each of the PN-acceptor compounds display all of the characteristics traditionally associated with the TADF process. They have relatively small Φ_F which are enhanced with oxygen purging. This, in addition to a long emissive lifetime, indicates that k_F is not as efficient for these compounds, allowing for other decay pathways to utilize the excited states. Their transient absorption spectra reveal long-lived triplet states which could undergo various decay pathways, including rISC. Using experimental methods and quantum chemical calculations, k_{rISC} was approximated for these compounds, which indicate that rISC is a viable pathway for each PN-acceptor compound. Thus, it was determined that these compounds are TADF-active emitters.

Structure-function relationships were also established, where the observed photophysics of the PN-acceptor compounds are the result of directly linking the donor to the acceptor unit. This

molecular design induces sufficient HOMO/LUMO separation, small ΔE_{ST}, and enhanced V_{SOC} between the triplet and singlet manifolds. By increasing the donor strength, i.e., using BF or BT as donors instead of carbazole, each of these factors are enhanced, which in turn enhances k_{rISC}. This finding indicates that sufficient donor contribution is required for TADF activity. It is our hope that our results can improve design principles of TADF compounds and highlight the importance of considering guest-host interactions for future measurements.

References

(1) Samanta, P. K.; Kim, D.; Coropceanu, V.; Brédas, J. L. Up-Conversion Intersystem Crossing Rates in Organic Emitters for Thermally Activated Delayed Fluorescence: Impact of the Nature of Singlet vs Triplet Excited States. *J. Am. Chem. Soc.* **2017**, *139*, 4042–4051. https://doi.org/10.1021/jacs.6b12124.

(2) Uoyama, H.; Goushi, K.; Shizu, K.; Nomura, H.; Adachi, C. Highly Efficient Organic Light-Emitting Diodes from Delayed Fluorescence. *Nature* **2012**, *492*, 234–238. https://doi.org/10.1038/nature11687.

(3) Vázquez, R. J.; Kim, H.; Zimmerman, P. M.; Goodson, T. Using Ultra-Fast Spectroscopy to Probe the Excited State Dynamics of a Reported Highly Efficient Thermally Activated Delayed Fluorescence Chromophore. *J. Mater. Chem. C* **2019**, *7*, 4210–4221. https://doi.org/10.1039/c8tc05957h.

(4) Gibson, J.; Penfold, T. J. Nonadiabatic Coupling Reduces the Activation Energy in Thermally Activated Delayed Fluorescence. *Phys. Chem. Chem. Phys.* **2017**, *19*, 8428–8434. https://doi.org/10.1039/c7cp00719a.

(5) Gibson, J.; Monkman, A. P.; Penfold, T. J. The Importance of Vibronic Coupling for Efficient Reverse Intersystem Crossing in Thermally Activated Delayed Fluorescence Molecules.

ChemPhysChem **2016**, 2956–2961. https://doi.org/10.1002/cphc.201600662.

(6) Hirata, S.; Sakai, Y.; Masui, K.; Tanaka, H.; Lee, S. Y.; Nomura, H.; Nakamura, N.; Yasumatsu, M.; Nakanotani, H.; Zhang, Q.; Shizu, K.; Miyazaki, H.; Adachi, C. Highly Efficient Blue Electroluminescence Based on Thermally Activated Delayed Fluorescence. *Nat. Mater.* **2015**, *14*, 330–336. https://doi.org/10.1038/nmat4154.

(7) Liu, Y.; Li, C.; Ren, Z.; Yan, S.; Bryce, M. R. All-Organic Thermally Activated Delayed Fluorescence Materials for Organic Light-Emitting Diodes. *Nat. Rev. Mater.* **2018**, *3*. https://doi.org/10.1038/natrevmats.2018.20.

(8) Yang, Z.; Mao, Z.; Xie, Z.; Zhang, Y.; Liu, S.; Zhao, J.; Xu, J.; Chi, Z.; Aldred, M. P. Recent Advances in Organic Thermally Activated Delayed Fluorescence Materials. *Chem. Soc. Rev.* **2017**, *46*, 915–1016. https://doi.org/10.1039/c6cs00368k.

(9) Kim, M.; Jeon, S. K.; Hwang, S. H.; Lee, J. Y. Stable Blue Thermally Activated Delayed Fluorescent Organic Light-Emitting Diodes with Three Times Longer Lifetime than Phosphorescent Organic Light-Emitting Diodes. *Adv. Mater.* **2015**, *27*, 2515–2520. https://doi.org/10.1002/adma.201500267.

(10) Kim, M.; Jeon, S. K.; Hwang, S. H.; Lee, S. S.; Yu, E.; Lee, J. Y. Correlation of Molecular Structure with Photophysical Properties and Device Performances of Thermally Activated Delayed Fluorescent Emitters. *J. Phys. Chem. C* **2016**, *120*, 2485–2493. https://doi.org/10.1021/acs.jpcc.5b09114.

(11) Masui, K.; Nakanotani, H.; Adachi, C. Analysis of Exciton Annihilation in High-Efficiency Sky-Blue Organic Light-Emitting Diodes with Thermally Activated Delayed Fluorescence. *Org. Electron.* **2013**, *14*, 2721–2726. https://doi.org/10.1016/j.orgel.2013.07.010.

(12) Schinabeck, A.; Rau, N.; Klein, M.; Sundermeyer, J.; Yersin, H. Deep Blue Emitting Cu(i)

Tripod Complexes. Design of High Quantum Yield Materials Showing TADF-Assisted Phosphorescence. *Dalt. Trans.* **2018**, *47*, 17067–17076. https://doi.org/10.1039/c8dt04093a.

(13) Rodriguez-Serrano, A.; Dinkelbach, F.; Marian, C. M. Intersystem Crossing Processes in The2CzPNemitter: A DFT/MRCI Study Including Vibrational Spin-Orbit Interactions. *Phys. Chem. Chem. Phys.* **2021**, *23*, 3668–3678. https://doi.org/10.1039/d0cp06011a.

(14) Vázquez, R. J.; Yun, J. H.; Muthike, A. K.; Howell, M.; Kim, H.; Madu, I. K.; Kim, T.; Zimmerman, P.; Lee, J. Y.; III, T. G. New Direct Approach for Determining the Reverse Intersystem Crossing Rate in Organic Thermally Activated Delayed Fluorescent (TADF) Emitters. *J. Am. Chem. Soc.* **2020**. https://doi.org/10.1021/jacs.0c01225.

(15) Adachi, C. Third-Generation Organic Electroluminescence Materials. *Jpn. J. Appl. Phys.* **2014**, *53*. https://doi.org/10.7567/JJAP.53.060101.

(16) Yu, J. G.; Han, S. H.; Lee, H. L.; Hong, W. P.; Lee, J. Y. A Novel Molecular Design Employing a Backbone Freezing Linker for Improved Efficiency, Sharpened Emission and Long Lifetime in Thermally Activated Delayed Fluorescence Emitters. *J. Mater. Chem. C* **2019**, *7*, 2919–2926. https://doi.org/10.1039/c9tc00214f.

(17) Chen, X. K.; Tsuchiya, Y.; Ishikawa, Y.; Zhong, C.; Adachi, C.; Brédas, J. L. A New Design Strategy for Efficient Thermally Activated Delayed Fluorescence Organic Emitters: From Twisted to Planar Structures. *Adv. Mater.* **2017**, *29*, 1–8. https://doi.org/10.1002/adma.201702767.

(18) Tsai, W. L.; Huang, M. H.; Lee, W. K.; Hsu, Y. J.; Pan, K. C.; Huang, Y. H.; Ting, H. C.; Sarma, M.; Ho, Y. Y.; Hu, H. C.; Chen, C. C.; Lee, M. T.; Wong, K. T.; Wu, C. C. A Versatile Thermally Activated Delayed Fluorescence Emitter for Both Highly Efficient Doped and Non-Doped Organic Light Emitting Devices. *Chem. Commun.* **2015**, *51*, 13662–13665.

https://doi.org/10.1039/c5cc05022g.

(19) Kim, I.; Cho, K. H.; Jeon, S. O.; Son, W.-J.; Kim, D.; Rhee, Y. M.; Jang, I.; Choi, H.; Kim, D. S. Three States Involving Vibronic Resonance Is a Key to Enhancing Reverse Intersystem Crossing Dynamics of an Organoboron-Based Ultrapure Blue Emitter. *JACS Au* **2021**, *1*, 987–997. https://doi.org/10.1021/jacsau.1c00179.

(20) Choi, J.; Ahn, D. S.; Oang, K. Y.; Cho, D. W.; Ihee, H. Charge Transfer-Induced Torsional Dynamics in the Excited State of 2,6-Bis(Diphenylamino)Anthraquinone. *J. Phys. Chem. C* **2017**, *121*, 24317–24323. https://doi.org/10.1021/acs.jpcc.7b07553.

(21) He, G.; Zhou, L. L.; Song, H.; Kuang, Z.; Wang, X.; Guo, Q.; Lu, H. Y.; Xia, A. Insights into the Effect of Donor Ability on Photophysical Properties of Dihydroindeno[2,1-c] Fluorene-Based Imide Derivatives. *Phys. Chem. Chem. Phys.* **2018**, *20*, 7514–7522. https://doi.org/10.1039/c7cp07985k.

(22) Franca, L. G.; Long, Y.; Li, C.; Danos, A.; Monkman, A. The Critical Role of Nπ∗ States in the Photophysics and Thermally Activated Delayed Fluorescence of Spiro Acridine-Anthracenone. *J. Phys. Chem. Lett.* **2021**, *12*, 1490–1500. https://doi.org/10.1021/acs.jpclett.0c03314.

(23) Lee, D. R.; Choi, J. M.; Lee, C. W.; Lee, J. Y. Ideal Molecular Design of Blue Thermally Activated Delayed Fluorescent Emitter for High Efficiency, Small Singlet-Triplet Energy Splitting, Low Efficiency Roll-off, and Long Lifetime. *ACS Appl. Mater. Interfaces* **2016**, *8*, 23190–23196. https://doi.org/10.1021/acsami.6b05877.

(24) Lee, D. R.; Hwang, S.; Jeon, S. K.; Lee, C. W.; Lee, J. Y. Benzofurocarbazole and Benzothienocarbazole as Donors for Improved Quantum Efficiency in Blue Thermally Activated Delayed Fluorescent Devices. **2015**, 8105–8107.

https://doi.org/10.1039/c5cc01940k.

(25) Vázquez, R. J.; Kim, H.; Kobilka, B. M.; Hale, B. J.; Jeffries-El, M.; Zimmerman, P.; Goodson, T. Evaluating the Effect of Heteroatoms on the Photophysical Properties of Donor-Acceptor Conjugated Polymers Based on 2,6-Di(Thiophen-2-Yl)Benzo[1,2-b:4,5-B′]Difuran: Two-Photon Cross-Section and Ultrafast Time-Resolved Spectroscopy. *J. Phys. Chem. C* **2017**, *121*, 14382–14392. https://doi.org/10.1021/acs.jpcc.7b01767.

(26) Rhys Williams, A. T.; Winfield, S. A.; Miller, J. N. Relative Fluorescence Quantum Yields Using a Computer-Controlled Luminescence Spectrometer. *Analyst* **1983**, *108*, 1067–1071. https://doi.org/10.1039/an9830801067.

(27) Whitaker, J. E.; Haugland, R. P.; Reese, M.; Haugland, R. P.; Moore, L.; Hewitt, C. Cascade Blue Derivatives : Water Soluble , Reactive , Blue Emission Dyes Evaluated as Fluorescent Labels and Tracers. **1991**, *130*, 119–130.

(28) Company, E. K. New Coumarin Dyes with Rigidized Structure for Flashlamp-Pumped Dye Lasers. **1975**, *13*, 3–6.

(29) Cai, Z.; Vázquez, R. J.; Zhao, D.; Li, L.; Lo, W. Y.; Zhang, N.; Wu, Q.; Keller, B.; Eshun, A.; Abeyasinghe, N.; Banaszak-Holl, H.; Goodson, T.; Yu, L. Two Photon Absorption Study of Low-Bandgap, Fully Conjugated Perylene Diimide-Thienoacene-Perylene Diimide Ladder-Type Molecules. *Chem. Mater.* **2017**, *29*, 6726–6732. https://doi.org/10.1021/acs.chemmater.7b01512.

(30) Madu, I. K.; Muller, E. W.; Kim, H.; Shaw, J.; Burney-Allen, A. A.; Zimmerman, P.; Jeffries-El, M.; Goodson, T. Heteroatom and Side Chain Effects on the Optical and Photophysical Properties: Ultrafast and Nonlinear Spectroscopy of New Naphtho[1,2- b:5,6-B′]Difuran Donor Polymers. *J. Phys. Chem. C* **2018**, *122*, 17049–17066.

https://doi.org/10.1021/acs.jpcc.8b03914.

(31) Doan, P. H.; Pitter, D. R. G.; Kocher, A.; Wilson, J. N.; Goodson, T. Two-Photon Spectroscopy as a New Sensitive Method for Determining the DNA Binding Mode of Fluorescent Nuclear Dyes. *J. Am. Chem. Soc.* **2015**, *137*, 9198–9201. https://doi.org/10.1021/jacs.5b02674.

(32) Keller, B.; Cai, Z.; Muthike, A. K.; Sahu, P. K.; Kim, H.; Eshun, A.; Zimmerman, P. M.; Zhang, D.; Goodson, T. Investigating the Optical Properties of Thiophene Additions to S-Indacene Donors with Diketopyrrolopyrrole, Isoindigo, and Thienothiophene Acceptors. *J. Phys. Chem. C* **2018**, *122*, 27713–27733. https://doi.org/10.1021/acs.jpcc.8b08567.

(33) Taylor, E. L.; Metcalf, K. J.; Carlotti, B.; Lai, C. T.; Modica, J. A.; Schatz, G. C.; Mrksich, M.; Goodson, T. Long-Range Energy Transfer in Protein Megamolecules. *J. Am. Chem. Soc.* **2018**, *140*, 15731–15743. https://doi.org/10.1021/jacs.8b08208.

(34) Abeywickrama, C. S.; Wijesinghe, K. J.; Plescia, C. B.; Fisher, L. S.; Goodson, T.; Stahelin, R. V.; Pang, Y. A Pyrene-Based Two-Photon Excitable Fluorescent Probe to Visualize Nuclei in Live Cells. *Photochem. Photobiol. Sci.* **2020**, *19*, 1152–1159. https://doi.org/10.1039/d0pp00107d.

(35) Devadas, M. S.; Kim, J.; Sinn, E.; Lee, D.; Goodson, T.; Ramakrishna, G. Unique Ultrafast Visible Luminescence in Monolayer-Protected Au 25 Clusters . *J. Phys. Chem. C* **2010**, *114*, 22417–22423. https://doi.org/10.1021/jp107033n.

(36) Ashenfelter, B. A.; Desireddy, A.; Yau, S. H.; Goodson, T.; Bigioni, T. P. Fluorescence from Molecular Silver Nanoparticles. *J. Phys. Chem. C* **2015**, *119*, 20728–20734. https://doi.org/10.1021/acs.jpcc.5b05735.

(37) Varnavski, O.; Leanov, A.; Liu, L.; Takacs, J. Femtosecond Luminescence Dynamics in a

Nonlinear Optical Organic Dendrimer. *Phys. Rev. B - Condens. Matter Mater. Phys.* **2000**, *61*, 12732–12738. https://doi.org/10.1103/PhysRevB.61.12732.

(38) Donehue, J. E.; Varnavski, O. P.; Cemborski, R.; Iyoda, M.; Goodson, T. Probing Coherence in Synthetic Cyclic Light-Harvesting Pigments. *J. Am. Chem. Soc.* **2011**, *133*, 4819–4828. https://doi.org/10.1021/ja108359w.

(39) Chai, J. Da; Head-Gordon, M. Long-Range Corrected Hybrid Density Functionals with Damped Atom-Atom Dispersion Corrections. *Phys. Chem. Chem. Phys.* **2008**, *10*, 6615–6620. https://doi.org/10.1039/b810189b.

(40) Chai, J. Da; Head-Gordon, M. Systematic Optimization of Long-Range Corrected Hybrid Density Functionals. *J. Chem. Phys.* **2008**, *128*. https://doi.org/10.1063/1.2834918.

(41) Beljonne, D.; Shuai, Z.; Pourtois, G.; Bredas, J. L. Spin-Orbit Coupling and Intersystem Crossing in Conjugated Polymers: A Configuration Interaction Description. *J. Phys. Chem. A* **2001**, *105*, 3899–3907. https://doi.org/10.1021/jp010187w.

(42) Zhu, Q.; Guo, X.; Zhang, J. Theoretical Study on Photophysical Properties of a Series of Functional Pyrimidine-Based Organic Light-Emitting Diodes Emitters Presenting Thermally Activated Delayed Fluorescence. *J. Comput. Chem.* **2019**, *40*, 1578–1585. https://doi.org/10.1002/jcc.25808.

(43) Epifanovsky, E.; Gilbert, A. T. B.; Feng, X.; Lee, J.; Mao, Y.; Mardirossian, N.; Pokhilko, P.; White, A. F.; Coons, M. P.; Dempwolff, A. L.; Gan, Z.; Hait, D.; Horn, P. R.; Jacobson, L. D.; Kaliman, I.; Kussmann, J.; Lange, A. W.; Lao, K. U.; et al Software for the Frontiers of Quantum Chemistry: An Overview of Developments in the Q-Chem 5 Package. *J. Chem. Phys.* **2021**, *155*, 084801. https://doi.org/10.1063/5.0055522.

(44) Li, H.; Li, J.; Liu, D.; Huang, T.; Li, D. Effects of Electron Affinity and Steric Hindrance

of the Trifluoromethyl Group on the π-Bridge in Designing Blue Thermally Activated Delayed Fluorescence Emitters. *Chem. - A Eur. J.* **2020**, *26*, 6899–6909. https://doi.org/10.1002/chem.202000926.

(45) Suzuki, K.; Kubo, S.; Shizu, K.; Fukushima, T.; Wakamiya, A.; Murata, Y.; Adachi, C.; Kaji, H. Triarylboron-Based Fluorescent Organic Light-Emitting Diodes with External Quantum Efficiencies Exceeding 20 %. *Angew. Chemie - Int. Ed.* **2015**, *54*, 15231–15235. https://doi.org/10.1002/anie.201508270.

(46) Wang, K.; Liu, W.; Zheng, C. J.; Shi, Y. Z.; Liang, K.; Zhang, M.; Ou, X. M.; Zhang, X. H. A Comparative Study of Carbazole-Based Thermally Activated Delayed Fluorescence Emitters with Different Steric Hindrance. *J. Mater. Chem. C* **2017**, *5*, 4797–4803. https://doi.org/10.1039/c7tc00681k.

(47) Tanaka, H.; Shizu, K.; Nakanotani, H.; Adachi, C. Twisted Intramolecular Charge Transfer State for Long-Wavelength Thermally Activated Delayed Fluorescence. *Chem. Mater.* **2013**, *25*, 3766–3771. https://doi.org/10.1021/cm402428a.

(48) Cho, Y. J.; Lee, A. R.; Kim, S. Y.; Cho, M.; Han, W. S.; Son, H. J.; Cho, D. W.; Kang, S. O. The Influence of π-Conjugation on Competitive Pathways: Charge Transfer or Electron Transfer in New D-π-A and D-π-Si-π-A Dyads. *Phys. Chem. Chem. Phys.* **2016**, *18*, 22921–22928. https://doi.org/10.1039/c6cp03259a.

(49) Hosokai, T.; Matsuzaki, H.; Nakanotani, H.; Tokumaru, K.; Tsutsui, T.; Furube, A.; Nasu, K.; Nomura, H.; Yahiro, M.; Adachi, C. Evidence and Mechanism of Efficient Thermally Activated Delayed Fluorescence Promoted by Delocalized Excited States. *Sci. Adv.* **2017**, *3*, 1–10. https://doi.org/10.1126/sciadv.1603282.

(50) Yamaguchi, Y.; Matsubara, Y.; Ochi, T.; Wakamiya, T.; Yoshida, Z. I. How the π

Conjugation Length Affects the Fluorescence Emission Efficiency. *J. Am. Chem. Soc.* **2008**, *130*, 13867–13869. https://doi.org/10.1021/ja8040493.

(51) Humbert-Droz, M.; Piguet, C.; Wesolowski, T. A. Fluorescence Quantum Yield Rationalized by the Magnitude of the Charge Transfer in π-Conjugated Terpyridine Derivatives. *Phys. Chem. Chem. Phys.* **2016**, *18*, 29387–29394. https://doi.org/10.1039/c6cp04252j.

(52) Patterson, L. K.; Porter, G.; Topp, M. R. Oxygen Quenching of Singlet and Triplet States. *Chem. Phys. Lett.* **1970**, *7*, 612–614. https://doi.org/10.1016/0009-2614(70)87019-1.

(53) Lee, W. H.; Lee, H.; Kim, J. A.; Choi, J. H.; Cho, M.; Jeon, S. J.; Cho, B. R. Two-Photon Absorption and Nonlinear Optical Properties of Octupolar Molecules. *J. Am. Chem. Soc.* **2001**, *123*, 10658–10667. https://doi.org/10.1021/ja004226d.

(54) Beerepoot, M. T. P.; Friese, D. H.; Ruud, K. Intermolecular Charge Transfer Enhances Two-Photon Absorption in Yellow Fluorescent Protein. *Phys. Chem. Chem. Phys.* **2014**, *16*, 5958–5964. https://doi.org/10.1039/c3cp55205e.

(55) Sun, L.; Zhu, W.; Wang, W.; Yang, F.; Zhang, C.; Wang, S.; Zhang, X.; Li, R.; Dong, H.; Hu, W. Intermolecular Charge-Transfer Interactions Facilitate Two-Photon Absorption in Styrylpyridine–Tetracyanobenzene Cocrystals. *Angew. Chemie - Int. Ed.* **2017**, *56*, 7831–7835. https://doi.org/10.1002/anie.201703439.

(56) Wang, X.; Wang, D.; Li, J.; Zhang, M.; Song, P. Physical Mechanism of Photoinduced Charge Transfer in Oneand Two-Photon Absorption in d-d-π-a Systems. *Materials (Basel).* **2021**, *14*. https://doi.org/10.3390/ma14143925.

(57) Zhang, W.; Kong, J.; Hu, D.; Tao, M.; Niu, X.; Vdović, S.; Aumiler, D.; Ma, Y.; Xia, A. Solvation-Dependent Excited-State Dynamics of Donor-Acceptor Molecules with Hybridized

Local and Charge Transfer Character. *J. Phys. Chem. C* **2020**, *124*, 5574–5582. https://doi.org/10.1021/acs.jpcc.0c00003.

(58) Maffeis, V.; Brisse, R.; Labet, V.; Jousselme, B.; Gustavsson, T. Femtosecond Fluorescence Upconversion Study of a Naphthalimide-Bithiophene-Triphenylamine Push-Pull Dye in Solution. *J. Phys. Chem. A* **2018**, *122*, 5533–5544. https://doi.org/10.1021/acs.jpca.8b05177.

(59) Ishimatsu, R.; Matsunami, S.; Shizu, K.; Adachi, C.; Nakano, K.; Imato, T. Solvent Effect on Thermally Activated Delayed Fluorescence by 1,2,3,5-Tetrakis(Carbazol-9-Yl)-4,6-Dicyanobenzene. *J. Phys. Chem. A* **2013**, *117*, 5607–5612. https://doi.org/10.1021/jp404120s.

(60) Mataga, N.; Kaifu, Y.; Koizumi, M. Solvent Effects upon Fluorescence Spectra and the Dipolemoments of Excited Molecules. *Bull. Chem. Soc. Jpn.* **1956**, *29*, 465–470. https://doi.org/10.1246/bcsj.29.465.

(61) Haseyama, S.; Niwa, A.; Kobayashi, T.; Nagase, T.; Goushi, K.; Adachi, C.; Naito, H. Control of the Singlet–Triplet Energy Gap in a Thermally Activated Delayed Fluorescence Emitter by Using a Polar Host Matrix. *Nanoscale Res. Lett.* **2017**, *12*, 1–5. https://doi.org/10.1186/s11671-017-2012-1.

(62) Cotts, B. L.; McCarthy, D. G.; Noriega, R.; Penwell, S. B.; Delor, M.; Devore, D. D.; Mukhopadhyay, S.; De Vries, T. S.; Ginsberg, N. S. Tuning Thermally Activated Delayed Fluorescence Emitter Photophysics through Solvation in the Solid State. *ACS Energy Lett.* **2017**, *2* , 1526–1533. https://doi.org/10.1021/acsenergylett.7b00268.

(63) Abdel-Shafi, A. A.; Worrall, D. R. Mechanism of the Excited Singlet and Triplet States Quenching by Molecular Oxygen in Acetonitrile. *J. Photochem. Photobiol. A Chem.* **2005**, *172* , 170–179. https://doi.org/10.1016/j.jphotochem.2004.12.006.

(64) McGown, L. B.; Nithipahkom, K. Molecular Fluorescence and Phosphorescence. *Appl. Spectrosc. Rev.* **2000**, *35* , 353–393. https://doi.org/10.1081/ASR-100101229.

(65) Goushi, K.; Yoshida, K.; Sato, K.; Adachi, C. Organic Light-Emitting Diodes Employing Efficient Reverse Intersystem Crossing for Triplet-to-Singlet State Conversion. *Nat. Photonics* **2012**, *6* , 253–258. https://doi.org/10.1038/nphoton.2012.31.

(66) Lee, H. L.; Lee, K. H.; Lee, J. Y. Indoloindole as a New Building Block of a Hole Transport Type Host for Stable Operation in Phosphorescent Organic Light-Emitting Diodes. *J. Mater. Chem. C* **2019**, *7* , 5988–5994. https://doi.org/10.1039/c9tc00701f.

(67) Jung, M.; Lee, K. H.; Lee, J. Y. Molecular Engineering of Isomeric Benzofurocarbazole Donors for Photophysical Management of Thermally Activated Delayed Fluorescence Emitters. *Chem. - A Eur. J.* **2020**, *26* , 4816–4821. https://doi.org/10.1002/chem.201905473.

(68) Byeon, S. Y.; Kim, J.; Lee, D. R.; Han, S. H.; Forrest, S. R.; Lee, J. Y. Nearly 100% Horizontal Dipole Orientation and Upconversion Efficiency in Blue Thermally Activated Delayed Fluorescent Emitters. *Adv. Opt. Mater.* **2018**, *6* , 1–6. https://doi.org/10.1002/adom.201701340.

(69) Sun, J. W.; Kim, K. H.; Moon, C. K.; Lee, J. H.; Kim, J. J. Highly Efficient Sky-Blue Fluorescent Organic Light Emitting Diode Based on Mixed Cohost System for Thermally Activated Delayed Fluorescence Emitter (2CzPN). *ACS Appl. Mater. Interfaces* **2016**, *8* , 9806–9810. https://doi.org/10.1021/acsami.6b00286.

(70) Kang, J. S.; Hong, T. R.; Kim, H. J.; Son, Y. H.; Lampande, R.; Kang, B. Y.; Lee, C.; Bin, J. K.; Lee, B. S.; Yang, J. H.; Kim, J.; Park, S.; Cho, M. J.; Kwon, J. H.; Choi, D. H. High-Performance Bipolar Host Materials for Blue TADF Devices with Excellent External Quantum Efficiencies. *J. Mater. Chem. C* **2016**, *4* , 4512–4520. https://doi.org/10.1039/c6tc00385k.

3.8 Supporting Information

Figure 3.8.1. Linear traces of the emissive lifetime characterization results for Cbz-Trz, BTCbz-Trz, 2Cbz-PN, and BTCbz-PN in unpurged and purged toluene solutions.

Figure 3.8.2. Logarithmic traces of the emissive lifetimes of the emissive lifetime characterization results for Cbz-Trz, BTCbz-Trz, 2Cbz-PN, and BTCbz-PN in unpurged and purged toluene solutions. The inserts is from 0 – 200 ns.

Figure 3.8.3. Nanosecond transient absorption spectra of Cbz-Trz (top) and BTCbz-Trz (bottom) in purged toluene solutions. The inserts display the stimulated emission at 80 ns.

Figure 3.8.4. Nanosecond transient absorption spectra of 2Cbz-PN (top) and BTCbz-PN (bottom) in purged toluene. The inserts display the stimulated emission at 80 ns.

Figure 3.8.5. Kinetic absorption traces of the Trz-acceptor compounds at wavelengths thought to represent excited state absorption signal in purged toluene solutions.

Figure 3.8.6. Ground state bleach (top) and excited state absorption (bottom) decay profiles of 2Cbz-PN in unpurged (UP) and purged (P) toluene solutions. The red lines represent the mono-exponential decay fits.

Figure 3.8.7. Ground state bleach (top) and excited state absorption (bottom) decay profiles of BTCbz-PN in unpurged (UP) and purged (P) toluene solutions. The red lines represent the mono-exponential decay fits.

Table 3.8.1. The ground and excited singlet and triplet geometries dihedral angles for PN- and Trz-acceptor compounds.

Figure 3.8.8. The optimized ground state (from ωB97X-D) dihedral angels of Cbz-Trz, BTCbz-Trz, 2Cbz-PN, and BTCbz-PN.

Figure 3.8.9. Natural transition orbitals (from ωB97X-D) for charge transfer states of 2Cbz-PN, BTCbz-PN, Cbz-Trz, and BTCbz-Trz.

Figure 3.8.10. Energy level diagrams of BFCbz-Trz and BFCbz-PN.

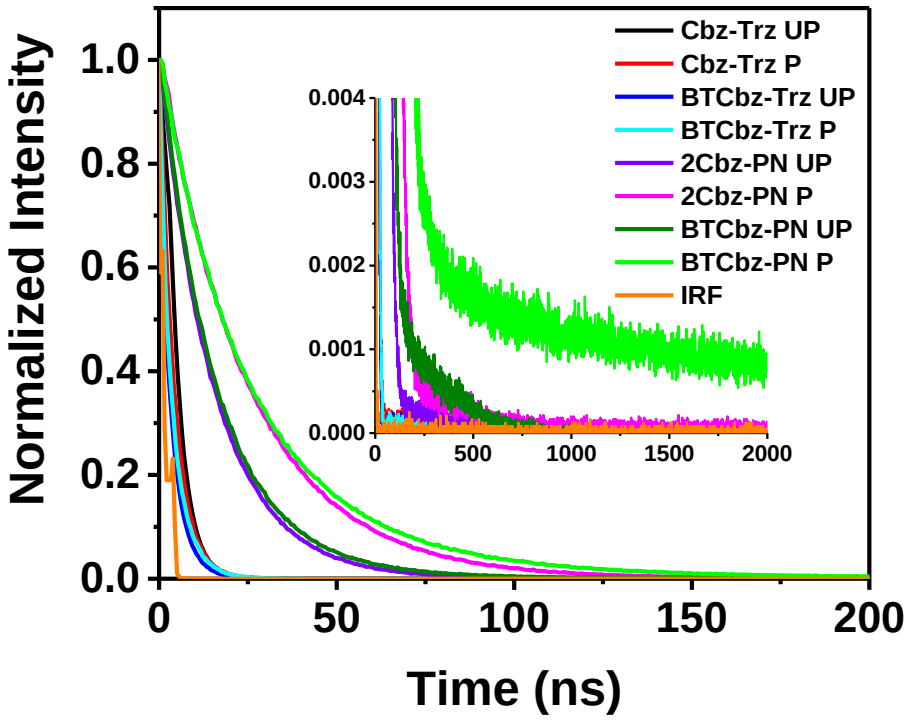


Figure 3.8.1. Emissive lifetime results of investigated compounds in toluene.

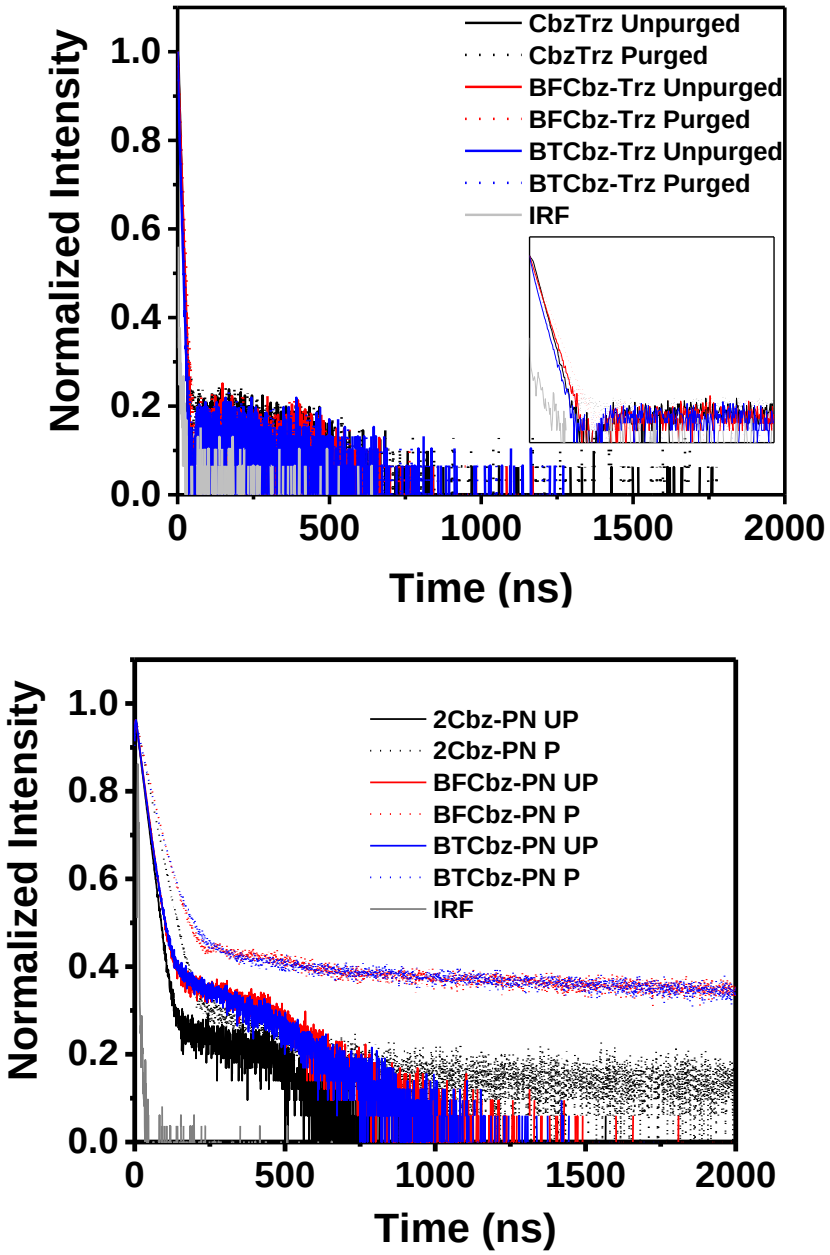


Figure 3.8.2. Logarithmic plots of emissive lifetime results of investigated compounds in toluene. Inset is from 0 – 200 ns.

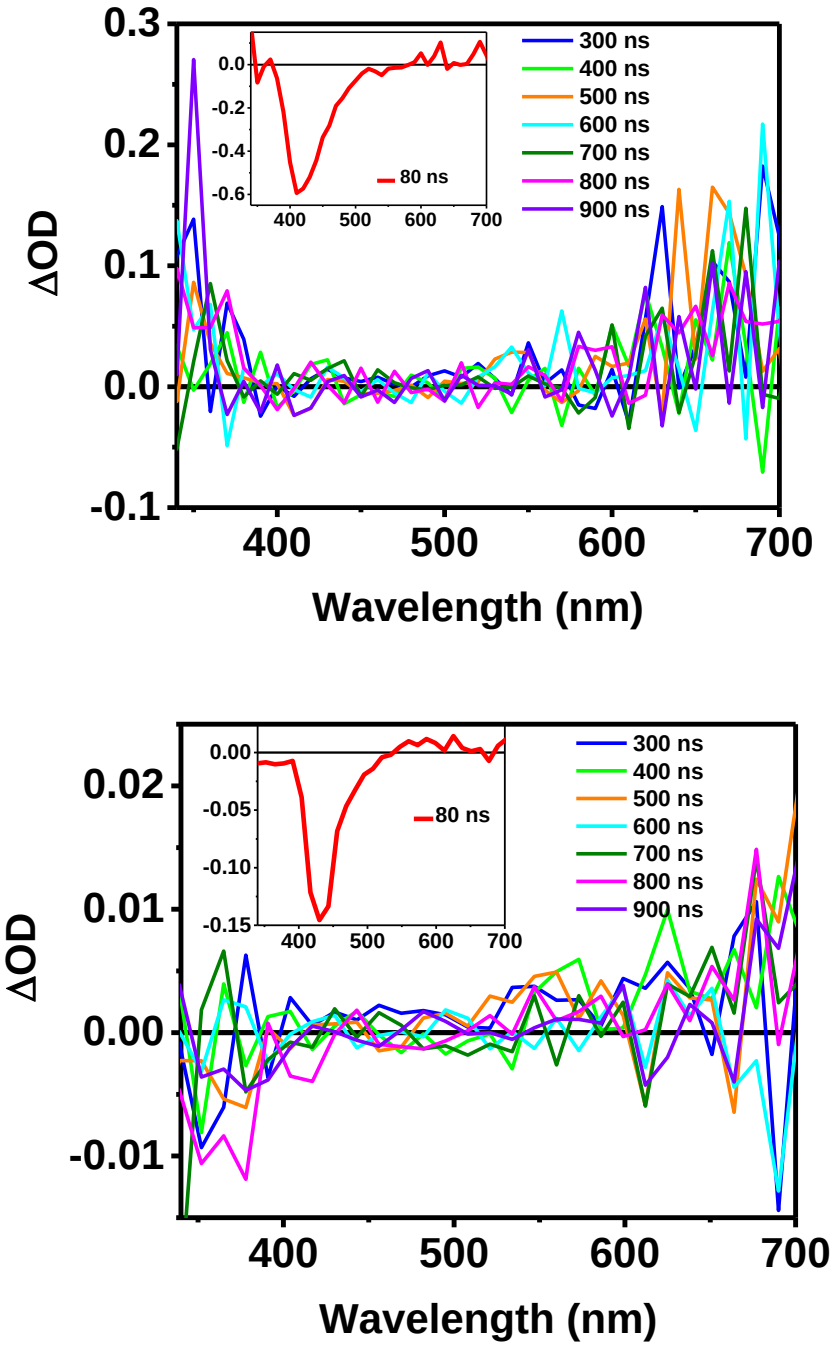


Figure 3.8.3. Nanosecond transient absorption spectra of Cbz-Trz (top) and BTCbz-PN (bottom) in purged toluene. The insets display the SE at 80 ns.

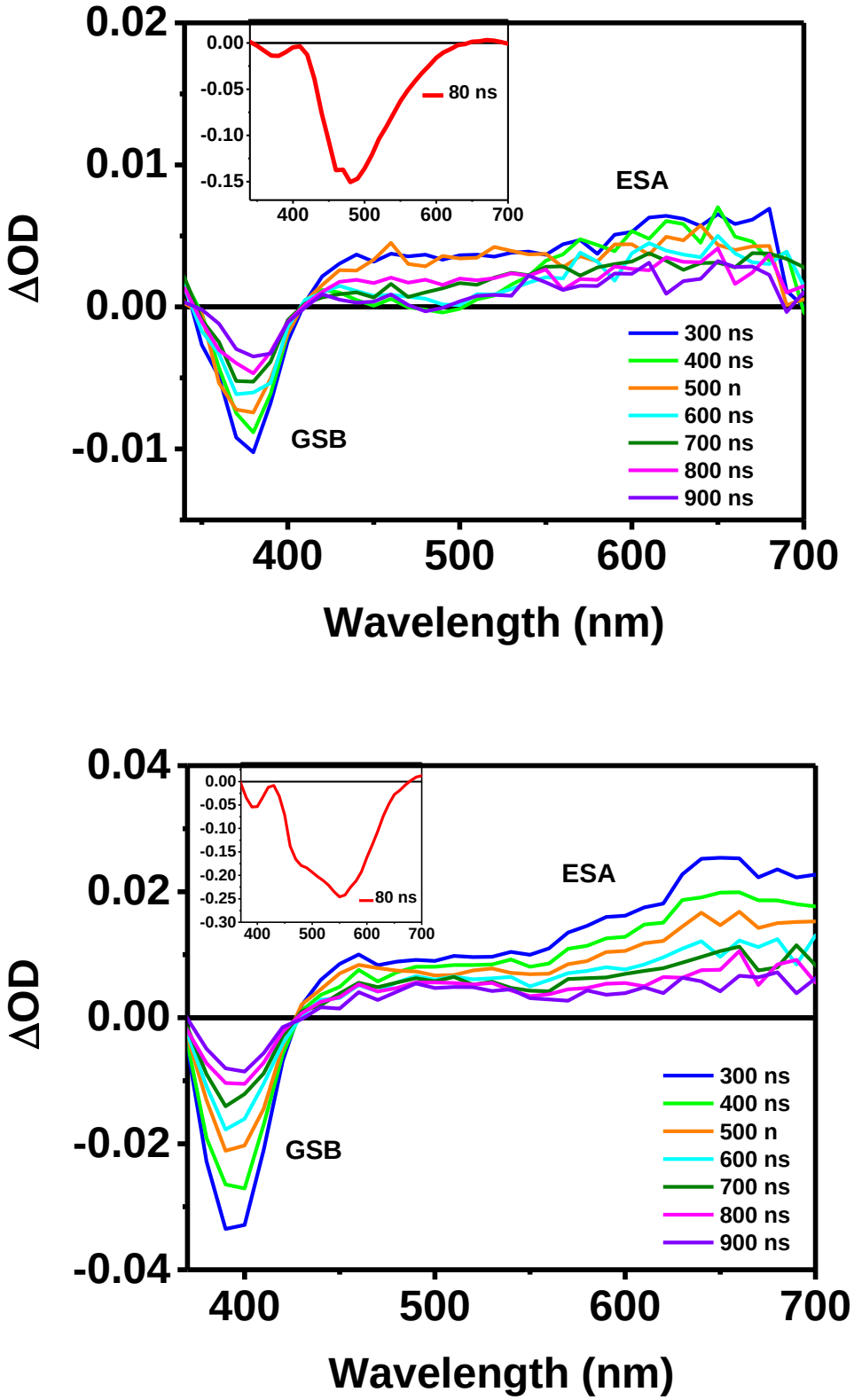
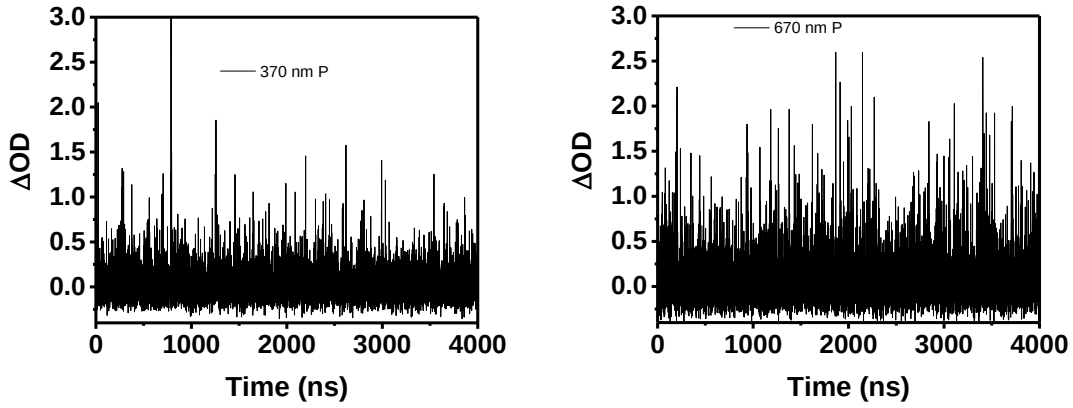
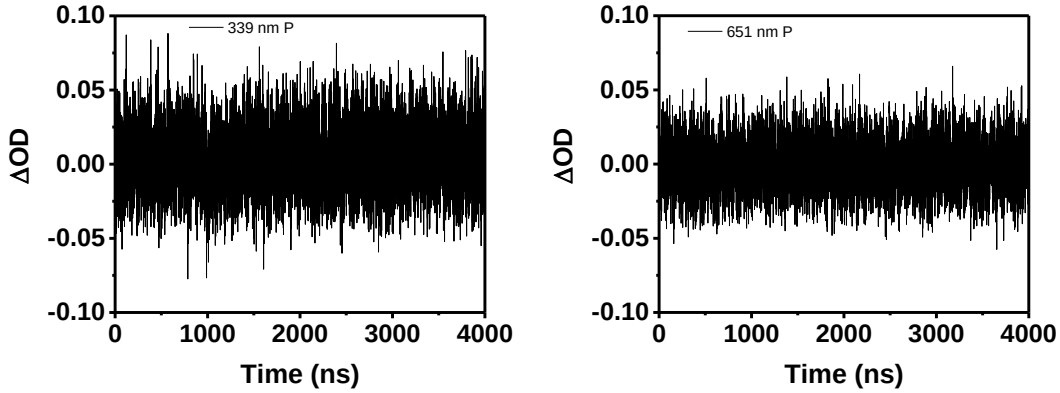


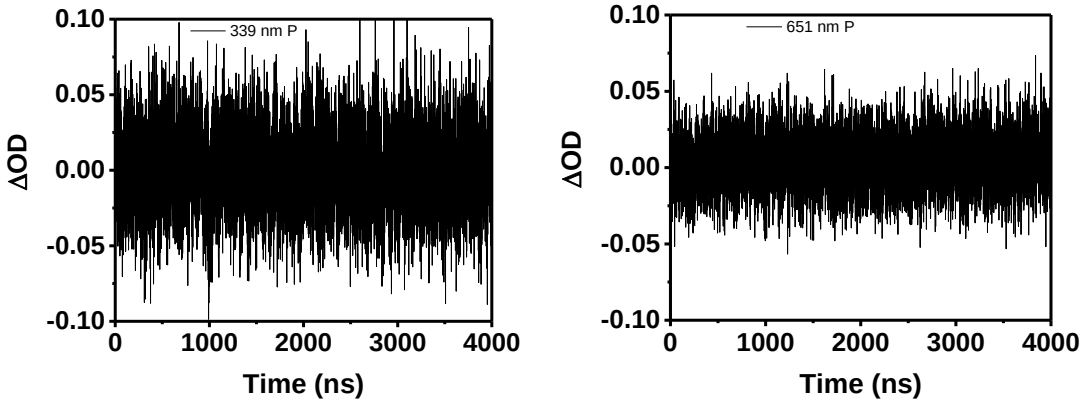
Figure 3.8.4. Nanosecond transient absorption spectra of 2Cbz-PN (top) and BTCbz-PN (bottom) in purged toluene. The insets display the SE at 80 ns.



<Cbz-Trz>



<BFCbz-Trz>



<BTCbz-Trz>

Figure 3.8.5. Kinetic traces of Trz-acceptor compounds taken at wavelengths thought to represent excited state absorption in purged toluene.

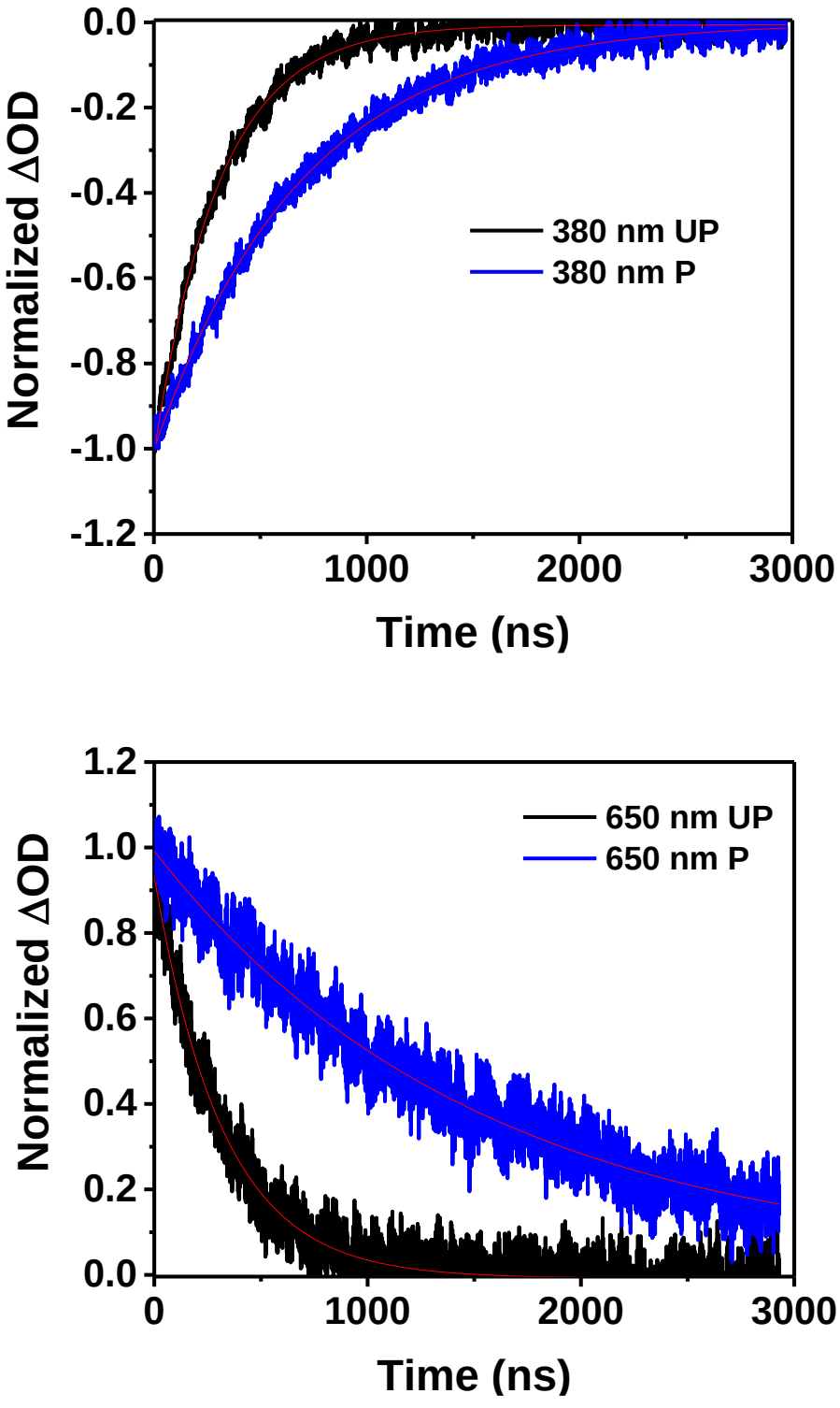


Figure 3.8.6. Ground state bleach (top) and excited state absorption (bottom) decays of 2Cbz-PN in unpurged and purged toluene. The red lines represent the mono-exponential decay fits.

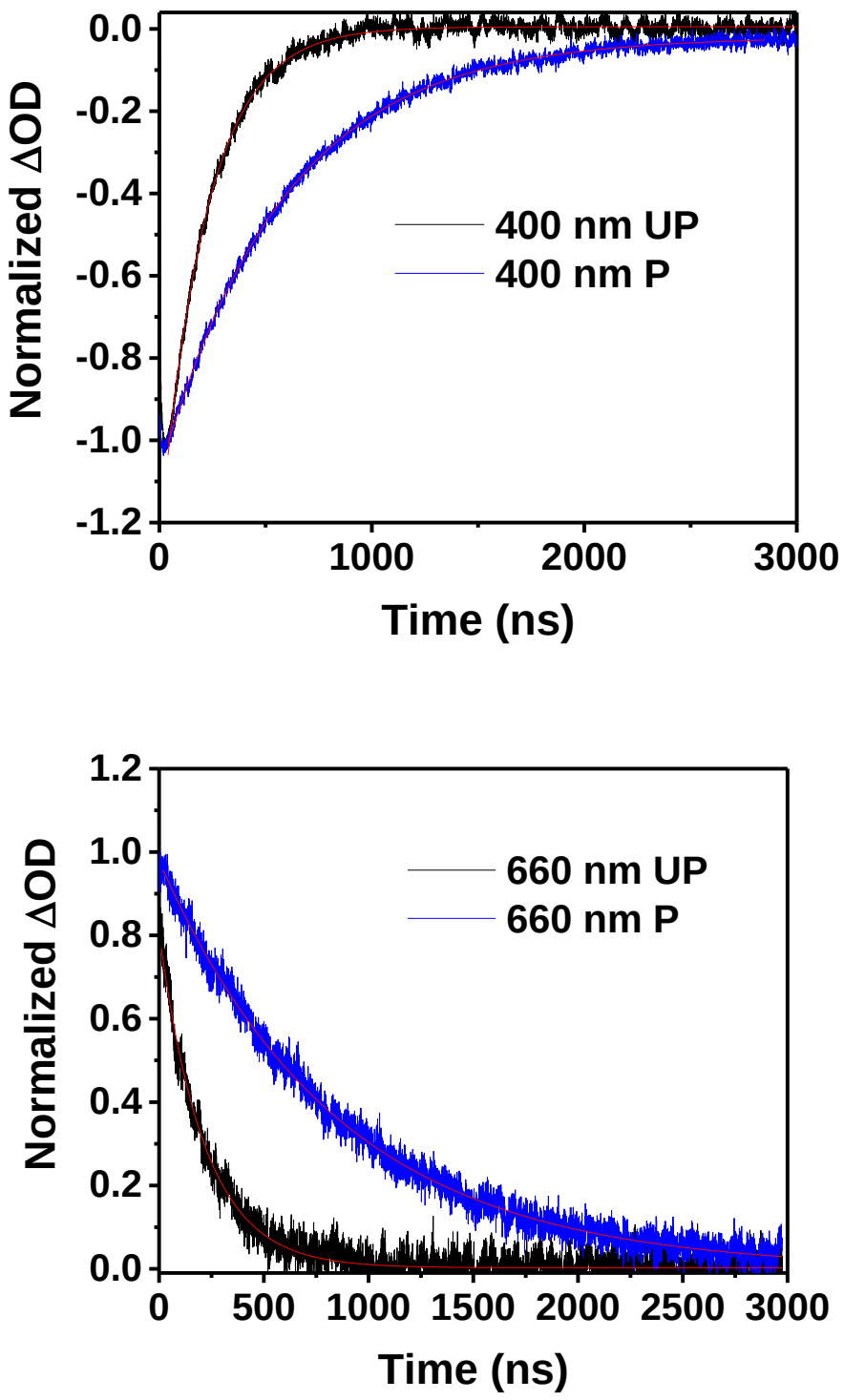


Figure 3.8.7. Ground state bleach (top) and excited state absorption (bottom) decays of BTCbz-PN in unpurged and purged toluene. The red lines represent the mono-exponential decay fits.

Excited Singlet State Dihedral Angles					
Compound	**Atoms**	**Torsion (°)**	**Compound**	**Atoms**	**Torsion (°)**
2Cbz-PN	C (r)-N (r)-C-C	75.1	Cbz-Trz	C (r)-N-C-C (r)	52.4
BTCbz-PN	C (r)-N-C-C	74.9	BTCbz-Trz	C-N-C-C (r) (S)	49.0
BFCbz-PN	C (r)-N-C-C	74.7	BFCbz-Trz	C-N-C-C (r) (O)	49.3
Excited Triplet State Dihedral Angles					
Compound	**Atoms**	**Torsion (°)**	**Compound**	**Atoms**	**Torsion (°)**
2Cbz-PN	C (r)-N (r)-C-C	45.1	Cbz-Trz	C (r)-N-C-C (r)	88.1
BTCbz-PN	C (r)-N-C-C	45.5	BTCbz-Trz	C-N-C-C (r) (S)	44.0
BFCbz-PN	C (r)-N-C-C	45.7	BFCbz-Trz	C-N-C-C (r) (O)	43.6

Table 3.8.1 Ground and Excited Singlet and Triplet Geometries Dihedral Angles for PN's and Trz's.

Quantum Chemical Calculations Experimental Details.

Description of formulas used to calculate the energy gap and reverse intersystem crossing rate. In addition, the explanation for choosing one functional exchange versus to another.

The adiabatic energy gap between excited singlet and triplet states (ΔE_{ST}) was calculated using the following formula:

$$\Delta E_{ST} = [E(S_1)] - [E(T_1)] \quad \textbf{Eqn. 3.8.1}$$

where, E_A is the adiabatic energies from optimized ground state (S_0), excited singlet state (S_1) and triplet state (T_1).

The reverse intersystem crossing rate (k_{rISC}) was calculated using:

$$k_{rISC} = \frac{2\pi}{\hbar} |V_{SOC}|^2 x \rho_{FCWD}^{SCMT} \qquad \textbf{Eqn. 3.8.2}$$

where, ρ_{FCWD}^{SCMT} , was the density of states based on semi-classical Marcus theory Frank-Condon weighted density:

$$\rho_{FCWD}^{SCMT} = \frac{1}{\sqrt{4\pi\lambda_s k_B T}} exp\left(\frac{(\Delta E_{ST}+\lambda_s)^2}{4\lambda k_B T}\right) \quad \textbf{Eqn. 3.8.3}$$

and spin orbit coupling constant (V_{SOC}) was calculated from the excited triplet geometry:[1,2]

$$|V_{SOC}|^2 = \frac{1}{3} \left|\langle S_{1n}|\widehat{H_{SOC}}|T_{1n}\rangle\right|^2 \qquad \textbf{Eqn. 3.8.4}$$

and singlet reorganization energy (λ_s) was the difference in energy between the excited singlet states from the excited triplet ($E_{Sn}(T_1)$) and singlet ($E_{Sn}(S_1)$) optimized geometries:

$$\lambda_s = E_{Sn}(T_1) - E_{Sn}(S_1) \qquad \textbf{Eqn. 3.8.5}$$

Based on the experimental steady-state absorption and emission measurements, the single-point energy results from functional exchange ωB97X-D are more in agreement compared to B3LYP. Specifically, the ωB97X-D singlet-point energy results from the ground to excited singlet states (S_0 -> S_n) of PN- and Trz-acceptor compounds shows similar trends as the absorption spectra. In addition, the calculated k_{rISC} showed the same trends as the experimental k_{rISC} derived from using the nsTAS technique. The calculated k_{rISC} from B3LYP functional exchange are comparable to other computational calculated k_{rISC}.[3] However, the k_{rISC} of B3LYP functional exchange do not follow the same trend as the experimental k_{rISC}. Since the ωB97X-D results are more in agreement to experimental results, for this paper all computational results are based on ωB97X-D functional exchange.

References

(1) Samanta, P. K.; Kim, D.; Coropceanu, V.; Brédas, J. L. Up-Conversion Intersystem Crossing Rates in Organic Emitters for Thermally Activated Delayed Fluorescence: Impact of the Nature of Singlet vs Triplet Excited States. *J. Am. Chem. Soc.* **2017**, *139* (11), 4042–4051.

(2) Beljonne, D.; Shuai, Z.; Pourtois, G.; Bredas, J. L. Spin-Orbit Coupling and Intersystem Crossing in Conjugated Polymers: A Configuration Interaction Description. *J. Phys. Chem. A* **2001**, *105* (15), 3899–3907.

(3) Zhu, Q.; Guo, X.; Zhang, J. Theoretical Study on Photophysical Properties of a Series of Functional Pyrimidine-Based Organic Light-Emitting Diodes Emitters Presenting Thermally Activated Delayed Fluorescence. *J. Comput. Chem.* **2019**, *40* (16), 1578–1585.

Chapter 4: Investigating the Opto-Electronic Properties of Carbazole-Substituted Benzobisoxazoles for Organic Light-Emitting Diodes

4.1 Original Publication Information and Author Contribution

Portions of this chapter are taken from the manuscript that was submitted for publication to *Journal of Materials Chemistry C* entitled:

"Carbazole-Substituted Benzobisoxazoles: Near-UV Fluorescent Emitters and Ambipolar Hosts for Organic Light-Emitting Diodes" David L. Wheeler, Lloyd Fisher, Jr., Pascal Friederich, Angelar K. Muthike, Alán Aspuru-Guzik, Theodore Goodson III, and Malika Jeffries-EL.

The manuscript is under review, so some changes may be made before publication and the final manuscript may have more or less content than what is presented in this dissertation. My contribution to this work was determining the quantum yields of the investigated chromophores, performing the nanosecond transient absorption spectroscopy measurements, and aiding in writing and data analysis. These experiments were critical for evaluating the TADF capabilities of the investigated systems by observing the excited state dynamics and assigning them to either the TADF mechanism or another emissive pathway.

4.2 Abstract

This study investigates the use of benzobisoxazole-based (BBO) materials with a donor-acceptor-donor structure towards the production of materials with thermally-activated delayed fluorescent (TADF) properties for use in organic light emitting diodes (OLED). Using computation methods (DFT/TD-DFT) as a guiding tool, six BBO-based materials were designed by changing

the conjugation position of carbazole-substituted phenyl substituents and the type of BBO isomer (*cis*- vs. *trans*-). Experimental steady-state and transient absorption spectroscopic techniques were utilized to probe the TADF activity of these molecules. Each material was then applied to functional OLED devices as either near-UV dopants or host with low singlet-triplet energy differences. The electroluminescent properties show that materials used as dopant provide near-UV emission ($CIE_y < 0.06$ and $CIE_x = 0.16$) while the BBO employed as hosts show reduced operating voltages and increased performance efficiencies when compared to commercial materials

4.3 Introduction

In recent years, there has been a renewed interest in organic light emitting diodes (OLED)s due to their potential for the development of next-generation devices such as flexible displays,[1] wearables[2] and solid-state lighting.[3] OLEDs have several advantages over conventional inorganic LEDs including the ability to fabricate them onto either rigid or flexible substrates, to accommodate irregular surfaces. They can also be fabricated almost entirely from solution-processing techniques, eliminating the need for energy-intensive fabrication methods such as thermal evaporation. OLEDs can also be used to make lightweight displays since they do not require backlighting.

Purely organic luminophores are promising because, these molecular or polymeric organic semiconductors (OSC)s can be modified through synthesis to produce materials with optical and electronic properties tailored for targeted applications.[4] OSCs also eliminate the need for toxic, expensive noble metals. However, achieving deep blue emission within the industry standards for color purity: National Television System Committee (NTSC) (CIE: 0.14, 0.08) and European Broadcasting Union (EBU) (CIE: 0.15,

0.06) using a purely organic emitter is challenging.[5] Further, since fluorescence OLEDs utilize singlet emission, the theoretical maximum internal quantum efficiencies (IQE) based on these materials is limited to 25% because the ratio of singlets and triplet generated under electroluminescent conditions is 1:3.[6] One solution to overcoming the theoretical limit for fluorescence is through the design of emitters that exhibit thermally activated delayed fluorescence (TADF).[7] Such materials can theoretically achieve an IQE of 100% through a process known as reverse intersystem crossing (rISC). This process converts non-emissive excited triplet (T_1) excitons to the emissive excited singlet state (S_1), albeit at a lower rate than intersystem crossing ($S_1 \square T_1$). By engineering materials with charge-transfer (CT) character, one can reduce the energetic difference between the S_1 and T_1 states (ΔE_{ST}), increasing the rate of rISC (k_{risc}) and induce TADF character.[8] This is typically accomplished by spatially separating the highest occupied molecular orbital (HOMO) and lowest unoccupied molecular orbital (LUMO).[9]

Tunable OSCs have been developed based on the benzo[1,2-*d*:4,5-*d*']bisoxazole (BBO) ring system, displayed in **Figure 4.3.1**. This electron-deficient heterocycle can readily be substituted with various aryl substituents in two ways: through the oxazole rings (2,6-axis) and/or the central benzene ring (4,8-axis). As a result, the BBO moiety can be used as a platform, to design a multitude of compounds with varying opto-electronic properties, using simple, scalable synthons.[10-13] Moreover, many aryl-substituted BBOs are highly fluorescent materials that are stable under normal atmosphere and at high temperatures, making them ideal candidates for OLEDs.[14: 15] Lastly, many aryl-BBOs possess spatially segregated frontier molecular orbitals (FMO)s, which is favorable to achieving a small $\Delta E_{ST.}$[13: 16] Previously, we reported a series of small-molecule BBO dopants which were

used in host-guest OLEDs which exhibited deep-blue EL ($^{EL}\lambda_{max} \approx 440$ nm; $CIE_y < 0.10$), but with external quantum efficiencies (EQE)s less than 3%.[14] The low efficiency of the devices was attributed in part to the traditional fluorophore character of the BBO dopants where ~75% of the excitons created were lost to various non-radiative pathways. Recently, we examined how steric hindrance impacts the opto-electronic properties of a series of aryl-substituted BBOs.[12] While theoretical predictions demonstrated that a considerable amount of overlap was observed between the HOMO and LUMO, materials did show potential for usage as for blue host and emissive materials.

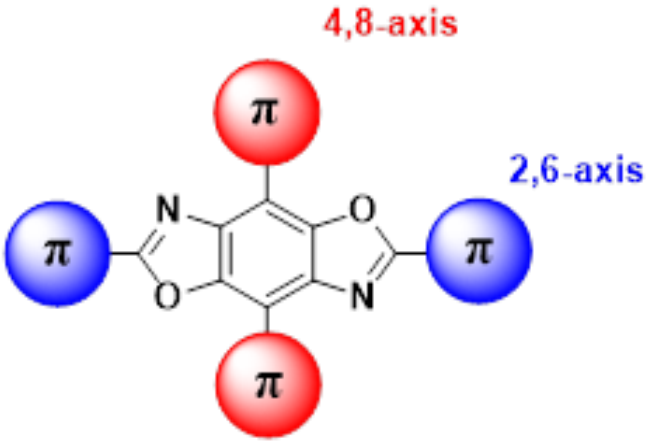


Figure 4.3.1. General structure of the BBO core. Conjugation can take part at the 2 and 6 positions (axis) or the 4,8 axis.

In this work, we seek to develop BBO based TADF emitters by functionalizing the BBO core with electron-rich carbazole pendants. Carbazole was selected as a substituent because of its high triplet energy and good hole-transporting abilities.[17] Accordingly, a series of six BBOs were produced with a donor-acceptor-donor (DAD) structure to help reduce the ΔE_{ST}. Of the six systems, **c**ompounds **C1**, **C3**, and **C5** bore BBO cores with 4-(*N*-carbazol-9-yl)phenyl- substituents while **C2**, **C4**, and **C6** contained 3,5-di(*N*-carbazol-9-yl)phenyl

groups. Herein, we report the synthesis of this novel BBO series and the corresponding computational and experimental findings. While none of the materials were deemed TADF-active, based on experimental results, each material was able to be employed into active OLED devices functioning as either fluorescent dopants or ambipolar hosts and are promising precursors to designing BBO-based TADF emitters.

4.4 Experimental Methods

4.4.1 Computational Methodology

We generated initial 3D structures from SMILES[25] codes using the molconvert tool from ChemAxon. We then used the GFN-xTB[26] based conformer search algorithm CREST[27] to find the lowest energy conformers of all molecules. DFT based analysis of the molecules was done using the procedure described in Gómez-Bombarelli et al.[28]The optimized geometry of the lowest energy conformers was obtained from CREST on a B3-LYP/6-31G* level of theory[27: 29] in gas phase and performed TDDFT calculations on the same level of theory to obtain HOMO and LUMO levels, permanent dipole moments, S_1 and T1 excitation energies as well as S_0 to S_1 transition dipole moments and oscillator strengths. We computed the TADF rates according to Equation (1) given in Gómez-Bombarelli et al.[28], which depends on the S_1 excitation energy, the S_1-T_1 gap and the oscillator strength for the S_0 to S_1 transition. We used n = 1 to be consistent with the data reported in Gómez-Bombarelli et al.[28] Using a more realistic n would not change the trends. All DFT calculations were done using the QChem package version 5.1.[30]

4.4.2 Materials and Characterization

4,8-dibromo-2,6-diethylbenzobisoxazole,[11]2,5-diaminohyroquinone ishydrochloride,[31] and 4,6-dinitroresorcinol[32] were synthesized according to literature procedures. THF was

dried using an Innovative Technologies solvent purification system. All other chemical reagents were purchased from commercial sources and used without further purification unless otherwise noted. Nuclear magnetic resonance (NMR) experiments were carried out in $CDCl_3$ at 500 MHz (^1H) AND 125 MHZ (^{13}C). In all spectra, chemical shifts are given in δ relative to residual protonated solvent peak, $CHCl_3$ (7.26 ppm, ^1H; 77.16 ppm, ^{13}C). Coupling constants are reported in hertz (Hz). High-resolution mass spectra were recorded on a double-focusing magnetic sector mass spectrometer using ESI. All UV-Vis and fluorescence spectra were obtained using quartz cuvettes with a 10 mm path length in $CHCl_3$ or as spin-casted thin films on a quartz slide (filtered 5 mg/mL solution in $CHCl_3$ spun at 1500 RPM). UV−vis spectra were collected on a Shimadzu UV-1800 UV spectrophotometer. Photoluminescence spectra were obtained on a Varian Cary Eclipse spectrophotometer. Absolute solution fluorescence quantum yields were obtained using a HORIBA spectrophotometer Nanolog FL3-2iHR equipped with a Quanta-phi integrating sphere. Ultraviolet photoelectron spectroscopy (UPS) was used to acquire the ionization potentials and approximate the HOMO values for each material. All substrates (positively doped silicon; 10 × 10 mm^2) had 40 nm of silver deposited via thermal evaporation. Samples were prepared by dissolution in $CHCl_3$ at a concentration of 5 mg/mL and stirred for a minimum of 4 h. Each solution was filtered to remove potential aggregates and sequentially spin-coated under a nitrogen atmosphere. Spectra were then acquired under ultrahigh vacuum at random positions on the formed film. The fluorescence quantum yields (φ) of the investigated compounds were calculated using the Williams comparative method.1 A series of increasingly dilute solutions, with optical density starting at 0.10, were utilized for the calculations. The quantum yields were calculated using **Eqn. 4.4.2.1**:[33]

$$\Phi=\Phi_{STD}\ (Grad_x\ \eta_x^2)/(Grad_{STD}\ \eta_{STD}^2)$$

Eqn. 4.4.2.1

Where Φ is the calculated quantum yield, η is the refractive index of the solvent, and $Grad$ is the slope obtained from plotting the integrated fluorescence area vs the optical density. The subscripts STD and x refer to the standard and investigated compound, respectively. Anthracene in cyclohexane was used as the standard for these calculations.2[34] The method for obtaining oxygen-free φ was to purge oxygen from the solutions via nitrogen bubbling for ten minutes. The decay lifetimes of transient states were investigated via the nanosecond transient absorption (nsTAS) technique.[18: 19]3,4 A LP980 (Edinburgh) transient system was coupled with a Spectra-Physics QuantaRay Nd:YAG nanosecond puled laser and a GWU Optical Parametric Oscillator tunable from 206 – 2600 nm for the excitation beam. For our purposes, the excitation beam was set to each sample's respective absorption maximum. A pulsed broadband xenon lamp beam was used to probe the excited states. These measurements were conducted in both oxygen rich and oxygen free solutions. The rate of reverse intersystem crossing (krISC) were calculated using **Eqn. 4.4.2.2**[19]

$$k_{rISC} = k_{ESA} * \Phi_{TADF}$$

Eqn. 4.4.2.2

Where k_{ESA} is the decay rate of the triplet state and φ_{TADF} is the difference between purged and unpurged φ.

4.4.3 Synthesis of Precursors

To a flask equipped with condenser and stir-bar was added an appropriate amount of 9*H*-carbazole (1 mmol eq. for mono-fluorinated substrates, 2 mmol eq. for di-fluorinated

substrates). The solid was dissolved in DMF to make a 1M solution followed by the addition of an equivalent mmol amount of potassium *tert*-butoxide. This solution was brought to 60 ^{o}C under normal atmospheric conditions before the dropwise addition of the fluorinated benzonitrile or bromobenzene derivative. The solution was brought to reflux allowed to stir for a maximum of 24 hours. After cooling to room temperature, the reaction mixture was added to distilled water and stirred for 30 minutes before filtering the newly formed solid. For compounds **1** and **2**, the solid was dissolved in DCM, washed twice with distilled water, dried over Na_2SO_4, concentrated onto silica gel and purified by column chromatography (hex:DCM gradient). For compounds **3** and **4**, the solid was stirred in hot methanol, cooled to -20 ^{o}C and filtered to give the final product. Below are the following yields:

9-(4-bromophenyl)-9*H*-carbazole (1)

White solid. (86%). ^{1}H NMR (500 MHz, $CDCl_3$) δ 8.15 (d, J = 7.8 Hz, 2H), 7.74 (d, J = 8.6 Hz, 2H), 7.49 – 7.37 (m, 6H), 7.35 – 7.28 (dd, J = 8.0, 8.0 Hz, 2H).

9,9'-(5-bromo-1,3-phenylene)bis(9H-carbazole) (2*)*

White solid. (65%). ^{1}H NMR (500 MHz, $CDCl_3$) δ 8.16 (d, *J* = 7.8 Hz, 4H), 7.87 (d, *J* = 1.9 Hz, 2H), 7.80 (t, *J* = 1.9 Hz, 1H), 7.56 (d, *J* = 8.2 Hz, 4H), 7.51 – 7.44 (dd, *J* = 7.7, 1.2 Hz, 4H), 7.34 (t, *J* = 7.4 Hz, 4H).

4-(9*H*-carbazol-9-yl)benzonitrile (3)

White solid. (78%). ^{1}H NMR (500 MHz, $CDCl_3$) δ 8.17 (dt, *J* = 7.8, 1.0 Hz, 2H), 7.89 – 7.86 (m, 2H), 7.72 – 7.68 (m, 2H), 7.48 – 7.45 (m, 4H), 7.37 (ddd, *J* = 8.0, 5.1, 3.0 Hz, 2H).

3,5-di(9*H*-carbazol-9-yl)benzonitrile (4)

White solid. (71%). ^{1}H NMR (500 MHz, $CDCl_3$) δ 8.16 (d, *J* = 7.9 Hz, 4H), 8.07 (t, *J* = 2.0 Hz, 1H), 7.97 (d, *J* = 1.8 Hz, 2H), 7.56 – 7.48 (m, 8H), 7.38 (td, *J* = 7.4, 6.9, 1.4 Hz, 4H).

General procedure for boronic ester formation

To an oven-dried, N_2 filled flask was added approximately 40 mL of anhydrous THF and 8 mmol of corresponding bromobenzene derivative. This solution was cooled to -78 ºC before the dropwise addition of 9.6 mmol of 2.5 M *n*-butyllithium. The organolithium species was allowed to stir at for 1 hour at before the dropwise addition of 12 mmol of 2-Isopropoxy-4,4,5,5-tetramethyl-1,3,2-dioxaborolane. The solution was allowed to come to room temperature for overnight stirring. Afterwards, 40 mL of distilled water and diethyl ether were added to the flask. The aqueous layer was separated, and the organic layer was then washed twice with distilled water, dried over Na_2SO_4, and concentrated onto silica gel. Column chromatography (hexanes: ethyl acetate gradient) was used to separate the product from impurities producing the following yields:

9-(4-(4,4,5,5-tetramethyl-1,3,2-dioxaborolan-2-yl)phenyl)-9*H*-carbazole (5)

Yellow viscous liquid (79%). ^{1}H NMR (500 MHz, $CDCl_3$) δ 8.16 (d, *J* = 7.7 Hz, 2H), 8.08 (d, *J* = 8.1 Hz, 2H), 7.62 (d, *J* = 8.2 Hz, 2H), 7.47 (d, *J* = 8.2 Hz, 2H), 7.42 (t, *J* = 7.6 Hz, 2H), 7.30 (t, *J* = 7.2 Hz, 2H), 1.42 (s, 12H).

9,9'-(5-(4,4,5,5-tetramethyl-1,3,2-dioxaborolan-2-yl)-1,3-phenylene)bis(9*H*-carbazole) (6)

White solid. (60%). ^{1}H NMR (500 MHz, $CDCl_3$) δ 8.16 (d, *J* = 7.8 Hz, 4H), 8.13 (d, *J* = 2.1 Hz, 2H), 7.89 (t, *J* = 2.1 Hz, 1H), 7.52 (d, *J* = 8.2 Hz, 4H), 7.46 (ddd, *J* = 8.2, 7.1, 1.2 Hz, 4H), 7.32 (ddd, *J* = 7.5, 1.1 Hz, 4H), 1.38 (s, 12H).

General hydrolysis procedure

To a flask equipped with a stir-bar and condenser was added 10 mmol of benzonitrile. This solid was then suspended in 20 mL of 6 M NaOH and 20 mL of reagent grade ethanol and brought to reflux for overnight stirring. After cooling to room temperature, the reaction slurry was poured into cold 6M HCl (excess) and stirred for 2 hours at room temperature. The solid was filtered and washed with 25 mL of cold water and 50 mL of cold methanol and allowed to dry under vacuum producing the following yields:

4-(9H-carbazol-9-yl)benzoic acid (7)

White solid. (95%). ^{1}H NMR (500 MHz, $CDCl_3$) δ 8.40 (d, *J* = 8.1 Hz, 2H), 8.16 (d, *J* = 7.8 Hz, 2H), 7.76 (d, *J* = 8.1 Hz, 2H), 7.53 (d, *J* = 8.2 Hz, 2H), 7.45 (t, *J* = 7.7 Hz, 2H), 7.34 (t, *J* = 7.4 Hz, 2H).

3,5-di(9H-carbazol-9-yl)benzoic acid (8)

White solid. (89%). ^{1}H NMR (500 MHz, $CDCl_3$) δ 8.46 (d, *J* = 2.0 Hz, 2H), 8.17 (d, *J* = 7.7 Hz, 4H), 8.11 (t, *J* = 2.0 Hz, 1H), 7.55 (d, *J* = 8.2 Hz, 4H), 7.47 (t, *J* = 7.7 Hz, 4H), 7.38 – 7.31 (t, *J* = 7.8 Hz, 4H).

General procedure for formation of C1 and C2

This precursor was prepared similar to literature procedures.[35] The general procedure is as follows: 0.2 mmol of 4,8-dibromo-2,6-diethylbenzobisoxazole was added to a 75-mL

pressure flask along with 5% mol equivalent PEPPSI-*i*Pr and 0.5 mmol of **5** or **6** and. To the same flask was added 1.3 mmol of cesium fluoride. These contents were dissolved in 10 mL of THF and degassed for 15 minutes. Afterwards, the flask was sealed and heated to 130 ^{o}C for 12 hours. After cooling to room temperature, the crude solution was diluted with DCM and concentrated onto silica gel for solid-loaded column chromatography using hexanes:$CHCl_3$ as the eluent to produce pure products.

4,8-bis(4-(9*H*-carbazol-9-yl)phenyl)-2,6-diethylbenzo[1,2-d:4,5-d']bis(oxazole) (C1)

Pale-green solid (60%). M.P > 240 ^{o}C. ^{1}H NMR (500 MHz, $CDCl_3$) δ 8.59 (d, *J* = 8.5 Hz, 4H), 8.19 (d, *J* = 7.7 Hz, 4H), 7.82 (d, *J* = 8.5 Hz, 4H), 7.62 (d, *J* = 8.2 Hz, 4H), 7.47 (ddd, *J* = 8.2, 7.1, 1.2 Hz, 4H), 7.33 (ddd, J = 7.9, 7.0, 1.0 Hz, 4H), 3.15 (q, *J* = 7.6 Hz, 4H), 1.58 (t, *J* = 7.6 Hz, 6H). ^{13}C NMR (126 MHz, $CDCl_3$) δ 169.18, 146.24, 140.77, 137.51, 137.17, 131.55, 131.52, 127.00, 126.00, 123.52, 120.33, 120.08, 113.32, 110.04, 77.26, 77.00, 76.75, 22.69, 11.37. HRMS (ESI) m/z: $[M+H]^+$ calcd for $C_{48}H_{35}N_4O_2$: 699.2760; found: 699.2778.

4,8-bis(3,5-di(9*H*-carbazol-9-yl)phenyl)-2,6-diethylbenzo[1,2-d:4,5-d']bis(oxazole) (C2)

Off-white solid. (37%). M.P > 240 ^{o}C. ^{1}H NMR (500 MHz, $CDCl_3$) δ 8.64 (s, 4H), 8.19 (d, *J* = 7.7 Hz, 8H), 7.96 (s, 2H), 7.87 (d, *J* = 8.3 Hz, 8H), 7.49 (t, *J* = 7.7 Hz, 8H), 7.34 (t, *J* = 7.5 Hz, 8H), 3.11 (q, *J* = 7.7 Hz, 4H), 1.58 (t, *J* = 7.6 Hz, 6H). ^{13}C NMR unable to be obtained. HRMS (ESI) m/z: $[M+H]^+$ calcd for $C_{72}H_{49}N_6O_2$: 1029.3917; found: 1029.3954.

General procedure for the synthesis of C3 – C6

To an oven-dried round bottom flask containing a stir-bar was added 1.00 g of P_2O_5. The flask was fitted with a condenser and purged with nitrogen three times followed by the

addition of 4 mL of *o*-dichlorobenzene and 2.1 mL of hexamethyldisiloxane. These reagents were brought to reflux and stirred for 2 hours. To solution was cooled to appx. 80 ^{o}C. Next, 1.5 mmol of **7** or **8** and 0.5 mmol of DAHQ · 2HCl were added quickly and simultaneous and the solution was heated to 190 ^{o}C for 2 days of stirring. Afterwards, the solution was cooled to room temperature and precipitated by pouring the mixture into methanol at -78 ^{o}C and filtered. The small molecules were purified according to methods A or methods B. Below, each molecules purification method is specified along with corresponding yields and characterization.

Method A – Compounds were passed through a hexanes:$CHCl_3$ plug. The solvent was removed, and crude material was then dissolved in $CHCl_3$ and decolorised with minimal activated charcoal. Filtering off the charcoal, the filtrate was then concentrated onto silica gel for purification via column chromatography (hex:$CHCl_3$ gradient).

Method B – Compounds were recrystallized twice in toluene using decolorizing carbon to remove black color. After filtering, the solid was spun in ample amounts of hot $CHCl_3$ and filtered three times.

2,6-bis(4-(9H-carbazol-9-yl)phenyl)benzo[1,2-d:4,5-d']bis(oxazole) (C3)

Method A; pale green solid (28%). M.P > 240 ^{o}C. ^{1}H NMR (500 MHz, $CDCl_3$) δ 8.54 (d, J = 8.5 Hz, 4H), 8.17 (d, *J* = 7.8 Hz, 4H), 8.02 (s, 2H), 7.81 (d, *J* = 8.5 Hz, 4H), 7.54 (d, *J* = 8.2 Hz, 4H), 7.46 (ddd, *J* = 8.2, 7.0, 1.3 Hz, 4H), 7.37 – 7.32 (ddd, *J* = 7.8, 6.8, 1.0 Hz, 4H). ^{13}C NMR (126 MHz, $CDCl_3$) δ 163.63, 148.78, 140.96, 140.67, 140.31, 129.27, 127.12, 126.21, 125.51, 123.82, 120.57, 120.47, 109.79, 101.14. HRMS (ESI) m/z: $[M+H]^+$ calcd for $C_{44}H_{27}N_4O_2$: 643.2134; found: 643.2139.

2,6-bis(3,5-di(9H-carbazol-9-yl)phenyl)benzo[1,2-d:4,5-d']bis(oxazole) (C4)

Method B; grey solid (29%). M.P > 240 °C. ^{1}H NMR (500 MHz, $CDCl_3$) δ 8.63 (s, 4H), 8.18 (d, *J* = 8.0 Hz, 8H), 8.03 (s, 2H), 7.97 (s, 2H), 7.62 (d, *J* = 8.0 Hz, 8H), 7.48 (t, *J* = 7.7 Hz, 8H), 7.35 (t, *J* = 7.7 Hz, 8H). ^{13}C NMR Unable to be obtained due to limited solubility. HRMS (ESI) m/z: $[M+H]^+$ calcd for $C_{68}H_{41}N_6O_2$: 973.3291; found: 973.3318.

2,6-bis(4-(9H-carbazol-9-yl)phenyl)benzo[1,2-d:5,4-d']bis(oxazole) (C5)

Method A; pale yellow solid (35%). M.P > 240 °C. ^{1}H NMR (500 MHz, $CDCl_3$) δ 8.53 (d, *J* = 8.1 Hz, 4H), 8.20 (s, 1H), 8.17 (d, *J* = 7.8 Hz, 4H), 7.88 (s, 1H), 7.81 (d, *J* = 8.2 Hz, 4H), 7.54 (d, *J* = 8.2 Hz, 4H), 7.46 (t, *J* = 7.6 Hz, 4H), 7.34 (t, *J* = 7.4 Hz, 4H). ^{13}C NMR (126 MHz, $CDCl_3$) δ 163.14, 149.10, 140.90, 140.32, 140.11, 129.20, 127.13, 126.21, 125.51, 123.81, 120.56, 120.47, 110.11, 109.79, 93.47. HRMS (ESI) m/z: $[M+H]^+$ calcd for $C_{44}H_{27}N_4O_2$: 643.2134; found: 643.2135.

2,6-bis(3,5-di(9H-carbazol-9-yl)phenyl)benzo[1,2-d:5,4-d']bis(oxazole) (C6)

Method B; grey solid (38%). M.P > 240 °C. ^{1}H NMR (500 MHz, $CDCl_3$) δ 8.62 (s, 4H), 8.18 (d, *J* = 8.0 Hz, 9H), 8.02 (s, 2H), 7.82 (s, 1H), 7.62 (d, *J* = 8.0 Hz, 8H), 7.48 (t, *J* = 7.6 Hz, 8H), 7.35 (t, *J* = 7.6 Hz, 8H). ^{13}C NMR Unable to be obtained due to limited solubility. HRMS (ESI) m/z: [M+H]+ calcd for $C_{68}H_{41}N_6O_2$: 973.3291; found: 973.3293.

4.5 Results and Discussion

4.5.1 Computational Predictions

The study began by modelling the six materials of interest using DFT/TD-DFT to determine the optimized geometries and predict optical and electronic properties (**Table 1**). Due to their likeness in conjugation and electronic structure, compounds **C1**, **C3**, and **C5** are referred to as the di-substituted carbazole (DC) group while the tetra-substituted carbazole (TC) group includes compounds **C2**, **C4** and **C6**. By altering the conjugation of the carbazoles relative to the BBO core, we hoped to identify trends leading to materials with small ΔE_{ST}.

We began the analysis by recognizing structure-property relationships between the HOMOs of each material. All BBO systems in the DC group were found to have HOMO energies between -5.2 – -5.4 eV while the TC group is slightly lower between -5.4 – -5.5 eV. The similarity in HOMO energies within each group is due to the similarity in localization of electron density between the three BBOs (Figure 2). However, the electron density for the DC group compounds is more delocalized compared the TC group. Furthermore, the HOMO energies of the DC-BBOs **C1**, **C3**, and **C5** are also computed to be slightly higher than the HOMO of their respective TC group partners. This delocalization and energetic increase can be attributed to the substituent position of the pendant carbazole moieties relative to the BBO core. For the DC group materials, the lone-pair electrons on the carbazole heteroatom are in direct conjugation to the BBO core when conjugated at the *para*-position while the *meta*-conjugation of the TC systems force these groups to be electronically orthogonal. Independent of the carbazole substitution, when the aryl substituents are substituted through the 4,8-axis of the BBO core, a slight increase in the HOMO energy is observed compared to those conjugated through the 2,6-axis. According

to the computations, there is negligible change in the HOMO energy whether the BBO core is the *trans*- or *cis*- isomer.

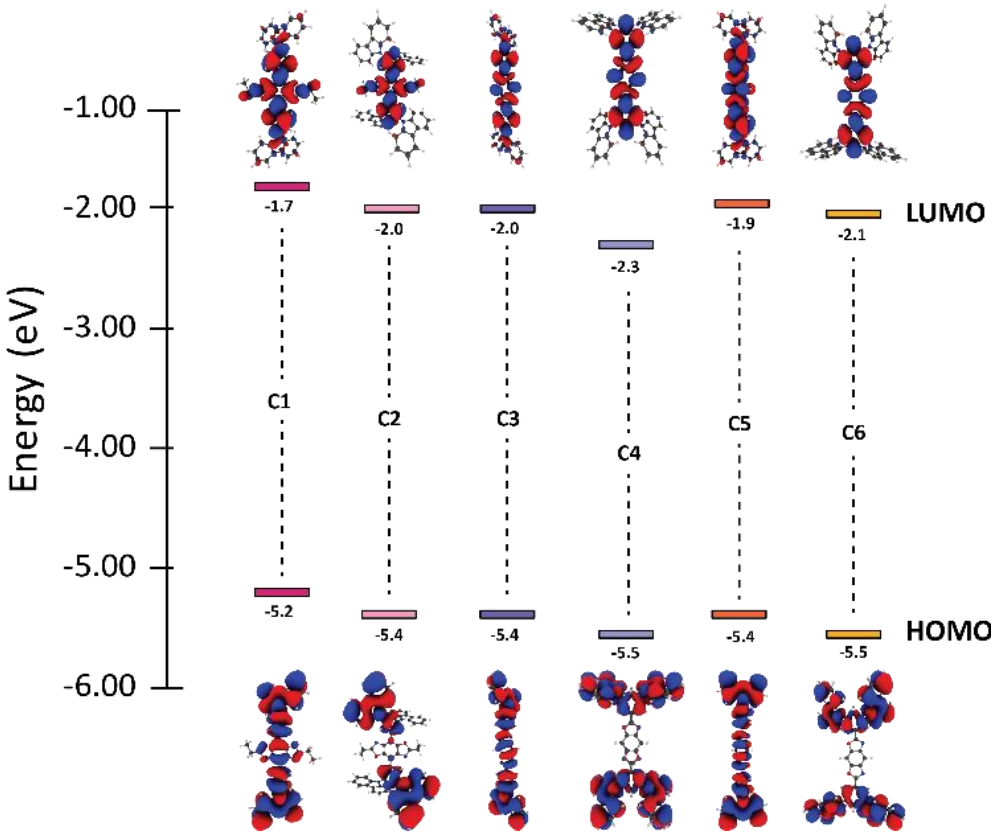


Figure 4.5.1.1. FMOs and electronic energy levels of C1(far left) through C6 (far right).

Next, trends between the LUMOs of each compound were analysed. The LUMO energy for the DC group is found to range between -1.7 – -2.0. The LUMO energy is lowered slightly for the TC group, ranging between -2.0 - -2.3 eV. For both groups, the addition of the BBO core helps lower the LUMO energy. However, the degree of separation between the HOMO and LUMO is more pronounced in the TC group than the DC group due to the conjugation position of the carbazole units. The axis of conjugation also affects the LUMO energy as **C1** is found to be 0.2 – 0.3 eV higher in energy compared to **C3** and **C5**. A similar result is found comparing **C2** to both **C4** and **C6**. Unlike the HOMO, inclusion of the *cis*-

core restricts the conjugation pathway of pi-electrons, thereby increasing the LUMO energy by 0.1 – 0.2 eV.

The band gaps for all BBOs were found to be suitable for deep-blue hosts or emissive materials due to their limited conjugation pathways (3.1 – 2.8 eV). Interestingly, the computations show compounds in the TC group have smaller band gaps when compared to their respective DC partners. This can be attributed to the higher CT character of compounds **C2**, **C4**, and **C6** which has significant impact on lowering the LUMO. As a result, these materials not only have a smaller band gap, but also a smaller ΔE_{ST} when compared to their DC partners. However, the S_1 oscillator strengths for compounds **C2**, **C4**, and **C6** are low ($<10^{-1}$) compared to **C1**, **C3** and **C5**, indicating the TC materials may not be as luminescent as their DC counterparts. Nonetheless, apart from **C1** and **C3**, all compounds were calculated to exhibit $\Delta E_{ST} < 0.50$ eV. With this knowledge, each compound was next synthesized to determine the experimental optical and electronic properties.

4.5.2 Synthesis and Characterization

The BBOs were synthesized using a simple three-step process, minimizing the need for inert atmosphere. The precursors were formed using the pathway outlined in **Figure 4.5.2.1**. All precursor materials were formed starting from commercially available fluorinated benzonitrile or bromobenzene derivatives. First, the commercial materials were heated with stoichiometric amounts of carbazole and potassium tert-butoxide in *N*,*N*-dimethylformamide under normal atmosphere to produce the carbazole-substituted bromobenzene (1; 86% and 2; 65%) and benzonitrile (3; 78% and 4; 71%) derivatives in moderate yields. Compounds 1 and 2 were dissolved in anhydrous tetrahydrofuran (THF),

lithiated with *n*-butyllithium, and quenched with 2-isopropoxy-4,4,5,5-tetramethyl-1,3,2-dioxaborolane to produce the desired boronic esters 5 (79%) and 6 (60%). Compounds **3** and **4** were hydrolysed under normal atmosphere using an aqueous 6 M sodium hydroxide solution and reagent alcohol to produce nearly quantitative yields of the substituted benzoic acid derivatives 7 (95%) and 8 (89%).

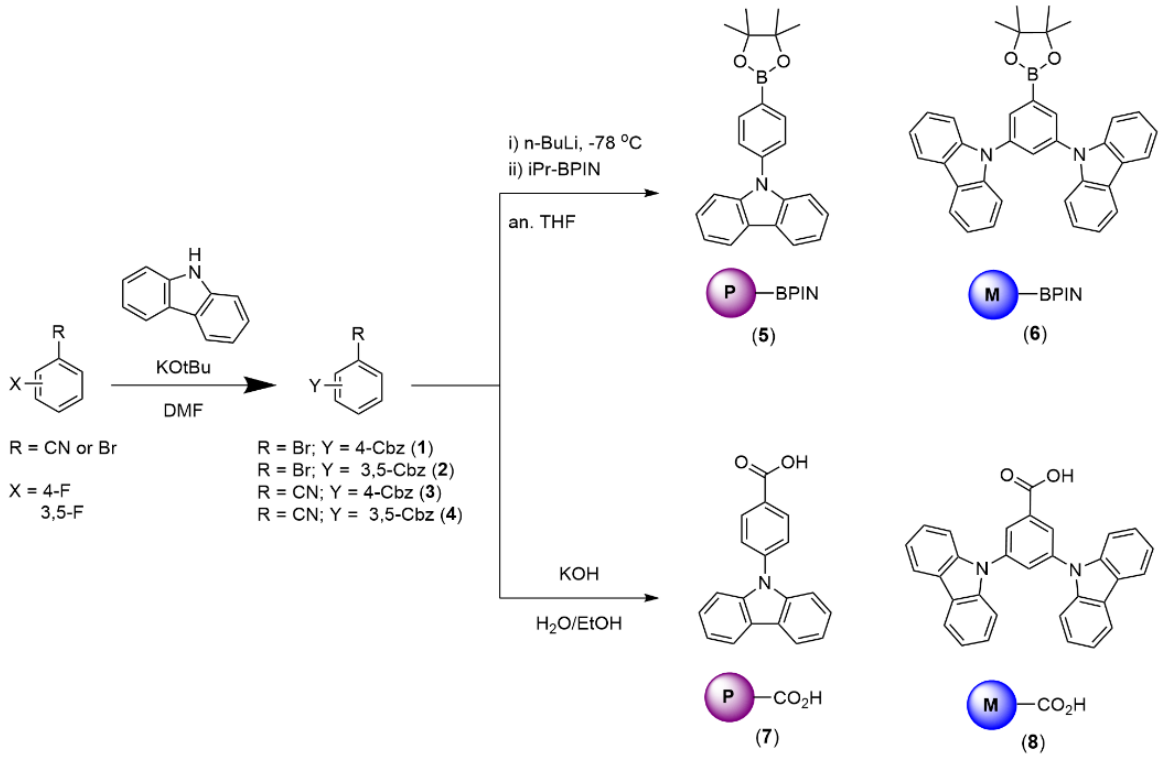


Figure 4.5.2.1. Synthesis of precursor material **1-8**.

The final step synthesis is illustrated in **Figure 4.5.2.2**. We elected to use high-pressure Suzuki-Miyaura conditions to form the 4,8-conjugated BBOs due to its low toxicity and effectiveness based off previous work.[12] Using cesium fluoride as the base and THF as the solvent, **C1** and **C2** were produced in yields of 60% and 37%, respectively. Lastly, the 2,6-conjugated BBOs were formed through a condensation technique using polyphosphoric acid trimethylsilyl ester (PPSE) as a desiccant with either 2,5-diaminohyroquinone bis-

hydrochloride or 4,6-dinitroresorcinol, producing **C3** – **C6** (28-38% yields). All compounds exhibit decent-to-low solubility in chlorinated solvents and where structurally characterized using NMR and high-resolution MS (ESI) techniques.

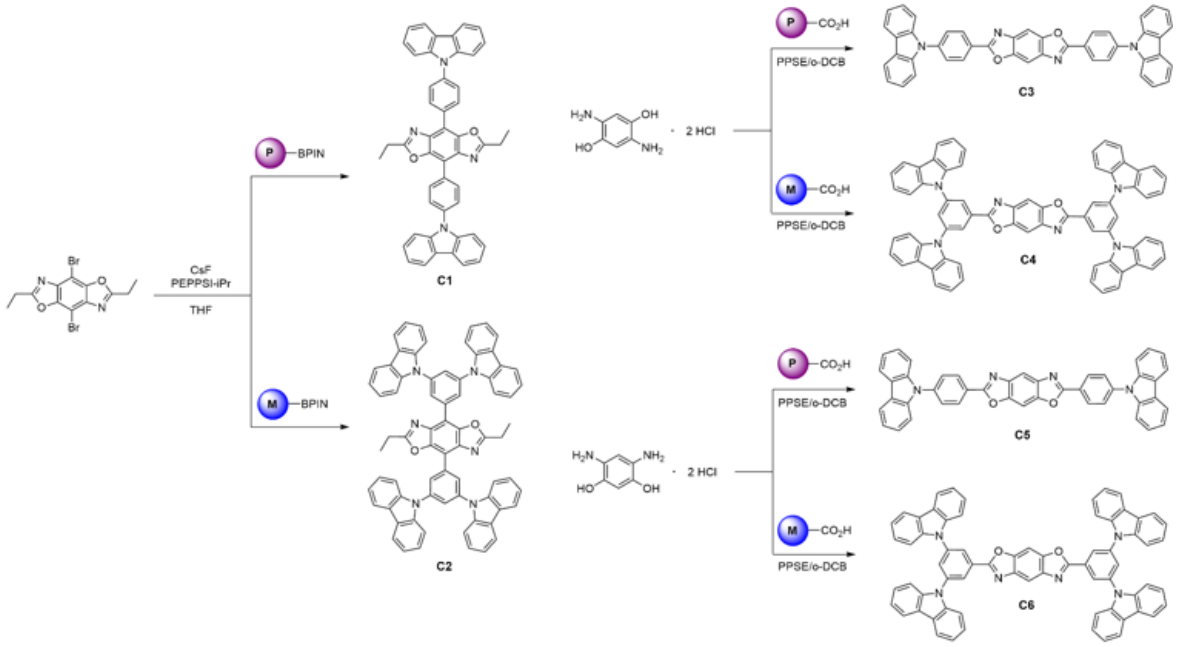


Figure 4.5.2.2. Synthesis of final molecules **C1 – C6**.

4.5.3 Electronic Properties

The theoretical and experimental electronic properties of **C1** – **C6** are listed in **Table 4.5.3.1**. The experimental HOMO energies were calculated using ionization potentials determined from ultraviolet photoelectron spectroscopy (UPS). We chose this technique over cyclic voltammetry due its lack of measurement limitations and its ability to measure the work function of materials with high accuracy. The optical HOMO □ LUMO transition energies (E_g^{opt}) were determined from the onset of each thin-film UV-Vis spectrum. LUMO levels were then calculated by adding the E_g^{opt} to the experimental HOMO energies.

In all cases, the HOMO and LUMO levels measured are like common commercial hosts/emitters for blue OLEDs. All experimental HOMO energies range from -6.1 to -5.8 eV, which are 0.3 – 0.7 eV deeper than the computationally predicted values. Similarly, the theoretical LUMO values (-2.3 to -1.7 eV) are calculated to be 0.5 – 1.2 eV higher in energy than the experimental values (-3.1 to -2.7 eV). The experimental E_g^{opt} suggest excellent potential as blue host/emitter materials for blue OLEDs as all compounds ranged from 2.9 to 3.3 eV. These values are in good agreement with computational findings (abs. diff. ≤ 0.3 eV). For BBOs **C1**, **C3**, and **C5**, the E_g^{opt} are lower in energy when compared to their 3,5-disubstituted analogues. This finding is attributed to the para-conjugation of each carbazole to the benzene ring, allowing the non-bonding electron pair of the heteroatom to contribute to the extended pi-system.

	Electronic Properties					Dihedral Angles	
BBO	**HOMO (eV)**	**LUMO (eV)**	**E_g^{opt} (eV)**	**ΔE_{ST} (eV)**	*f*	**2,6 (^{O})**	**4,8 (^{O})**
C1	**-5.20**	-1.74	3.06	0.64	8.8e-01	-	29.6
C2	-5.39	-1.96	3.01	0.46	1.8e-02	-	33.7
C3	-5.39	-20.1	2.96	0.59	1.5e+00	0.5	-
C4	-5.50	-2.26	2.83	0.38	4.1e-02	4.5	-
C5	-5.42	-1.93	3.06	0.47	1.3e+00	3.9	-
C6	-5.50	-2.15	2.92	0.22	1.3e-02	1.0	-

Table 4.5.3.1. Computed electronic and geometric properties of the six BBO materials.

4.5.4 Steady-State Optical Properties

The optical property investigation began by analysing the steady-state absorbance and emission profiles of **C1** – **C6.** Each compound was examined as a 0.01 gL^{-1} solution dissolved in chloroform (**Figure 4.5.4.1**) and as a thin film (**Figure 4.6.19**). We first examined the difference in absorption profiles between BBOs in solution. In all cases, one can see two main absorption bands characteristic of chromophores with donor-acceptor

configurations, demonstrating their CT nature.[18: 19] The high energy bands can be ascribed to the localized excitations due to π-π* transition of the moieties, while the low energy bands can be ascribed to the n-π* charge transfer transition among the moieties.[18: 20] It is interesting to note that the more prominent CT absorption band is obtained from the systems with DC compounds rather than the TC systems. One would expect that **C2**, **C4**, and **C6** would exhibit higher donor strength and yield more prominent charge transfer features.[21] However, the multiple carbazole subunits of the **C2**, **C4**, and **C6** materials make the localized absorption transition more prominent. Of all materials, the DC group BBOs show

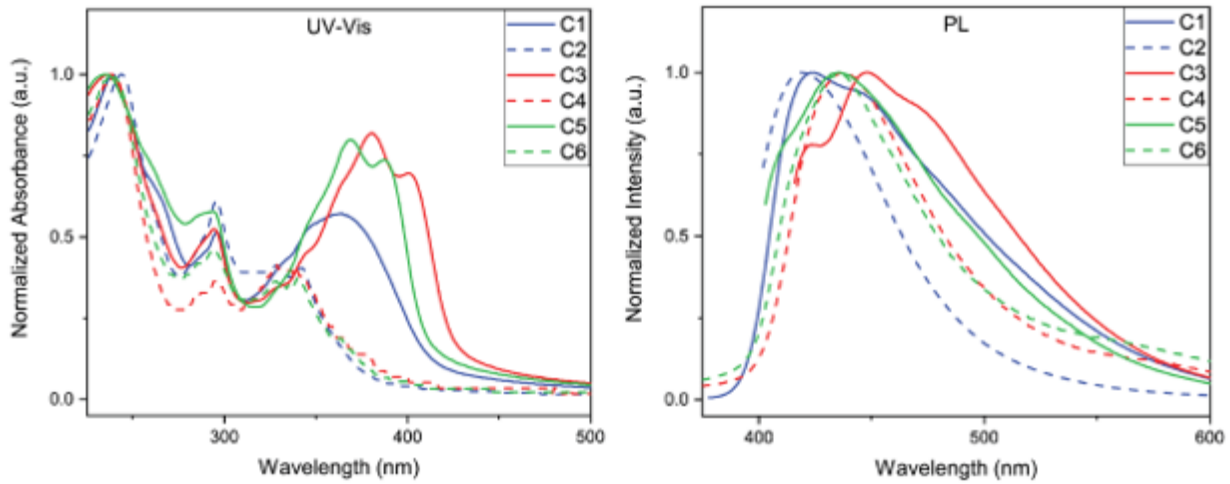


Figure 4.5.4.1. Steady-state absorbance spectra of **C1-C6** in chloroform (left) at 0.01 gL^{-1} and photoluminescence spectra of **C1- C6** thin-film (right).

bathochromic absorption when compared to the TC systems. This is a direct consequence of the lower E_g^{opt} and substitution pattern of carbazole units for **C1**, **C3**, and **C5**.

Compounds which contain the *cis*-isomeric core exhibit hypsochromic shift in absorption relative to the BBOs with the *trans*-moiety. When the aryl substituents are conjugated through the 4,8-axis, an enhanced hypsochromic shift is observed compared to the BBOs with 2,6-axis substituents. angle that exists between the angle that exists between the BBO core and aryl substituent, as supported from DFT calculations (Table 1). As thin

films, **C1**, **C3**, and **C5** still demonstrate a bathochromic shift in absorption when compared to their TC group partners. While changing the *cis*-core to the *trans*-isomer provides a red-shift in absorbance, this effect is not as intense when compared to the same observation in solution.

The photoluminescence (PL) spectra were measured to determine emission profiles and quantum yields for each BBO (**Figure 4.5.4.1; Table 4.5.4.1**). In solution, C1, C3, and C5 all produce emission at approximately 415 nm with quantum yields ranging from 27-68%. A secondary peak at 433 nm is observed for C3 but is not observed for the structural isomer, C5. For the TC systems, the experimental observations closely matched the DFT predictions as the emission intensities of these materials are low with broad profiles and quantum yields ranging from 3 – 10 %. When measured as thin films, all compounds were found to exhibit emission maxima between 419-448 nm. The emission profiles for C1, C3, and C5 broaden and produce bathochromic emission compared to their solution-state spectra. These observations are attributed to each compound's ability to undergo π-π stacking readily. Conversely, C2, C4, and C6 undergo slight hypsochromic emission with little change in peak breadth. Due to the bulky nature of these compounds, we believe the pi-systems of each molecule are unable to interact effectively in a macroscopic environment, thereby producing similar emission profiles when compared to their solution spectra. This property is expected to be highly beneficial for bipolar host material that can facilitate energy-transfer without radiative quenching.

The quantum yields (φ) of the investigated compounds were analysed in both unpurged and purged chloroform solutions (See SI). In the case of the C5, a φ value (27%) was obtained in unpurged solution. An appreciable φ enhancement was also obtained for the C5

chromophore after purging oxygen from the solution (33 %). It has been suggested that the difference of the φ before and after the oxygen purging process is due to excited state dynamics governed by a delayed fluorescence mechanism.[22] Contrarily to C5, a very small φ (4.8 %) was obtained for C6, which suggests a poor fluorescence decay in oxygen-rich environments but is enhanced when oxygen is expelled from the solution (6.2%).[18] Such a small enhancement indicates that other decay pathways for the excited states outcompete fluorescence decay. Similar results were obtained for the remaining mono-carbazole donor moiety emitters and their respective bi-carbazole donor moiety counterparts. Based on these results, we sought to further investigated these compounds using time-resolved techniques at the nanosecond timescale.

	Optical Properties							**Electronic Properties**		
	Solution					**Thin Film**				
BBO	$\varepsilon(10^4)$ ($M^{-1}cm^{-1}$)	$^{abs}\lambda_{max}$ (nm)	$^{em}\lambda_{max}$ (nm)	Φ (%)	ΔE_{ST} (eV)	$^{abs}\lambda_{max}$ (nm)	$^{em}\lambda_{max}$ (nm)	^{a}HOMO (eV)	^{b}LUMO (eV)	$E_g{}^{c}$ (eV)
C1	3.4	**347**	**415**	68	0.59	**363**	**424**, 445	-5.9	-2.9	3.0
C2	5.7	313, **326**, 340	**428**	10	0.22	**329**, 342	**419**	-6.1	-2.8	3.3
C3	6.0	**372**, 388	**416**, 433	42	0.46	**380**, 401	423, **448**, 470	-6.0	-3.1	2.9
C4	6.9	**337**, 351, 370	**448**	3.9	0.47	**329**, 340	**437**	-5.8	-2.7	3.1
C5	5.4	**363**, 377	**414**	27	0.64	**369**, 388	**436**	-6.0	-3.0	3.0
C6	7.6	327, **341**, 360	**440**	4.8	0.38	**329**, 340	**435**	-5.9	-2.7	3.2

Table 4.5.4.1. Measured steady-state optical and electronic properties for BBOs **C1-C6**. Bold values indicate wavelength of maximum absorbance/emission. a) Measured using UPS. b) measured using the following equation: LUMO = HOMO +E_g. c) Calculated from onset of absorbance.

4.5.5 nsTAS

Transient absorption (TA) spectra of the investigated compounds were obtained to gain insight into their emissive mechanism (**Figure 4.5.5.1**). In each spectrum, positive ΔOD peaks are representative of excited state absorption (ESA) while negative peaks are representative of either ground state bleaching (GSB) or stimulated emission (SE). The lifetimes of each peak were then investigated to aid in determining what emissive mechanisms are accessible by these compounds. Each TA spectrum of the mono-carbazole donor DC emitters display a SE peak that is in good agreement with the steady-state fluorescence results (**Table 4.5.5.1**). No other peaks are readily observable, indicating that the lifetime of both the GSB and ESA are below the time resolution of this technique. This suggests that fluorescence emission is efficient for these compounds and outcompetes other radiative decay pathways.

Contrary to **C1**, **C3**, and **C5**, the TA spectra of the bi-carbazole donor TC emitters display a GSB, SE, ESA, and a third negative peak. To determine the lifetime of the ESA and third negative peak, transient decay traces were obtained (**Figure 4.6.20**). For **C6**, the ESA lifetime (430 nm) in unpurged chloroform is 632 ns, which is a longer timescale compared to typical singlet states. However, this lifetime is enhanced with oxygen purging, increasing the timescale just nearly into the microsecond regime (992 ns), indicating that this state has significant triplet character. Similar results are obtained for the third negative

peak at ~700 nm observed after 70 ns (Figure 4) which has a lifetime of 576 ns in the oxygenated solution. However, this peak is not indicative of GSB or SE as GSB is observed at ~340 nm and overlaps well with the steady-state absorption spectrum while SE is observed at ~430 nm and overlaps well with the steady-state emission spectrum. Thus, we determine that this state is representative of phosphorescence emission. The significant enhancement of this state's lifetime with oxygen purging to 1152 ns supports this, as oxygen is known to quench the triplet state. These lifetimes match well with that of the ESA in both the oxygenated and oxygen-purged solutions, suggesting that this emission is the result of the ESA decay. It should be noted that the sharp peak observed at ~700 nm at 50 ns is the result of the second harmonic of the excitation beam and not emission of **C6**. Similar results were obtained for **C2** and **C4** with the most noticeable difference being that both emitters have longer ESA and phosphorescence lifetimes than **C6** (**Figure 4.6.20**).

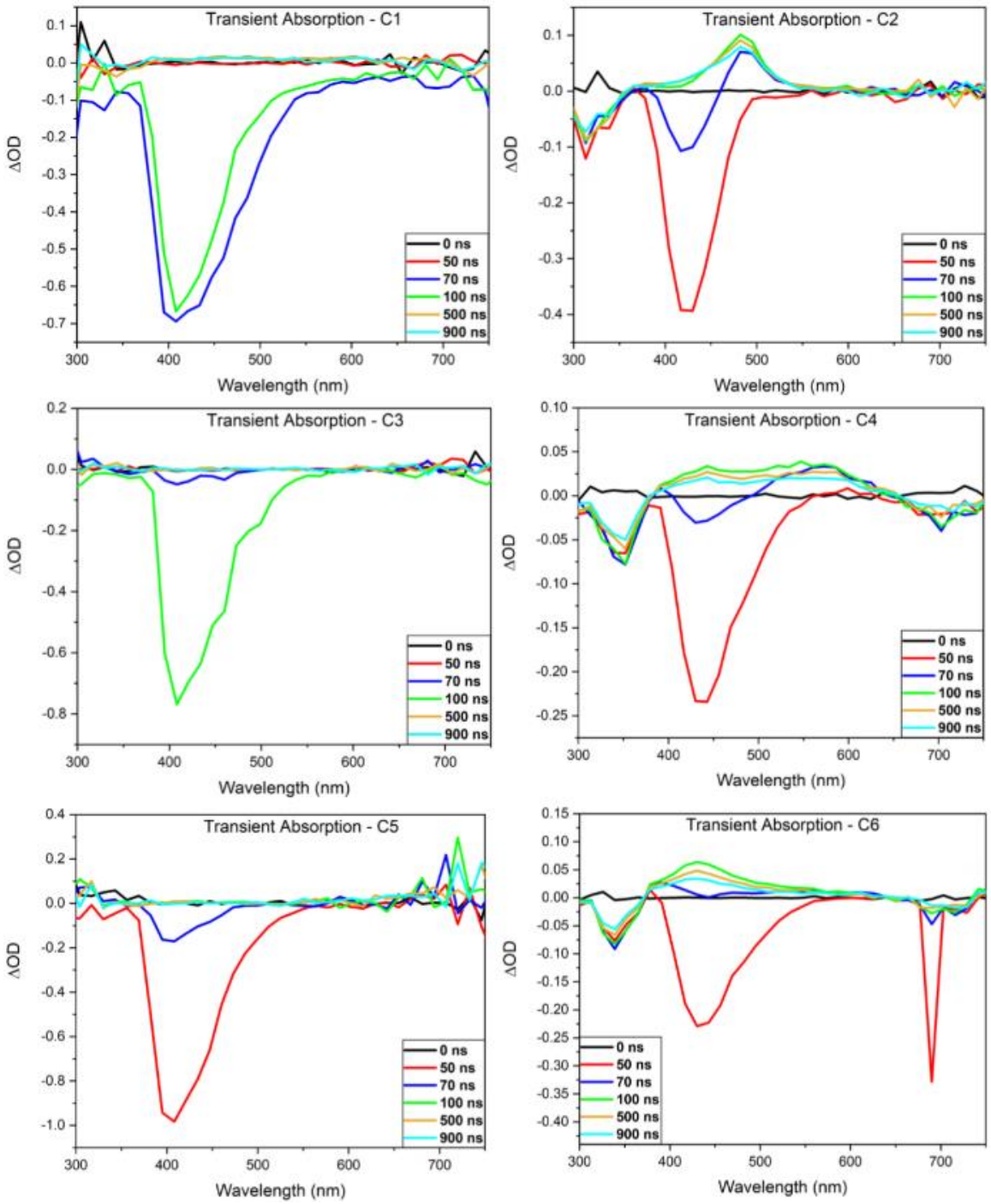


Figure 4.5.5.1. Nanosecond transient absorption spectra of the six BBOs.

The ESA lifetime results were used to calculate the rate of reverse intersystem crossing (k_{rISC}) and determine if any of the emitters are capable of TADF.[19: 23] No k_{rISC} could be determined for the DC emitters, as they possessed no ESA that could be measured by the

nanosecond TA technique. Based on the timescale of relaxation, we believe **C1**, **C3**, and **C5** to be traditional fluorophores. The k_{rISC} values calculated for the TC emitters are displayed in Table 3 along with the rate of phosphorescence (k_{phos}). Both k_{rISC} and k_{phos} compete for the triplet ESA, where k_{phos} values are an order of magnitude greater than the k_{rISC} results, in all cases. Therefore, it is determined that the TC emitters are more efficient phosphorescent compounds than TADF compounds.

Based on the steady-state and transient spectral data, it is evident that **C1**, **C3**, and **C5** exhibit properties useful as fluorescent dopant materials as seen in their PL spectra and moderate-to-high PLQYs in oxygen-free environments. Unfortunately, none of the BBO materials display any TADF characteristics. Conversely, **C2**, **C4**, and **C6** show quite narrow ΔE_{ST} and long-lived triplet lifetimes before phosphorescence decay (+1 μs). While the rate of k_{rISC} is an order of magnitude smaller than the k_{phos}, these materials do not exhibit bright emission and could be useful as potential BBO-based phosphorescent/TADF host materials. Therefore, **C1**, **C3**, and **C5** were optimized into solution processed devices as active layer materials while **C2**, **C4**, and **C6** were paired with commercial TADF emitter 2,3,4,5,6-pentakis(3,6-di-tert-butyl-9H-carbazol-9-yl)benzonitrile (5TCzBN) to evaluate preliminary results as ambipolar hosts.

BBO	GSB (nm)	SE (nm)	ESA (nm)	k_{rISC} (s^{-1})	τ_{ESA} (s)	k_{ESA} (s^{-1})	τ_{ph} (s)	k_{ph} (s^{-1})
C1	-	410	-	-	-	-	-	-
C2	325	424	487	4.30E+04	1.16E-06	8.59E+05	1.92E-06	5.21E+05
C3	-	408	-	-	-	-	-	-
C4	350	438	547	5.68E+03	1.41E-06	7.10E+05	1.54E-06	6.51E+05
C5	-	408	-	-	-	-	-	-
C6	340	430	430	1.41E+04	9.92E-07	1.01E+06	1.15E-06	8.68E+05

Table 4.5.5.1. Transient properties and kinetic traces of the T group BBOS. GSB = ground state bleaching. SE = stimulated emission. ESA = excited state absorbance. k_{rISC} = rate of

reverse intersystem crossing. k_{ph} = rate of phosphorescence. τ_{ESA} = ESA lifetime. τ_{ph} = phosphorescence lifetime.

4.5.6 Device Properties

We studied OLED characteristics of **C1**, **C3**, and **C5** as solution-processed dopants in a mixed host matrix. The device architecture consisted of the following: ITO (100 nm)/PEDOT:PSS (35 nm)/Active Layer (mixed host: 5% BBO)/TmPyPB (35 nm)/LiF (1 nm)/Al (100 nm). Shown in Figure 5 is the band diagram of all active layer materials and efficiency graphs while Table 4 collates the electroluminescent (EL) properties of the devices using BBO-based dopants.

The EL spectra of each dopant exhibit a relatively minor red-shift when compared to their solution-state PL spectrum. Of the three dopants, **C5** was found to exhibit the most blue-shifted emission of the set at 405 nm, with a second band at 424 nm. **C1** and **C3** show emission maxima at 413 nm and 417 nm, respectively. The peak widths at half max for all EL spectra were less than 55 nm, indicating good color purity for organic molecules. Furthermore, all three dopants exhibit CIE_y values < 0.06 and CIE_x values of 0.16. While these compounds nearly meet the National Television Systems Committee and European Broadcasting Union's requirements for deep-blue emission, the larger CIE_x value indicates near-UV emission, providing a purple hue to the emitted light. Each device demonstrates operating voltages (measured at 100 cd/m^2) less than 4.8 V and max luminance between 300 – 900 cd/m^2. The best performing dopant of the set was **C3**, achieving a current efficiency (CE) of 0.53, power efficiency (PE) of 0.34, and a max EQE of 0.88. While small, the efficiencies of all materials are comparable to other materials which emit near UV emission using identical doping concentrations.[24] While specific measurements would be required for support, we attribute the low EQE of these devices to the emission

mechanism of the molecule and the traditional host guest architecture of the system. However, two methods of overcoming the latter argument would be to employ these systems into (1) a thermally evaporated device with (2) the use of a TADF-sensitizer to obtain near-UV hyperfluorescence emission. Unfortunately, due to the constraints of the thermal evaporator, this architecture could not be obtained. These architectures will be investigated in the future, when possible.

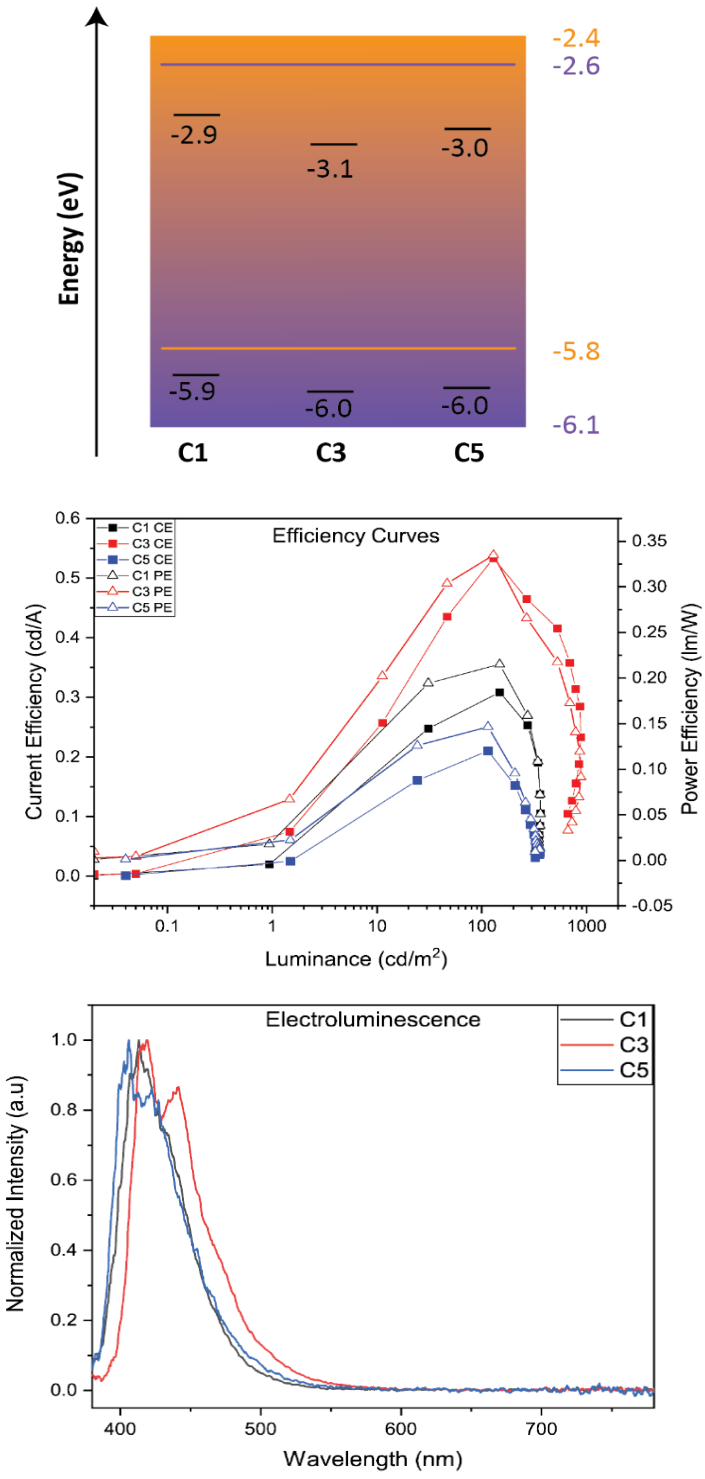


Figure 4.5.6.1. (top) Bond diagram of active layer materials using BBO-based dopants. In purple are the HOMO/LUMO levels for 26DCzPPY while in orange is TCTA. (center) Power and current efficiency curves. (bottom) Normalized electroluminscence spectra.

We next preliminarily evaluated **C2**, **C4**, and **C6** as a host material. Each system was thermally evaporated with the commercial TADF dopant, 5TCzBN. The device architecture used was ITO (100 nm)/PEDOT:PSS (35 nm)/Active Layer (host: 20% 5TCzBN)/TmPyPB (35 nm)/LiF (1 nm)/Al (100 nm). BBOs **C2**, **C4**, and **C6** produced more promising results when compared to the device using the commercial *m*CP host. Demonstrated by the RMS values from AFM measurements (See SI), the TC group show very similar active layer morphologies, resulting in hosts which do not alter the emission maxima by more than 5 nm. However, the BBO hosts drastically reduce the operating voltage by as much as 4.0 V when compared to the device using *m*CP as the host. This is attributed to the ambipolar nature of the materials; providing better energetic agreement between the LUMO levels of the host and dopant. As a result, the BBO hosts were able to attain higher CE, PE and EQEs while some produced comparable brightness when compared to the *m*CP device. From these preliminary devices, the BBO materials indicate great potential as hosts due to their improved operating voltages and efficiencies when compared to commercially available *m*CP.

	BBO	$^{EL}\lambda_{Max}$ (nm)	V_{100} (V)	L_{Max} (cd/m^2)	CE_{Max} (cd/A)	PE_{Max} (lm/W)	EQE_{Max} (%)
Dopants	**C1**	**413**	4.3	363.4	0.308	0.215	0.874
	C2	**417,** 441	4.8	884.7	0.533	0.335	0.881
	C3	**405,** 424	4.4	358.6	0.210	0.147	0.538
Host	**C5**	**481**	8.4	1247	0.106	0.033	0.049
	mCP	**485**	4.4	1476	0.454	0.246	0.200
	C2	**484**	4.5	835.0	0.487	0.306	0.864
	C4	**486**	5.1	1200	0.915	0.448	0.356
	C6	**413**	4.3	363.4	0.308	0.215	0.874

Table 4.5.6.1 Device properties of the fabricated OLEDs.

4.6 Conclusions

In summary, six BBO materials with a DAD motif were computationally modelled to evaluate their potential as TADF emitters. DFT calculations suggested only three of the six BBOs could potentially exhibit TADF character. To confirm predictions, each material was synthesized in three steps and evaluated using a variety of steady-state and transient absorption spectroscopic techniques to understand their opto-electronic properties. The results indicate twofold. First, *meta*- conjugation of electron rich aryl substituents on a phenyl spacer conjugated to the BBO core effectively isolates the HOMO and LUMO. This pattern enhances the CT character of the materials and reduces the ΔE_{ST} of the molecule, but suppresses photoluminescence, reducing the PLQY of the system. Secondly, *para*-conjugation of the carbazole moieties result in the opposite effect where the LE character of the molecule is increased, reintroducing fluorescence but sacrificing TADF character. Fortuitously, **C1**, **C3**, and **C5** demonstrated attractive opto-electronic qualities as near-UV emitting generation 1 dopants while **C2**, **C4**, and **C6** were repurposed as ambipolar hosts. The solution-processed dopants demonstrated excellent near-UV emission ($CIE_y < 0.06$; $CIE_x = 0.16$) and competitive efficiencies to currently reported near-UV organic emitters. The BBO hosts paired with a commercial TADF emitter demonstrated reduced turn-on voltages and increased efficiencies in comparison to the p-type host, *m*CP. While these preliminary results show great promise for the candidates in the field of organic electronics, future works include further optimization of both sets of BBO materials using an evaporator with more extensive capabilities to attempt hyperfluorescent architectures (**C1**, **C3**, **C5**) and using the **C2**, **C4**, and **C6** as sensitizers for triplet recycling materials. Additionally, the TC group scaffold can be further improved to reintroduce fluorescent behaviour towards the production of TADF-active BBO emitters.

References

(1) Y.-F. Liu, J. Feng, Y.-G. Bi, D. Yin and H.-B. Sun, Advanced Materials Technologies, 2019, 4, 1800371.

(2) A. Zhou, H. Wang, Y. Zhang and C. Hu, iber Integr. Opt., 2022, DOI: 10.1080/01468030.2022.2083532, 1-25; J. Song, H. Lee, E. G. Jeong, K. C. Choi and S. Yoo, Adv. Mater., 2020, 32, 1907539; C. Murawski and M. C. Gather, Advanced Optical Materials, 2021, 9, 2100269.

(3) R. Pode, Renewable and Sustainable Energy Reviews, 2020, 133, 110043; H. Sasabe and J. Kido, Chem. Mater., 2011, 23, 621-630; G. M. Phelan, Information Display, 2018, 34, 10-15.

(4) G. Gryn'ova, K.-H. Lin and C. Corminboeuf, J. Am. Chem. Soc., 2018, 140, 16370-16386; H. Bronstein, C. B. Nielsen, B. C. Schroeder and I. McCulloch, Nature Reviews Chemistry, 2020, 4, 66-77; R. M. Pankow and B. C. Thompson, Polymer, 2020, 207, 122874.

(5) J. Tagare and S. Vaidyanathan, J. Mater. Chem. C, 2018, 6, 10138-10173; M. Zhu and C. Yang, Chem. Soc. Rev., 2013, 42, 4963-4976; Z. Xu, B. Z. Tang, Y. Wang and D. Ma, J. Mater. Chem. C, 2020, 8, 2614-2642; A. Monkman, ACS Applied Materials & Interfaces, 2022, 14, 20463-20467.

(6) M. A. Baldo, D. F. O'Brien, Y. You, A. Shoustikov, S. Sibley, M. E. Thompson and S. R. Forrest, Nature, 1998, 395, 151.

(7) X. Cai and S.-J. Su, Adv. Funct. Mater., 2018, 28, 1802558; Y.-Z. Shi, H. Wu, K. Wang, J. Yu, X.-M. Ou and X.-H. Zhang, Chemical Science, 2022, 13, 3625-3651.

(8) C. A. Parker and E. J. Bowen, Proceedings of the Royal Society of London. Series A. Mathematical and Physical Sciences, 1963, 276, 125-135; H. Uoyama, K. Goushi, K. Shizu, H. Nomura and C. Adachi, Nature, 2012, 492, 234-238.

(9) Y. Im, M. Kim, Y. J. Cho, J.-A. Seo, K. S. Yook and J. Y. Lee, Chem. Mater., 2017, 29, 1946-1963; I. Zoh, M. Imai-Imada, J. Bae, H. Imada, Y. Tsuchiya, C. Adachi and Y. Kim, The Journal of Physical Chemistry Letters, 2021, 12, 7512-7518.

(10) B. C. Tlach, A. L. Tomlinson, A. Bhuwalka and M. Jeffries-El, The Journal of Organic Chemistry, 2011, 76, 8670-8681.

(11) B. C. Tlach, A. L. Tomlinson, A. G. Ryno, D. D. Knoble, D. L. Drochner, K. J. Krager and M. Jeffries-El, J. Org. Chem., 2013, 78, 6570-6581.

(12) D. L. Wheeler, A. V. Diodati, A. L. Tomlinson and M. Jeffries-El, ACS Omega, 2020, 5, 12374-12384.

(13) A. A. Burney-Allen, J. Shaw, D. L. Wheeler, L. Diodati, V. Duzhko, A. L. Tomlinson and M. Jeffries-El, Asian Journal of Organic Chemistry, 2021, 10, 215-223.

(14) R. Chavez III, M. Cai, B. Tlach, D. L. Wheeler, R. Kaudal, A. Tsyrenova, A. L. Tomlinson, R. Shinar, J. Shinar and M. Jeffries-El, J. Mater. Chem. C, 2016, 4, 3765-3773.

(15) D. Wheeler, S. Tannir, E. Smith, A. Tomlinson and M. Jeffries-El, Materials Advances, 2022, 3, 3842-3852; X. Yin, T. Zhang, Q. Peng, T. Zhou, W. Zeng, Z. Zhu, G. Xie, F. Li, D. Ma and c. yang, J. Mater. Chem. C, 2015, 3, 7589-7596.

(16) Y. Sagara, K. Shizu, H. Tanaka, H. Miyazaki, K. Goushi, H. Kaji and C. Adachi, Chem. Lett., 2015, 44, 360; J. Lim, T. A. Albright, B. R. Martin and O. Š. Miljanić, J. Org. Chem., 2011, 76, 10207-10219.

(17) J. Luo, S. Gong, Y. Gu, T. Chen, Y. Li, C. Zhong, G. Xie and C. Yang, J. Mater. Chem. C, 2016, 4, 2442-2446.

(18) R. J. Vázquez, H. Kim, P. M. Zimmerman and T. Goodson, J. Mater. Chem. C, 2019, 7, 4210-4221.

(19) R. J. Vázquez, J. H. Yun, A. K. Muthike, M. Howell, H. Kim, I. K. Madu, T. Kim, P. Zimmerman, J. Y. Lee and T. G. Iii, J. Am. Chem. Soc., 2020, 142, 8074-8079.

(20) R. J. Vázquez, H. Kim, B. M. Kobilka, B. J. Hale, M. Jeffries-El, P. Zimmerman and T. Goodson, The Journal of Physical Chemistry C, 2017, 121, 14382-14392.

(21) B. Carlotti, Z. Cai, H. Kim, V. Sharapov, I. K. Madu, D. Zhao, W. Chen, P. M. Zimmerman, L. Yu and T. Goodson, Chem. Mater., 2018, 30, 4263-4276; Z. Cai, R. J. Vázquez, D. Zhao, L. Li, W.-y. Lo, N. Zhang, Q. Wu, B. Keller, A. Eshun, N. Abeyasinghe, H. Banaszak-Holl, T. Goodson and L. Yu, Chem. Mater., 2017, DOI: 10.1021/acs.chemmater.7b01512; B. Keller, Z. Cai, A. K. Muthike, P. K. Sahu, H. Kim, A. Eshun, P. M. Zimmerman, D. Zhang and T. Goodson, The Journal of Physical Chemistry C, 2018, 122, 27713-27733.

(22) S. Hirata, Y. Sakai, K. Masui, H. Tanaka, S. Y. Lee, H. Nomura, N. Nakamura, M. Yasumatsu, H. Nakanotani, Q. Zhang, K. Shizu, H. Miyazaki and C. Adachi, Nat. Mater., 2015, 14, 330.

(23) L. Fisher, R. J. Vázquez, M. Howell, A. K. Muthike, M. E. Orr, H. Jiang, B. Dodgen, D. R. Lee, J. Y. Lee, P. Zimmerman and T. Goodson, Chem. Mater., 2022, 34, 2161-2175.

(24) J. Tagare, R. Boddula, S. S. Sudheendran, D. K. Dubey, J.-H. Jou, S. Patel and S. Vaidyanathan, J. Mater. Chem. C, 2020, 8, 16834-16844.

(25) D. Weininger, Journal of Chemical Information and Computer Sciences, 1988, 28, 31-36.

(26) S. Grimme, C. Bannwarth and P. Shushkov, Journal of Chemical Theory and Computation, 2017, 13, 1989-2009; C. Bannwarth, S. Ehlert and S. Grimme, Journal of Chemical Theory and Computation, 2019, 15, 1652-1671.

(27) P. Pracht, F. Bohle and S. Grimme, Physical Chemistry Chemical Physics, 2020, 22, 7169-7192.

(28) R. Gomez-Bombarelli, J. Aguilera-Iparraguirre, T. D. Hirzel, D. Duvenaud, D. Maclaurin, M. A. Blood-Forsythe, H. S. Chae, M. Einzinger, D. G. Ha, T. Wu, G. Markopoulos, S. Jeon, H. Kang, H. Miyazaki, M. Numata, S. Kim, W. Huang, S. I. Hong, M. Baldo, R. P. Adams and A. Aspuru-Guzik, Nat. Mater., 2016, 15, 1120.

(29) A. D. Becke, The Journal of Chemical Physics, 1993, 98, 1372-1377.

(30) Y. Shao, Z. Gan, E. Epifanovsky, A. T. B. Gilbert, M. Wormit, J. Kussmann, A. W. Lange, A. Behn, J. Deng, X. Feng, D. Ghosh, M. Goldey, P. R. Horn, L. D. Jacobson, I. Kaliman, R. Z. Khaliullin, T. Kuś, A. Landau, J. Liu, E. I. Proynov, Y. M. Rhee, R. M. Richard, M. A. Rohrdanz, R. P. Steele, E. J. Sundstrom, H. L. Woodcock, P. M. Zimmerman, D. Zuev, B. Albrecht, E. Alguire, B. Austin, G. J. O. Beran, Y. A. Bernard, E. Berquist, K. Brandhorst, K. B. Bravaya, S. T. Brown, D. Casanova, C.-M. Chang, Y. Chen, S. H. Chien, K. D. Closser, D. L. Crittenden, M. Diedenhofen, R. A. DiStasio, H. Do, A. D. Dutoi, R. G. Edgar, S. Fatehi, L. Fusti-Molnar, A. Ghysels, A. Golubeva-Zadorozhnaya, J. Gomes, M. W. D. Hanson-Heine, P. H. P. Harbach, A. W. Hauser, E. G. Hohenstein, Z. C. Holden, T.-C. Jagau, H. Ji, B. Kaduk, K. Khistyaev, J. Kim, J. Kim, R. A. King, P. Klunzinger, D. Kosenkov, T. Kowalczyk, C. M. Krauter, K. U. Lao, A. D. Laurent, K. V. Lawler, S. V. Levchenko, C. Y. Lin, F. Liu, E. Livshits, R. C. Lochan, A. Luenser, P. Manohar, S. F. Manzer, S.-P. Mao, N. Mardirossian, A. V. Marenich, S. A. Maurer, N. J. Mayhall, E. Neuscamman, C. M. Oana, R. Olivares-Amaya, D. P. O'Neill, J. A. Parkhill, T. M. Perrine, R. Peverati, A. Prociuk, D. R. Rehn, E. Rosta, N. J. Russ, S. M. Sharada, S. Sharma, D. W. Small, A. Sodt, T. Stein, D. Stück, Y.-C. Su, A. J. W. Thom, T. Tsuchimochi, V. Vanovschi, L. Vogt, O. Vydrov, T. Wang, M. A. Watson, J.

Wenzel, A. White, C. F. Williams, J. Yang, S. Yeganeh, S. R. Yost, Z.-Q. You, I. Y. Zhang, X. Zhang, Y. Zhao, B. R. Brooks, G. K. L. Chan, D. M. Chipman, C. J. Cramer, W. A. Goddard, M. S. Gordon, W. J. Hehre, A. Klamt, H. F. Schaefer, M. W. Schmidt, C. D. Sherrill, D. G. Truhlar, A. Warshel, X. Xu, A. Aspuru-Guzik, R. Baer, A. T. Bell, N. A. Besley, J.-D. Chai, A. Dreuw, B. D. Dunietz, T. R. Furlani, S. R. Gwaltney, C.-P. Hsu, Y. Jung, J. Kong, D. S. Lambrecht, W. Liang, C. Ochsenfeld, V. A. Rassolov, L. V. Slipchenko, J. E. Subotnik, T. Van Voorhis, J. M. Herbert, A. I. Krylov, P. M. W. Gill and M. Head-Gordon, Mol. Phys., 2015, 113, 184-215.

(31) M. Inbasekaran and R. Strom, OPPI Briefs, 1994, 23, 447-450.

(32) R. J. Schmitt, D. S. Ross, J. R. Hardee and J. F. Wolfe, J. Org. Chem., 1988, 53, 5568-5569.

(33) A. T. R. Williams, S. A. Winfield and J. N. Miller, Analyst, 1983, 108, 1067-1071.

(34) I. B. Berlman, in Handbook of Fluorescence Spectra of Aromatic Molecules (Second Edition), ed. I. B. Berlman, Academic Press, 1971, DOI: https://doi.org/10.1016/B978-0-12-092656-5.50009-5, pp. 67-95.

(35) A. K. Sharma, K. Gowdahalli, J. Krzeminski and S. Amin, J. Org. Chem, 2007, 72, 8987-8989.

4.7 Supporting Information

Figure 4.7.1 ^{1}H NMR of 1.

Figure 4.7.2 ^{1}H NMR of 2.

Figure 4.7.3 ^{1}H NMR of 3.

Figure 4.7.4 ^{1}H NMR of 4.

Figure 4.7.5 ^{1}H NMR of 5.

Figure 4.7.6 ^{1}H NMR of 6.

Figure 4.7.7 ^{1}H NMR of 7.

Figure 4.7.8 ^{1}H NMR of 8.

Figure 4.7.9 ^{1}H NMR of C1.

Figure 4.7.10 ^{13}C NMR of C1.

Figure 4.7.11 ^{1}H NMR of C2.

Figure 4.7.12 ^{1}H NMR of C3.

Figure 4.7.13 ^{13}C NMR of C3.

Figure 4.7.14 ^{1}H NMR of C4.

Figure 4.7.15 ^{1}H NMR of C5.

Figure 4.7.16 ^{13}C NMR of C5.

Figure 4.7.17 ^{1}H NMR of C6.

Figure 4.7.18 UV-vis (left) and photoluminescence (right) spectra of the six BBOs as thin-films.

Figure 4.7.19 Kinetic traces of the excited state absorbance (right column) and phosphorescent (left column) features. Excitation peak was taken from the maxima of each feature in the transient absorbance curves.

Figure 4.7.20 AFM images of the active layer of each OLED device.

Figure 4.7.21 Current-voltage-luminance data of the six BBOs.

4.7.1 Materials and Measurements

4,8-dibromo-2,6-diethylbenzobisoxazole, bis(hydrochloride) 2,5-diamino-p-hydroquinone and 2,4-diaminoresorcinol were synthesized according to literature procedures. THF was dried using an Innovative Technologies solvent purification system. All other chemical reagents were purchased from commercial sources and used without further purification unless otherwise noted. Nuclear magnetic resonance (NMR) experiments were carried out in $CDCl_3$ at 500 MHz (H^1) and 125 MHz (C^{13}). All chemical shifts are given relative to tetramethylsilane and coupling constants are reported in hertz (Hz). High-resolution mass spectra were recorded on a double-focusing magnetic sector mass spectrometer using ESI. Melting points were determined using a MelTemp II apparatus. Ultraviolet photoelectron spectroscopy (UPS) was used to acquire the ionization potentials and approximate the HOMO values for each material. All substrates (positively doped silicon; 10 × 10 mm2) had 40 nm of silver deposited via thermal evaporation. Samples were prepared by dissolution in CHCl3 at a concentration of 5 mg/mL and stirred for a minimum of 4 h. Each solution was filtered to remove potential aggregates and sequentially spin-coated under a nitrogen atmosphere at 4000 RPM. Spectra were then acquired under ultrahigh vacuum at random positions on the formed film. All UV-Vis and fluorescence spectroscopy were obtained using quartz cuvettes with a 10 mm path length in $CHCl_3$ for solution-state or as spin-cast thin films on a quartz slide (5 mg/mL solution in $CHCl_3$ spun at 1500 RPM). UV−vis spectra were collected on a Shimadzu UV-1800 UV spectrophotometer. Photoluminescence spectra were obtained on a Varian Cary Eclipse spectrophotometer.

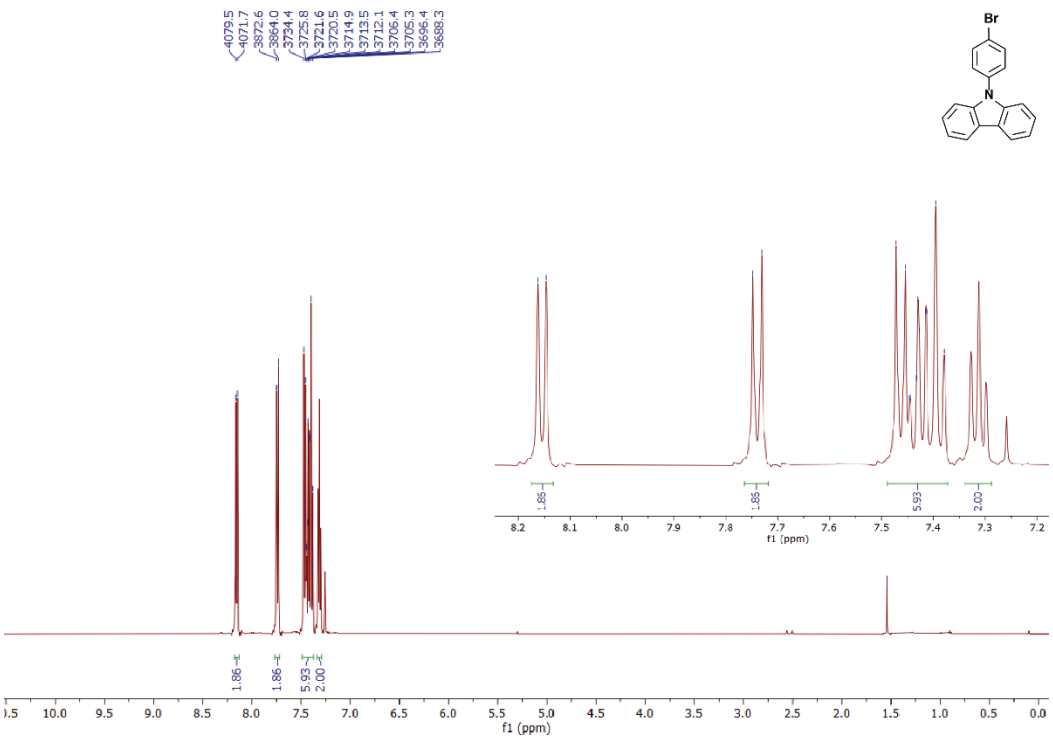


Figure 4.7.1. ^{1}H NMR of 1

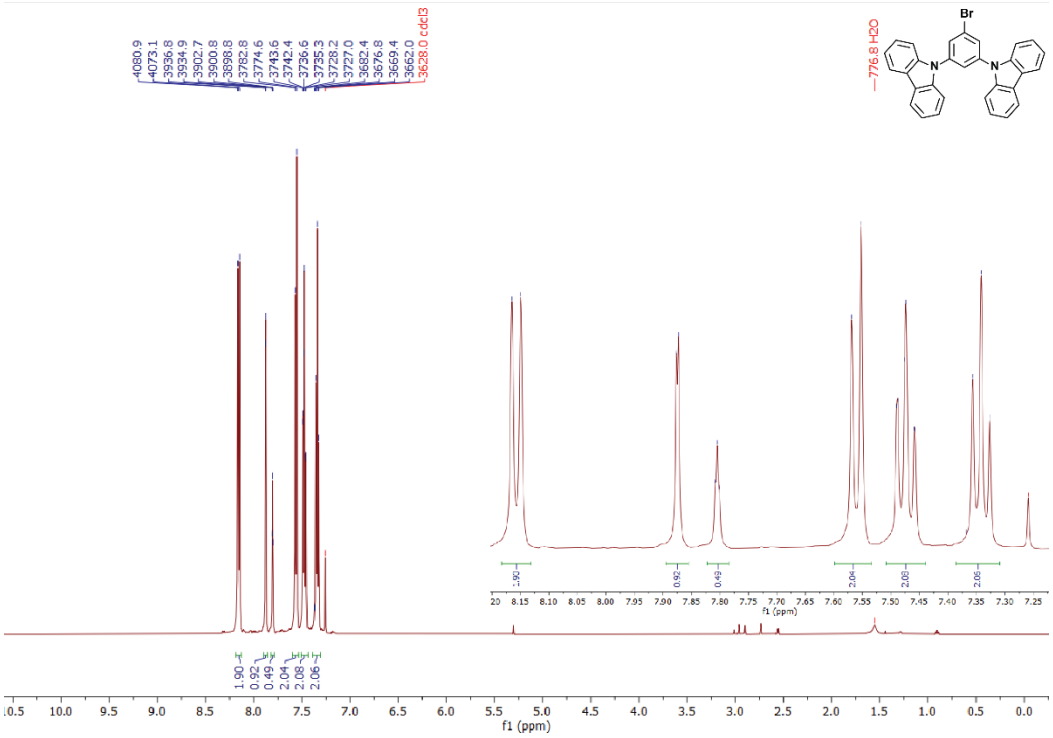


Figure 4.7.2. ^{1}H NMR of 2

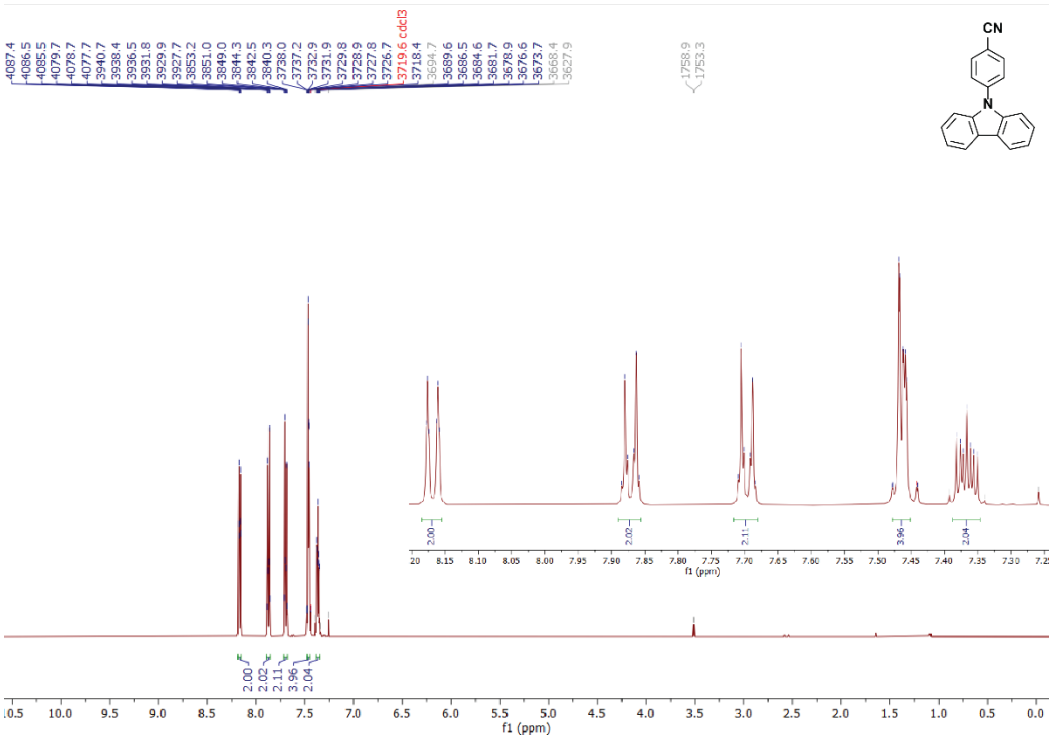


Figure 4.7.3. ^{1}H NMR of 3

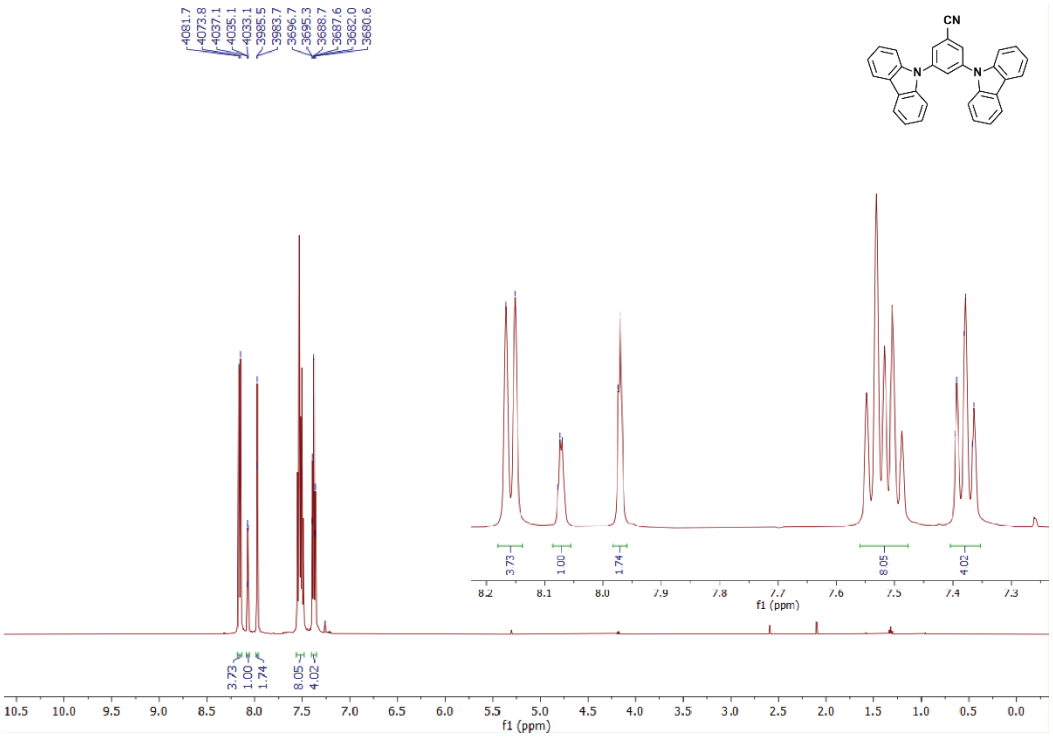


Figure 4.7.4. ^{1}H NMR of 4

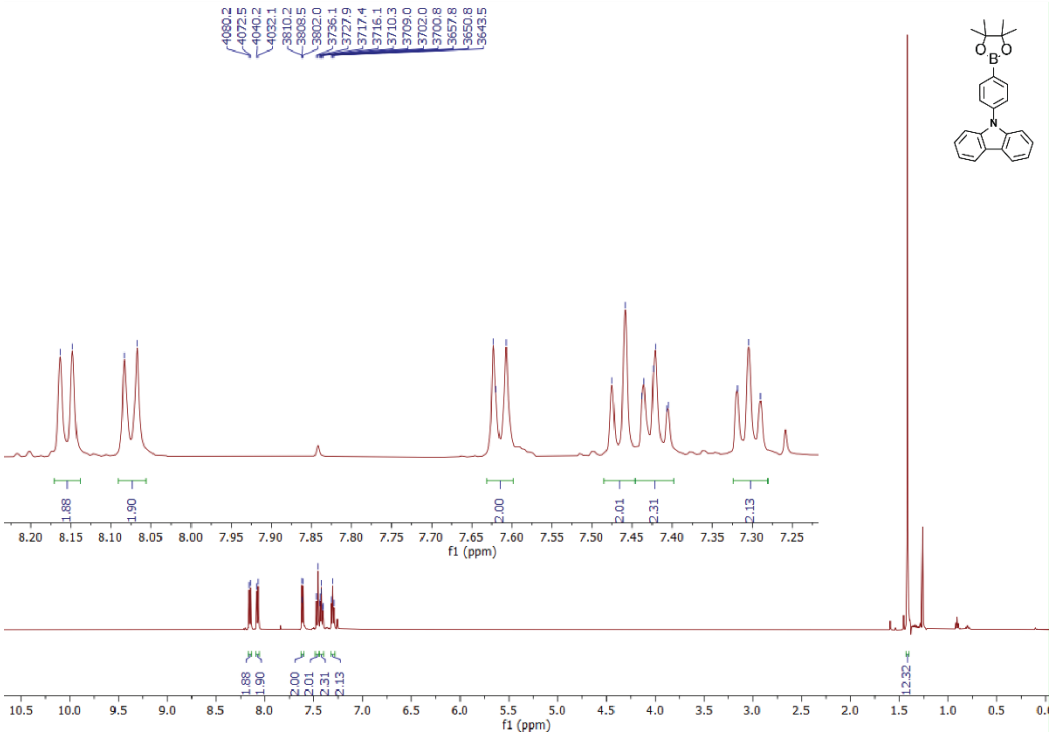


Figure 4.7.5. ^{1}H NMR of 5

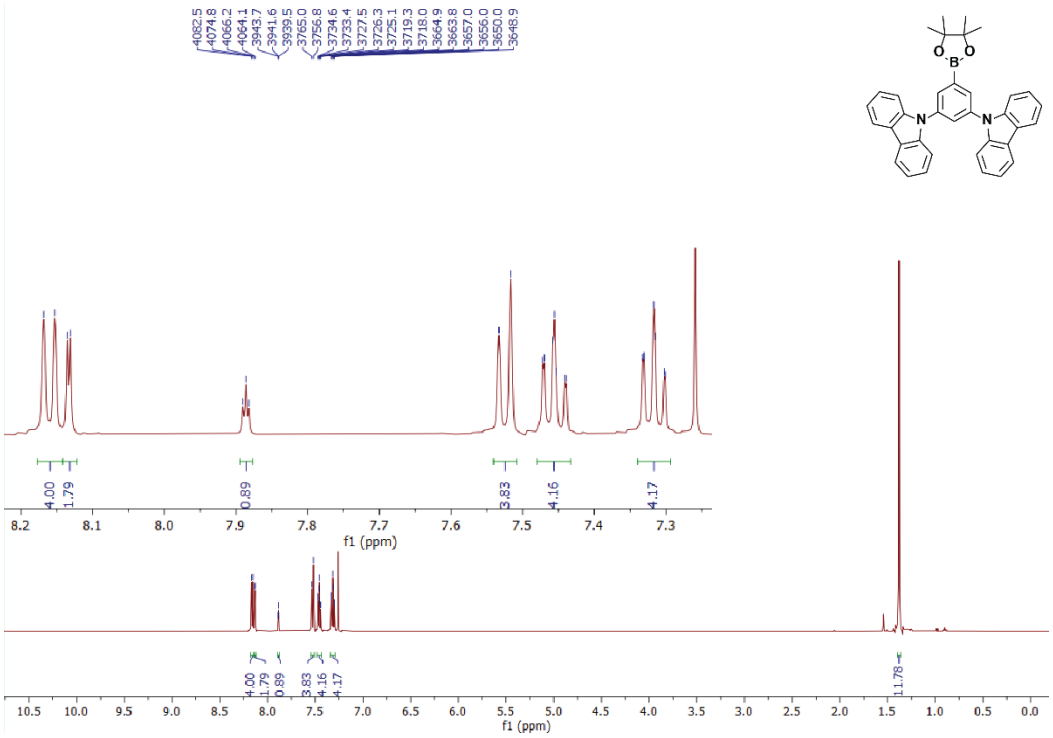


Figure 4.7.6. ^{1}H NMR of 6

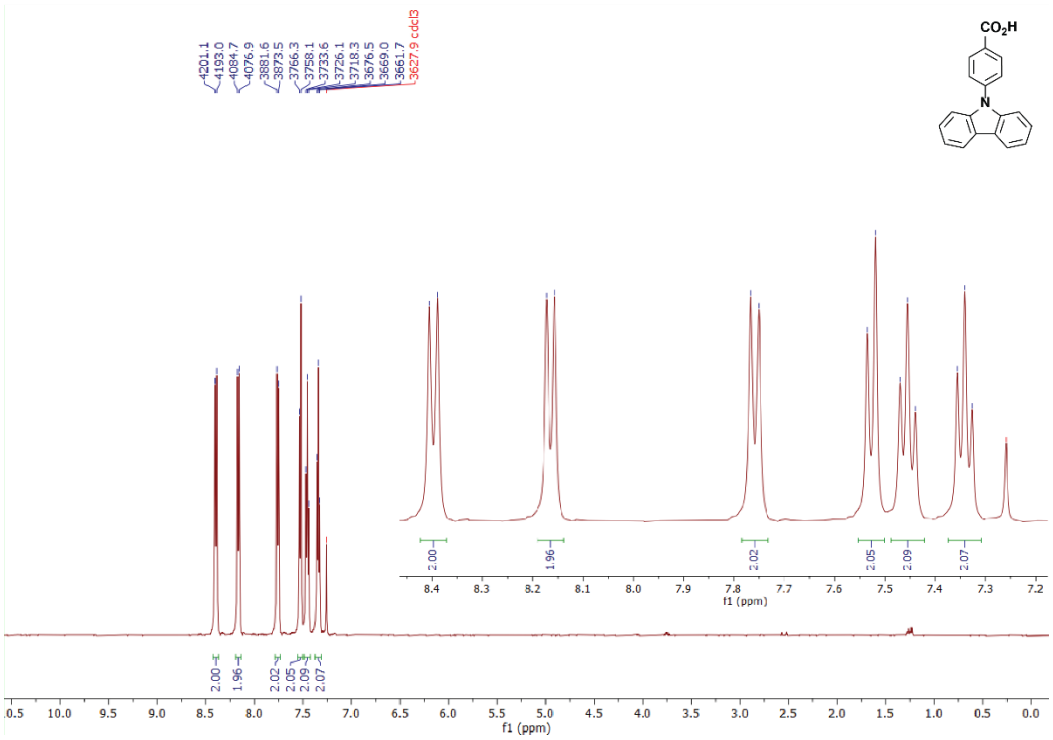


Figure 4.7.7. ^{1}H NMR of 7

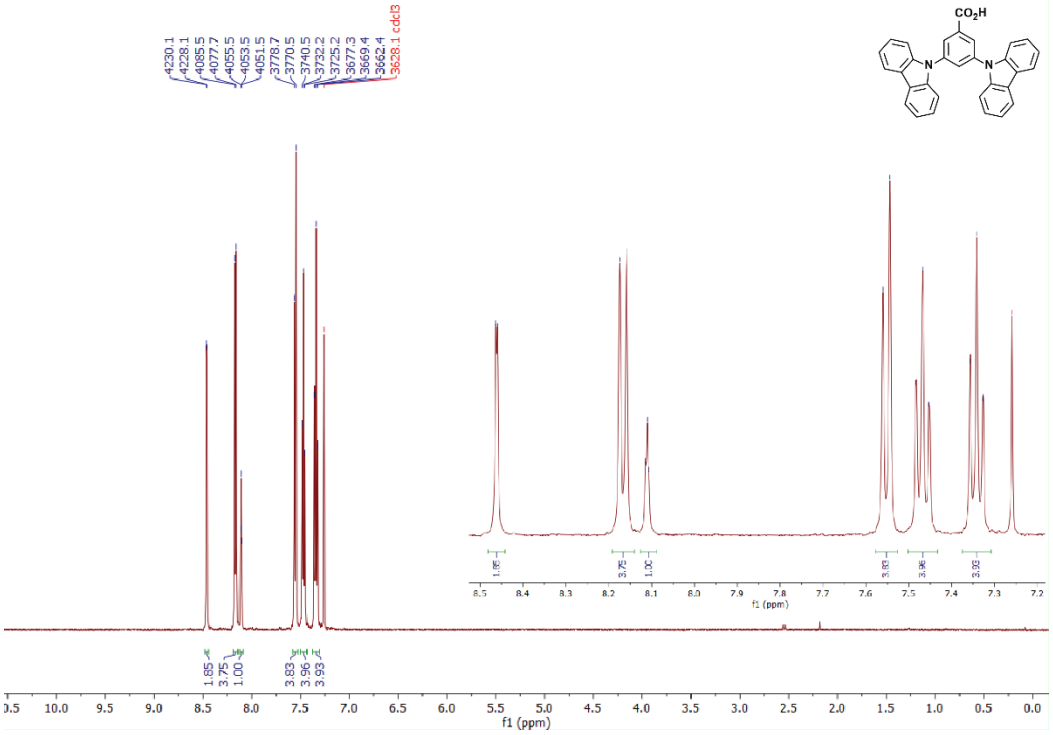


Figure 4.7.8. ^{1}H NMR of 8

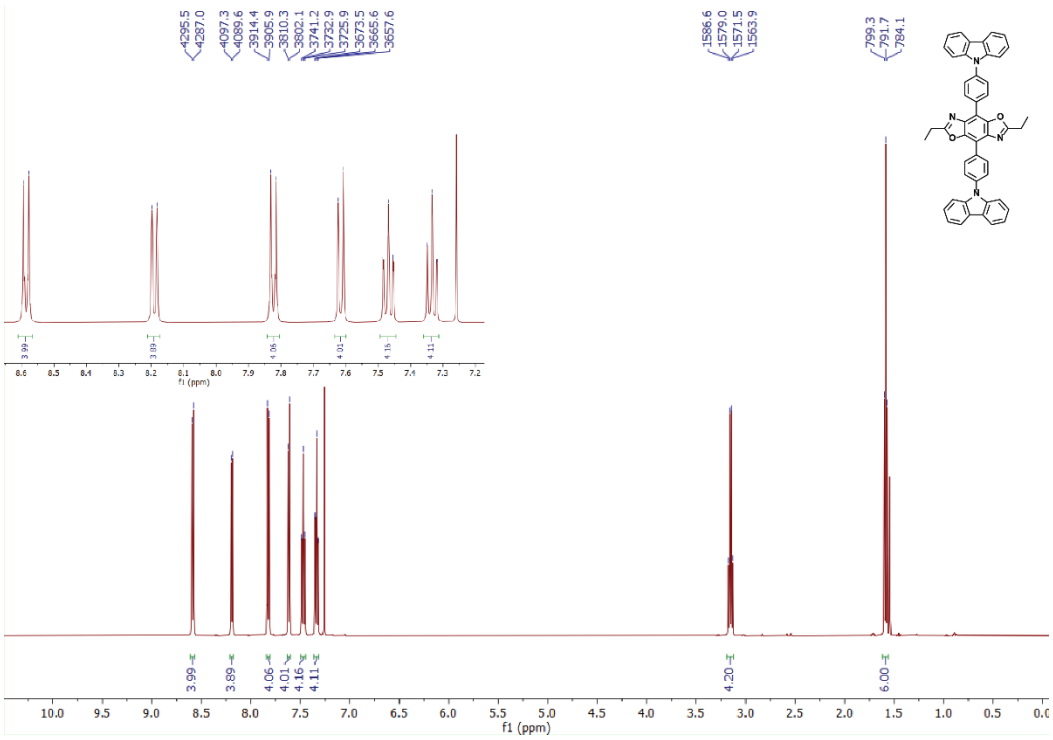


Figure 4.7.9. ^{1}H NMR of C1

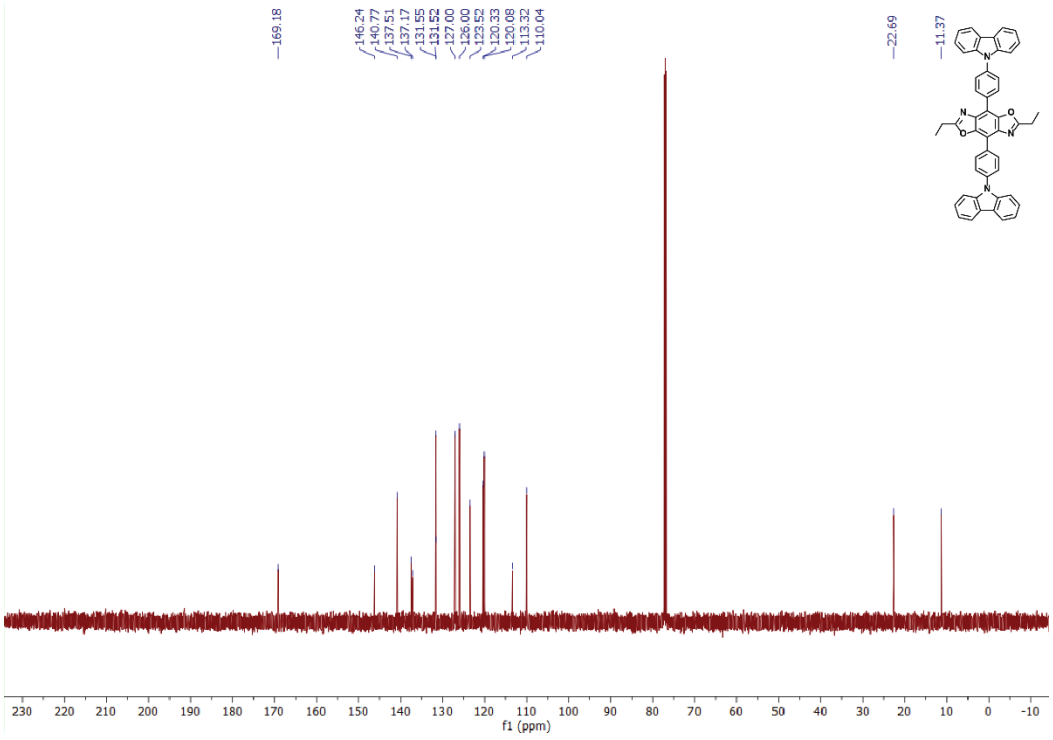


Figure 4.7.10. ^{13}C NMR of C1

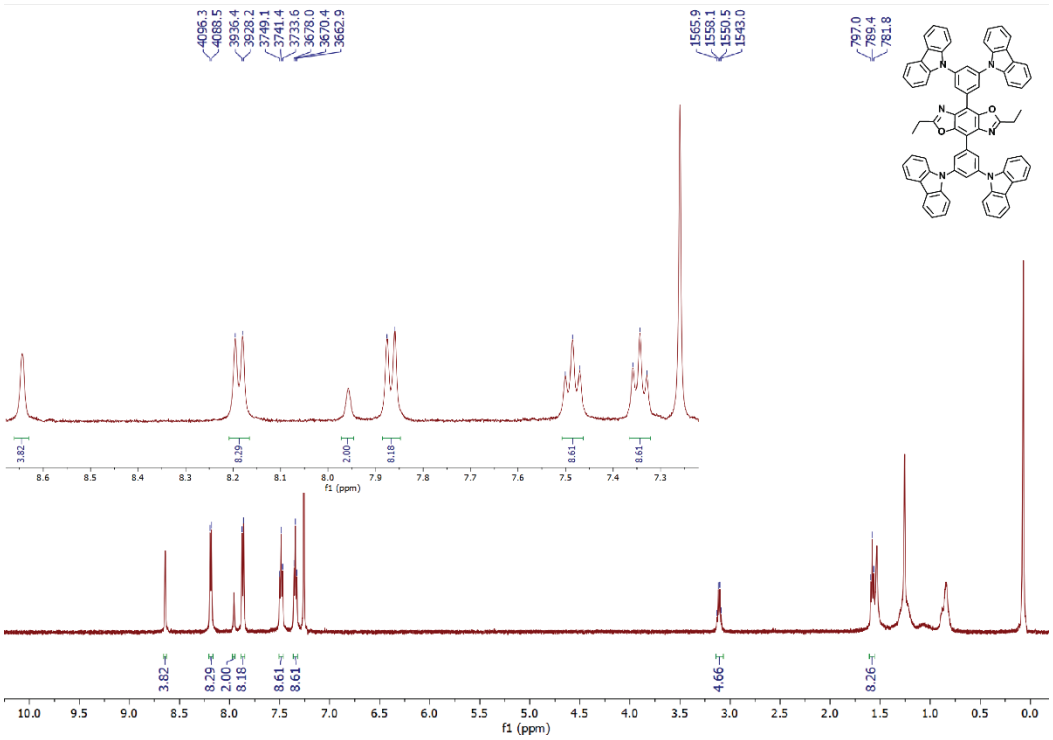


Figure 4.7.11. ^{1}H NMR of C2

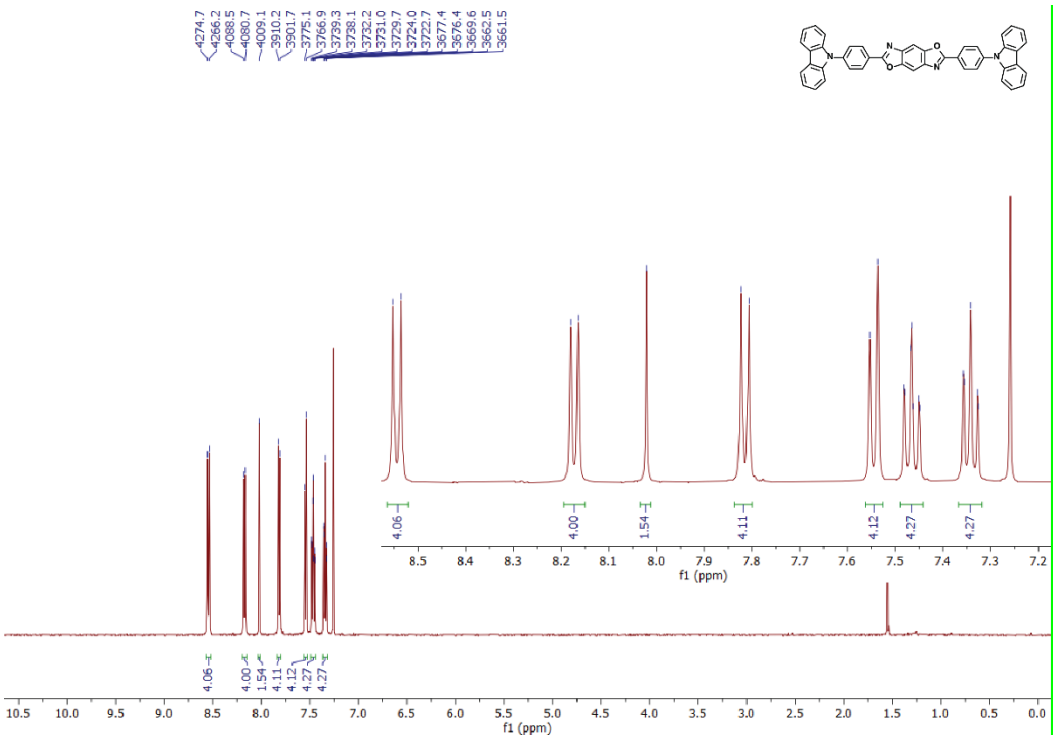


Figure 4.7.12. ^{1}H NMR of C3

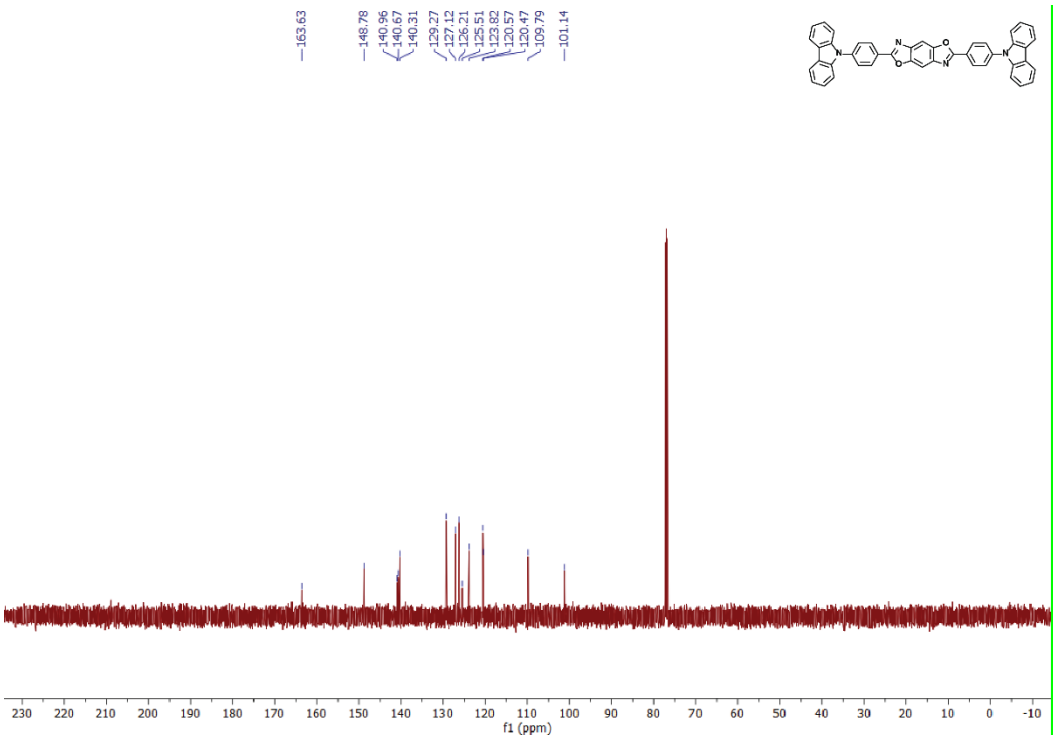


Figure 4.7.13. ^{13}C NMR of C3

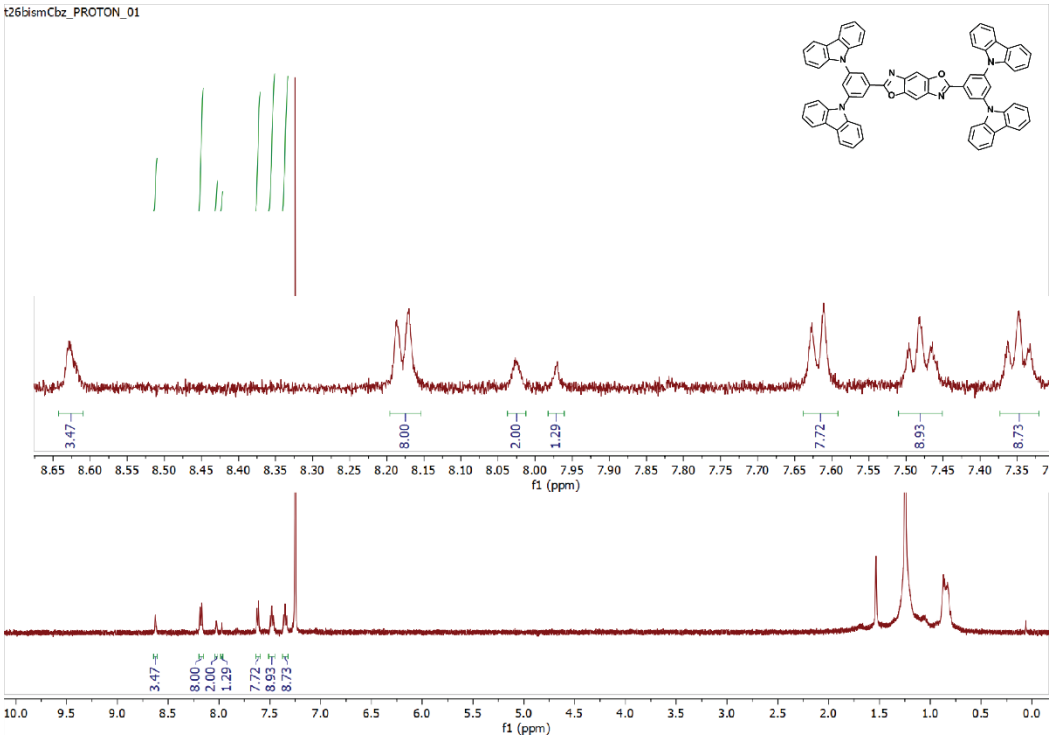


Figure 4.7.14. ^{1}H NMR of C4

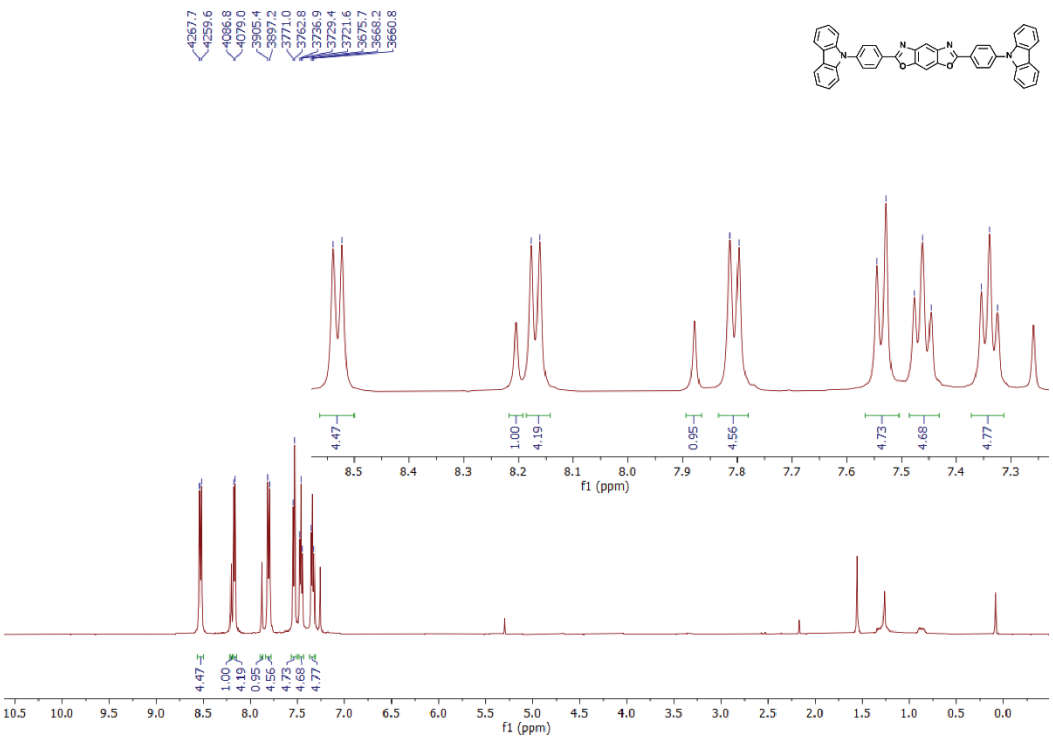


Figure 4.7.15. ^{1}H NMR of C5

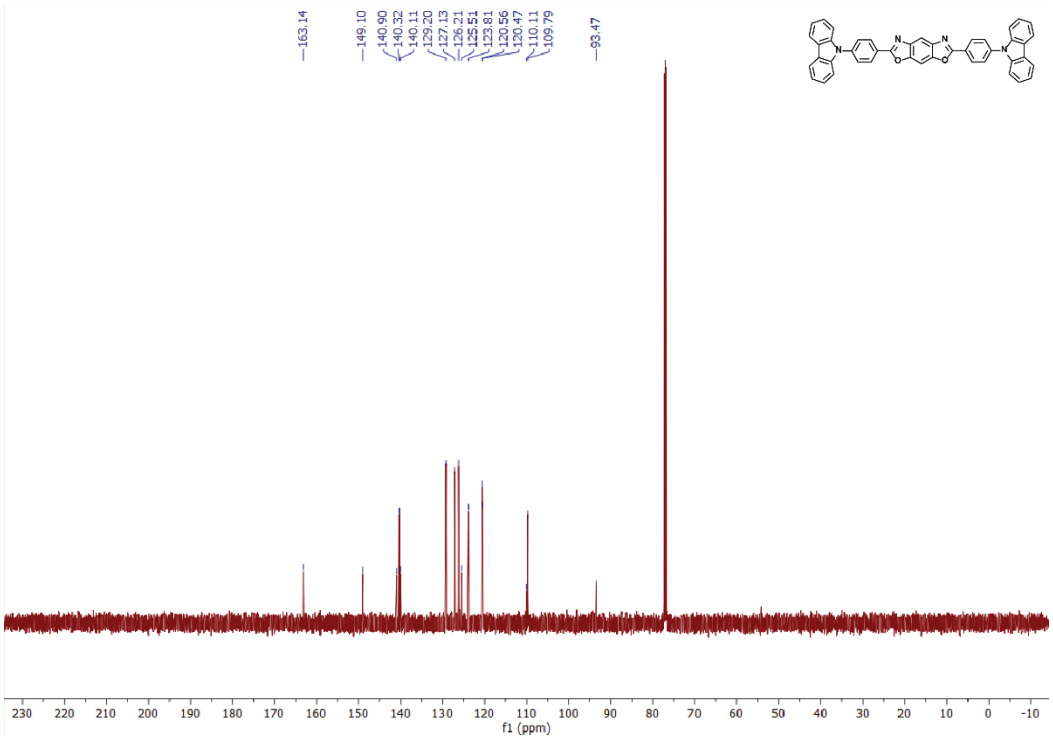


Figure 4.7.16. ^{13}C NMR of C5

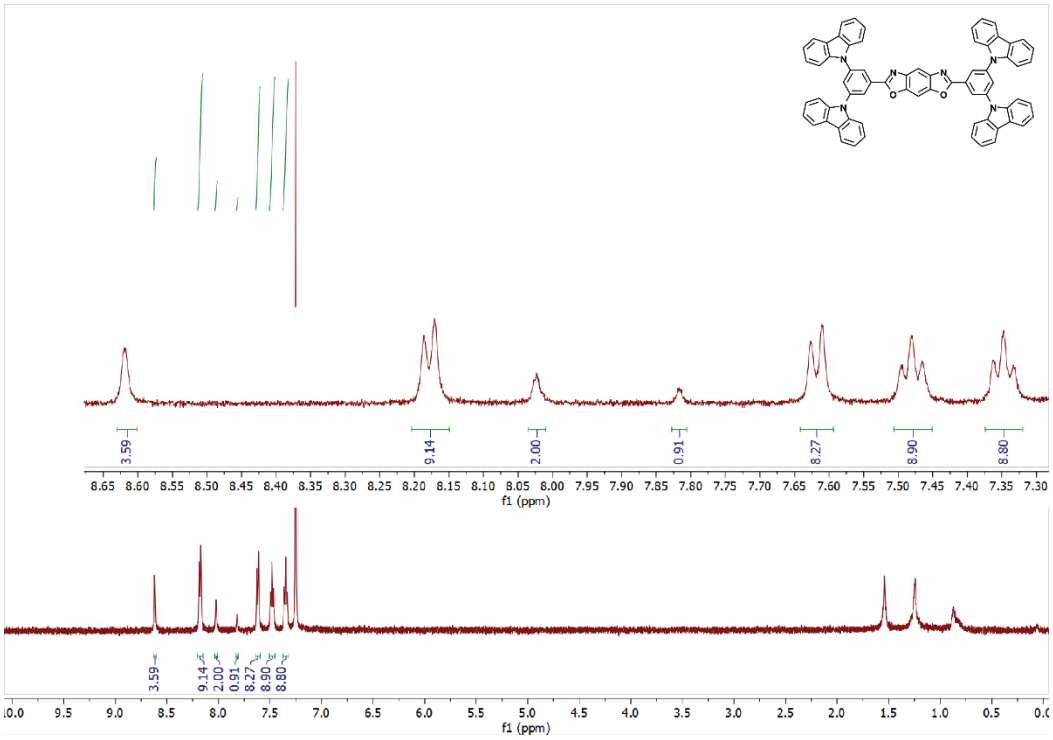


Figure 4.7.17. ^{1}H NMR of C6

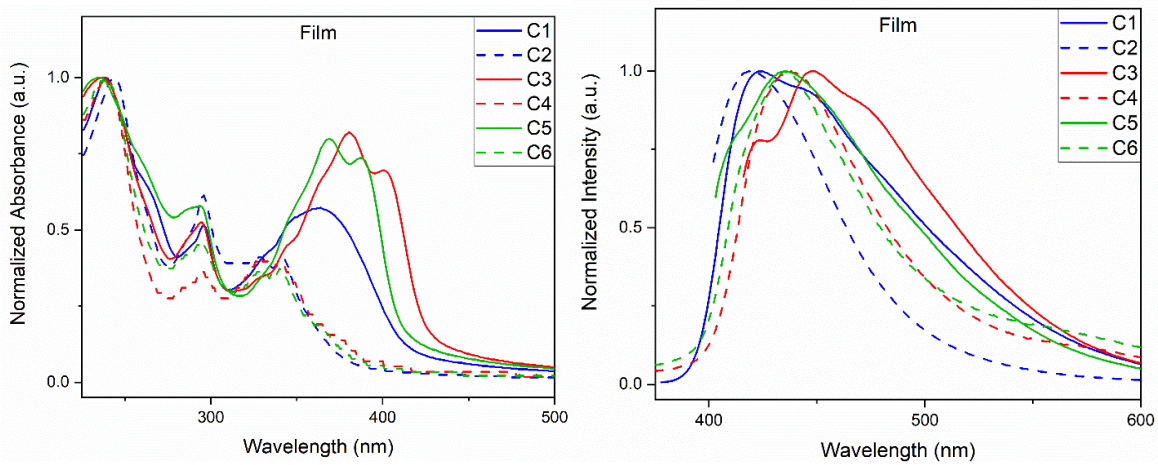


Figure 4.7.18. UV-vis (left) and photoluminescence (right) spectra of the six BBOs as thin-films.

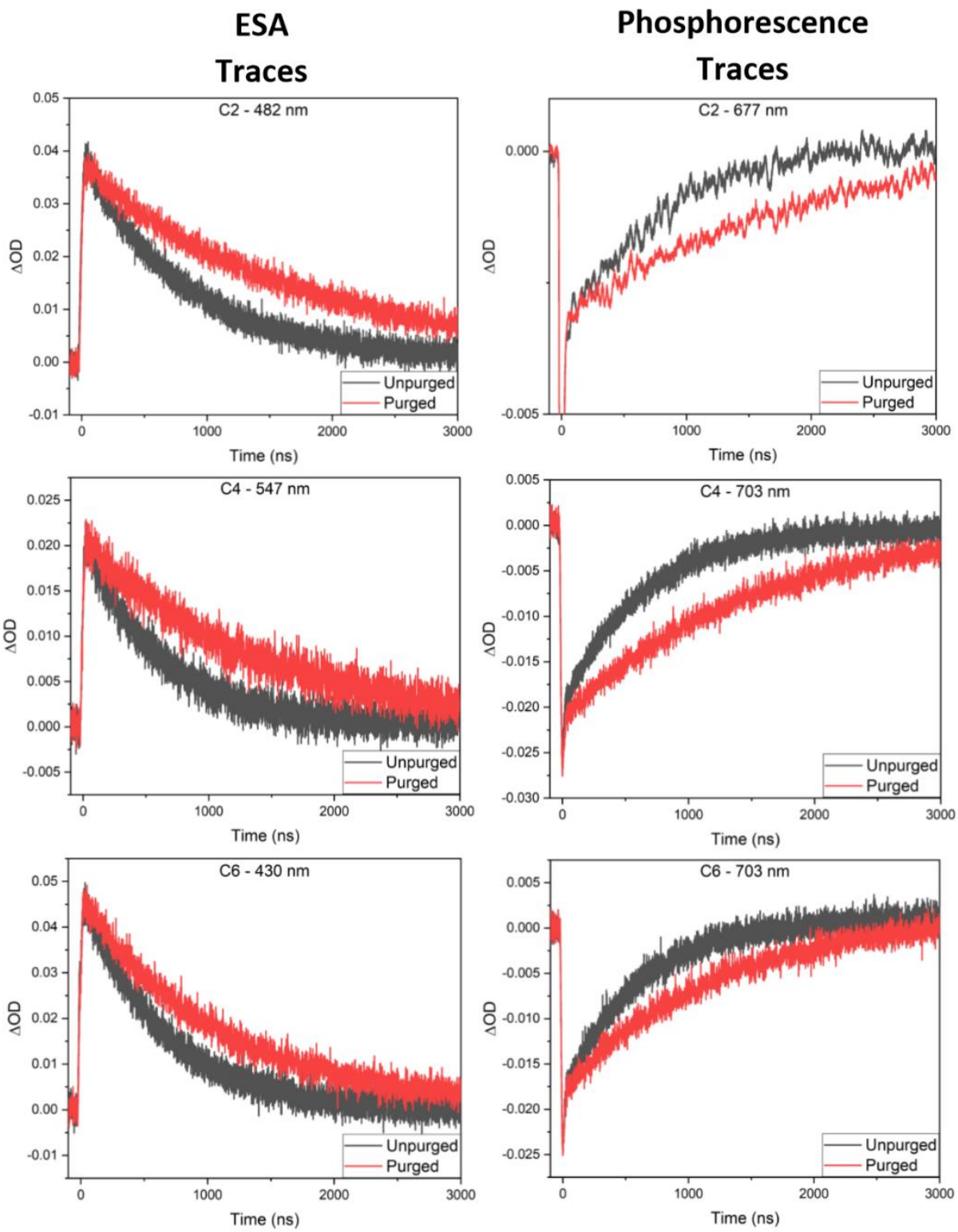
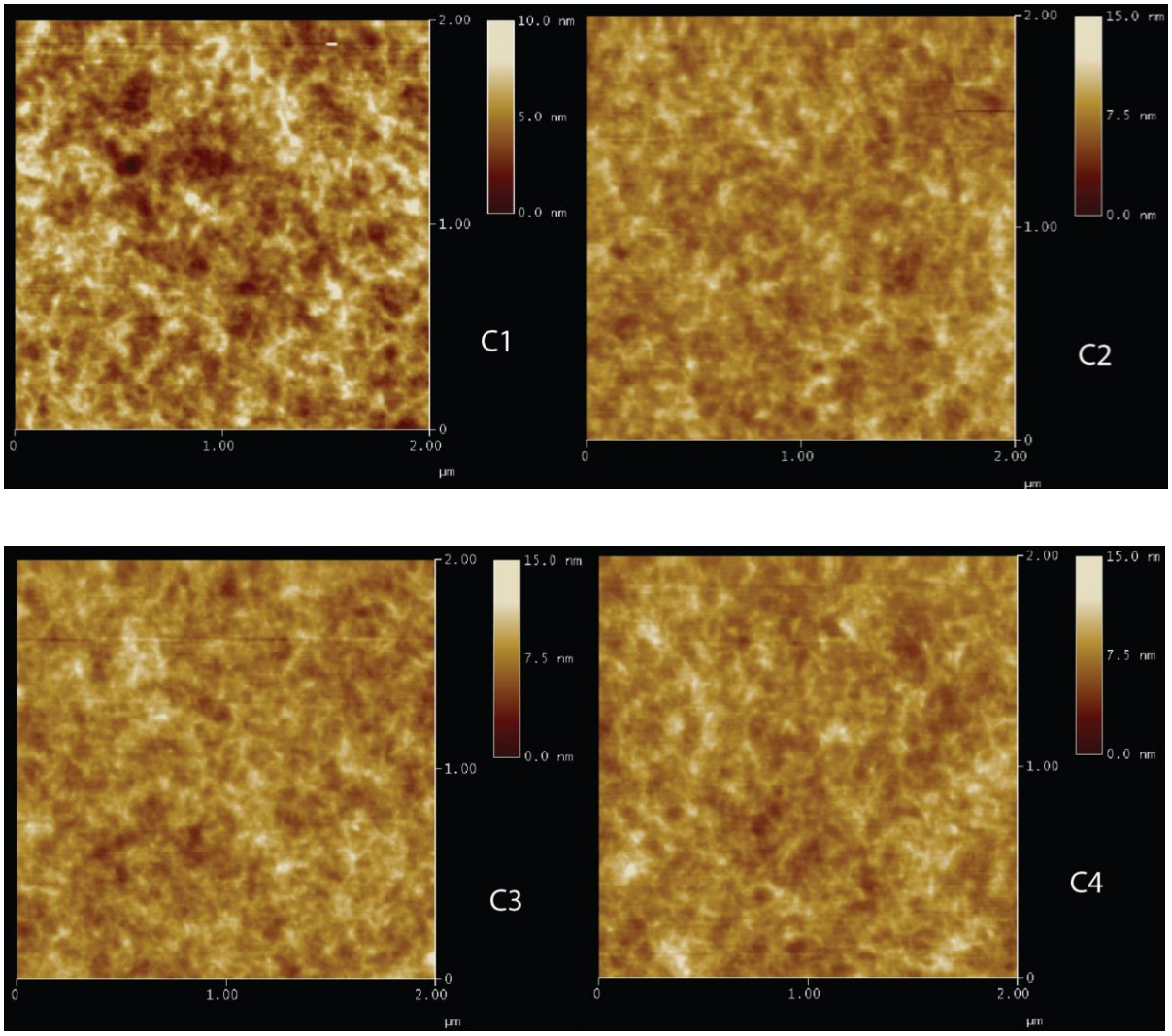

ESA
Traces
Phosphorescence
Traces
C2 - 482 nm
C2 - 677 nm
C4 - 547 nm
C4 - 703 nm
C6 - 430 nm
C6 - 703 nm
ΔOD
Time (ns)
Unpurged
Purged

Figure 4.7.19. Kinetic traces of the excited state absorbance (right column) and phosphorescent (left column) features. Excitation peak was taken from the maxima of each feature in the transient absorbance curves.



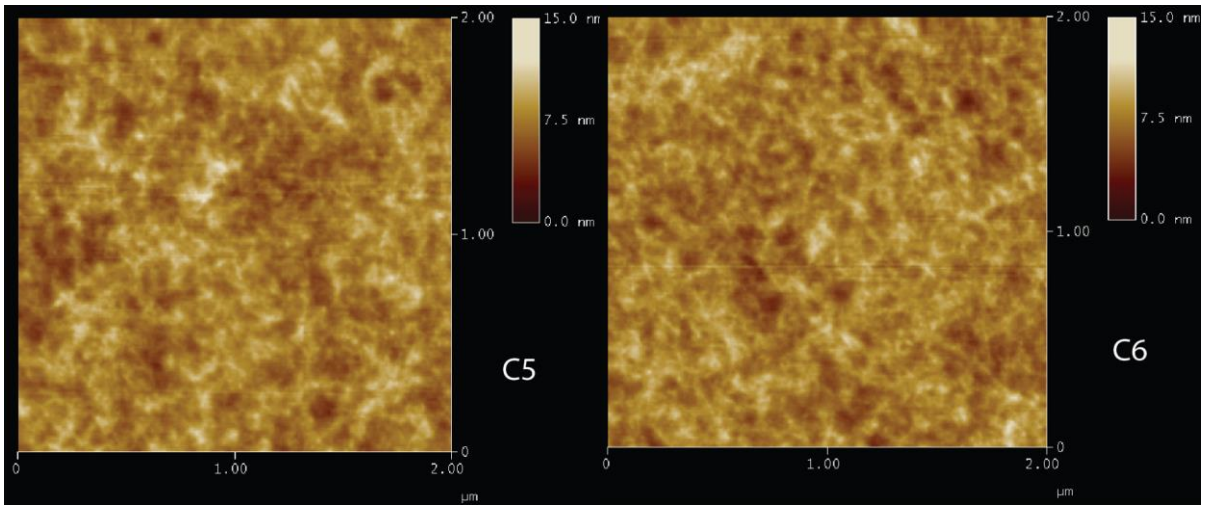


Figure 4.7.20. AFM images of the active layer of each OLED device.

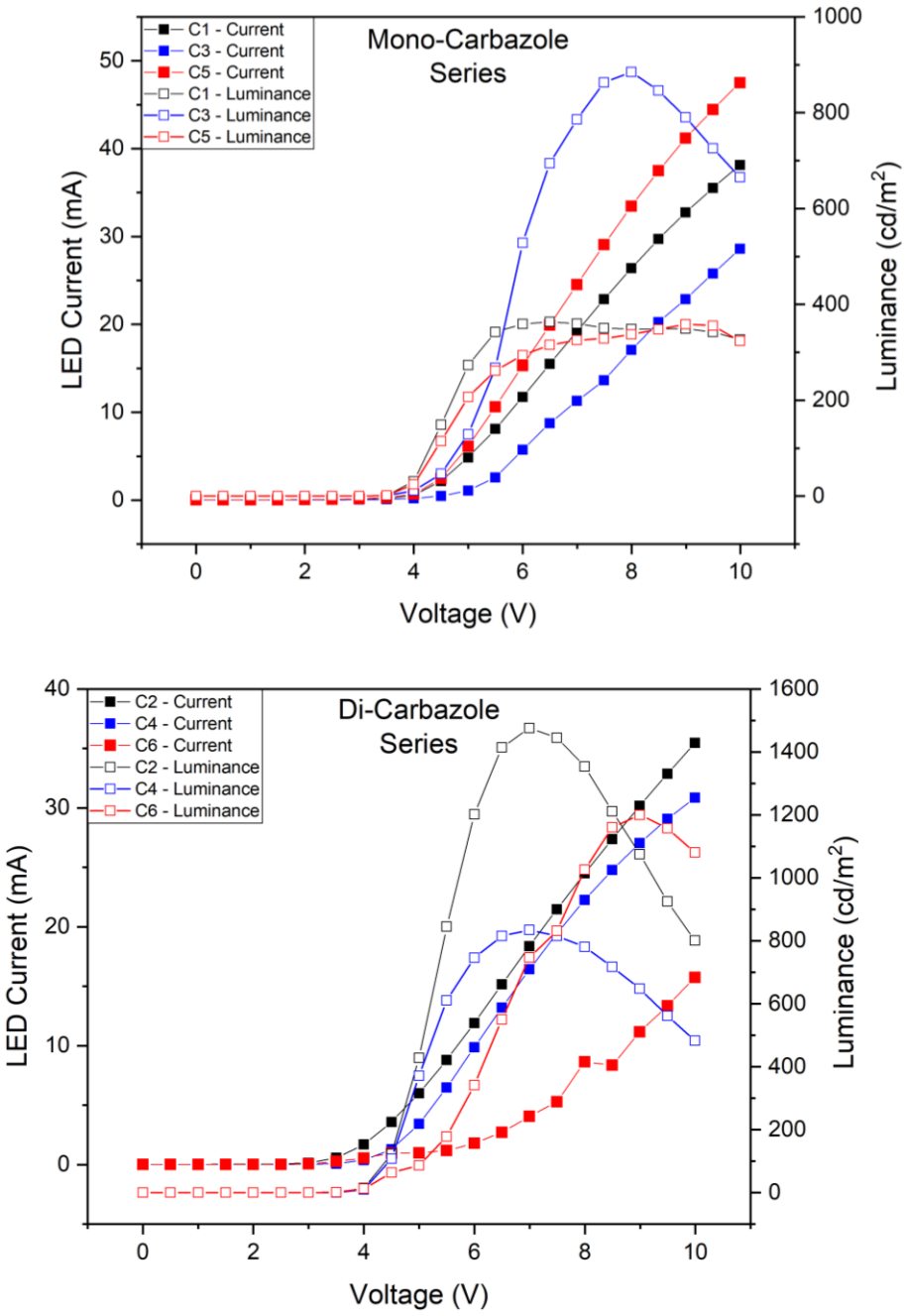


Figure 4.7.21. Current-voltage-luminance data of the six BBOs.

References

1. Tlach, B. C.; Tomlinson, A. L.; Bhuwalka, A.; Jeffries-EL, M. Tuning the Optical and Electronic Properties of 4,8-Disubstituted Benzobisoxazoles via Alkyne Substitution. *J. Org. Chem.* **2011**, *76* (21), 8670–8681.

2. Tlach, B. C.; Tomlinson, A. L.; Ryno, A. G.; Knoble, D. D.; Drochner, D. L.; Krager, K. J.; Jeffries-El, M. Influence of Conjugation Axis on the Optical and Electronic Properties of Aryl-Substituted Benzobisoxazoles. *J. Org. Chem.* **2013**, *78* (13), 6570–6581.
3. Mike, J. F.; Makowski, A. J.; Jeffries-EL, M. An Efficient Synthesis of 2,6-Disubstituted Benzobisoxazoles: New Building Blocks for Organic Semiconductors. *Org. Lett.* **2008**, *10* (21), 4915–4918.
4. Gidron, O.; Dadvand, A.; Sheynin, Y.; Bendikov, M.; Perepichka, D. F. Towards "Green" Electronic Materials. α-Oligofurans as Semiconductors. *Chem. Commun.* **2011**, *47* (7), 1976–1978.
5. Liu, Y.; Wu, P.; Jiang, J.; Wu, J.; Chen, Y.; Tan, Y.; Tan, C.; Jiang, Y. Conjugated Polyelectrolyte Nanoparticles for Apoptotic Cell Imaging. *ACS Appl. Mater. Interfaces* **2016**, *8* (34), 21984–21989..
6. Shcherbina, M. A.; Borshchev, O. V; Pleshkova, A. P.; Ponomarenko, S. A.; Chvalun, S. N. When Dendrimers Are Not Better – Rational Design of Nanolayers for High-Performance Organic Electronic Devices. *Nanoscale* **2019**, *11* (10), 4463–4470.

Chapter 5: A Spectroscopic Investigation to Better Understand the Changes in the Excited State Dynamics and Emissive Mechanism of BCC-TPTA from Solution to Solid-State

5.1. Overview

The work presented in this chapter is part of a study that seeks to determine what role guest-host interactions play in altering the excited state and emissive dynamics of the BCC-TPTA emitter. I have conducted all experiments and interpreted all data presented in this chapter. The results indicate that the guest-host interactions play a significant role in determining the emissive mechanism that will be utilized by the emitter, whether that be thermally activated delayed fluorescence, triplet-triplet annihilation up-conversion, or aggregate induced emission. It is determined that the emission from BCC-TPTA films is the result of a mixture of the aforementioned emissive mechanisms. Suggestions for future experiments that would further elucidate the specific guest-host interactions and to what degree aggregation plays in the emissive dynamics are also provided.

5.2. Abstract

Choosing the proper host material for the emitter is important for achieving organic light emitting diodes (OLEDs) with high external quantum efficiencies. As such considerable research is being conducting to better understand the influence of the host material on emitter photophysics. BCC-TPTA is an emitter that was reported to be a TADF-active emitter. However, it was determined by other previous investigations that BCC-TPTA does not display TADF-

characteristics, such as a two-component emission, in solution. Instead, it was determined that such TADF-characteristics are observed when placed in a film that utilizes DPEPO as the host material. In this contribution, steady-state and time-resolved spectroscopic techniques are utilized to the influence of the host material on the emitter excited state and emissive dynamics. Specifically, we investigate whether guest-host induced TADF-activity is unique to the BCC-TPTA/DPEPO interaction or can it be observed with other host materials with different physical and chemical properties. Our results indicate that the film emission is a result of multiple interactions and emissive mechanisms, and that the host material determines which of these emissive mechanisms are dominant. In particular, we observe not only TADF, but also triplet-triplet annihilation up-conversion and aggregate emission in solid-state films using BCC-TPTA as the guest emitter.

5.3. Introduction

There is an ever-growing need for high-quality organic light-emitting diodes (OLEDs) for use in various display technologies. One of the most pressing issues is how to best utilize the generated excited states. That is because, due to spin-statistics, 25% of the generated excited states are singlet (S_1) with the remaining 75% being triplet (T_1). Which of these excited states is used by the emitter directly impacts the theoretical maximum efficiency that an OLED can achieve.[1,2] Fluorescent OLEDs, for example, typically have external quantum efficiencies (EQE) within the single digits, due to them being limited to the 25% S_1. Conversely, phosphorescent OLEDs are able to achieve considerably greater EQEs due to having access to the 75% T_1.[3] They are able to utilize the T_1 due largely to their molecular design, which often incorporates a heavy meatal atom, such as iridium or platinum.[4] Such ions induce what is known as the *heavy atom effect*, and increases spin-orbit coupling between the singlet and triplet manifolds.[5,6] However, there are sustainability and cost

concerns with this class of emitters due to the rarity of the heavy metals they use.[7] There is also a need for efficient blue emitters for use in OLEDs, as the high energy required to achieve blue emission leads to material degradation and reduced device performance.[8]

One proposed alternative to phosphorescence-based OLEDs is thermally activated delayed fluorescence (TADF). TADF is the idea that typically non-emissive triplets can be up-converted to emissive singlets through the absorption of the thermal energy of the surroundings.[9] The singlet will then fluoresce to the ground state through what is known as *delayed fluorescence* (**Figure 5.3.1**). This would theoretically allow for 100% internal quantum efficiency, as the TADF mechanism allows for the utilization of both the triplet and singlet excited states. However, TADF is a rare mechanism that requires the emitter to have certain physical properties such as a small singlet-triplet energy gap (ΔE_{ST} = 0.2 eV) and sufficient separation between the HOMO and LUMO.[10–13]

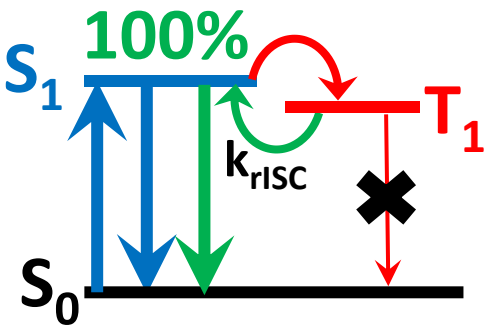


Figure 5.3.1. Diagram displaying the thermally activated delayed fluorescence mechanism.

There have been numerous investigations into the design and synthesis of TADF-emitters with appreciable EQE being achieved.[14–23] One common design strategy is to link a donor and acceptor via a phenylene bridge. However, there are drawbacks to this designs such as the ring bridged not being favorable for the separation of the HOMO and LUMO and the resulting high ΔE_{ST}.[24] One

method of circumventing this limitation is to utilize multiple donor units, a method employed by Hirata and coworkers.[15] Through this method they were able to develop an emitter with an internally quantum efficiency of nearly 100%, highlighting the possibilities of TADF emitters.

Another design strategy involves directly attaching the donor and linker unit without the use of a ringed bridge, allowing for relatively easy tunability of the emissive color.[25] However, this design motif could lead to room-temperature phosphorescence if the HOMO and LUMO aren't sufficiently separated. This issue can be overcome by attaching multiple identical donor or acceptor units. Incorporating multiple identical donors or acceptor units results in different π-conjugation patterns for the hole and electron wave function. This enhances the spin-orbit coupling between the singlet and triplet excited state manifolds, critical for high k_{rISC}.[10] One could also increase the strength of the donor unit, which should ideally have a smaller HOMO/LUMO energy gap than the previous donor, resulting in a lower HOMO/LUMO energy gap for the overall emitter. This is because lowering the HOMO/LUMO energy gap of the donor or acceptor subunit stabilizes the lowest lying triplet excited state with charge-transfer character, critical for efficient reverse intersystem crossing.[10,13,26,27]

With the various design strategies explored for TADF, it would be useful for the establishment of structure-function relationships between emitter design and resulting TADF-activity. To this end, our lab has conducted spectroscopic measurements on emitters that utilize either the donor-linker-acceptor design or multiple donor-directly linked to the acceptor. One such study was conducted by Ricardo and coworkers on the reported TADF-active emitter, BCC-TPTA.[28] In this study it was determined that BCC-TPTA is not TADF-active. This determination was due to none of the characteristics expected of a TADF-emitter, such as a second long-lived emissive component or triplet excited states, being observed in either unpurged or purged solution.

Our most recent investigation focused on comparing the two design motifs and determining which of these design strategies better achieved TADF-activity.[29] The structures of the investigated compounds are displayed in **Figure 5.3.2**. We found that the emitters that incorporate a linker in their design, Cbz-Trz and its derivatives, are less suited for TADF. The lack of TADF-activity was determined to be due to the linker impeding sufficient HOMO/LUMO separation for the investigated emitters. In contrast to this, the emitters that directly linked the acceptor, 2Cbz-PN and its derivatives, are TADF-active in even in solution. This is due to this design lending itself to better HOMO/LUMO separation. This separation, and subsequent k_{rISC}, was enhanced when the carbazole donor was replaced with either the BFCbz or BTCbz donor groups. Based on these results, it was determined that directly linking the donor to the acceptor unit is the design that is better suited to TADF-activity.

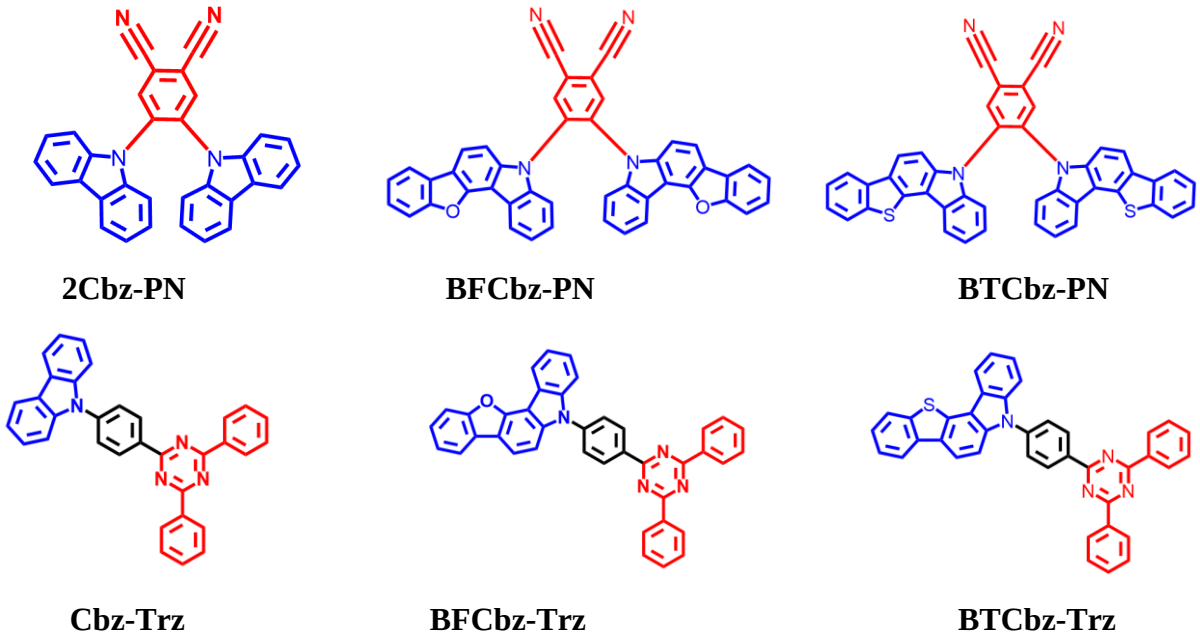


Figure 5.3.2. The emitters investigated in our most recent spectroscopic study of relating TADF-activity to emitter structure.

However, the design of the emitter is not the only metric of note when discussing TADF systems. Various studies have been conducted to determine the influence of the host material on the emissive mechanism. These investigations have reported that the host plays a major role in altering the singlet-triplet energy gap, the emission color, degree of aggregation, and protection of the triplet excited states.[30–37] The host material can even induce TADF-activity in a TADF-inactive emitter, as reported by Wu and coworkers in their investigation on guest-host interactions.[38] In their study, they describe the possibility for a transient triplet charge transfer exciplex to exist between the BCC-TPTA emitter and DPEPO host material. This exciplex is utilized as a bridge between BCC-TPTA's singlet and triplet local exciton states and facilitates TADF.

The host material also plays a significant role in controlling the degree of emitter aggregation.[39–42] This is an important metric to consider when choosing a host material, as aggregation has been shown to cause emission quenching which is detrimental to device performance.[43] However, studies have reported that TADF can be achieved through aggregation, converting a previous determinant into a benefit.[44] The aggregation induced TADF has been attributed to sufficiently strong $\pi-\pi$ stacking and intramolecular hydrogen bonding.[45,46]

There are also investigations that report a similar mechanism to TADF that occurs alongside it, this mechanism being triplet-triplet annihilation up-conversion (TTA-UC). While TTA-UC is similar to TADF, in that they both convert non-emissive triplets into emissive singlets, it is quite different in mechanism. This is largely due to TADF being a monomolecular process, whereas TTA-UC is a bi-molecular process where two emitters in the triplet excited state interact with each other and an emissive singlet state is produced.[47–51] Just as with TADF, there are various ways to achieve TTA-UC such as guest-assembly and host mediated TTA-UC, molecular aggregation, and how well the host material confines the triplet energy of the emitter.[42,52–55] As

the approaches to achieving TTA-UC are so similar to TADF, it would be easy to mistake one for the other. Thus, it is important to perform the proper experiments to determine which is taking place in a particular system.

One such experiment would be to determine the dependence of emission intensity on the excitation energy. In this experiment, the emission intensity is obtained as the energy of the excitation beam is altered. A log-log plot of integrated emission intensity vs excitation energy is created. The slope of this plot provides information regarding the emissive mechanism of the investigated system. A slope of one is indicative of a monomolecular emissive process, such as fluorescence, phosphorescence, or TADF. A slope of two is indicative of a bimolecular emissive process, such as TTA-UC.[56] Finally, a slope of 0.5 is indicative of a bimolecular emission quenching mechanism or dimer emission.[57] These slopes can change over the range of the excitation energy, such as a TTA-UC system giving a slope of two at low energies and then changing to a slope of one at higher energies.[47,50,51,58] This is due to the triplet population increasing significantly at the higher energies, thus increasing the rate of TTA-UC and giving the appearance of a monomolecular mechanism. Thus, it is important to cover a wide range of excitation energies to properly determine the emissive mechanism of a system.

In this contribution, multiple steady-state and time-resolved spectroscopic techniques are utilized to elucidate the changes in the excited state dynamics of the BCC-TPTA emitter when it is placed in solid-state host materials. We focus on determining the influence of the environment on the excited state and emissive dynamics of BCC-TPTA when in dilute solutions, aggregate solutions, and different host materials (**Figure 5.3.2**). In our investigation we observe the development of a second emissive component when emitter aggregation is induced. An enhancement of this second emissive component is observed when BCC-TPTA is placed in most

host materials. It is widely accepted that a two-component emission is a characteristic of the TADF mechanism.[2,15,16,59,60] However this is not the only metric of note, as TADF-activity should also be accompanied by fluorescent quantum yield (Φ) enhancement, significant triplet excited state lifetime, and a single emissive maximum. Through our measurements we observed a decrease in Φ, varying triplet state lifetimes that are dependent on the emitter environment, and multiple emissive peaks in the time-resolved emission spectra. In addition to this, emission intensities of the films displayed a mixture of monomolecular and bimolecular dependence on laser excitation energy. These results indicate that while TADF may be induced by guest-host interactions, it is not the only emissive process that occurs in solid-state films. It is thus determined that the observed emissive and excited state dynamics are the result of a combination of guest-host interactions and emitter aggregation.

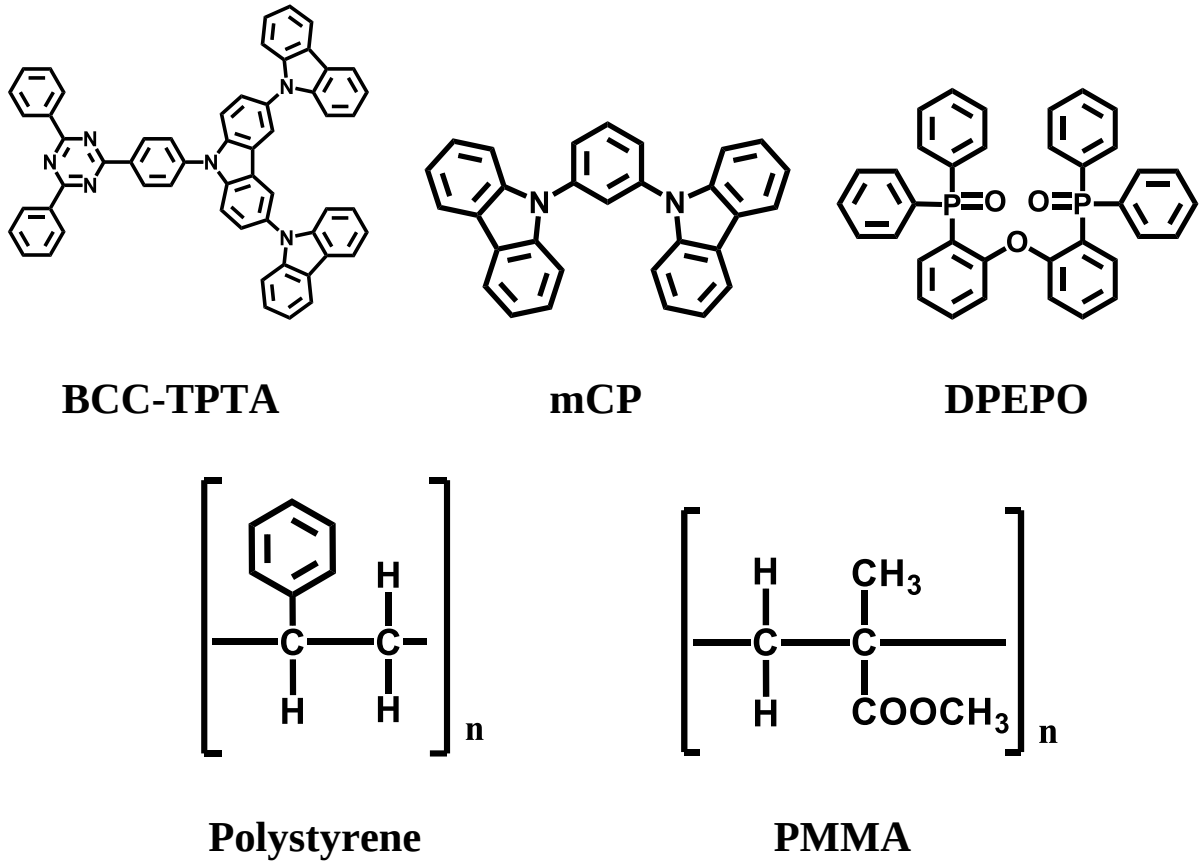


Figure 5.3.3. Molecular structures of the BCC-TPTA emitter and host materials used in this study.

5.4. Experimental Methods

5.4.1. Aggregate Solution and Film Fabrication. The aggregate solutions were made using different fractions of THF and water.[43,61,62] The concentration of BCC-TPTA remained constant for each solution. This was ensured by creating a stock solution of BCC-TPTA in THF. Using a micropipette, 0.1 mL of this stock solution was added to the required amount of pure THF. The proper amount of water was then added to this solution to create 0%, 20%, 40%, 60%, 80%, 99% H_2O fractions.

The 5wt% BCC-TPTA solid-state films were fabricated by weighing out 5 mg of BCC-TPTA and 95 mg of bis[2-(diphenylphosphino)phenyl] ether oxide (DPEPO), 1,3-bis(N-

carbazolyl)benzene (mCP), polymethyl methacrylate (PMMA), and polystyrene (PS), respectively. These were then dissolved in 1.5 mL of chloroform and the resulting solutions were spin-casted on cleaned quartz substrate at 1500 rpm for 20 seconds. The newly spin-casted film was then dried in an oven for 15 minutes at 80 ºC.

5.4.2. Steady-State Absorption and Emission. The absorption and emission spectra were obtained using an Agilent 8341 spectrophotometer and FluoroMax-4 fluorimeter respectively. The acquisition settings for obtaining the emission spectra had the entrance slits and exit slits of the fluorimeter each set to 1.0 nm, a step-size of 1 nm, and an integration time of 0.1 s. Quartz cuvettes with a 1.0 cm pathlength were used for all the solution measurements.

5.4.3. Absolute Photoluminescence Quantum Yields. The absolute photoluminescence quantum yields of each sample were obtained using a Horiba Fluorolog-QM equipped with a 75 W Xenon arc lamp as the excitation source and a Horiba QuantaPhi-2 integrating sphere. For these measurements the films were fabricated on glass substrate.

5.4.4. Time-Correlated Single Photon Counting. The time-correlated single-photon counting (TCSPC) technique, used to obtain the emissive lifetime of the different samples, has been described previously.[28,29,63] The decay lifetimes were obtained by using a mono- or dual-exponential fit to log plots of the decay traces as appropriate. The TCSPC system utilizes an output beam of 800 nm from the Kapteyn Murnane mode-locked Ti-sapphire laser with a pulse-width of ~30 fs. The 800 nm output beam is frequency-doubled to 400 nm by focusing it on a nonlinear BBO crystal. The beam is then directed to the sample cuvette (quartz, 1.0 cm pathlength) or film (quartz substrate) using a lens with a focal length of 11.5 cm. The sample emission is collected perpendicularly to the incident beam, with the monochromator being set to the sample's emission maximum. The output of the monochromator is coupled to a photomultiplier tube.

5.4.5. Nanosecond Transient Absorption and Time-Resolved Emission Spectra. The time-resolved emission and transient absorption spectra of the samples were collected using the nanosecond transient absorption system which has been described previously.[28,29,59] The LP980 spectrometer (Edinburgh) is coupled with a Spectra-Physics QuantaRay Nd:YAG nanosecond pulsed laser (pulse width of <10 ns and fundamental 1064 nm energy of 850 $(mJ/p)^2$) and GWU optical parametric oscillator (OPO) with at tunable excitation wavelength range of 250 nm to 2600 nm. The excitation beam was tuned to 343 nm to obtain time-resolved emission spectra. The excitation beam was directed to the sample cuvette (quartz, 1.0 pathlength) or sample film (quartz substrate). Both the transient absorption and time-resolved emission measurements are discussed in greater detail in in Section 2.6.

5.4.6. Emission Intensity vs Laser Excitation Energy. Log/log plots of integrated emission intensity vs the laser excitation energy have been used to determine whether the emissive mechanism is a monomolecular or bimolecular process.[47,56,64] Specifically, the slope of the log/log plot provides this information, where a slope of 1 is related to the monomolecular emission and a slope of 2 is related to a bimolecular emission mechanism. This is similar to the two-photon absorption experiment discuss in Section 2.3. As the Vázquez method could not be used to determine k_{rISC} for aggregate solutions or 5wt% films, a new experimental setup was constructed using the nsTAS system as a base.[28]

In this setup, the Nd:YAG-OPO laser system is used as normal to generate the excitation beam at the appropriate wavelength. The beam is then directed to a neutral density filter to adjust the energy of the excitation beam that enters the sample chamber. A glass slide, placed after the neutral density filter, then directs approximately 15% of the beam energy to a power meter that is placed at a fixed position. It is important to note that the glass slide and power meter both being fixed to

one position throughout the measurement is critical for accurate determination of the laser energy as it excites the sample. The remaining 85% of the laser then enter the sample chamber and interacts with either a solution or film sample, held in the previously unused Edinburgh Laser-Induced Emission or Edinburgh Thin-Film sample holder, respectively. Note that the angle at which the excitation beam interacts with the film sample will affect the observed emission intensity. Thus, it is recommended that the film sample holder be set at a 45^{o} angle throughout the measurement.

The settings of the LP980 software will affect both the speed and clarity of the measurement, similar to what's described in **Section 2.6**. Recommended settings are to have a step-size of 5 nm with an average of 1, as this experiment only aims to determine the emission intensity as a function of the laser excitation energy and emission intensity is typically well above the noise level. Users of this new setup should measure the emission intensity at the highest laser intensity they plan to use, being sure to set the bandwidth so that the emission signal does not surpass 0.6 (A.U.) in the software. This bandwidth setting should remain fixed during the measurement so that an accurate determination of the effect of laser energy on emission intensity can be made.

The user should also take note to not switch the nsTAS system from external to internal triggering between scans, as the laser energy will be different between these settings. Instead, the user should set the instrument to run in the Setup window during internal triggering to keep the laser energy consistent between measurements. Users should also wait for approximately 30 seconds when measuring the laser energy after the neutral density filter, to ensure that the laser energy is stable. The laser energy should also be monitored during the emission scan to be sure that no spikes in laser energy occur during the measurement that would affect the final results.

The obtained results will be the same as the time-resolved emission spectra, though with decreasing emission intensity as the laser energy is lowered. When analyzing the results, the user should slice the spectra the same way for each laser energy. I suggest a slicing up to 1000 ns and 100 slices. Then, using the integration function of the Origin Software, obtain the integrated emission intensity of a single slice (say 50 ns). It is important that the same slice be used across the analysis, so if the user choses 50 ns for the first emission scan that same time should be used for each consecutive scan. Within Origin, the user should then create a log-log plot of the integrated emission vs the laser excitation energy. The slope of the plot can now be obtained and provide information regarding the emissive mechanism utilized by the sample.

5.5. Results

5.5.1. Steady-State Absorbance. The steady-state absorption spectra of BCC-TPTA in the 0% and 80% H_2O fractions and different host materials are displayed in **Fig. 5.1.1.1** with the remaining THF/H_2O fractions being presented in **Figure 5.8.1.** The relevant data is summarized in **Table 5.5.2.1**. Multiple absorption bands typical of charge-transfer compounds are observed. The high energy peaks (<350 nm) are attributed to the n-π^* transitions of the carbazole units of the BCC-TPTA emitter.[65–67] The lower energy shoulder (>350 nm) is attributed to the charge-transfer state.[28]. Slight broadening of the charge-transfer band is observed at the 80% H_2O fraction where aggregates are most likely to form. This is accompanied by a slight red-shift of the peak at 350 nm. These are consistent with observations in other aggregate systems and can be attributed to exciton coupling or charge-transfer bands being formed.[68–71] This is further supported by the substantial red-shift that's observed for the 99% H_2O fraction, where a shoulder is observed at 346 nm and the carbazole absorption peaks are now centered at 360 and 373 nm. The charge

transfer peak is also shifted to be centered around 460 nm. The numerous shoulders that are present in the charge-transfer band could be the result of aggregates of different sizes.

The DPEPO and PMMA films also display less structured absorption spectra, indicating a suppression of molecular motions. It could also indicate some degree of aggregation, as they are similar to the 80% H_2O spectrum. The PS spectrum is more consistent with the 0% H_2O spectrum, possibly indicative of a lower degree of aggregation than the other DPEPO.

5.5.2. Steady-State Fluorescence. The emission spectra of BCC-TPTA in the different THF/water solutions and host materials are displayed in **Fig. 5.5.2.1** with the relevant data being

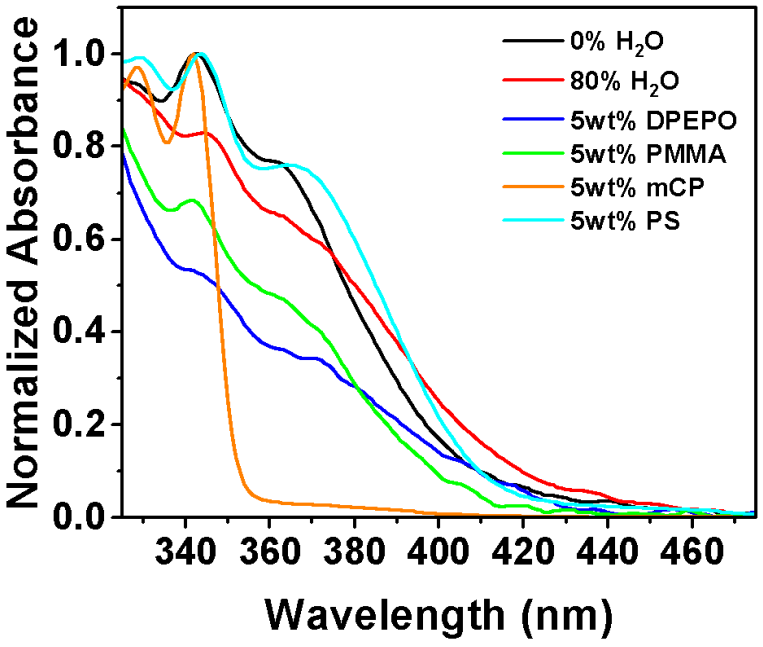


Figure 5.5.1.1. Absorbance spectra of BCC-TPTA in THF/water solutions and solid-state host materials.

summarized in **Table 5.5.2.1**. There is a noticeable red-shift in emission from the 0% H_2O – 40% H_2O fractions. Such observations are consistent with low-emission aggregate formation. Surprisingly, a drastic blue-shift of emission occurs at 60% H_2O along with the appearance of

multiple shoulders in the emission spectrum. This emission is from the aggregate state, confirmed by illuminating the fractions with UV light (**Fig 5.5.2.2**). Such shifts in emission upon aggregation have previously been attributed to the combination of weak π–π interactions of the aggregated emitter, restricted molecular rotation in the aggregate state, and a decrease in energy transfer from the donor to acceptor unit as aggregation increases.[72,73]

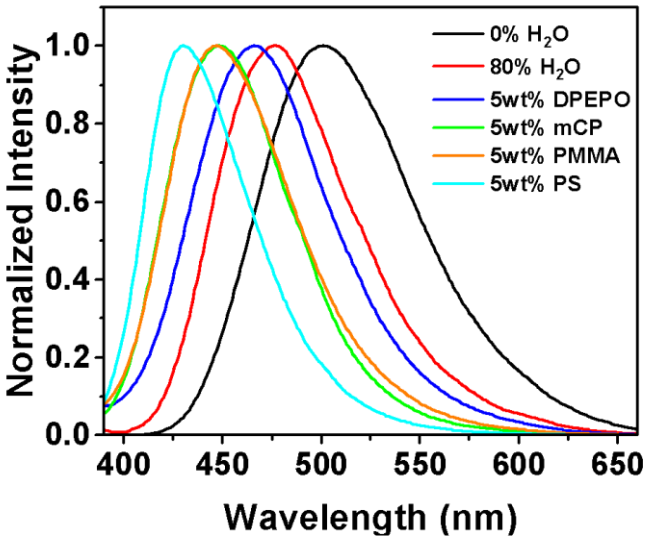


Figure 5.5.2.1. Normalized steady-state fluorescence spectra of BCC-TPTA 0% and 80% H_2O fractions and host materials.

The emission of the 5wt% in DPEPO is further blue-shifted from the 80% H_2O fraction with a slightly enhanced emission intensity (**Figure 5.8.2**). This enhancement is attributed to both the molecular motions of the monomer being suppressed and decreased solvation effects.[69,74,75] The PMMA and mCP films have similar emission maxima, with the mCP film having the higher intensity. Finally, the PS film is the most blue-shifted and has the greatest emission intensity. These results indicate that the host polarity plays little role in the emissive dynamics. PMMA is more polar ($\varepsilon = 3.41$) than mCP ($\varepsilon = 2.84$) and less polar than DPEPO ($\varepsilon = 6.12$), so one would expect it to have an emission maximum between mCP and DPEPO.[76–78] However, it is the same maximum as the less polar mCP. This indicates that the host polarity is not the main contributor to the emission maximum, consistent with other reports.[76,77] Instead, it is much more likely that the rigidity of the host material affects the observed emission maximum, where PS is the most rigid host and DPEPO is the least rigid host.[75]

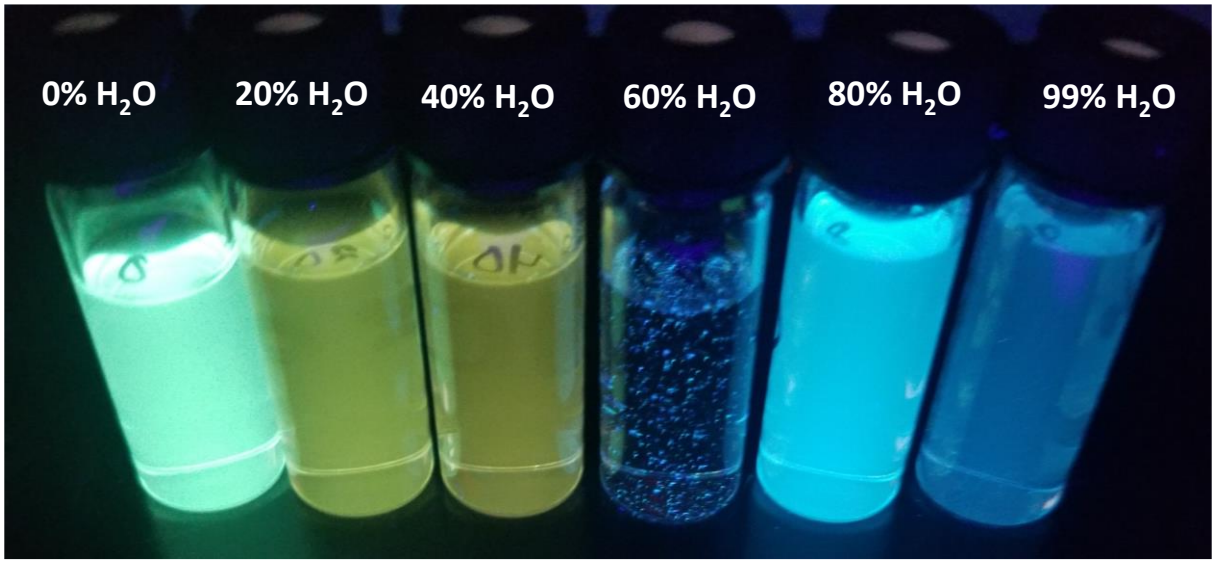


Figure 5.5.2.2. The different THF/H_2O fractions, where 0% H_2O represents pure THF solution, under UV excitation.

The 0% H_2O fraction has the greatest quantum yield (Φ) of the solution samples at 42.5% (**Table 5.5.2.1**). This value decreases as the percent water is increased, being 1.2% for the 60%

H_2O fraction. Surprisingly, the Φ increases to 16.1% at 80% H_2O and again decreases to 9.6% for the 99% H_2O fraction. These results indicate different packing structure for the aggregates in the different water fractions which then affects the Φ. The Φ for the films are interesting, with the DEPEPO and PS films having similar values of 15.5% and 16.9%, respectively. The mCP and PMMA films also shar similar values of 55.7% and 60.9%, respectively. The similarities of these values suggest that similar mechanisms are occurring within the small molecule and polymer films and warrant the use of more in-depth spectroscopic techniques.

Sample	Abs. Max (nm)	Emis. Max (nm)	Φ (%)
0% H_2O	343	500	42.5
20% H_2O	343	526	6.3
40% H_2O	343	526	3.7
60% H_2O	343	480	1.2
80% H_2O	347	474	16.1
99% H_2O	346	468	9.6
5wt% in DPEPO	343	468	15.5
5wt% in mCP	343	449	55.7
5 wt% in PMMA	343	447	60.9
5wt% in PS	343	430	16.9

Table 5.5.2.1. Photophysical properties of BCC-TPTA in different THF/water solutions and film.

5.5.3. Nanosecond Transient Absorption Spectra. The nanosecond transient absorption spectroscopy (nsTAS) technique was utilized to observe the emissive and non-emissive species of the BCC-TPTA emitter in different environments. These are represented as either positive or negative changes in optical absorption (ΔOD) and are associated with ground state bleach, spontaneous emission (SE), or excited state absorption (ESA). The lifetimes of these states will assist in determining the influence of the environment on the excited state and emissive dynamics. The transient absorption spectra of the 20% - 99% H_2O fractions are provided in **Figure 5.8.3**. The transient absorption spectra of the 0% H_2O fraction and 5wt% mCP film sample is provided in

Figure 5.5.3.1, with the transient absorption spectra of the remaining film samples being provided in **Figure 5.8.4**.

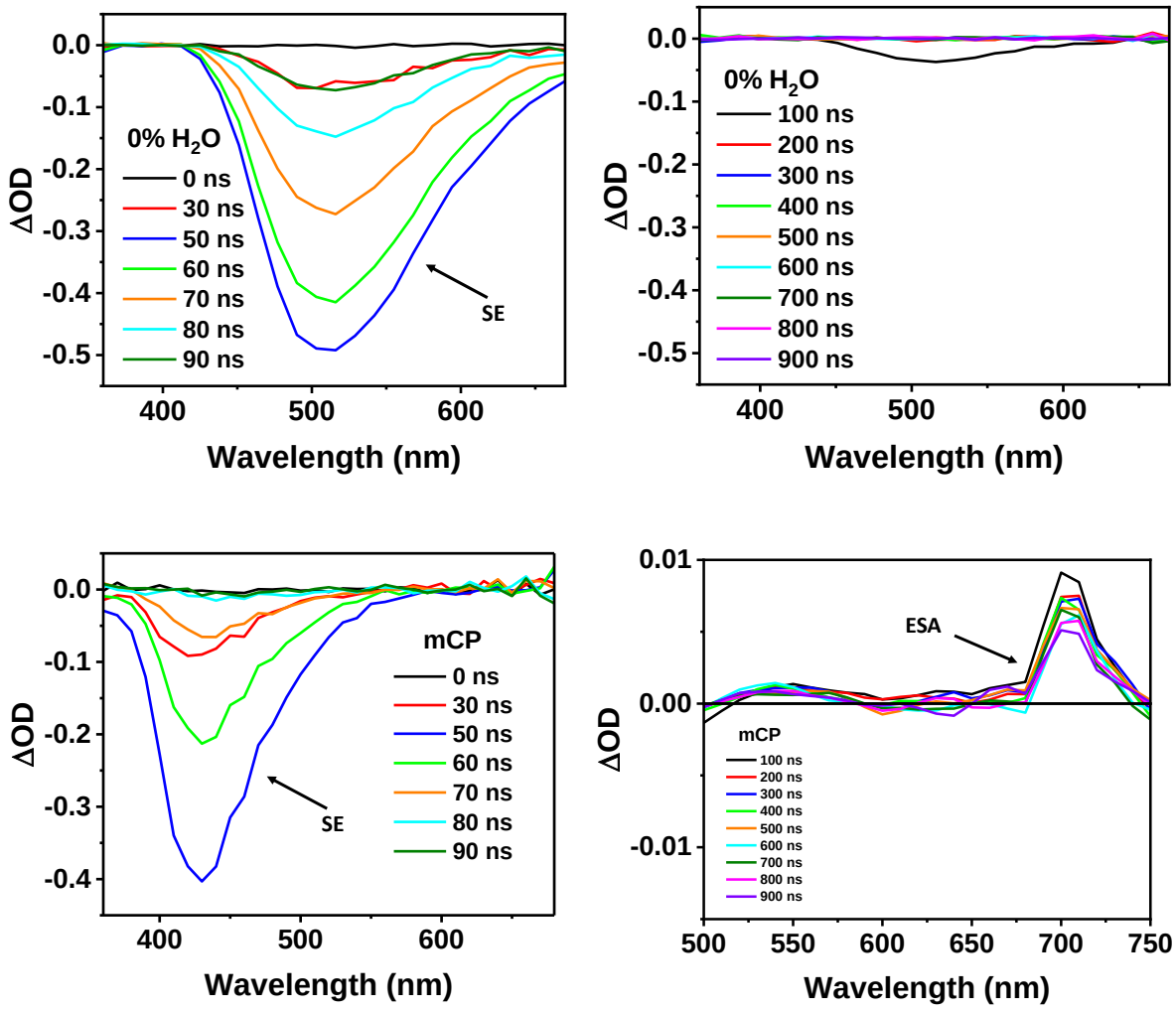


Figure 5.5.3.1. Transient absorption spectra of BCC-TPTA in 0% H_2O fraction and mCP host material.

The transient absorption spectra of the 0% - 40% H_2O fractions are consistent with those of a fluorophore where only a SE peak is observed. This is consistent with previous reports of the BCC-TPTA emitter in solution and is in good agreement with the steady-state fluorescence spectra.[28] Unfortunately, the degree of aggregation within the 60% - 99% H_2O fractions interfere with the transmission of the xenon probe beam that is required for the cross-beam geometry used in this

measurement. As such, we are unable to observe the excited state dynamics of these aggregate solutions.

Fortunately, this is not the case for the film samples where an intense SE signal is observed. The SE signals of the films are in good agreement with the steady-state fluorescence spectra. We also observed a significantly less intense ESA signal in the 600 – 700 nm region for each film that is concealed by the SE signal. Thankfully, the nsTAS system is able to determine the lifetime of these ESAs despite their relatively low intensities. The kinetics traces are presented in **Figure 5.5.3.2** and the lifetimes are provided in **Table 5.5.3.1**. The ESA lifetimes of DPEPO and PS are similar to each other, being 4,773 ns and 4,450 ns, respectively. Those of the mCP and PMMA films are also similar being 1,663 ns and 1,852 ns, respectively. Due to their long lifetimes, these states are determined to be triplet excited states. The trend in ESA lifetimes is similar to what was observed for the Φ results, indicating a relationship between the triplet state lifetimes and the observed Φ.

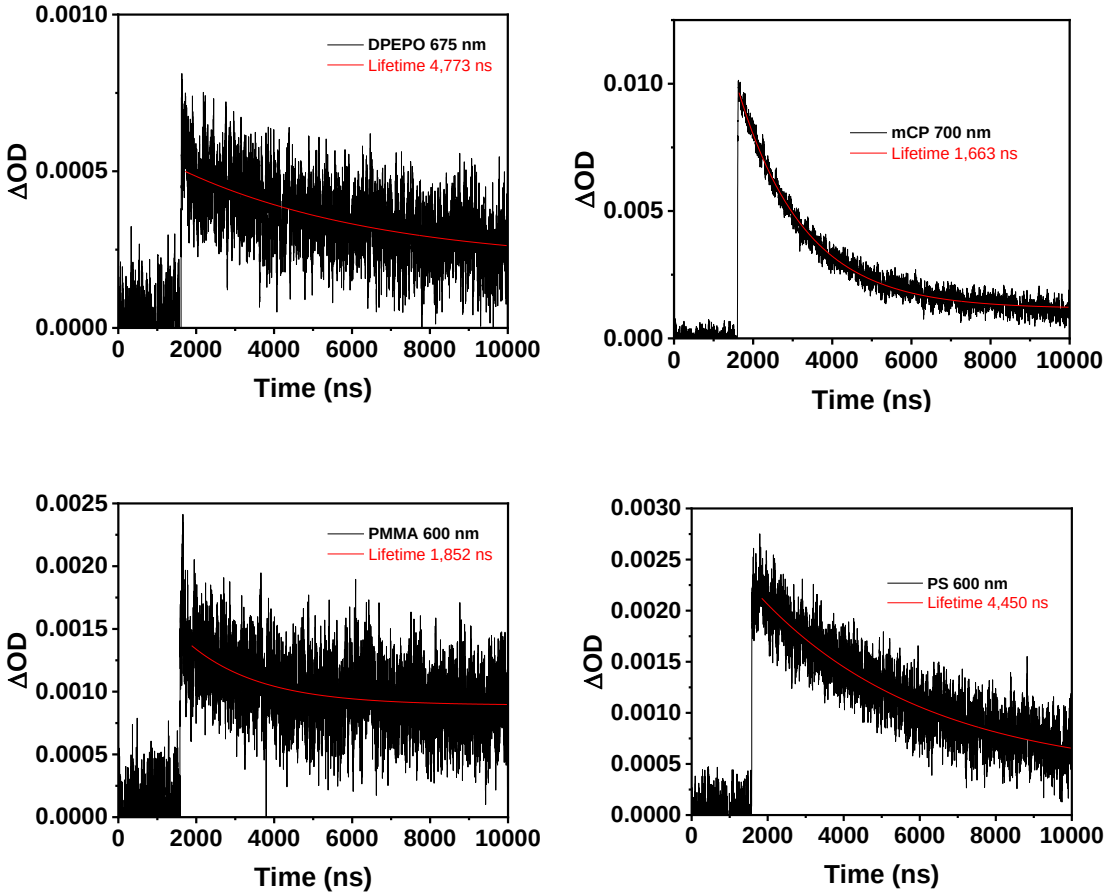


Figure 5.5.3.2. Kinetic lifetime traces of the BCC-TPTA excited states in different host materials.

Sample	τ_{ESA} (ns)
5wt% in DPEPO	4,773
5wt% in mCP	1,663
5 wt% in PMMA	1,852
5wt% in PS	4,450

Table 5.5.3.1 Excited state lifetimes observed for the BCC-TPTA films.

5.5.4. Time-Resolved Emission Spectra. The time-resolved emission spectra of BCC-TPTA in the THF/water solutions and different host materials display changes in emission intensity as a function of time and aids in the understanding of the emissive dynamics and what interactions

occur between the emitter and its environment. The time-resolved emission spectra of the 0% and 80% H_2O fractions are provided in **Figure 5.5.4.1** while those of the remaining fractions are provided in **Figure 5.8.5.** The time-resolved emission spectra of the films are provided in **Figure 5.5.4.2**.

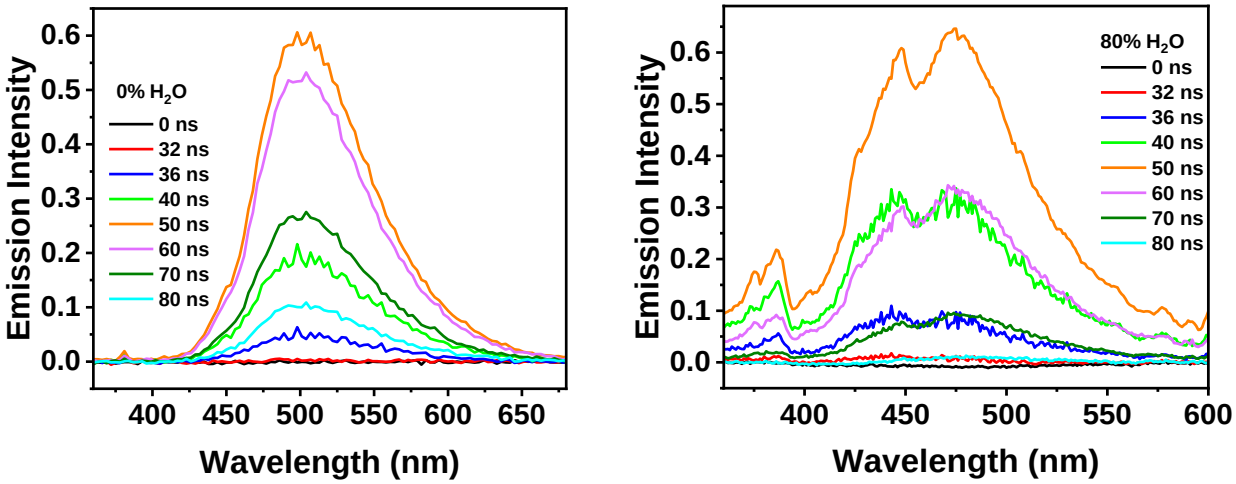


Figure 5.5.4.1. Time-resolved emission spectra of BCC-TPTA in 0% and 80% H_2O fractions.

The time-resolved emission spectra of the 0% - 99% H_2O fractions display two emission peaks that shift within the 350 - 390 nm region. Similar peaks have been attributed to emission from carbazole excimers, with the relative intensities of these peaks being used to determine the degree of carbazole aggregation.[79–85] Specifically, the high and low energy peaks are attributed to the 0-0 and 0-1 transitions, respectively.[83] Indeed, as the fraction of water is increased from 0% to 60%, we observe a decrease in the 0-0 transition emission peak's intensity along with an increase in the intensity of the 0-1 transition emission. The 0-0 transition emission peak reappears for the 80% H_2O fraction but is again absent for the 99% H_2O spectrum. It is determined then that the aggregate emission intensity is related to the degree of π–π stacking of the carbazole units and the type of aggregation that is occurring, as such interactions are known to cause emission quenching.[72,86]

Thus, the aggregates of the 80% H_2O fraction must have a different packing structure than the other fractions which allows for better AIE.

The time-resolved emission spectra of the 0% - 40% H_2O fractions are in good agreement with the steady-state emission spectra. However, numerous emissive peaks and shoulders appear in the time-resolved emission spectra upon increasing the percent of water to 60%. These are also present at 80% and 99% H_2O and are attributed to emission from aggregates of different sizes.[87,88] The wavelengths of these peaks are provided in **Table 5.5.4.1**. These peaks are essentially the same for each of the aggregate solutions, with the only significant change being their relative intensities.

The numerous emissive shoulders are not observed in the time-resolved emission spectra of the solid-state films. Their absence is likely a combination of the hosts suppressing aggregate formation and the excimer emission being within the region of the main emission peaks. However, two main peaks are observed for the film samples similar to the aggregate solutions. This is surprising as it was expected that the films would display a time-resolved emission spectra similar to the 0% H_2O monomer solution, due to host materials typically suppressing aggregate formation at low guest concentrations. It is likely that these peaks are the result of monomer and aggregate emission.[89] This is assignment is based on the temporal shift in maxima for the high energy peak while the low energy peak does not shift that is observed for each film.

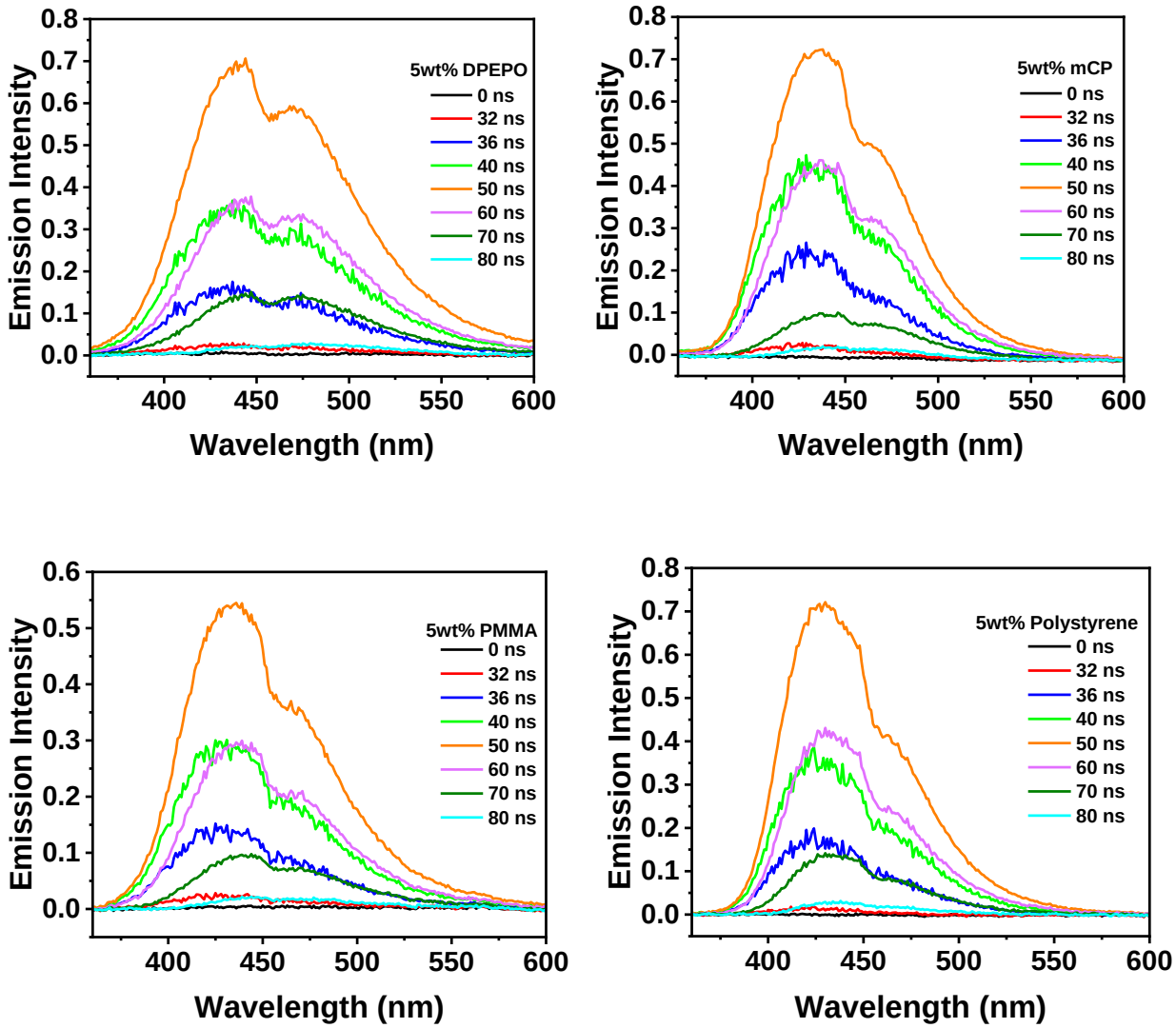


Figure 5.5.4.2. Time-resolved emission spectra of BCC-TPTA in solid-state hosts.

Such shifts in emission have been related to conformational disorder of the monomer in host materials, where the more rigid host prevents such shifts in emission maxima.[76] Indeed, the shift in maxima is diminished for the more rigid hosts being only 10 nm (430 nm – 440 nm) for mCP and PMMA and 5 nm (430 – 435 nm) for PS. Thus, the high energy peak is determined to be from monomer emission. Interestingly, such a shift in maxima is not observed for the low energy peak which is consistent over time. Thus it is determined that this emission is from an aggregate, as

aggregates would not undergo the same conformational changes as a monomer due to rotational and vibrational motions being restricted upon aggregation.[90,91] These assignments also explain the relative intensities of the two peaks, where the monomer emission is more intense than the aggregate emission, as emission intensity is related to concentration.[92] This is consistent with the expectation that a greater number of monomers should be observed in the low guest concentration solid-state films.

Sample	1st Emis. Max (nm)	2nd Emis. Max (nm)
0% H_2O	500	–
20% H_2O	526	–
40% H_2O	526	–
60% H_2O	450	480
80% H_2O	447	474
99% H_2O	446	468
5wt% in DPEPO	447	468
5wt% in mCP	436	465
5 wt% in PMMA	436	465
5wt% in PS	430	462

Table 5.5.4.1. Emissive peaks observed for the different samples in the time-resolved emission spectra.

Kinetics traces taken at the first emissive maxima of the 80% H_2O fraction and solid-state films were obtained using the nsTAS system (**Figure 5.5.4.2**). There we observe a second emissive component that indicates that the triplet excited state is utilized for emission by these samples. The lifetimes of the observed second emissive components are provided in **Table 5.5.4.2**. Interestingly, these lifetimes do not follow the same trend as the excited state and Φ results. As this is a new method for our research group, the time-correlated single-photon counting (TCSPC) technique was used as a comparison to these results.

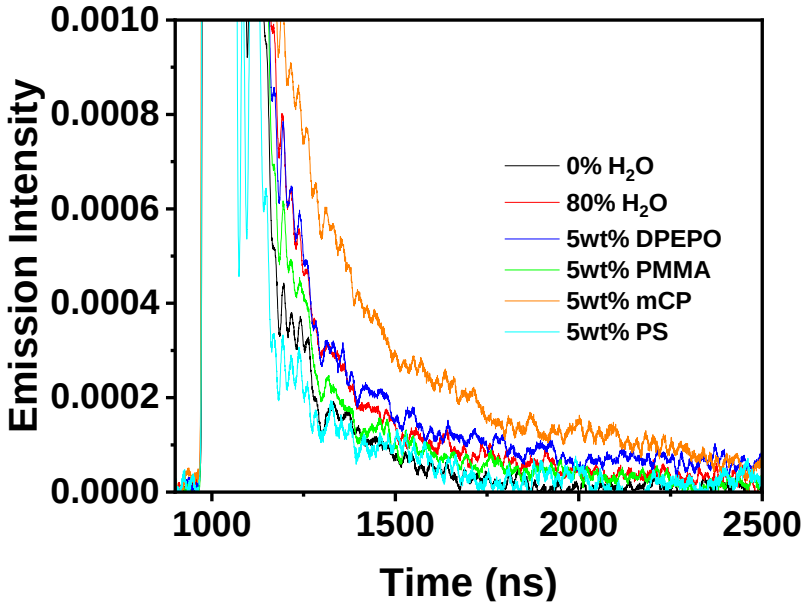


Figure 5.5.4.3 Emission lifetime traces of the emissive peaks observed in the time-resolved emission spectra of the 0% and 80% H_2O fractions and 5wt% films, zoomed in to display the second-emissive component.

Sample	τ (ns)
0% H_2O	–
80% H_2O	309
5wt% in DPEPO	422
5wt% in mCP	643
5 wt% in PMMA	412
5wt% in PS	330

Table 5.5.4.2. Lifetimes of the second emissive components observed for the 80% H_2O fractions and solid-state films.

5.5.5. Time-Correlated Single-Photon Counting (TCSPC) Results. Emissive lifetime traces for each sample that displayed two emissive maxima are displayed in **Figure 5.5.5.1**. Emission decay traces for the 0% - 40% H_2O fractions are provided in **Figure 5.8.6**. The lifetimes of these maxima are provided in **Table 5.5.5.1**. The emissive lifetime of the 0% H_2O fraction (9 ns) is consistent with a fluorescent compound and is in good agreement with previous studies.[28] A decrease in emissive lifetime is seen as the fraction of water is increased to 20% and 40%. This is

in-line with the observed decrease in Φ for these fractions. Only one emissive lifetime was determined for these fractions as only one emissive peak was observed in their time-resolved emission spectra. Surprisingly, we observe the rise of a new second emission component at 60% H_2O, though its lifetime is still relatively short at 37 ns. The second emissive component's lifetime is increased to 80 ns for the 80% H_2O fraction. It then decreases for the 99% H_2O fraction, having a lifetime of 69 ns. The changes in emissive lifetime between the 60% - 99% H_2O aggregate solutions is determined to be the result of emission from aggregates of different sizes.[40]

The lifetime of the first and second emissive components are significantly enhanced in the solid-state compared to the aggregate solutions. This indicates the suppression of intermolecular and intramolecular interactions that would quench fluorescence in the solid-state. The lifetime of the second component of the DPEPO, mCP, and PMMA films are all similar, being 357 ns, 351 ns, and 356 ns, respectively. In PS host, the second component has a significantly shorter lifetime than what's observed for any of the other host materials, being 50 ns. These results are similar to what was observed with the nsTAS system, where the 80% H_2O fraction and PS film have the shortest second-component lifetime.

Sample	τ_1 (ns)	τ_2 (ns)
0% H_2O	9	–
20% H_2O	3	–
40% H_2O	3	–
60% H_2O	4	37
80% H_2O	9	80
99% H_2O	13	69
5wt% in DPEPO	44	357
5wt% in mCP	43	351
5wt% in PMMA	50	356
5wt% in PS	50	50

Table 5.5.5.1. Emissive lifetimes of BCC-TPTA in the different H_2O fractions and host materials taken at the emissive maxima observed in the time-resolved emission spectra.

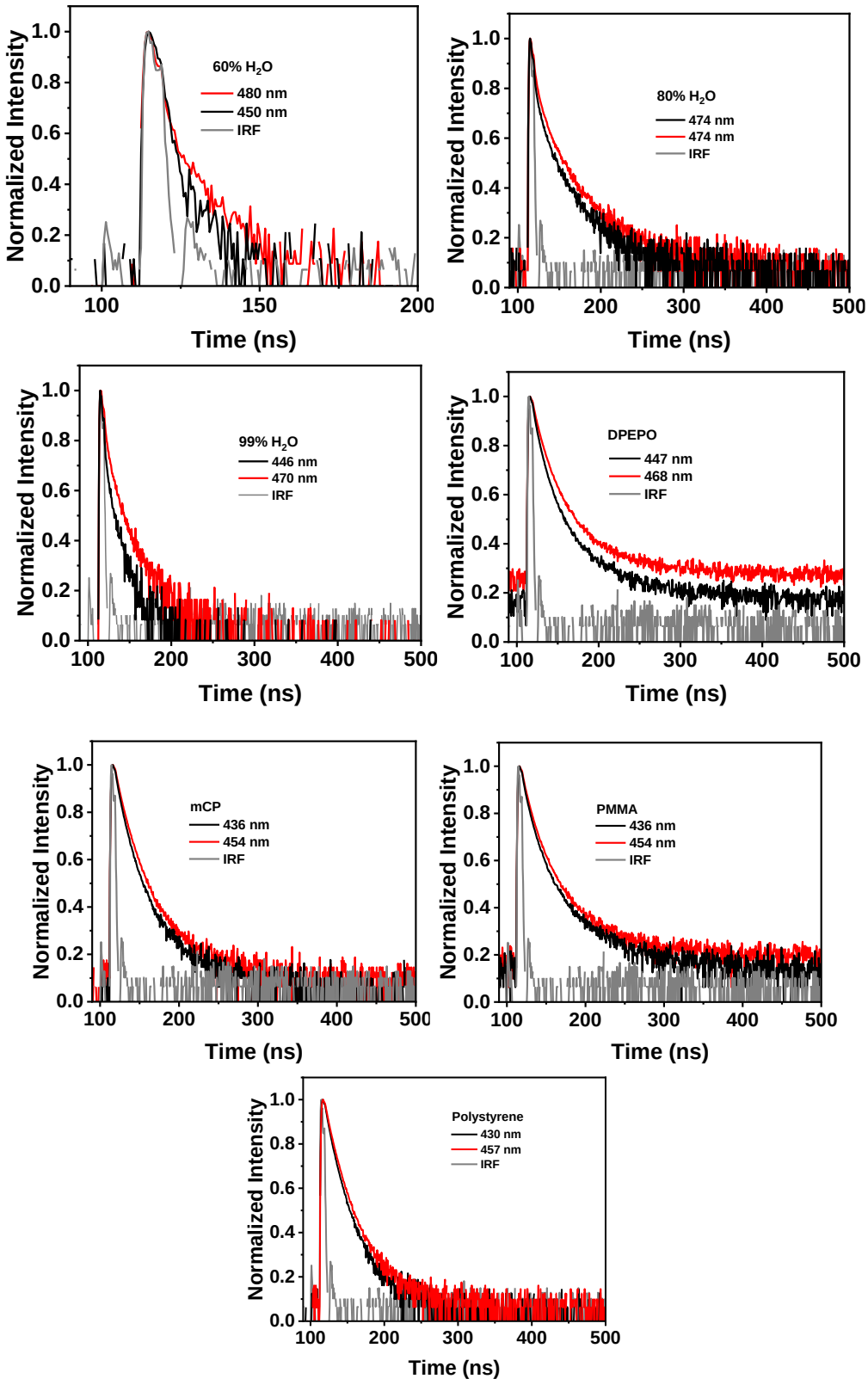


Figure 5.5.5.1. Emission decay traces of the two emissive maxima seen in the time-resolved emission.

5.5.6. Emission Intensity vs Laser Energy

Log/log plots of the integrated emission intensity vs the laser excitation energy were obtained to better determine the emissive mechanism that takes place within the aggregate and film samples. This is due to concerns that other emissive mechanisms similar to TADF, such as triplet-triplet annihilation upconversion, may be taking place within the films.[56] Such questions would normally be addressed by calculating the rate of reverse intersystem crossing (k_{rISC}) using the Vázquez method. However, as the Vázquez method requires both the purged and unpurged values of the triplet excited state lifetime and fluorescence quantum yield it can't be used.[28] This is because neither the triplet excited state lifetimes of the aggregate solutions nor purged lifetimes of the films are obtainable with the current nsTAS setup. Thus, a new experimental setup that expands on the emissive detection capabilities of the nsTAS system was designed to obtain the log/log plots (**Figure 5.5.6.1**).

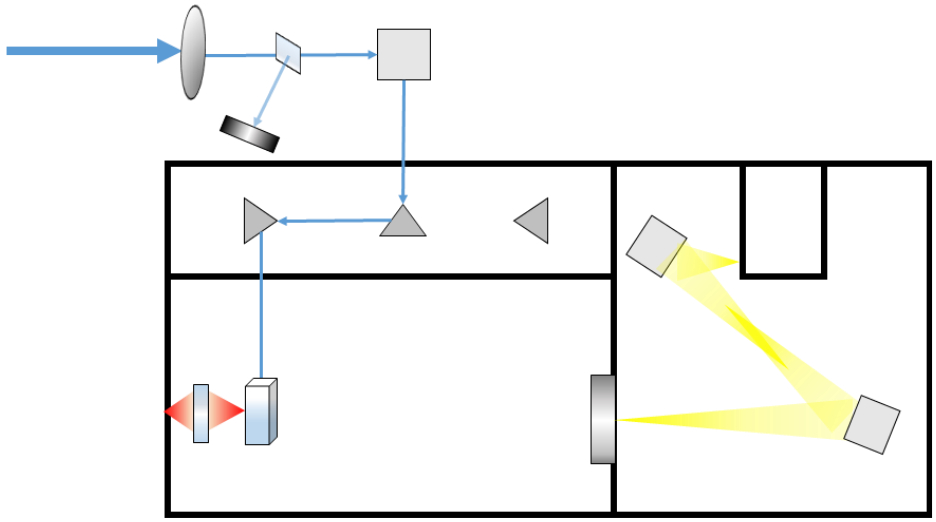


Figure 5.5.6.1. New nsTAS laser setup used to obtain log/log plots of emission intensity vs laser energy. The laser excitation beam (blue) is directed towards a neutral density filter. The diminished beam then has approximately 15% of its energy directed towards a power meter and the rest into the sample chamber. There it excites the sample and the sample's emission (presented as red) is collected by the detector. The probe beam (yellow) is not used in this

The log/log plots of the 0% fraction H_2O, 80% H_2O fraction, and solid-state films were obtained as they are representative of their respective sample classes, those being monomer solution, aggregate solution, and solid-state films, respectively. The log-log plots of the films are presented in **Figure 5.5.6.2**, while those of the 0% and 80% H_2O fraction are presented in **Figure 5.8.7.** The 0% H_2O fraction has a slope of ~1, indicating a monomolecular emissive mechanism.[47] This is consistent with the previous measurements that indicate the 0% H_2O fraction utilizes fluorescence.

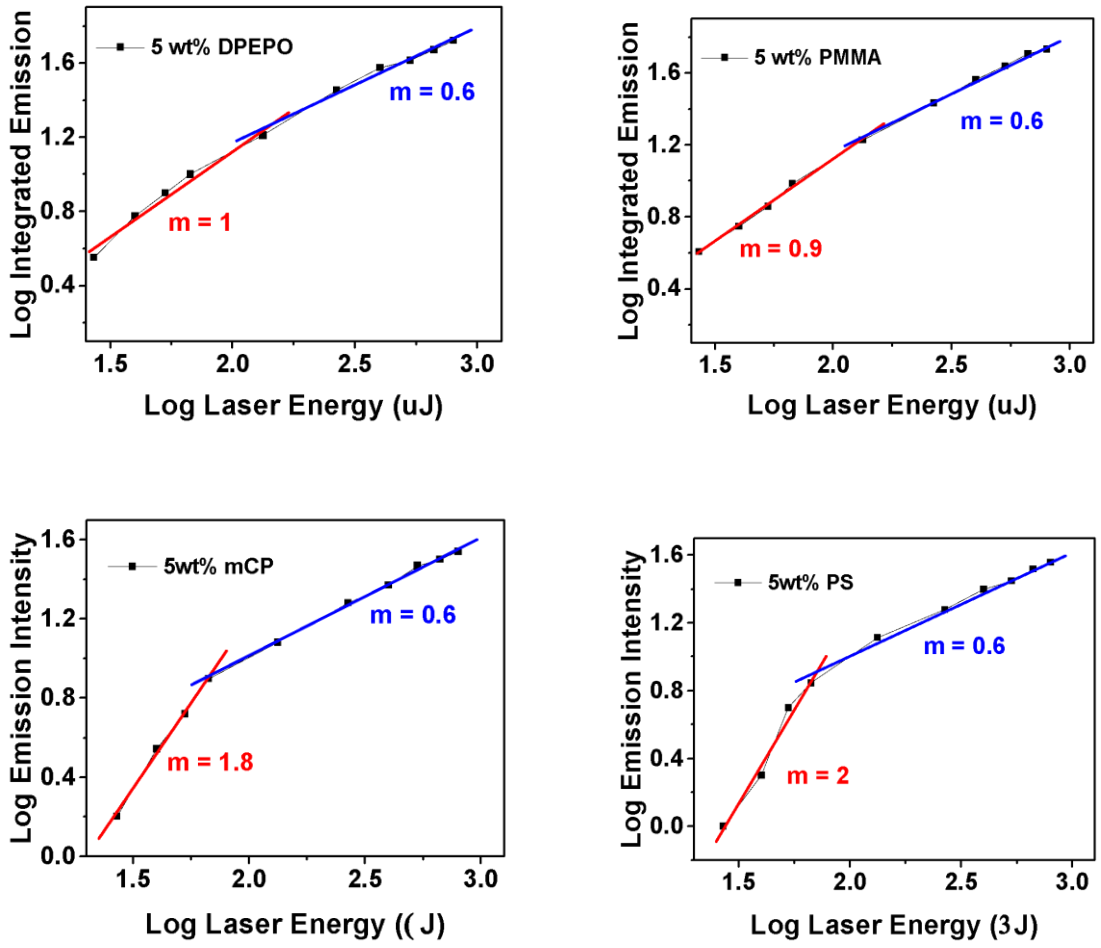


Figure 5.5.6.2. Log/log plots of integrated emission intensity vs laser energy of the 5wt% films.

The 80% H_2O fraction displays a slope of 0.5. This has been observed with phosphorescence at high excitation energy.[47] Such a slope is likely the result of a triplet quenching mechanism that results in the square dependence.[57,93] This correlates well with the diminished Φ observed for the aggregate solution.

The DPEPO and PMMA films also display slopes of ~1 at low excitation energy, indicating a monomolecular emissive mechanism. This, along with the emissive lifetime characterization experiments, strongly indicates that the DPEPO and PMMA films utilize the TADF mechanism.[56] However, both films display a slope of 0.6 at high excitation energies. This suggests a triplet quenching mechanism occurs at higher excitation energies, similar to what was observed for the 80% H_2O fraction.

Interestingly, the mCP and PS films display a slope of ~2 at low excitation energies. Such a slope has been attributed to a delayed emission mechanism known as triplet-triplet annihilation upconversion.[47,54,56] This suggests a unique interaction between the BCC-TPTA emitter and the mCP and PS host materials that is not present for the DPEPO and PMMA hosts. However, a slope of 0.6 is observed at high excitation energies, just as was observed for the DPEPO and PMMA films. This suggests that while different emissive mechanisms are dominant at the lower excitation energies, each film utilizes the same emissive mechanism at sufficiently high excitation energy.

5.6. Discussion

The steady-state broadening and red-shift of the absorption spectra as the percent of water is increased is a good indicator of aggregate formation at higher water percentages.[94] This is confirmed by the visual observation of aggregates in the 60% H_2O fraction. The observed red-shift in emission as the water fraction is increased to 40% is consistent with solvation effects on charge-transfer emitters, where the polar charge-transfer state is stabilized by the polar solvent.[95] The

sudden blue-shift is then attributed to aggregation induced emission (AIE), again observed visually in solution. The changes in emission intensity from 60% to 99% H_2O is attributed to different degrees of aggregation and packing structures at these fractions.[86,88]

The nanosecond transient absorption measurements display a large SE peak for the 0% - 40% solutions, indicating that any excited states are below the temporal resolution of the nsTAS system. However, each of the film samples display a long-lived excited within the 600 – 700 nm range. The long-lifetime of these states and their agreement with previous studies lead to the determination that these ESAs are triplet excited states.[38] The similar trends observed for the ESA lifetimes and the quantum yield results of the films indicate that the triplet states play a significant role in the emissive mechanism of these systems. The emissive dynamics were investigated to better determine what emissive mechanism is being utilized by the films.

The time-resolved emission spectra provide some insight as to the properties of the emitter, whether they be monomer or aggregates. Only one emissive peak is observed for the low water fraction solutions (0% - 40% H_2O). These peaks are in good agreement with the steady-state emission spectra and indicate only one emissive species. Upon aggregation (60% - 99% H_2O) multiple emissive peaks and shoulders are observed. Its determined that the peaks observed for the aggregate solutions are the result of emission from aggregates of different sizes.[88]

The time-resolved emission spectra of the film samples also display different two emissive peaks. Such emissive peaks are typically indicators of emission from different species.[96] These two peaks also display different temporal dynamics, further indicating that they are different emissive species. Specifically, the high energy peak observed for each film shifts over time while the low energy peak remains constant with respect to time. It is noted that the temporal shift of the high energy peak of the PS film is smaller than it is for the other host materials. This observation

led to the determination that the high energy peak is the result of monomer emission with the low energy peak being from an aggregate state. Multiple factors lead to these determinations. First, the high energy peak shifting over time can be attributed to slow conformational changes of the monomer in solid-state environments with the degree of peak shift is determined by host rigidity.[76] This explains why no shift is observed for the low energy peak, as aggregates would not undergo such conformational changes. Second, the differences in energy between the two peaks is consistent with the expectation for the aggregate emission being lower energy than the monomer emission when both are in the same environmet.[97] Finally, the relative intensities of the high and low energy peaks match expectations for the degree of aggregation expected in film., where the host material controls the conformational differences and degree of aggregation.[41,76] This indicates that DPEPO as the least rigid host allows for a greater degree of aggregation while the most rigid PS host has the least aggregation.[76]

The emissive lifetime characterization obtained by the nsTAS system also provide information as to the emissive mechanism. Only one short-lived emissive component is observed in monomer solution (0% H_2O). However, two emissive components are observed for the aggregate solutions (60 – 99% H_2O). This is an interesting observation, as it was expected that the two-component emission would be the result of guest-host interactions. The lifetime of the second component was enhanced when the emitter was placed in solid-state host materials, with DPEPO, mCP, and PMMA having the greatest lifetimes. A similar trend was observed between the second component lifetime and Φ. These observations, including the trend in emissive lifetimes, were also observed using the TCSPC system, further confirming the validity of the results. However, the emissive dynamics could be attributed to either TADF or TTA-UC. Log-log

plots of integrated emission intensity vs. excitation energy will allow for proper determination of the emissive mechanism.

The log/log plots of emission intensity vs laser energy reveal that the emissive mechanism of the 0% H_2O fraction is monomolecular. This, combined with the previous results, confirm that the emissive mechanism of this fraction is fluorescence. This is not the case for the aggregate 80% H_2O fraction, where the slope was 0.5. This indicates either a bimolecular quenching mechanism or excimer emission, as expected of aggregates.[57] The films display a more interesting slope that changes with excitation energy.

Both the DPEPO and PS films display a slope of ~ 1 at low excitation energies. This, in combination with previous results, namely the transient absorption and emissive lifetime characterization, indicates TADF as the emissive mechanism for these films. Both the mCP and PS films display slopes of ~2, indicating a bimolecular emissive mechanism. This confirms that the TTA-UC mechanism is dominant at low excitation energies. This is because a monomolecular mechanism, such as TADF or phosphorescence, would display a slope of ~1. The emissive lifetime characterization results also support this, as they display a two-component emission for these films similar to previously reported TTA-UC systems.[98]

Interestingly, every film displays a slope of 0.6 at higher excitation energies. This is quite similar to the slope obtained for the aggregate 80% H_2O fraction. This indicates that the rates at which TADF and TTA-UC occur for the different systems is unable to fully outcompete the rate of an emission quenching mechanism. This is likely aggregate emission, as aggregate emission was observed in the time-resolved emission spectra and it overlaps significantly with the monomer emission.

The difference in emission mechanisms at low excitation energies is likely related to the orientation of the BCC-TPTA emitter in film as the host material has been reported to have significant influence over emitter orientation and emitter orientation can influence the efficiency of an emissive mechanism in solid-state.[99–102] It is likely that hydrogen bonding occurs between BCC-TPTA and the DPEPO and PMMA host materials, leading to an orientation that is better suited for TADF-activity. In the case of mCP and PS films, it is likely that nonbonding interactions between the aromatic moieties of the host and emitter lead to an orientation that is better suited for TTA-UC.[103] However, it is clear that aggregation plays a significant role in the emission of these films and that TADF/TTA-UC-like dynamics can be observed free of guest-host interactions.

5.7. Conclusion

A new experimental setup was designed and implemented for the nsTAS system, expanding its use for film samples. The results obtained using this setup indicate that the long-lived second emissive component observed for the BCC-TPTA emitter in solid-state host material is the result of TADF, TTA-UC, and guest-guest interactions with the degree of each mechanism being dependent on the emitter's environment. Indeed, the second emissive component is observed in aggregate solutions free of guest-host interactions, supporting this determination. The time-resolved emission spectra also indicate that aggregates are present in the films, further indicating that guest-guest interactions play a role in film emission. It's apparent that the host material plays an integral role in which emissive mechanism is enhanced or suppressed. Further studies should focus on determining to what extent aggregation plays a role in film emission. This could be done by altering the wt% of the emitter to where there are no aggregates in film to neat film. Other investigations could focus on determining if similarly TADF-inactive emitters can be made to be TADF-active through guest-host interactions. It is our hope that through this study, our results

highlight that the emissive mechanisms of films can be more complicated than assigning one emissive mechanism, and can be an interplay between the guest-guest, guest-host, and other emissive mechanisms depending on the choice of host material.

References

(1) Hosokai, T.; Matsuzaki, H.; Nakanotani, H.; Tokumaru, K.; Tsutsui, T.; Furube, A.; Nasu, K.; Nomura, H.; Yahiro, M.; Adachi, C. Evidence and Mechanism of Efficient Thermally Activated Delayed Fluorescence Promoted by Delocalized Excited States. *Sci. Adv.* **2017**, *3*, 1–9.

(2) Yang, Z.; Mao, Z.; Xie, Z.; Zhang, Y.; Liu, S.; Zhao, J.; Xu, J.; Chi, Z.; Aldred, M. P. Recent Advances in Organic Thermally Activated Delayed Fluorescence Materials. *Chem. Soc. Rev.* **2017**, *46*, 915–1016. https://doi.org/10.1039/c6cs00368k.

(3) Hong, G.; Gan, X.; Leonhardt, C.; Zhang, Z.; Seibert, J.; Busch, J. M.; Bräse, S. A Brief History of OLEDs—Emitter Development and Industry Milestones. *Adv. Mater.* **2021**, *33*, 1–24. https://doi.org/10.1002/adma.202005630.

(4) Yersin, H.; Rausch, A. F.; Czerwieniec, R.; Hofbeck, T.; Fischer, T. The Triplet State of Organo-Transition Metal Compounds. Triplet Harvesting and Singlet Harvesting for Efficient OLEDs. *Coord. Chem. Rev.* **2011**, *255*, 2622–2652. https://doi.org/10.1016/j.ccr.2011.01.042.

(5) Rortais, F.; Lee, S.; Ohshima, R.; Dushenko, S.; Ando, Y.; Shiraishi, M. Spin-Orbit Coupling Induced by Bismuth Doping in Silicon Thin Films. *Appl. Phys. Lett.* **2018**, *113*. https://doi.org/10.1063/1.5046781.

(6) Franca, L. G.; Long, Y.; Li, C.; Danos, A.; Monkman, A. The Critical Role of Nπ∗ States in the Photophysics and Thermally Activated Delayed Fluorescence of Spiro Acridine-Anthracenone. *J. Phys. Chem. Lett.* **2021**, *12* (5), 1490–1500. https://doi.org/10.1021/acs.jpclett.0c03314.

(7) Volz, D.; Wallesch, M.; Fléchon, C.; Danz, M.; Verma, A.; Navarro, J. M.; Zink, D. M.; Bräse, S.; Baumann, T. From Iridium and Platinum to Copper and Carbon: New Avenues for More Sustainability in Organic Light-Emitting Diodes. *Green Chem.* **2015**, *17*, 1988–2011. https://doi.org/10.1039/c4gc02195a.

(8) Volz, D. Review of Organic Light-Emitting Diodes with Thermally Activated Delayed Fluorescence Emitters for Energy-Efficient Sustainable Light Sources and Displays. *J.*

Photonics Energy **2016**, *6*. https://doi.org/10.1117/1.jpe.6.020901.

(9) Zhang, Q.; Li, J.; Shizu, K.; Huang, S.; Hirata, S.; Miyazaki, H.; Adachi, C. Design of E Ffi Cient Thermally Activated Delayed Fluorescence Materials for Pure Blue Organic Light Emitting Diodes. *J. Am. Chem. Soc.* **2012**, *134*, 1470–14709. https://doi.org/10.1021/ja306538w.

(10) Samanta, P. K.; Kim, D.; Coropceanu, V.; Brédas, J. L. Up-Conversion Intersystem Crossing Rates in Organic Emitters for Thermally Activated Delayed Fluorescence: Impact of the Nature of Singlet vs Triplet Excited States. *J. Am. Chem. Soc.* **2017**, *139*, 4042–4051. https://doi.org/10.1021/jacs.6b12124.

(11) Im, Y.; Lee, J. Y. Recent Progress of Green Thermally Activated Delayed Fluorescent Emitters. *J. Inf. Disp.* **2017**, *18*, 101–117. https://doi.org/10.1080/15980316.2017.1333046.

(12) Rodriguez-Serrano, A.; Dinkelbach, F.; Marian, C. M. Intersystem Crossing Processes in The2CzPNemitter: A DFT/MRCI Study Including Vibrational Spin-Orbit Interactions. *Phys. Chem. Chem. Phys.* **2021**, *23* (5), 3668–3678. https://doi.org/10.1039/d0cp06011a.

(13) Gibson, J.; Penfold, T. J. Nonadiabatic Coupling Reduces the Activation Energy in Thermally Activated Delayed Fluorescence. *Phys. Chem. Chem. Phys.* **2017**, *19*, 8428–8434. https://doi.org/10.1039/c7cp00719a.

(14) Kim, M.; Jeon, S. K.; Hwang, S. H.; Lee, S. S.; Yu, E.; Lee, J. Y. Correlation of Molecular Structure with Photophysical Properties and Device Performances of Thermally Activated Delayed Fluorescent Emitters. *J. Phys. Chem. C* **2016**, *120*, 2485–2493. https://doi.org/10.1021/acs.jpcc.5b09114.

(15) Hirata, S.; Sakai, Y.; Masui, K.; Tanaka, H.; Lee, S. Y.; Nomura, H.; Nakamura, N.; Yasumatsu, M.; Nakanotani, H.; Zhang, Q.; Shizu, K.; Miyazaki, H.; Adachi, C. Highly Efficient Blue Electroluminescence Based on Thermally Activated Delayed Fluorescence. *Nat. Mater.* **2015**, *14*, 330–336. https://doi.org/10.1038/nmat4154.

(16) Wex, B.; Kaafarani, B. R. Perspective on Carbazole-Based Organic Compounds as Emitters and Hosts in TADF Applications. *J. Mater. Chem. C* **2017**, *5* (34), 8622–8653. https://doi.org/10.1039/c7tc02156a.

(17) Kawasumi, K.; Wu, T.; Zhu, T.; Chae, H. S.; Van Voorhis, T.; Baldo, M. A.; Swager, T. M. Thermally Activated Delayed Fluorescence Materials Based on Homoconjugation Effect of Donor-Acceptor Triptycenes. *J. Am. Chem. Soc.* **2015**, No. 37, 11908–11911. https://doi.org/10.1021/jacs.5b07932.

(18) Cho, Y. J.; Jeon, S. K.; Chin, B. D.; Yu, E.; Lee, J. Y. The Design of Dual Emitting Cores for Green Thermally Activated Delayed Fluorescent Materials. *Angew. Chemie - Int. Ed.* **2015**, *54* (17), 5201–5204. https://doi.org/10.1002/anie.201412107.

(19) Tao, Y.; Yuan, K.; Chen, T.; Xu, P.; Li, H.; Chen, R.; Zheng, C.; Zhang, L.; Huang, W. Thermally Activated Delayed Fluorescence Materials towards the Breakthrough of Organoelectronics. *Adv. Mater.* **2014**, No. 47, 7931–7958. https://doi.org/10.1002/adma.201402532.

(20) Wang, K.; Liu, W.; Zheng, C. J.; Shi, Y. Z.; Liang, K.; Zhang, M.; Ou, X. M.; Zhang, X. H. A Comparative Study of Carbazole-Based Thermally Activated Delayed Fluorescence Emitters with Different Steric Hindrance. *J. Mater. Chem. C* **2017**, *5*, 4797–4803. https://doi.org/10.1039/c7tc00681k.

(21) Chen, X. K.; Bakr, B. W.; Auffray, M.; Tsuchiya, Y.; Sherrill, C. D.; Adachi, C.; Bredas, J. L. Intramolecular Noncovalent Interactions Facilitate Thermally Activated Delayed Fluorescence (TADF). *J. Phys. Chem. Lett.* **2019**, No. 12, 3260–3268. https://doi.org/10.1021/acs.jpclett.9b01220.

(22) Sun, J. W.; Kim, K. H.; Moon, C. K.; Lee, J. H.; Kim, J. J. Highly Efficient Sky-Blue Fluorescent Organic Light Emitting Diode Based on Mixed Cohost System for Thermally Activated Delayed Fluorescence Emitter (2CzPN). *ACS Appl. Mater. Interfaces* **2016**, *8*, 9806–9810. https://doi.org/10.1021/acsami.6b00286.

(23) Hua, T.; Zhan, L.; Li, N.; Huang, Z.; Cao, X.; Xiao, Z.; Gong, S.; Zhou, C.; Zhong, C.; Yang, C. Heavy-Atom Effect Promotes Multi-Resonance Thermally Activated Delayed Fluorescence. *Chem. Eng. J.* **2021**, *426*, 1–8. https://doi.org/10.1016/j.cej.2021.131169.

(24) Niu, R.; Li, J.; Liu, D.; Dong, R.; Wei, W.; Tian, H.; Shi, C. A Versatile Carbazole Donor Design Strategy for Blue Emission Switching from Normal Fluorescence to Thermally Activated Delayed Fluorescence. *Dye. Pigment.* **2021**, *194* (June). https://doi.org/10.1016/j.dyepig.2021.109581.

(25) Uoyama, H.; Goushi, K.; Shizu, K.; Nomura, H.; Adachi, C. Highly Efficient Organic Light-Emitting Diodes from Delayed Fluorescence. *Nature* **2012**, *492*, 234–238. https://doi.org/10.1038/nature11687.

(26) Lee, D. R.; Hwang, S.; Jeon, S. K.; Lee, C. W.; Lee, J. Y. Benzofurocarbazole and Benzothienocarbazole as Donors for Improved Quantum Efficiency in Blue Thermally Activated Delayed Fluorescent Devices. **2015**, No. 440, 8105–8107. https://doi.org/10.1039/c5cc01940k.

(27) Gibson, J.; Monkman, A. P.; Penfold, T. J. The Importance of Vibronic Coupling for

Efficient Reverse Intersystem Crossing in Thermally Activated Delayed Fluorescence Molecules. *ChemPhysChem* **2016**, No. 1, 2956–2961. https://doi.org/10.1002/cphc.201600662.

(28) Vázquez, R. J.; Kim, H.; Zimmerman, P. M.; Goodson, T. Using Ultra-Fast Spectroscopy to Probe the Excited State Dynamics of a Reported Highly Efficient Thermally Activated Delayed Fluorescence Chromophore. *J. Mater. Chem. C* **2019**, *7* (14), 4210–4221. https://doi.org/10.1039/c8tc05957h.

(29) Fisher, L.; Vázquez, R. J.; Howell, M.; Muthike, A. K.; Orr, M. E.; Jiang, H.; Dodgen, B.; Lee, D. R.; Lee, J. Y.; Zimmerman, P.; Goodson, T. Investigation of Thermally Activated Delayed Fluorescence in Donor-Acceptor Organic Emitters with Time-Resolved Absorption Spectroscopy. *Chem. Mater.* **2022**, *34*, 2161–2175. https://doi.org/10.1021/acs.chemmater.1c03668.

(30) Northey, T.; Stacey, J.; Penfold, T. J. The Role of Solid State Solvation on the Charge Transfer State of a Thermally Activated Delayed Fluorescence Emitter. *J. Mater. Chem. C* **2017**, 11001–11009. https://doi.org/10.1039/C7TC04099G.

(31) Imbrasas, P.; Lygaitis, R.; Kleine, P.; Scholz, R.; Hänisch, C.; Buchholtz, S.; Ortstein, K.; Talnack, F.; Mannsfeld, S. C. B.; Lenk, S.; Reineke, S. Dimers or Solid-State Solvation? Intermolecular Effects of Multiple Donor–Acceptor Thermally Activated Delayed Fluorescence Emitter Determining Organic Light-Emitting Diode Performance. *Adv. Opt. Mater.* **2021**, *9* (14), 1–11. https://doi.org/10.1002/adom.202002153.

(32) Cotts, B. L.; McCarthy, D. G.; Noriega, R.; Penwell, S. B.; Delor, M.; Devore, D. D.; Mukhopadhyay, S.; De Vries, T. S.; Ginsberg, N. S. Tuning Thermally Activated Delayed Fluorescence Emitter Photophysics through Solvation in the Solid State. *ACS Energy Lett.* **2017**, *2* (7), 1526–1533. https://doi.org/10.1021/acsenergylett.7b00268.

(33) Wang, C.; Zhang, Q. Understanding Solid-State Solvation-Enhanced Thermally Activated Delayed Fluorescence Using a Descriptor-Tuned Screened Range-Separated Functional. *J. Phys. Chem. C* **2019**, *123* (7), 4407–4416. https://doi.org/10.1021/acs.jpcc.8b08228.

(34) Delor, M.; McCarthy, D. G.; Cotts, B. L.; Roberts, T. D.; Noriega, R.; Devore, D. D.; Mukhopadhyay, S.; De Vries, T. S.; Ginsberg, N. S. Resolving and Controlling Photoinduced Ultrafast Solvation in the Solid State. *J. Phys. Chem. Lett.* **2017**, *8* (17), 4183–4190. https://doi.org/10.1021/acs.jpclett.7b01689.

(35) Serevičius, T.; Skaisgiris, R.; Kreiza, G.; Dodonova, J.; Kazlauskas, K.; Orentas, E.; Tumkevičius, S.; Juršenas, S. TADF Parameters in the Solid State: An Easy Way to Draw Wrong Conclusions. *J. Phys. Chem. A* **2021**, *125* (7), 1637–1641. https://doi.org/10.1021/acs.jpca.0c10391.

(36) Ihn, S. G.; Lee, N.; Jeon, S. O.; Sim, M.; Kang, H.; Jung, Y.; Huh, D. H.; Son, Y. M.; Lee, S. Y.; Numata, M.; Miyazaki, H.; Gómez-Bombarelli, R.; Aguilera-Iparraguirre, J.; Hirzel, T.; Aspuru-Guzik, A.; Kim, S.; Lee, S. An Alternative Host Material for Long-Lifespan Blue Organic Light-Emitting Diodes Using Thermally Activated Delayed Fluorescence. *Adv. Sci.* **2017**, *4* (8), 1–7. https://doi.org/10.1002/advs.201600502.

(37) Zhang, J.; Ding, D.; Wei, Y.; Xu, H. Extremely Condensing Triplet States of DPEPO-Type Hosts through Constitutional Isomerization for High-Efficiency Deep-Blue Thermally Activated Delayed Fluorescence Diodes. *Chem. Sci.* **2016**, *7*, 2870–2882. https://doi.org/10.1039/c5sc04848f.

(38) Wu, X.; Su, B. K.; Chen, D. G.; Liu, D.; Wu, C. C.; Huang, Z. X.; Lin, T. C.; Wu, C. H.; Zhu, M.; Li, E. Y.; Hung, W. Y.; Zhu, W.; Chou, P. T. The Role of Host–Guest Interactions in Organic Emitters Employing MR-TADF. *Nat. Photonics* **2021**, *15*, 780–786. https://doi.org/10.1038/s41566-021-00870-3.

(39) Reineke, S.; Baldo, M. A. Room Temperature Triplet State Spectroscopy of Organic Semiconductors. *Sci. Rep.* **2014**, *4*, 1–8. https://doi.org/10.1038/srep03797.

(40) Noriega, R.; Barnard, E. S.; Ursprung, B.; Cotts, B. L.; Penwell, S. B.; Schuck, P. J.; Ginsberg, N. S. Uncovering Single-Molecule Photophysical Heterogeneity of Bright, Thermally Activated Delayed Fluorescence Emitters Dispersed in Glassy Hosts. *J. Am. Chem. Soc.* **2016**, *138*, 13551–13560. https://doi.org/10.1021/jacs.6b05488.

(41) Dou, F.; Li, J.; Men, H.; Zhang, X. Controlling Molecule Aggregation and Electronic Spatial Coherence in the H-Aggregate and J-Aggregate Regime at Room Temperature. *Polymers (Basel).* **2020**, *12*, 1–10. https://doi.org/10.3390/POLYM12040786.

(42) Bennison, M. J.; Collins, A. R.; Zhang, B.; Evans, R. C. Organic Polymer Hosts for Triplet-Triplet Annihilation Upconversion Systems. *Macromolecules* **2021**, *54* (12), 5287–5303. https://doi.org/10.1021/acs.macromol.1c00133.

(43) Ma, X.; Sun, R.; Cheng, J.; Liu, J.; Gou, F.; Xiang, H.; Zhou, X. Fluorescence Aggregation-Caused Quenching versus Aggregation-Induced Emission: A Visual Teaching Technology for Undergraduate Chemistry Students. *J. Chem. Educ.* **2016**, *93* (2), 345–350. https://doi.org/10.1021/acs.jchemed.5b00483.

(44) Yu, M.; Huang, R.; Guo, J.; Zhao, Z.; Tang, B. Z. Promising Applications of Aggregation-Induced Emission Luminogens in Organic Optoelectronic Devices. *PhotoniX* **2020**, *1* (1), 1–33. https://doi.org/10.1186/s43074-020-00012-y.

(45) Ma, F.; Zhao, G.; Zheng, Y.; He, F.; Hasrat, K.; Qi, Z. Molecular Engineering of Thermally Activated Delayed Fluorescence Emitters with Aggregation-Induced Emission

via Introducing Intramolecular Hydrogen-Bonding Interactions for Efficient Solution-Processed Nondoped OLEDs. *ACS Appl. Mater. Interfaces* **2020**, *12* (1), 1179–1189. https://doi.org/10.1021/acsami.9b17545.

(46) Zhang, X.; Lu, T.; Zhou, C.; Liu, H.; Wen, Y.; Shen, Y.; Li, B.; Zhang, S. T.; Yang, B. Thermally Activated Delayed Fluorescence of Aggregates Induced by Strong π-π Interactions and Reversible Dual-Responsive Luminescence Switching. *CCS Chem.* **2022**, *4* (2), 625–637. https://doi.org/10.31635/ccschem.021.202000731.

(47) Hertel, D.; Bassler, H. Triplet-Triplet Annihilation in a Poly(Fluorene) - Derivative. *J. Chem. Phys.* **2009**, No. 21, 10007–10013. https://doi.org/10.1063/1.1415446.

(48) Ieuji, R.; Goushi, K.; Adachi, C. Triplet–Triplet Upconversion Enhanced by Spin–Orbit Coupling in Organic Light-Emitting Diodes. *Nat. Commun.* **2019**, No. 1, 1–10. https://doi.org/10.1038/s41467-019-13044-1.

(49) King, S. M.; Cass, M.; Pintani, M.; Coward, C.; Dias, F. B.; Monkman, A. P.; Roberts, M. The Contribution of Triplet-Triplet Annihilation to the Lifetime and Efficiency of Fluorescent Polymer Organic Light Emitting Diodes. *J. Appl. Phys.* **2011**, *109* (7). https://doi.org/10.1063/1.3561430.

(50) Wei, Y.; Li, Y.; Li, Z.; Xu, X.; Cao, X.; Zhou, X.; Yang, C. Efficient Triplet–Triplet Annihilation Upconversion in Solution and Hydrogel Enabled by an S-T Absorption Os(II) Complex Dyad with an Elongated Triplet Lifetime. *Inorg. Chem.* **2021**, No. 24, 19001–19008. https://doi.org/10.1021/acs.inorgchem.1c02846.

(51) Fan, C.; Wei, L.; Niu, T.; Rao, M.; Cheng, G.; Chruma, J. J.; Wu, W.; Yang, C. Efficient Triplet-Triplet Annihilation Upconversion with an Anti-Stokes Shift of 1.08 EV Achieved by Chemically Tuning Sensitizers. *J. Am. Chem. Soc.* **2019**, No. 38, 15070–15077. https://doi.org/10.1021/jacs.9b05824.

(52) Lai, H.; Zhao, T.; Deng, Y.; Fan, C.; Wu, W.; Yang, C. Assembly-Enhanced Triplet-Triplet Annihilation Upconversion in the Aggregation Formed by Schiff-Base Pt(II) Complex Grafting-Permethyl-β-CD and 9, 10-Diphenylanthracence Dimer. *Chinese Chem. Lett.* **2019**, *30* (11), 1979–1983. https://doi.org/10.1016/j.cclet.2019.09.009.

(53) Ligthart, A.; de Vries, X.; Zhang, L.; Pols, M. C. W. M.; Bobbert, P. A.; van Eersel, H.; Coehoorn, R. Effect of Triplet Confinement on Triplet–Triplet Annihilation in Organic Phosphorescent Host–Guest Systems. *Adv. Funct. Mater.* **2018**, No. 52, 1–10. https://doi.org/10.1002/adfm.201804618.

(54) You, A.; Be, M. A. Y.; In, I. Triplet — Triplet Annihilation and Delayed Fluorescence in Molecular Aggregates. *J. Chem. Phys.* **1962**, No. 38.

(55) Healy, C.; Hermanspahn, L.; Kruger, P. E. Photon Upconversion in Self-Assembled Materials. *Coord. Chem. Rev.* **2021**, *432*. https://doi.org/10.1016/j.ccr.2020.213756.

(56) Dias, F. B.; Penfold, T. J.; Monkman, A. P. Photophysics of Thermally Activated Delayed Fluorescence Molecules. *Methods Appl. Fluoresc.* No. 1. https://doi.org/10.1088/2050-6120/aa537e.

(57) Jaffé, H. H.; Miller, A. L. The Fates of Electronic Excitation Energy. *J. Chem. Educ.* **1966**, *43* (9), 469–473. https://doi.org/10.1021/ed043p469.

(58) Wei, Y.; Zhou, M.; Zhou, Q.; Zhou, X.; Liu, S.; Zhang, S.; Zhang, B. Triplet-Triplet Annihilation Upconversion Kinetics of C60-Bodipy Dyads as Organic Triplet Photosensitizers. *Phys. Chem. Chem. Phys.* **2017**, *19* (33), 22049–22060. https://doi.org/10.1039/c7cp03840b.

(59) Vázquez, R. J.; Yun, J. H.; Muthike, A. K.; Howell, M.; Kim, H.; Madu, I. K.; Kim, T.; Zimmerman, P.; Lee, J. Y.; III, T. G. New Direct Approach for Determining the Reverse Intersystem Crossing Rate in Organic Thermally Activated Delayed Fluorescent (TADF) Emitters. *J. Am. Chem. Soc.* **2020**. https://doi.org/10.1021/jacs.0c01225.

(60) Chen, X. K.; Tsuchiya, Y.; Ishikawa, Y.; Zhong, C.; Adachi, C.; Brédas, J. L. A New Design Strategy for Efficient Thermally Activated Delayed Fluorescence Organic Emitters: From Twisted to Planar Structures. *Adv. Mater.* **2017**, *29*, 1–8. https://doi.org/10.1002/adma.201702767.

(61) Jiao, J.; Kang, J. X.; Ma, Y.; Zhao, Q.; Li, H.; Zhang, J.; Chen, X. Aggregation-Induced Fluorescence of Carbazole and o-Carborane Based Organic Fluorophore. *Front. Chem.* **2019**, *7*, 1–10. https://doi.org/10.3389/fchem.2019.00768.

(62) Mei, J.; Hong, Y.; Lam, J. W. Y.; Qin, A.; Tang, Y.; Tang, B. Z. Aggregation-Induced Emission: The Whole Is More Brilliant than the Parts. *Adv. Mater.* **2014**, *26*, 5429–5479. https://doi.org/10.1002/adma.201401356.

(63) Muthike, A. K.; Carlotti, B.; Madu, I. K.; Jiang, H.; Kim, H.; Wu, Q.; Yu, L.; Zimmerman, P. M.; Goodson, T. The Role of the Core Attachment Positioning in Triggering Intramolecular Singlet Exciton Fission in Perylene Diimide Tetramers. *J. Phys. Chem. B* **2021**, *125*, 5114–5131. https://doi.org/10.1021/acs.jpcb.1c02534.

(64) Dias, F. B. Kinetics of Thermal-Assisted Delayed Fluorescence in Blue Organic Emitters with Large Singlet – Triplet Energy Gap. *Philos. Trans. R. Soc. A* **2015**, No. 373.

(65) Rahimi-Nasrabadi, M.; Zahedi, M. M.; Pourmortazavi, S. M.; Heydari, R.; Rai, H.; Jazayeri, J.; Javidan, A. Simultaneous Determination of Carbazole-Based Explosives in

Environmental Waters by Dispersive Liquid-Liquid Microextraction Coupled to HPLC with UV-Vis Detection. *Microchim. Acta* **2012**, *177* (1–2), 145–152. https://doi.org/10.1007/s00604-012-0762-0.

(66) Siraj, N.; Das, S.; Hasan, F.; Lu, C.; Kiruri, L. W.; Steege Gall, K. E.; Warner, I. M. Enhanced S2 Emission in Carbazole-Based Ionic Liquids. *RSC Adv.* **2015**, *5* (13), 9939–9945. https://doi.org/10.1039/c4ra12362j.

(67) Hu, M.; Liu, Y.; Chen, Y.; Song, W.; Gao, L.; Mu, H.; Huang, J.; Su, J. Highly Efficient Triazine/Carbazole-Based Host Material for Green Phosphorescent Organic Light-Emitting Diodes with Low Efficiency Roll-Off. *RSC Adv.* **2017**, *7* (12), 7287–7292. https://doi.org/10.1039/c6ra27770e.

(68) Ju, K. Y.; Fischer, M. C.; Warren, W. S. Understanding the Role of Aggregation in the Broad Absorption Bands of Eumelanin. *ACS Nano* **2018**, *12*, 12050–12061. https://doi.org/10.1021/acsnano.8b04905.

(69) Mataga, N.; Kaifu, Y.; Koizumi, M. Solvent Effects upon Fluorescence Spectra and the Dipolemoments of Excited Molecules. *Bull. Chem. Soc. Jpn.* **1956**, *29* (4), 465–470. https://doi.org/10.1246/bcsj.29.465.

(70) Wang, H.; Kong, H.; Zheng, J.; Peng, H.; Cao, C.; Qi, Y.; Fang, K.; Chen, W. Systematically Exploring Molecular Aggregation and Its Impact on Surface Tension and Viscosity in High Concentration Solutions. *Molecules* **2020**, *25*, 1–9.

(71) Potai, R.; Kamphan, A.; Traiphol, R. On the Formation of Non-Emissive and Emissive Aggregates of Regioregular Poly(3-Octylthiophene) in Different Local Environments. *Synth. Met.* **2014**, *187* (1), 136–144. https://doi.org/10.1016/j.synthmet.2013.10.033.

(72) Younis, O.; Tolba, M. S.; Orabi, E. A.; Kamal, A. M.; Hassanien, R.; Tsutsumi, O.; Ahmed, M. Biologically-Active Heterocyclic Molecules with Aggregation-Induced Blue-Shifted Emission and Efficient Luminescence Both in Solution and Solid States. *J. Photochem. Photobiol. A Chem.* **2020**, *400*. https://doi.org/10.1016/j.jphotochem.2020.112642.

(73) Liu, H.; Gu, Y.; Dai, Y.; Wang, K.; Zhang, S.; Chen, G.; Zou, B.; Yang, B. Pressure-Induced Blue-Shifted and Enhanced Emission: A Cooperative Effect between Aggregation-Induced Emission and Energy-Transfer Suppression. *J. Am. Chem. Soc.* **2020**, *142*, 1153–1158. https://doi.org/10.1021/jacs.9b11080.

(74) Imato, T. Solvent Eff Ect on Thermally Activated Delayed Fluorescence By. *J. Phys. Chem. A* **2013**, *117*, 5607–5612.

(75) Northey, T.; Stacey, J.; Penfold, T. J. The Role of Solid State Solvation on the Charge Transfer State of a Thermally Activated Delayed Fluorescence Emitter. *J. Mater. Chem. C* **2017**, *5*, 11001–11009. https://doi.org/10.1039/C7TC04099G.

(76) Serevičius, T.; Skaisgiris, R.; Dodonova, J.; Fiodorova, I.; Genevičius, K.; Tumkevičius, S.; Kazlauskas, K.; Juršėnas, S. Temporal Dynamics of Solid-State Thermally Activated Delayed Fluorescence: Disorder or Ultraslow Solvation? *J. Phys. Chem. Lett.* **2022**, *13* (7), 1839–1844. https://doi.org/10.1021/acs.jpclett.1c03810.

(77) Kumar, M.; Pereira, L. Effect of the Host on Deep-Blue Organic Light-Emitting Diodes Based on a TADF Emitter for Roll-off Suppressing. *Nanomaterials* **2019**, *9* (9). https://doi.org/10.3390/nano9091307.

(78) Debye, P.; Bueche, F. The Dielectric Constant of Polystyrene Solutions. **1950**, 235–238. https://doi.org/10.1201/b15897-2.

(79) Cho, Y. J.; Wee, K. R.; Son, H. J.; Cho, D. W.; Kang, S. O. A Detailed Investigation of Light-Harvesting Efficiency of Blue Color Emitting Divergent Iridium Dendrimers with Peripheral Phenylcarbazole Units. *Phys. Chem. Chem. Phys.* **2014**, *16* (10), 4510–4521. https://doi.org/10.1039/c3cp53797h.

(80) Mao, T.; Gou, Y.; Wang, J.; Wang, H. Synthesis and Properties of Well-Defined Carbazole-Containing Fluorescent Star Polymers of Different Arms. *E-Polymers* **2017**, *17* (1), 15–22. https://doi.org/10.1515/epoly-2016-0076.

(81) Jou, J. H.; Kumar, S.; Tavgeniene, D.; An, C. C.; Fang, P. H.; Zaleckas, E.; Grazulevicius, J. V.; Grigalevicius, S. Wet-Process Feasible Novel Carbazole-Type Molecular Host for High Efficiency Phosphorescent Organic Light Emitting Diodes. *J. Mater. Chem. C* **2014**, *2* (41), 8707–8714. https://doi.org/10.1039/c4tc01423e.

(82) Joseph, V.; Thomas, K. R. J.; Singh, M.; Sahoo, S.; Jou, J. H. Manipulation of Donor–Acceptor Interactions in Carbazole-Based Emitters by Chromophore Choice To Achieve Near-UV Emission. *European J. Org. Chem.* **2017**, *2017* (45), 6660–6670. https://doi.org/10.1002/ejoc.201701285.

(83) Zheng, C.; Xiang, X. Spectroscopic Study of Aggregation of Carbazole Units. *J. Fluoresc.* **2019**, *29* (6), 1343–1348. https://doi.org/10.1007/s10895-019-02457-2.

(84) Hoffmann, S. T.; Schrögel, P.; Rothmann, M.; Albuquerque, R. Q.; Strohriegl, P.; Köhler, A. Triplet Excimer Emission in a Series of 4,4′-Bis(N -Carbazolyl)-2,2′-Biphenyl Derivatives. *J. Phys. Chem. B* **2011**, *115* (3), 414–421. https://doi.org/10.1021/jp107408e.

(85) Benten, H.; Jiamo, G.; Ohkita, H.; Ito, S.; Yamamoto, M.; Sakumoto, N.; Hori, K.; Tohda,

Y.; Tani, K. Intramolecular Singlet and Triplet Excimers of Triply Bridged [3.3.n](3,6,9)Carbazolophanes. *J. Phys. Chem. B* **2007**, *111*, 10905–10914. https://doi.org/10.1021/jp0723214.

(86) Ge, S.; Li, B.; Meng, X.; Yan, H.; Yang, M.; Dong, B.; Lu, Y. Aggregation-Induced Emission, Multiple Chromisms and Self-Organization of N-Substituted-1,8-Naphthalimides. *Dye. Pigment.* **2018**, *148*, 147–153. https://doi.org/10.1016/j.dyepig.2017.08.013.

(87) Savchenko, V. V.; Zimin, A. A.; Ignatova, N. Y.; Kimberg, V.; Gel'Mukhanov, F.; Polyutov, S. P. Size-Dependent Blinking of Molecular Aggregate Total Emission. *J. Phys. Conf. Ser.* **2017**, *917*. https://doi.org/10.1088/1742-6596/917/6/062051.

(88) Ghosh, A.; De, C. K.; Chatterjee, T.; Das, A.; Roy, D.; Routh, T.; Mandal, P. K. Correlation between Size of Nano-Aggregates and Excitation Wavelength Dependent Fluorescence Emission in Room Temperature Ionic Liquids: A Case Study with Emim[FAP]. *Chem. Phys. Impact* **2021**, *3*, 100054. https://doi.org/10.1016/j.chphi.2021.100054.

(89) Witte, F.; Rietsch, P.; Nirmalananthan-Budau, N.; Weigert, F.; Götze, J. P.; Resch-Genger, U.; Eigler, S.; Paulus, B. Aggregation-Induced Emission Leading to Two Distinct Emissive Species in the Solid-State Structure of High-Dipole Organic Chromophores. *Phys. Chem. Chem. Phys.* **2021**, *23*, 17521–17529. https://doi.org/10.1039/d1cp02534a.

(90) Jimenez, E. R.; Rodríguez, H. Aggregation-Induced Emission: A Review of Promising Cyano-Functionalized AIEgens. *J. Mater. Sci.* **2020**, *55* (4), 1366–1387. https://doi.org/10.1007/s10853-019-04157-5.

(91) He, Z.; Ke, C.; Tang, B. Z. Journey of Aggregation-Induced Emission Research. *ACS Omega* **2018**, *3*, 3267–3277. https://doi.org/10.1021/acsomega.8b00062.

(92) Kumar, K.; Tarai, M.; Mishra, A. K. Unconventional Steady-State Fluorescence Spectroscopy as an Analytical Technique for Analyses of Complex-Multifluorophoric Mixtures. *TrAC - Trends Anal. Chem.* **2017**, *97*, 216–243. https://doi.org/10.1016/j.trac.2017.09.004.

(93) Irkhin, P.; Najafov, H.; Podzorov, V. Steady-State Photoconductivity and Multi-Particle Interactions in High-Mobility Organic Semiconductors. *Sci. Rep.* **2015**, *5*, 1–9. https://doi.org/10.1038/srep15323.

(94) Banerjee, S.; Both, A. K.; Sarkar, M. Probing the Aggregation and Signaling Behavior of Some Twisted 9,9′-Bianthryl Derivatives: Observation of Aggregation-Induced Blue-Shifted Emission. *ACS Omega* **2018**, *3*, 15709–15724.

https://doi.org/10.1021/acsomega.8b02232.

(95) Zhang, W.; Kong, J.; Hu, D.; Tao, M.; Niu, X.; Vdović, S.; Aumiler, D.; Ma, Y.; Xia, A. Solvation-Dependent Excited-State Dynamics of Donor-Acceptor Molecules with Hybridized Local and Charge Transfer Character. *J. Phys. Chem. C* **2020**, *124* (10), 5574–5582. https://doi.org/10.1021/acs.jpcc.0c00003.

(96) Wen, Y.; Liu, H.; Zhang, S.; Gao, Y.; Yan, Y.; Yang, B. One-Dimensional π-π Stacking Induces Highly Efficient Pure Organic Room-Temperature Phosphorescence and Ternary-Emission Single-Molecule White Light. *J. Mater. Chem. C* **2019**, *7*, 12502–12508. https://doi.org/10.1039/c9tc04580e.

(97) Chakraborty, S.; Debnath, P.; Dey, D.; Bhattacharjee, D.; Hussain, S. A. Formation of Fluorescent H-Aggregates of a Cyanine Dye in Ultrathin Film and Its Effect on Energy Transfer. *J. Photochem. Photobiol. A Chem.* **2014**, *293*, 57–64. https://doi.org/10.1016/j.jphotochem.2014.07.018.

(98) Kondakov, D. Y. Triplet-Triplet Annihilation in Highly Efficient Fluorescent Organic Light-Emitting Diodes: Current State and Future Outlook. *Philos. Trans. R. Soc. A Math. Phys. Eng. Sci.* **2015**, No. 2044. https://doi.org/10.1098/rsta.2014.0321.

(99) Naqvi, B. A.; Schmid, M.; Crovini, E.; Sahay, P.; Naujoks, T.; Rodella, F.; Zhang, Z.; Strohriegl, P.; Bräse, S.; Zysman-Colman, E.; Brütting, W. What Controls the Orientation of TADF Emitters? *Front. Chem.* **2020**, *8* (September), 1–11. https://doi.org/10.3389/fchem.2020.00750.

(100) Serevičius, T.; Skaisgiris, R.; Dodonova, J.; Kazlauskas, K.; Juršenas, S.; Tumkevičius, S. Minimization of Solid-State Conformational Disorder in Donor-Acceptor TADF Compounds. *Phys. Chem. Chem. Phys.* **2019**, *22* (1), 265–272. https://doi.org/10.1039/c9cp05907e.

(101) Kim, K. H.; Kim, J. J. Origin and Control of Orientation of Phosphorescent and TADF Dyes for High-Efficiency OLEDs. *Adv. Mater.* **2018**, *30* (42). https://doi.org/10.1002/adma.201705600.

(102) Zimmermann, J.; Mulet, R.; Scholes, G. D.; Wellens, T.; Buchleitner, A. Improving Triplet-Triplet-Annihilation Based Upconversion Systems by Tuning Their Topological Structure. *J. Chem. Phys.* **2014**, No. 141. https://doi.org/10.1063/1.4901336.

(103) Noriega, R.; Barnard, E. S.; Ursprung, B.; Cotts, B. L.; Penwell, S. B.; Schuck, P. J.; Ginsberg, N. S. Uncovering Single-Molecule Photophysical Heterogeneity of Bright, Thermally Activated Delayed Fluorescence Emitters Dispersed in Glassy Hosts. *J. Am. Chem. Soc.* **2016**, *138* (41), 13551–13560. https://doi.org/10.1021/jacs.6b05488.

5.8. Supporting Information

Figure 5.8.1 Normalized absorbance spectra of the 20% - 60% and 99% H_2O fractions.

Figure 5.8.2 Emission intensities of the investigated THF/H_2O solutions and films.

Figure 5.8.3 Transient absorption spectra of BCC-TPTA in 20% - 99% H_2O fractions.

Figure 5.8.4 Transient absorption spectra of BCC-TPTA in DPEPO, PMMA, and PS films.

Figure 5.8.5 Time-resolved emission spectra of the 20% - 60% and 99% H_2O fractions.

Figure 5.8.6. Emission lifetime traces of the 0% - 40% H_2O fractions obtained using the TCSPC technique.

Table 5.8.1 Emissive lifetime values of the second emissive component for the peaks observed in the time-resolved emission spectra.

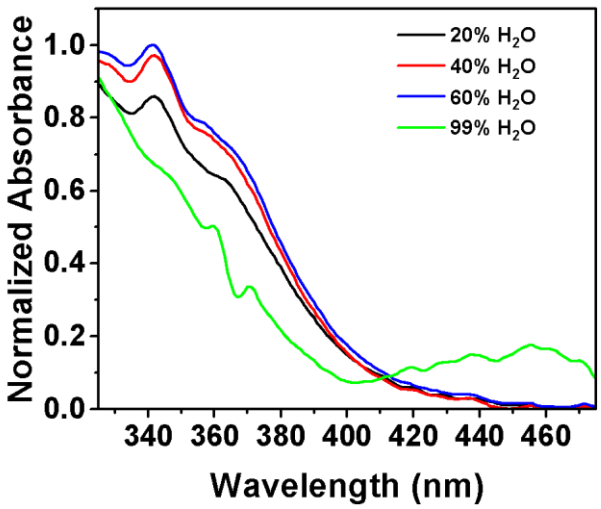


Figure 5.8.1 Normalized absorbance spectra of the 20% - 60% and 99% H_2O fractions.

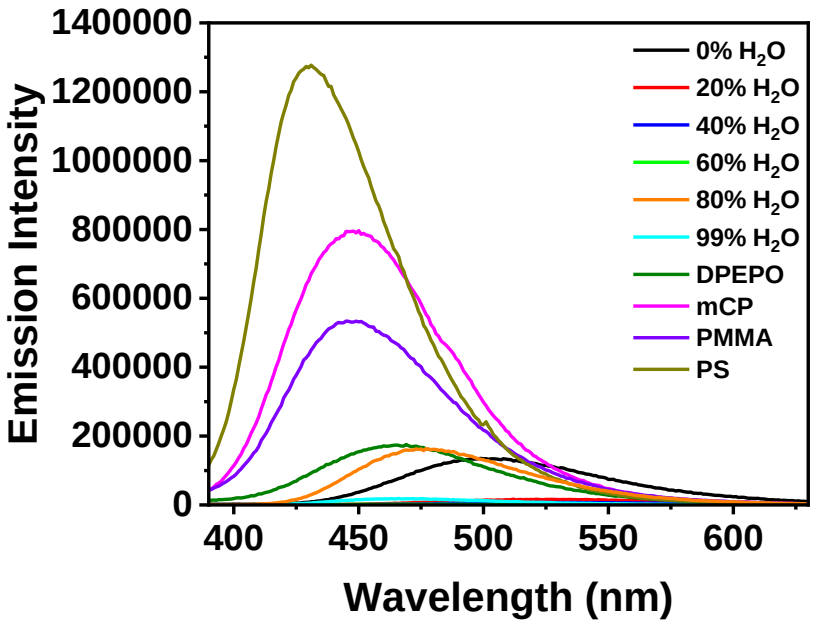


Figure 5.8.2 Emission intensities of the investigated THF/H_2O solutions and films.

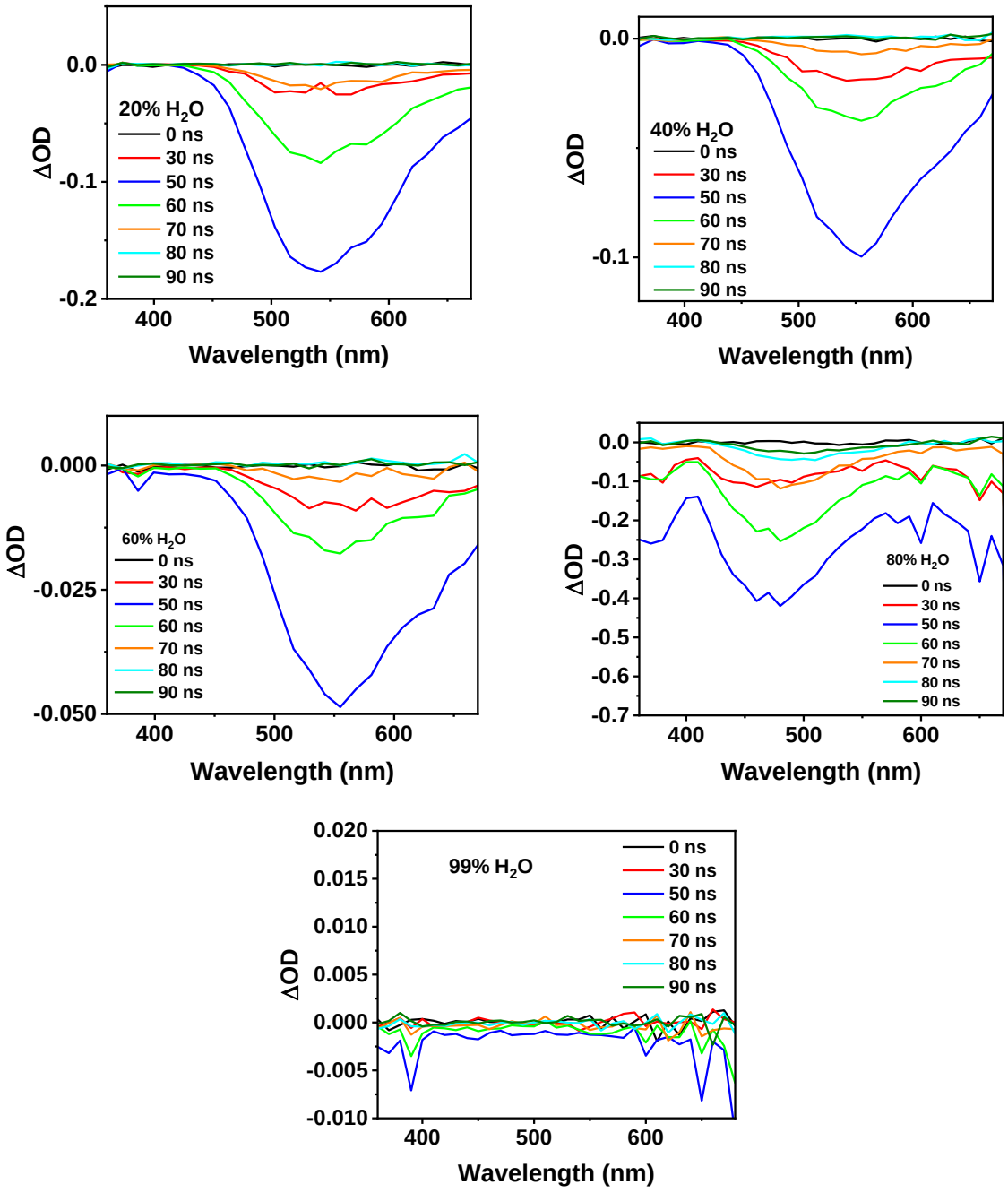


Figure 5.8.3 Transient absorption spectra of BCC-TPTA in 20% - 99% H_2O fractions.

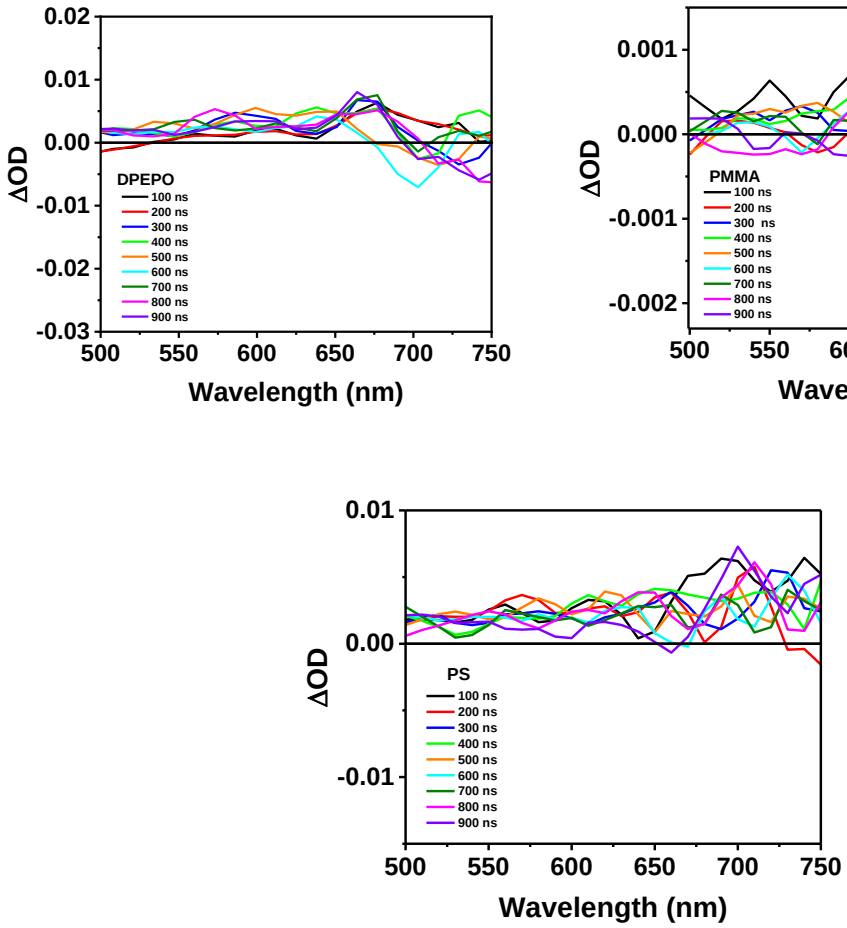


Figure 5.8.4 Transient absorption spectra of BCC-TPTA in DPEPO, PMMA, and PS films.

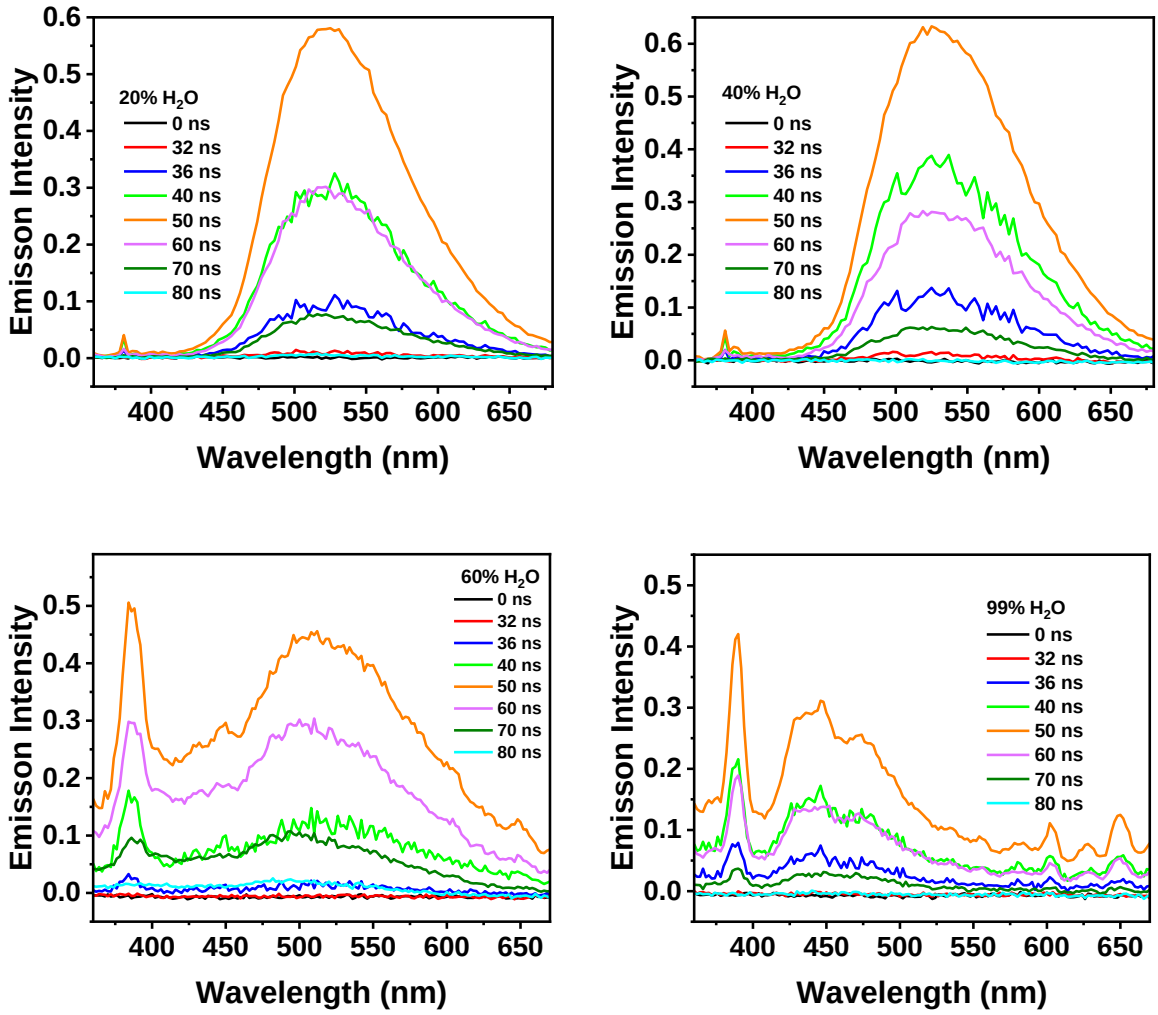


Figure 5.8.5 Time-resolved emission spectra of the 20% - 60% and 99% H_2O fractions.

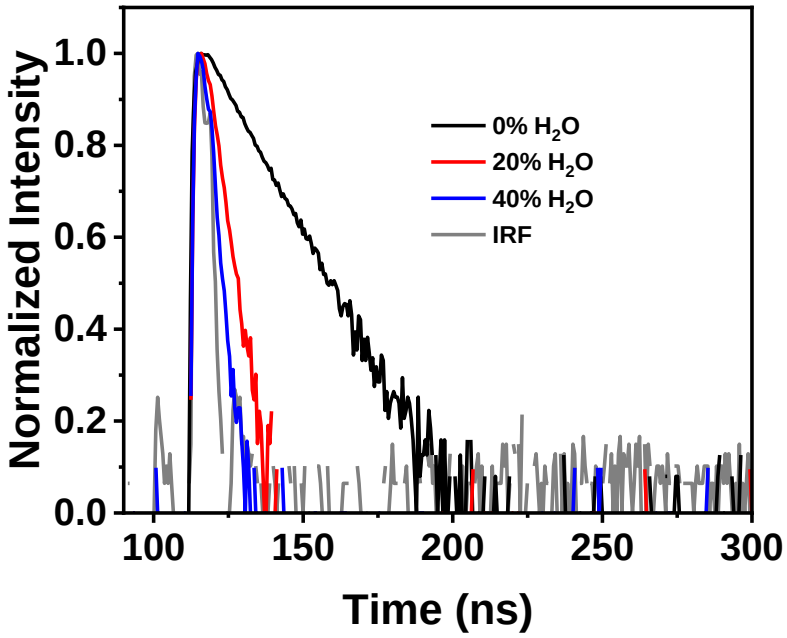


Figure 5.8.6. Emission lifetime traces of the 0% - 40% H_2O fractions obtained using the TCSPC technique.

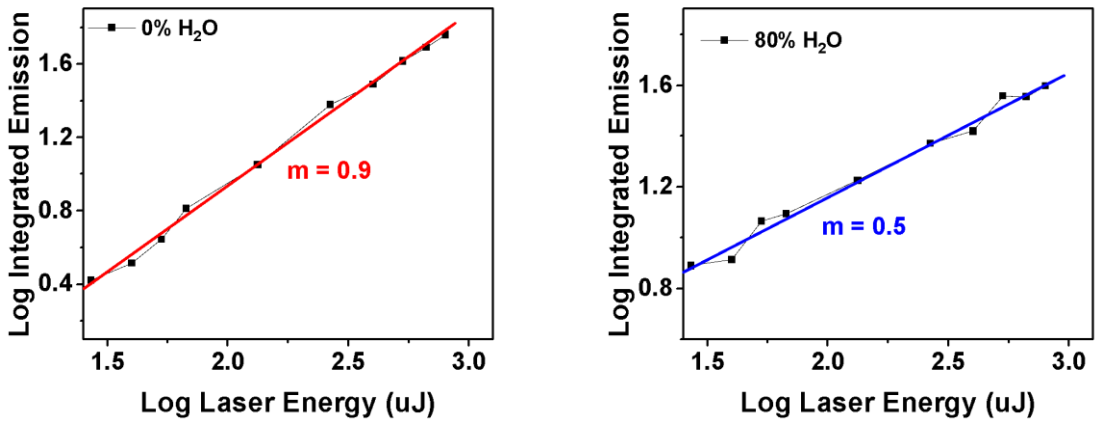


Figure 5.8.7. Log-log plots of emission intensity vs excitation energy of the 0% and 80% H_2O fractions.

Sample	1st λ_{em} τ_2 (ns)	2nd λ_{em} τ_2 (ns)
0% H_2O	–	–
20% H_2O	–	–

40% H_2O	–	–
60% H_2O	–	–
80% H_2O	15	26
99% H_2O	23	26
5wt% in DPEPO	28	27
5wt% in mCP	25	27
5wt% in PMMA	25	22
5wt% in PS	60	63

Table 5.8.1. The lifetime values of the second emissive component for the peaks observed in the time-resolved emission spectra.

Chapter 6: Dissertation Summary, Conclusions, and Future Outlook

6.1 Dissertation Summary

There were two main goals of this dissertation: 1) to better the understanding of structure-function relationships regarding which design motif is better suited for TADF-activity and 2) elucidate the influence of the host material on the guest emitter photophysics. This work would not only aid in the development of higher quality OLEDs, but also provide valuable information regarding the influence of host materials which would have impact over multiple fields.

In chapter one, a history concerning the development of OLED technology with a focus on the emitter design is provided. There are three generations of OLEDs discussed in this chapter: the first-generation fluorescent-based OLEDs, the second-generation phosphorescence-based OLEDs, and the third-generation TADF-based OLEDs. The first generation of OLED suffered from low EQEs within the single digits due to only having access to the 25% S_1. The blue emitters from this generation also suffered from aggregation quenching effects which lead to further issues. The second generation of phosphorescent-based OLEDs were able to achieve significantly greater EQEs, largely due to having access to the 75% T_1. The emitters used in this generation typically incorporated heavy rare metals into their molecular design such as iridium and platinum. Reliance on such rare metals makes these emitters relatively expensive to produce and comes with sustainability concerns. In addition to this, the OLEDs of this generation suffered from triplet-triplet annihilation which decreases device EQE along with the blue OLEDs suffering greater degradation than their red and green counterparts.

TADF emitters arose as a means to address the concerns from the previous generations' emitters. With the TADF mechanism, non-emissive triplets can be upconverted into emissive singlets through the absorption of the surrounding thermal energy. These emitters are also completely organic making them cheaper than their phosphorescent counterparts. Being fully organic allows for a wide range of emissive designs to be explored. However, this freedom has lead to some false assignments of being TADF-active. Thus, this dissertation seeks to elucidate the properties that govern the TADF mechanism. Namely, it investigates the structure-function relationship of TADF to determine what emitter design motif is best suited for this process and it investigates the change in emitter photophysics from solution to solid-state.

In chapter two, the experimental techniques used in this dissertation are described. Linear, nonlinear, steady-state, and time-resolved optical spectroscopic techniques are utilized to characterize the excited state and emissive dynamics of reported TADF emitters. They include: 1) steady-state absorption and emission which is used to determine the absorbance and emission spectra of the materials, calculate the molar extinction coefficient, and the fluorescence quantum yield, 2) two-photon absorption spectroscopy which is utilized to calculate the two-photon absorption cross-sections which are then related to the charge-transfer characteristics of the emitters, 3) ultrafast fluorescence up-conversion which provides insight into the emissive lifetime on the femtosecond timescale, 4) time-resolved correlated single-photon counting which provides insight into the emissive lifetime on the nanosecond timescale, and 5) nanosecond transient absorption spectroscopy which is essential to this study for probing the emissive and non-emissive excited state, calculate the rate of reverse intersystem crossing, obtain the time resolved emission spectra, and ultimately determine the emissive mechanism.

The first study of this dissertation is described in chapter three, where the structure-function relationship between emitter design and emissive mechanism are investigated. Here, two design motifs are compared to determine their suitability for achieving TADF-activity. The first motif consists of a carbazole-based donor unit being attached to a diphenyl triazine by a phenylene linker (Trz-acceptor compounds). The second motif consists of a carbazole-based donor unit being directly linked to a phthalonitrile acceptor unit (PN-acceptor compounds). Comparison of these two motifs revealed that the motif adopted by the Trz-acceptor compounds is not well suited for TADF-activity. This is due largely to the linker inhibiting sufficient HOMO/LUMO separation that causes a greater ΔE_{ST} and decreased SOC. In contrast, the PN-acceptor compounds are better suited to TADF-activity due to them having greater HOMO/LUMO separation. This allows for a smaller ΔE_{ST} and SOC. It was found that the PN-acceptor compounds have a $k_{rISC} \geq 10^3$, which is sufficient to outcompete phosphoresce.

In chapter four, the influence of the linker is investigated further. Here, a BBO core is used as the acceptor unit with multiple carbazole donors being attached to it via a phenylene linker. It was found that the emitters with two carbazole donors are fluorescent compounds, not displaying any of the characteristics associated with TADF-activity. Interestingly, the emitters with four carbazole donors did not achieve TADF-activity, but instead displayed characteristics typical of a phosphorescent compound. These findings indicate that it is possible to enhance SOC between the singlet and triplet manifolds through the addition of multiple donor units. However, the linker still inhibits sufficient HOMO/LUMO separation and this is a critical requirement for TADF-activity.
In chapter 5, an investigation was conducted to determine the degree of influence the emitter's environment has on its photophysics. Specifically, the emissive and excited state dynamics of the BCC-TPTA emitter in monomer solution, aggregate solution, and solid-state films using hosts of

varying properties were observed and compared. The quantum yield measurements revealed that two films that utilize mCP and PMMA as the host materials have significantly enhanced quantum yields than the monomer solution. Transient absorption and emissive lifetime characterization measurements indicated that the triplet-excited state played a significant role in the emissive mechanism of the solid-state films. Interestingly, aggregate emission was observed in the time-resolved emission spectra of each film where the aggregate emission has a high degree of overlap with the monomer emission. It was determined, via log-log plots of emission intensity vs laser excitation energy, that the DPEPO and PMMA films utilize the TADF mechanism and the mCP and PS films utilize the TTA-UC mechanism. However, at higher excitation energies, all films display a slope similar to that of the aggregate solution. This was related to the guest-host interactions and guest-guest interactions, where the TADF-active films are capable of hydrogen bonding interactions with the emitter and the TTA-UC films are capable of guest-host aromatic ring interactions. Such interactions have been known to determine the orientation of the emitter which affects the efficiency of the emissive mechanism. The host material also affects the degree of emitter aggregation, where aggregates could be beneficial or detrimental to the emissive mechanism.

6.2 Conclusions

Overall, the use of time-resolved and nonlinear optical spectroscopic techniques in this dissertation has allowed for the investigation of the excited state dynamics of different types of emitters in different environments. This work has highlighted the need for proper characterization of newly developed emitters, specifically designating emitters as either TADF-inactive or TADF-active. This work also serves to highlight the importance of considering the properties of the host material as they play a significant role in the emissive and excited state dynamics, as described in

chapter five. Three main conclusions can be drawn from these studies: 1) the use of a linker in the molecular design inhibits sufficient HOMO/LUMO separation, which impedes TADF-activity, and it is thus better to utilize multiple donors that are directly linked to the acceptor unit, 2) the use of multiple donors and a linker does succeed in enhancing the SOC within the emitter but may induce phosphorescence instead of the desired TADF emission due to the linker again inhibiting sufficient HOMO/LUMO separation, and 3) the observed second emissive component is not unique to a particular guest-host pairing for the BCC-TPTA emitter. Instead, the observed emission dynamics are the result of multiple and simultaneous emissive mechanisms including aggregate emission, TADF, and TTA-UC. The contribution of each of the emissive mechanisms is influenced by the guest-host interactions, specifically hydrogen bonding or non-bonding interactions between the aromatic moieties of the guest and host molecules.

These conclusions may prove useful for the next generation of OLEDs that utilize TADF emitters, either as the main emissive component or as sensitizers for other compounds. For example, the emerging 4th generation of OLEDs utilize TADF emitters to transfer energy to other chromophores. Having knowledge of the relative tendencies of different host materials to form aggregates and a better understanding of guest-host interactions will be imperative for choosing the proper host for a particular TADF-based OLED. Such information is also useful for other fields that utilize solid-state films.

6.3 Future Outlook

While the work described in this dissertation expands upon the current knowledge within the field of TADF, more work is required to fully understand all parameters that play a role in the observed emission dynamics. Thus, suggestions are made here that would be of use for the next researcher(s) to tackle such an investigation. These suggestions include: 1) determining which of

guest-host interactions or aggregates within the film have a greater influence over the observed emissive and excited state dynamics, and 2) enhancing the ESA signal obtained for solution and solid-state film samples.

Regarding the first suggestion, I suggest first determining what method of film fabrication results in the lowest degree of emitter aggregation, such as comparing thermally assisted vaporization and spin-coating. Once this is completed, experiments can be conducted where the wt% of the emitter is changed from extremely low (ex. 0.01 wt%) to as high as possible while still not inducing aggregation. Doing so will aid in quantitatively determining the degree of influence guest-host interactions have over the emissive mechanism. For example, should hydrogen bonding have a significant impact on TADF efficiency in the BCC-TPTA/DPEPO film, then an increase in TADF-activity is expected as the BCC-TPTA wt% is increased as more of these favorable interactions would be occurring at the higher wt%. Then, aggregation can be induced once the influence of the guest-host interactions is determined. If TADF-activity begins to diminish upon introducing aggregates to the film then it would be clear which has the greatest degree of positive influence, guest-host interactions or aggregate formation. This experiment can be repeated for other guest-host pairing and emissive mechanisms.

Regarding the second suggestion, some of the ESA signals obtained for the studies described in previous chapters are significantly smaller than the SE signals for both film and solution samples. Thus, work was initiated to develop a method that would improve the ESA signal intensity to where it could be easily detected by the nsTAS system. What follows is a description of this work, with the method being based on Beer's Law (**Eqn. 6.3.1**) and an investigation conducted by Oh and coworkers.[1]

$$A = \varepsilon c l \qquad \textbf{Equation 6.3.1}$$

In the above equation A is the optical absorbance of the sample, ε is the molar extinction coefficient in units $cm^{-1} * M^{-1}$, c is the sample concentration in units M, and l is the optical pathlength in units cm. With this in mind there are three ways to increase the optical absorbance: 1) change the molar extinction coefficient, 2) increase the sample concentration, or 3) increase the optical pathlength. Of these options only one would be applicable to most systems and that would be increasing the pathlength. This is because ε is a property of the emitter and changing the concentration would also cause issues as that allows for potential aggregation that would alter the emitter photophysics. Therefore, increasing the pathlength through changing the cuvette or sample chamber configuration is the best method of increasing the optical absorbance signal.

This was the approach utilized by Oh and coworkers, where they enhanced the optical steady-state absorbance signal through the use of a custom built scattering chamber.[1] This chamber (**Figure 6.3.1**) increases the number of times that the probe light interacts with the sample, as opposed to the traditional method where the probe light only interacts with the sample once. The

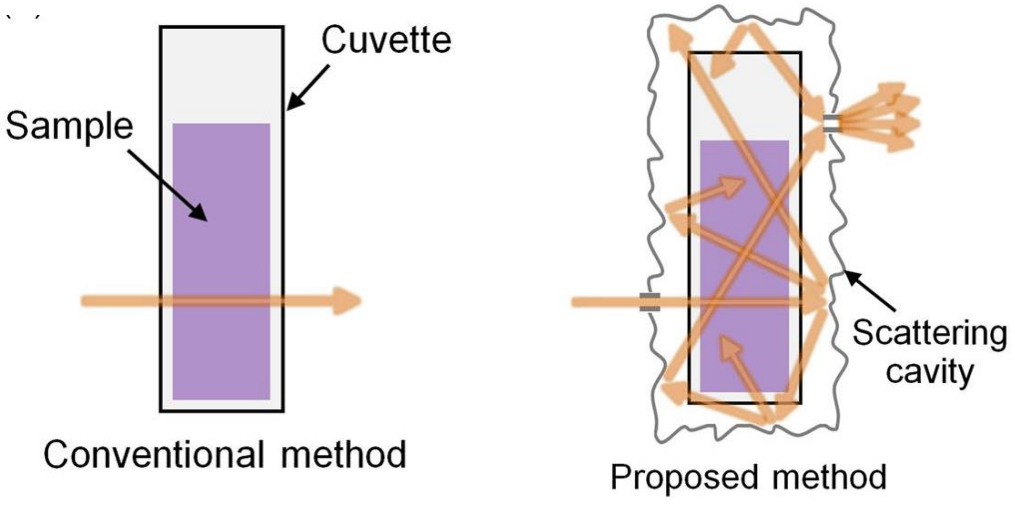


Figure 6.3.1 Schematic of the conventional absorbance setup vs the scattering chamber setup.

researchers achieved this by utilizing the highly reflective material h-BN to fabricate their chamber.

The researchers tested the validity of their method using low concentration solutions (1 mM) of malachite green and crystal violet. They observed a near tenfold increase in absorbance signal through the use of the scattering chamber. This study provides a basis for developing a similar system for use in transient absorption spectroscopy where signal of the excited state absorption (ESA) can be significantly lower than that of the stimulated emission (SE). Though one must keep in mind additional factors that are present in the nsTAS system, such as: the intense excitation laser beam, the intense white probe light, and the timing of the different components. Though what follows did not succeed in increasing the ESA signal it does provide a framework that can be improved upon and, through different generations, should lead to the development of a scattering chamber that provides the desired results.

Though the ultimate goal is to develop a scattering chamber that can be used for films, initial scattering chamber tests were conducted with solutions. This was done with the understanding that solution measurements would be the best comparison to the work described in the previous section and have fewer complications than starting out with film measurements. As such, a dilute solution of the transient absorption standard $[Ru(bpy)_3]^{2+}$ was utilized for this study.

Polytetrafluoroethylene (PTFE) material used to fabricate this first-generation scattering chamber as it was readily available, easily shaped, and has a high degree of reflectance over the wavelength range of interest (**Figure 6.3.2)**.[2] The scattering chamber was fabricated to fit over the solution sample chamber of the nsTAS system. The entry hole for the xenon probe beam and laser excitation beams were placed at the center of their respective faces. The exit hole for the scattered light was offset from the xenon probe's entry hole to ensure that any exiting light had scattered within the chamber.

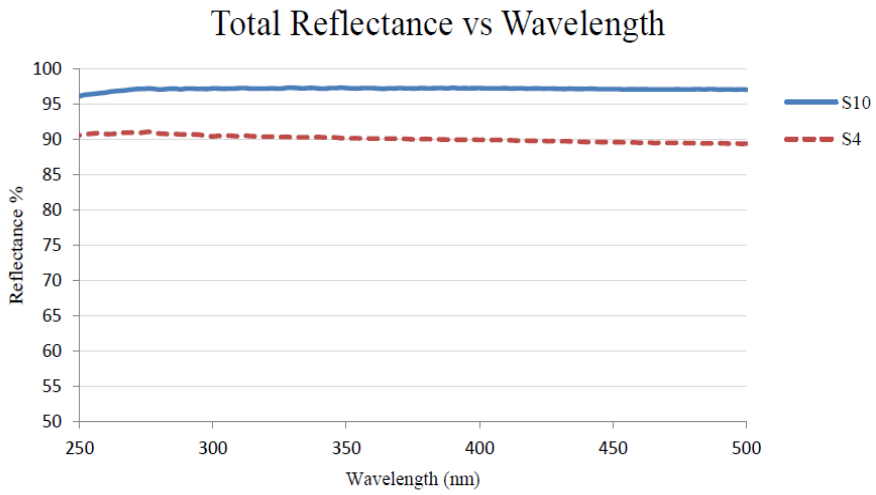


Figure 6.3.2. Total reflectance of PTFE sheet at 0.5 mm thickness (S4) and 2 mm thickness (S10).

Light was verified to escape the scattering chamber by performing the transient absorption measurement without a sample and with the scattering chamber placed on the holder. The signal was expected to be similar to that observed when no sample or chamber is used (**Figure 6.3.3**). There a flat response is observed, indicating no absorbance as expected. However, the signal that's obtained with the sample chamber is slightly different (**Figure 6.3.3.**). Sharp peaks can be observed in the spectrum that utilizes the scattering chamber, suggesting some interference that occurs in the chamber. The source of this interference is still not entirely clear and is still being investigated, though the sharp peaks are reproducible which indicates that the source of the interference is not a randomly generate event.

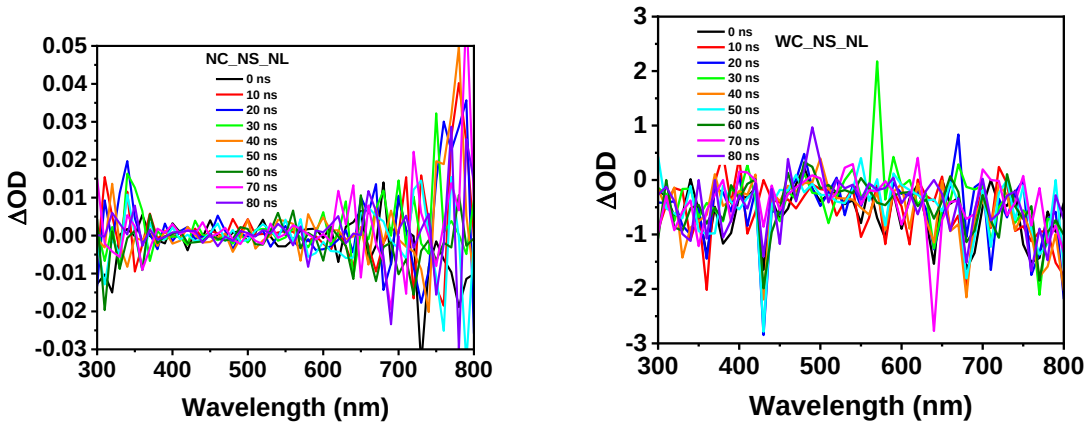


Figure 6.3.3 Signal obtained with no scattering chamber (left) and with the scattering chamber (right), each without a sample placed in the holder.

A dilute solution of the $[Ru(bpy)_3]^{+2}$ standard was used to test the efficiency of the scattering chamber. Transient absorption spectra of the solution were obtained both with and without the scattering chamber being used (**Figure 6.3.4**). Strong ESA and SE signals typical of the standard are observed without the scattering chamber. However, once the scattering chamber is utilized

these distinct peaks are absent. Instead, a spectrum similar to that in **Figure 6.3.3** is observed, indicating that the same interference decreases ESA signal instead of enhancing it.

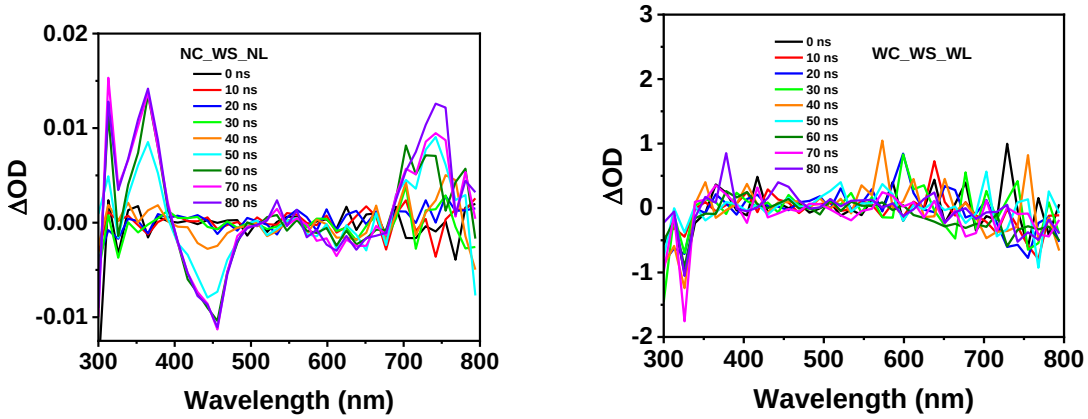


Figure 6.3.4 Transient absorption spectra of dilute $[Ru(bpy)_3]^{2+}$ solution obtained without the scattering chamber (left) and with the scattering chamber (right).

Clearly, alterations to the design of the scattering chamber are required to properly enhance the ESA signal. Such alterations could include changing: 1) the material of the chamber itself, 2) the geometry of the chamber interior, or 3) the placement and size of the entry and exit holes. It is my hope that these suggestions will be of use to the next researchers, allowing them to build upon this work effectively and efficiently.

References

(1) Oh, J.; Lee, K. R.; Park, Y. K. Enhancing Sensitivity in Absorption Spectroscopy Using a Scattering Cavity. *Sci. Rep.* **2021**, No. 1, 1–7. https://doi.org/10.1038/s41598-021-94028-4.

(2) Quill, T.; Weiss, S.; Hirschler, C.; Pankadzh, V.; DiBattista, G.; Arthur, M.; Chen, J. Ultraviolet Reflectance of Microporous PTFE. *Reflection, Scatt. Diffr. from Surfaces* **2008**.